Ph.D. Dissertation

Lidar and S–band radar profiling of the atmosphere: Adaptive processing for Boundary-Layer monitoring, optical-parameter error estimation, and application cases

A thesis submitted to the Universitat Politècnica de Catalunya
in partial fulfillment for the degree of

Doctor of Philosophy

Diego Lange Vega

UNIVERSITAT POLITÈCNICA DE CATALUNYA BARCELONATECH

Remote Sensing Laboratory
Department of Signal Theory and Communications

Doctorate program in
Signal Theory and Communications

Supervisor: Dr. Francesc Rocadenbosch Burillo

Barcelona, June 2014

Lidar and S–band radar profiling of the atmosphere: Adaptive processing for Boundary-Layer monitoring, optical-parameter error estimation, and application cases

[a] Remote Sensing Laboratory
Dept. of Signal Theory and Communications (TSC)
Universitat Politècnica de Catalunya (UPC) / Institut d'Estudis Espacials de Catalunya (IEEC/CRE)
08034 Barcelona, Spain

[b] Agencia Española de Cooperación Internacional para el Desarrollo (AECID)
Ministerio de Asuntos Exteriores y de Cooperación (MAEC)
Barcelona, Spain

Dedicado a mi hermosa y amada familia...

Acknowledgments

The following institutions are gratefully acknowledged for their contribution to this work:

- *Spanish Ministry of Foreign Affairs and Cooperation* (Ministerio de Asuntos Exteriores y de Cooperación, MAEC) - Agencia Española de Cooperación Internacional para el Desarrollo (AECID), for the doctoral studies grant, held by the author from Oct. 1, 2010 to Sept. 30, 2013 (BOE-A-2010-14078).

- *Microwave Remote Sensing Laboratory* (MIRSL) from the Department of Electrical and Computer Engineering at the University of Massachusetts (UMass), for hosting the author during the research stay carried out in this Ph.D.

- *Generalitat de Catalunya - Agency for Management of University and Research Grants* (AGAUR) for the BE-DGR 2012 mobility grant, held by the author from Sept. 17, 2012 to Jan. 10, 2013 (DOGC-6156-25.6.2012).

- *Spanish Ministry of Science and Innovation* (MICINN) and FEDER (European Regional Development Fund) under the R&D projects, TEC2009-09106 and TEC2012-34575, and complementary action CGL2008-01330-E/CLI, funding the RSLab lidar and the measurement campaigns carried out in this Ph.D.

- *European Commission* under the ACTRIS (Aerosols, Clouds, and Trace gases Research InfraStructure Network) FP7 Grant Agreement no. 262254 and EARLINET-ASOS (European Aerosol Research Lidar Network-Advanced Sustainable Observation System) FP6 contract no. RICA-025991 funding the European Lidar Network EARLINET.

- *European Space Agency* (ESA) under the contract no. 21487/08/NL/HE funding CALIPSO-satellite ground-based cal/val lidar measurements at the RSLab.

- *NOAA* Air Resources Laboratory (ARL) for the provision of the HYSPLIT transport and dispersion model; the *German Weather Service* for the air mass backtrajectory analysis, the *Barcelona Supercomputing Center* for forecasts with the Dust Regional Atmospheric Model (DREAM) and the Data User Element of the *European Space Agency* Data for data available from "ATSRWorld Fire Atlas", and The NASA MPLNET data, funded by the *NASA Earth Observing System and Radiation Sciences Program*, tools used in this Ph.D. thesis.

Ante todo, agradezco a Dios por haberme dado el don de la vida, y por la hermosa familia a la que pertenezco, sin la cual difícilmente estaría escribiendo estas líneas. María, Mili, Maiza, que sin importar los títulos familiares, son, desde el principio, tres pilares de mi vida, las tres madres que me enorgullezco de tener. Luís, mi padre que mientras estuvo en este mundo me dio lo mejor de sí, en las buenas y en las malas, sin importar el sacrificio que implique. Sergio, mi hermano menor, que me ha enseñado el valor y la fortaleza de un hermano e hijo en las buenas y en las malas.

A Carola, mi amiga y compañera en este largo viaje, por su amor y comprensión.

My sincere gratitude to my Ph.D. advisor, Dr. Francesc Rocadenbosch for his guidance and strong support during all the thesis stages. It would have been impossible to successfully finish this journey, without his wise advice. I am indebted to him.

I am grateful to Prof. Adolfo Comerón and Dr. Michaël Sicard, for their support, lidar measurement campaigns around Spain, group meetings and CALIPSO nights. I am also grateful to the other faculty and staff members of RSLab, for their support and suggestions during the research work. Special thanks to Dr. Jordi Tiana, Dr. Dhiraj Kumar, Dr. Sergio Tomás, and Umar Saeed for their advice, help and cooperation.

My sincere gratitude is also due to Dr. Stephen Frasier (Microwave Remote Sensing Laboratory, University of Massachusetts) and the rest of the MIRSL staff members for his kind support and help during the research stay carried out in Amherst, MA.

Finally, I would like to express my sincere thanks to Deborah Hutchins and all those who have directly or indirectly assisted me to complete this research work.

Abstract

This Ph.D. thesis addresses remote sensing of the atmosphere by means of lidar and S-band clear-air weather radar, and related data signal processing. Active remote sensing by means of these instruments offers unprecedented capabilities of spatial and temporal resolutions for vertical atmospheric profiling and the retrieval of key optical and physical atmospheric products in an increasing environmental regulatory framework.

The first goal is this Ph.D. concerns the estimation of error bounds in the inversion of the profile of the atmospheric backscatter coefficient from elastic lidar signals (i.e., without wavelength shift in reception when interacting with atmospheric scatterers) by means of the two-component inversion algorithm (the so-called Klett-Fernald-Sasano's algorithm). This objective departs from previous works at the Remote Sensing Lab. (RSLab) of the Universitat Politècnica de Catalunya (UPC) and derives first-order error-propagated bounds (approximate) and total-increment bounds (exact). As distinctive feature in the state of the art, the error bounds merge into a single body both systematic (i.e., user-calibration inputs) and random error sources (finite signal-to-noise ratio, SNR) yielding an explicit mathematical form.

The second goal, central to this Ph.D., tackles retrieval of the Atmospheric Boundary Layer Height (ABLH) from elastic lidar and S-band Frequency-Modulated Continuous-Wave (FMCW) radar observations by using adaptive techniques based on the Extended Kalman Filter (EKF). The filter is based on morphological modeling of the Mixing-Layer-to-Free-Troposphere transition and continuous estimation of the noise covariance information. In the lidar-EKF realization the proposed technique is shown to outperform classic ABLH estimators such as those based on derivative techniques, thresholded decision, or the variance centroid method. The EKF formulation is applied to both ceilometer and UPC lidar records in high- and low-SNR scenes. The lidar-EKF approach is re-formulated and successfully extended to S-band radar scenes (Bragg's scattering) in presence of interferent noise sources (Rayleigh scattering from e.g., insects and birds). In this context, the FMCW feature enables the range-resolved capability. EKF-lidar and EKF-radar ABLH estimates are cross-examined from field campaign results.

Finally, the third goal deals with exploitation of the existing UPC lidar station: In a first introductory part, a modified algorithm for enhancing the dynamic range of elastic lidar channels by "gluing" analog and photon-counting data records is formulated. In a second part, two case examples (including application of the gluing algorithm) are presented to illustrate the capabilities of the UPC lidar in networked atmospheric observation of two recent volcano eruption events as part of the EARLINET (European Aerosol Research Lidar Network). The latter is part of GALION (Global Atmospheric Watch Atmospheric Lidar Observation Network)-GEOSS (Global Earth Observation System of Systems) framework.

Contents

List of Figures

List of Tables

List of Symbols

Roman Symbols

a	Aerosol radius [m]
abs	Sub/super-index term for absorption [·]
aer	Sub/super-index term for aerosol [·]
AOD	Aerosol Optical Depth [·]
AOD_{aero}	Interpolated values of AOD [·]
A_r	Telescope effective area [m^2]
c	Speed of light in vacuum (2.998×10^8 [$m\,s^{-1}$])
D	Radar scatterers diameter [m]
D'	Modified lidar log-range-corrected signal
ΔR	Raw spatial resolution [m]
E	Energy pulse [J]
e	Partial pressure of water vapour [hPa]
E_{in}	Incident laser power density [$W\,m^{-2}$]
f_b^+	Maximum value of f_b[Hz]
f_b^-	Maximum value of f_b[Hz]
f_{br}	Radar beat frequency, moving target [Hz]
f_b	Radar beat frequency, stationary target [Hz]
f_d	Doppler frequency shift [Hz]
f_e	Emitter radar frequency [Hz]
f_r	Received radar frequency [Hz]
G	Radar antenna gain [·]
G_T	Preamplifier gain [V/A]
h	Plank's constant (6.625×10^{-34}[J s])
C_n^2	Refractive index structure function parameter [·]
I	Range interval [samples]
i	Sample index
n	Refractive index [·]
I_0	Initial intensity [$W\,m^{-2}$]
j	Sample index
K	Lidar system constant [$W\,m^3$]
K_{sca}	Backscattered power per solid angle unit [$W\,sr^{-1}$]
M	Multiplication factor [·]
Mie	Subindex term for Mie [·]
mol	Sub/super-index term for molecular [·]
N	Radioelectric refractivity [·]
$N(D)$	Particle size distribution [scatterers/m^3]
NRB	Normalized Relative Backscatter [·]
N_{aer}, N_g, N_R	Aerosol, Gas, Nitrogen molecule number concentration [m^{-3}]
opt	Sub/super-index term for optimal [·]
P	Backscattered power [W]
p	Atmospheric pressure [hPa]
P_0	Emitted laser power [W]
P_r	Radar received power [W]
P_r	Radar transmitted power [W]
Q_{abs}	Absorption efficiency [·]
Q_{back}	Backscatter efficiency [·]
Q_{ext}	Extinction efficiency [·]
Q_{sca}	Scattering efficiency [·]
R	Observation range [m]
Ray	Subindex term for Rayleigh [·]
R_{io}	Detector intrinsic current responsivity [A/W]
R_v	Voltage responsivity [V/W]
R'_v	Net voltage responsivity [V/W]
S_{aer}	Aerosol extinction-to-backscatter ratio (aerosol lidar ratio) [sr]
sca	Sub/super-index term for scattering [·]
S_{mol}	Rayleigh ratio (molecular lidar ratio) [sr]
SR	Scattering Ratio [·]
S_{tot}	Total lidar ratio [sr]

T	Atmospheric transmissivity [·]
t	Time delay [s]
tot	Subindex term for total [·]
U	Range-corrected signal [W m^2]
Va	V_a Analog voltage signal [V]
V_m	Visibility margin [m]
V_{pc}	Photon-counted signal [cps]
V_{sca}	Scattering volume [m^3]
Z	Radar reflectivity factor [·]
Z_e	Equivalent radar reflectivity factor [·]

Greek Symbols

α	Extinction coefficient [m^{-1}]
β	Backscatter coefficient [m^{-1}sr^{-1}]
σ	Cross-section [m^2]
$\Delta\nu$	Frequency shift [Hz]
$\Delta R'$	Effective spatial pulse length [m]
η	Volume radar reflectivity [m^{2}m^{-3}]
κ	Wavelength shift [m^{-1}]
λ, λ_0, λ_R	Wavelength, elastic wavelength, Raman wavelength [nm]
ν_0	Incident frequency [Hz]
ν_R	Frequency shift [Hz]
τ	Optical depth [·]
τ_{dead}	Dead time [s]
τ_l	Pulse duration [s]
ξ_{net}	Optical transmissivity [·]
ζ	Scaling factor [·]

List of Acronyms

ABL Atmospheric Boundary Layer.

ABLH Atmospheric Boundary Layer Height.

ADC Analog-to-Digital Conversion.

AERONET Aerosol Robotic Network.

APD Avalanche Photo-Diode.

ATSR Advanced Along Track Scanning Radiometer.

ca Cabauw (The Netherlands).

CALIOP Cloud-Aerosol LIdar with Orthogonal Polarization.

CALIPSO Cloud-Aerosol Lidar and Infrared Pathfinder Satellite Observation.

CBL Convective Boundary Layer.

CE Central Europe.

CEAMA Centro Andaluz de Medio Ambiente - Universidad de Granada.

CM Central Mediterranean.

CNR-IMAA Consiglio Nazionale delle Ricerche - Istituto di Metodologie per l' Analisi Ambientale.

CW Continuous Wave.

DFT Discrete Fourier Transform.

DIAL Differential Absorption Lidar.

DREAM Dust REgional Atmospheric Model.

EARLINET European Aerosol Research LIdar Network to Establish an Aerosol Climatology.

EAT East Africa Time.

EE Eastern Europe.

EKF Extended Kalman Filter.

EM Eastern Mediterranean.

ESA European Space Agency.

EURAD EURopean Air Pollution Dispersion.

ev Evora (Portugal).

EZ Entrainment Zone.

FMCW Frequency Modulated Continuous Wave.

FOV Field-Of-View.

FT Free Troposphere.

GALION GAW Atmospheric Lidar Observation Network.

GAW Global Atmosphere Watch.

GDAS Global Data Assimilation System.

GEOSS Global Earth Observation System of Systems.

GLAS Geoscience Laser Altimeter System.

GM Gradient Method.

gr Granada (Spain).

GSFC Goddard Space Flight Center.

GUI Graphic User Interface.

hh Hamburg (Germany).

HPBW Half Power BandWidth.

HSRL High Spectral Resolution Lidar.

HYSPLIT Hybrid Single Particle Lagrangian Integrated Trajectory Model.

IB Integrated Backscatter.

IPM Inflexion Point Method.

is Ispra (Italy).

ISNR$_a$ Inverse Analog Signal-to-Noise-Ratio.

KF Kalman Filter.

KFS Klett-Fernald-Sasano two-component inversion algorithm.

KLT Klett one-component inversion algorithm.

la L'Aquila (Italy).

lc Lecce (Italy).

le Leipzig (Germany).

LGM Logarithmic Gradient Method.

lidar LIght Detection And Ranging.

LOS Line-Of-Sight.

LT Local Time.

ma Maisach (Germany).

MIRSL Microwave Remote Sensing Laboratory.

ML Mixing Layer.

MLO Mauna Loa Observatory.

MPLNET Micro Pulse Lidar Network.

na Naples (Italy).

NASA U.S. National Aeronautics and Space Administration.

Nd:YAG Neodymium-doped Yttrium Aluminum Garnet.

NDACC Network for the Detection of Atmospheric Composition Change.

NEP Noise Equivalent Power.

NIR Near InfraRed.

NLSQ Non-Linear Least-SQuares estimators.

OHP Observatoire de Haute-Provence.

OVF Overlap Factor.

PBL Planetary Boundary Layer.

PC Photon-Counting mode.

pl Palaiseau (France).

PMT Photo-Multiplier Tubes.

po Potenza (Italy).

PR Pulsed Radar.

radar RAdio Detection And Ranging.

RASS Radio Acoustic Sounding System.

RF Radio Frequency.

RSLab Remote Sensing Laboratory.

SCC Single Calculus Chain.

SNR Signal-to-Noise ratio.

sodar SOnic Detection And Ranging.

SPALINET Spanish and Portuguese Aerosol LIdar Network.

THM Threshold Method.

UHF Ultra High Frequency.

UMass University of Massachusetts.

UPC Universitat Politècnica de Catalunya.

UTC Coordinated Universal Time.

UV UltraViolet.

VAAC Toulouse Volcanic Ash Advisory Center.

VHF Very High Frequency.

VIS VISible.

WM Wavelet Method.

Chapter 1

Introduction

This Chapter gives an overview of the UPC RSLab multi-spectral lidar system and UMass S-band profiler radar in the context of atmospheric aerosol remote sensing. Next, it proceeds to present the motivation, objectives and organization of this Ph.D. thesis.

1.1 Atmospheric Remote Sensing through lidar and radar

Climate change and air quality are governed by emission, transport and transformation of key atmospheric components (e.g., aerosols, clouds, greenhouse and trace gases) and their interaction with solar radiation. Contrary to greenhouse gases, there are still great uncertainties in the estimates of radiative forcing by short-lived trace gases and aerosol particles.

In this context, "aerosols" can be understood as small particles in suspension in the atmosphere, which interact directly in the Earth's radiation balance, dispersing and absorbing solar and infrared radiation and indirectly modifying cloud formation processes, e.g., by increasing the density/size of water droplets and/or reducing the efficiency of precipitation. The aerosols which most substantially affect the climate are those generated by mankind (industrial pollution), desert dust outbreaks and volcanic eruptions. It is thought that aerosol cooling may partially offset the experienced and expected global warming that is attributed to increases in the amount of carbon dioxide from human activity [*Bösenberg and Hoff*, 2007]. Sustained long-term observations of a comprehensive suite of atmospheric and, in particular, aerosol-profile parameters can be accomplished from multiple coordinated in-situ and ground-based remote sensing sensors, since aerosols can act as tracers of these atmospheric transport processes.

Usually aerosols are located in the lowest part of the atmosphere, commonly know as the *Atmospheric Boundary Layer (ABL)*. According to *Stull* [1988a], the ABL can be defined as *that part of the troposphere that is directly influenced by the presence of Earth's surface, and responds to surface forcings with a time scale of about an hour or less. These forcings include frictional drag, evaporation and transpiration, heat transfer, pollutant emission, and terrain flow modification* (Fig. 1.1). ABL thickness can vary between hundred of meters to few kilometers.

In the low troposphere, the ABL limit is marked by a transition interface known as the *Entrainment Zone (EZ)*, where two different air masses, the *Mixing Layer (ML)* and the *Free Troposphere*

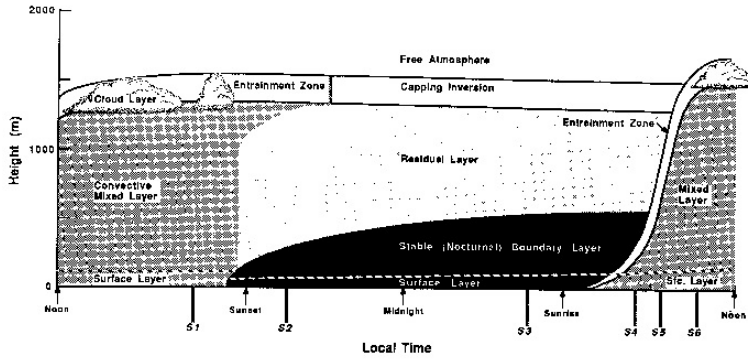

Figure 1.1: 24-hours cycle showing the zones in the ABL. Source: [*Stull*, 1988a].

(FT), merge and interact. Fig. 1.2 shows the location of these layers. Measurements in this transition region provide useful parameters such as the *Atmospheric Boundary Layer Height (ABLH)* or the EZ thickness. These parameters are highly valuable inputs to environmental models since they describe the extension and evolution of the transport of atmospheric constituents [*Stull*, 1988a]. *Radar (Radio Detection and Ranging)* remote sensing systems use microwave radiation to interact with atmosphere constituents and solid targets as "reflecting targets". Basically, radar systems radiate energy into the propagation medium (usually free space) and detects the echo signal from these "reflecting targets" [*Skolnik*, 2001]. The information retrieved can include their shape and location. Unlike common known radars designed to detect aircrafts or ships, weather radar "reflecting targets" can be defined as atmosphere volumes that include the morphology of turbulence and small scale temperature, pressure and humidity variations [*Stull*, 1988b]. These variations and turbulence can cause small refractive index irregularities, which scatter the radar radiated energy [*Sauvageot*, 1992a]. Weather radar systems include, among others, wind profilers and *Frequency Modulated Continuous Wave (FMCW)* radars. A FMCW radar ABL detection example can be seen in Fig. 1.3a.

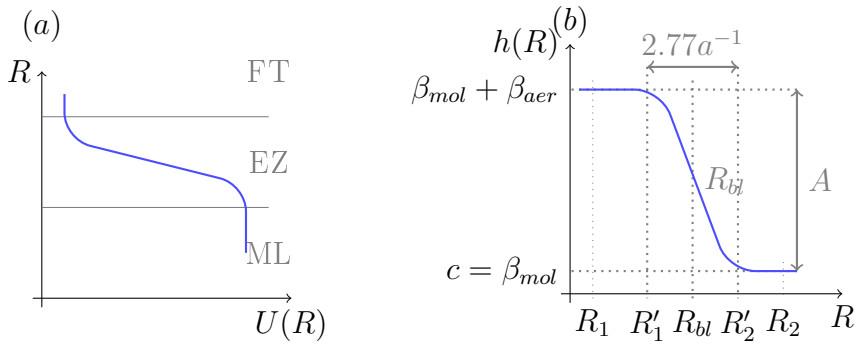

Figure 1.2: Oversimplified description of the ABL. (a) In the ABL model, $U(R)$ is the range-corrected lidar signal (noiseless). ML stands for the "Mixing Layer", EZ for the "Entrainment Zone", and FT for the "Free Troposphere". (b) Idealized ABL erf-curve transition model, $h(R)$, for the total backscatter coefficient with characteristic parameters, R_{bl}, a, A, and c. R_1 and R_2 are the start- and end-range limits defining the length of the observation vector passed to the filter. R'_1 and R'_2 are the start-range and end-range limits of the erf-like ABL transition. Source: *Lange et al.* [2013].

On the other hand, *lidar (Light Detection And Ranging)* remote sensing systems [*Fiocco and*

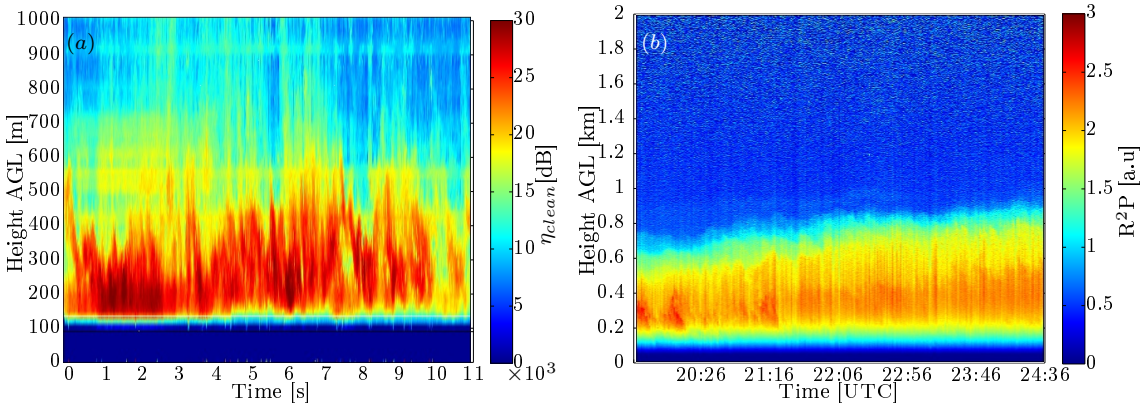

Figure 1.3: ABL case examples from two different remote sensing instruments, the RSLAB multi-spectral lidar and the UMass FMCW S–band atmospheric profiling radar. (*a*) Time-height plot of the volume radar reflectivity signal (Boulder CO, August, 20, 2007). (*b*) Time-height plot of the range-corrected lidar signal for the 1064 nm channel (Barcelona, December, 16, 2010).

Smullin, 1963] are synonyms of laser radar and represent the nearest counterpart to microwave radars, with the exception that microwave radiation has now been replaced by laser radiation. Lidars are currently used on land (fixed-location or transportable) and as sensors mounted in aircraft and satellites for the observation of the terrestrial atmosphere at local and global scale.

Lidar systems offer unprecedented capabilities of environmental, meteorological and spectroscopic probing (with typical spatial resolutions of meters and temporal ones of minutes), thanks to the strong interaction between the laser beams and atmospheric molecules and particles. An ABL detection example for an elastic lidar is depicted in Fig. 1.3b. Besides, the potential interaction mechanisms at play such as elastic and inelastic (i.e. Raman) scattering, absorption, and fluorescence, have extended the applications of these systems to aerosol [*Rocadenbosch*, 2003b], wind, and spectroscopic (e.g., DIAL) lidar sensing [*Collis and Russell*, 1976; *Rocadenbosch*, 2003c].

In lidar systems, the emission of a short laser pulse is followed by the reception of laser radiation scattered from these atmospheric constituents, such as molecules, aerosols, and clouds. The interaction of the incident radiation with these constituents changes the laser beam intensity, the wavelength, or both, depending on the strength of this optical interaction and on the concentration of the interacting species. Consequently, it is possible to retrieve information about the physical state of the atmosphere along the exploration beam path.

1.2 The UPC RSLab in the international context

This Ph.D. study is carried out at the *Remote Sensing Lab (RSLab)* of the *Universitat Politècnica de Catalunya (UPC)*, Barcelona. To outline the lidar activities of the RSLab in the international context, it is first necessary to present EARLINET.

In the European context, *EARLINET (European Aerosol Research Lidar Network to Establish an Aerosol Climatology)*, established in 2000, is the first coordinated ground-based aerosol lidar network whose key remit is the provision of a comprehensive, quantitative, and statistically significant database on the spatial and temporal aerosol distribution on a continental scale [*Bösenberg*

and Matthias, 2003]. At present (2013), the network includes 27 stations distributed over Europe (see Table 1.1, Fig. 1.4a).

The RSLab lidar group of the UPC is part of the EARLINET (Table 1.1, Fig. 2), which is also one of the leading components of *GAW (Global Atmosphere Watch)* programme *GALION (GAW Atmospheric Lidar Observation Network)* since its inception in the year 2000 [*Bösenberg and Hoff*, 2007; *Hoff et al.*, 2008]. The RSLab is also founder of the *Spanish and Portuguese Aerosol Lidar Network (SPALINET)* [*Sicard et al.*, 2009b; *SPALINET*, 2007].

Lidar observations within EARLINET are performed on a regular schedule since May 2000, allowing for the collection of long-term data sets for climatological studies [*Matthias et al.*, 2004a]. In addition to coordinated routine measurements, further observations are devoted to the monitoring of special events such as Saharan dust outbreaks [*Ansmann et al.*, 2003; *Mona et al.*, 2006; *Papayannis et al.*, 2008], forest fires [*Müller et al.*, 2007] and volcanic eruptions [*Pappalardo et al.*, 2004a, 2013; *Wang et al.*, 2008; *Mattis et al.*, 2010; *Sawamura et al.*, 2012; *Sicard et al.*, 2012].

Table 1.1: List of contributing EARLINET lidar systems.

Site	Country	Altitude a.s.l. (m)	Lat. (N)	Long. (E)
Andenes	Norway	380	69.28	16.01
Athens	Greece	200	37.96	23.78
Barcelona	**Spain**	**115**	**41.39**	**2.11**
Belsk	Poland	180	51.84	20.79
Bucharest-Magurele	Romania	93	44.45	26.03
Cabauw	the Netherlands	1	51.97	4.93
Cork	Ireland	75	51.89	-8.49
Evora	Portugal	293	38.57	-7.91
Garmisch-Partenkirchen	Germany	730	47.48	11.06
Granada	Spain	680	37.16	-3.61
Hamburg	Germany	25	53.57	9.97
Ispra	Italy	209	45.82	8.63
L'Aquila	Italy	683	42.38	13.32
Lecce	Italy	30	40.30	18.10
Leipzig	Germany	100	51.35	12.44
Linkoping	Sweden	80	58.39	15.57
Madrid	Spain	669	40.45	-3.73
Maisach	Germany	515	48.21	11.26
Minsk	Belarus	200	53.92	27.60
Munich	Germany	539	48.15	11.57
Naples	Italy	118	40.84	14.18
Neuchatel	Switzerland	487	47.00	6.96
Palaiseau	France	162	48.70	2.20
Payerne	Switzerland	456	46.81	6.94
Potenza-Tito Scalo	Italy	760	40.60	15.72
Sofia	Bulgaria	550	42.67	23.33
Thessaloniki	Greece	60	40.63	22.95

Data quality has been assured by inter-comparisons at instrument level using the available transportable systems (Fig. 1.4b and Fig. 1.4c) [*Matthias et al.*, 2004b; *Freudenthaler et al.*, 2010; *Molero et al.*, 2011]. Data quality assurance also includes the inter-comparison of group-specific retrieval algorithms for both backscatter and Raman lidar data ([*Böckmann et al.*, 2004; *Pappalardo et al.*, 2004b]. Based on well-defined common standards, the routinely performed quality-assurance exercises of lidar instruments and algorithms ensure that the data products provided by the individual stations are homogeneous and continuously of highest possible reliability. Efforts to guarantee and

improve the quality of data derived from observations in EARLINET are continuous [*Freudenthaler et al.*, 2010].

All measured profiles are stored in a standardized data format in a centralized database which allows for easy access to the complete data set for further scientific studies. Presently, the EARLINET database represents the largest collection of ground-based data of the vertical aerosol distribution on a continental scale [*Pappalardo et al.*, 2007; *EARLINET*, 2013].

In the global context, the *Micro Pulse Lidar Network (MPLNET)* [*Welton et al.*, 2001] is a global network of low-power lidars providing long-term observations of aerosol and cloud properties. Most MPLNET stations are collocated with *AERONET (Aerosol Robotic Network)* [*Holben et al.*, 1998] sites that provide column-integrated properties of aerosols and clouds. Also, the *Network for the Detection of Atmospheric Composition Change (NDACC)* is composed of more than 70 remote sensing research stations with observational capabilities which include lidars, spectrometers, microwave radiometers and ozone and aerosol sondes. Actually, the RSLab also hosts one MPLNET lidar system, in D3 building, Campus Nord, Barcelona, Spain.

The RSLab has a long-lasting experience in the field of lidar (started in 1993) which today fulfills part of the GAW programme of observation of atmospheric aerosols. According to *Bösenberg and Hoff* [2007], GAW's strategic goal for 2008–2015 is *the determination of the spatio-temporal distribution of properties of atmospheric aerosols related with climate change and air quality in multi-decade time scales.* More specifically, GALION is to provide the vertical component of aerosol distribution by means of advanced-specifications lidar systems organized into a network of cooperative networks as part of the *GEOSS (Global Earth Observation System of Systems).*

Organizations like U.S. *National Aeronautics and Space Administration (NASA)* and the *European Space Agency (ESA)* develop programs of global climate monitoring based on space- and satellite-borne lidar such as the *Geoscience Laser Altimeter System (GLAS)* (cloud and stratospheric temperature monitoring) [*Werner*, 2005; *Winker et al.*, 2006], the *Cloud-Aerosol Lidar and Infrared Pathfinder Satellite Observation (CALIPSO)* (aerosol and clouds) [*CALIPSO*, 2014], and others. Ground-based lidar networks at continental and local scales such as EARLINET, and SPALINET are major lidar data providers.

1.2.1 The RSLab 3+2+1 multi-spectral Elastic/Raman lidar system

The RSLab has currently set-up a 6-channel atmospheric lidar system including 3+2 elastic/Raman aerosol channels and one water-vapour channel [*Kumar et al.*, 2011] (Fig. 1.5). The lidar system uses a Q–switched Nd:YAG laser at 1064–, 532– (2^{nd} harmonic) and 355– nm (3^{th} harmonic) wavelengths. The return signal is collected by a 40-cm aperture telescope. A fiber bundle conveys the light return from the telescope focal plane to a polychromator, the spectrally selective unit in reception, designed with a view to minimize optical losses and physical dimensions. The reception field of view, which is limited by the fiber bundle characteristics, is virtually the same for all wavelengths. The backscattered received optical power is separated into the 355-, 532-, and 1064-nm elastic wavelengths as well as the 386.7- and 607.4-nm N_2 Raman-shifted wavelengths, and the

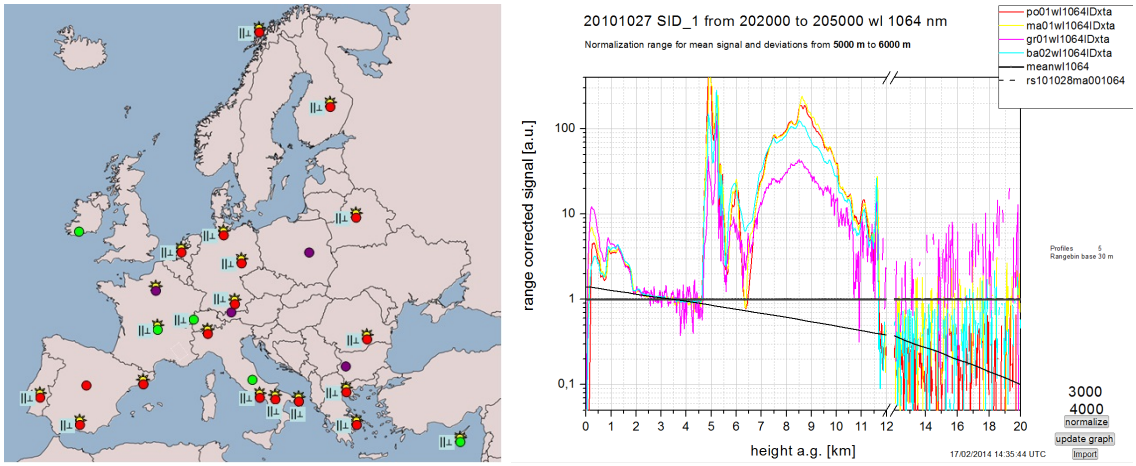

Figure 1.4: The RSLAB lidar station (Barcelona–Spain) in the EARLINET. *a*) Map of the EARLINET stations currently active (July, 2013). (Red dots) multi-spectral Raman lidar stations (EARLINET core stations). (Green dots) Stations with at least one Raman channel. (Violet dots) Stations with only elastic backscatter channel. ($\|\perp$) Stations with depolarization-measurement capabilities. ($\odot$) Stations with an AERONET sun-photometer collocated [*Pappalardo et al.*]. *b*) EARLINET – ASOS lidar inter-comparison campaign held in Madrid (Oct, 18 - Nov 7, 2010), showing the range-corrected signal inter-comparison among the participant lidar systems for 1064 nm channel (December, 27, 2010) [(PO: Potenza (Italy), MA: Madrid, GR: Granada, BA: UPC-Barcelona (Spain) and EV: Évora (Portugal)].

407.5-nm water-vapour Raman-shifted wavelength (Table 1.2).

Signal detection is achieved by using an *Avalanche Photo-Diode (APD)* at 1064 nm and *Photo-Multiplier Tubes (PMTs)* at all other wavelengths. A simultaneous analog/photon-counting acquisition unit is used. All the engineering details can be found in *Kumar et al.* [2006]. The assessment of system performance has been presented in terms of range-corrected power returns, *Signal-to-Noise ratio (SNR)* and maximum system range, and in *Lange et al.* [2012a], the measured backscattered elastic-lidar power returns against the link-budget theoretical ones [*Kumar et al.*, 2012].

1.3 Ph.D. mobility context: The UMass MIcrowave Remote Sensing Laboratory

The *Microwave Remote Sensing Laboratory (MIRSL)* is the largest research laboratory of the Department of Electrical and Computer Engineering at the *University of Massachusetts (UMass)*, Amherst. Co-directed by Professors Stephen Frasier and Paul Siqueira, the MIRSL laboratory includes 16 graduate students, four faculty, and two staff (September, 2012). The laboratory occupies over 3000 square feet of space in the Knowles Engineering Building and is well outfitted with modern *Radio Frequency (RF)* and microwave test equipment.

MIRSL researchers specialize in the conception, design, implementation, and evaluation of novel microwave and optical remote sensing instruments and methods. These are used to study aspects of the geophysical environment including the oceans (winds, waves, and currents) [*İnce et al.*, 2003; *Contreras and Frasier*, 2008; *Frasier et al.*, 2008], atmosphere (severe storms, atmospheric boundary layer) [*Contreras and Frasier*, 2008; *Pollard et al.*, 2000], and land (topography, ice,

Table 1.2: Main specifications of the RSLab multi-spectral lidar system.

Emitter			
Laser	Model	Quantel Brilliant, 1997	
	Output [nm]	Nd:YAG	355/532/1064
	Pulse Energy total [J]		0.060/0.160/0.350
	Pulse repetition rate [Hz]	20	
	Pulse length [ns]	3.6	
	Laser beam diameter [mm]	6	
Receiver			
Telescope	Model	Celestron, Classic 8, 1989	
	Type	Schmidt-Cassegrain, primary spherical	
	Aperture diameter [mm]	203.2	
	Obscuration diameter [mm]	69.85	
	Focal length [m]	2.032	
	Field of View [mrad]	1.48	
Optical fiber	Type	Bundle	
	Numerical Aperture	0.12	
	Telescope-laser axes distance [m]	0.18	
	Collimation system type	Double-convex lens	
	Collimation focal length [mm]	27	

Detection channels						
Central wavelength [nm]	532.1	607.4	1064	407.5	386.7	354.7
Scattering mechanism	Elastic	Rot.Raman N_2	Elastic	Rot.Raman H_2O	Rot.Raman N_2	Elastic
Detector type	PMT	PMT	APD	PMT	PMT	PMT
Daytime capability	yes	no	yes	yes	yes	yes
Spectral Bandwidth, $\Delta\lambda$ [nm]	1	1	1	1	1	1
Detector NEP [fW $\cdot$ Hz$^{-1/2}$]	0.192	0.296	36.6	0.892	0.0407	0.0444
Channel NEP [fW $\cdot$ Hz$^{-1/2}$]	7.7	3.0	925	26.2	6.4	7.7

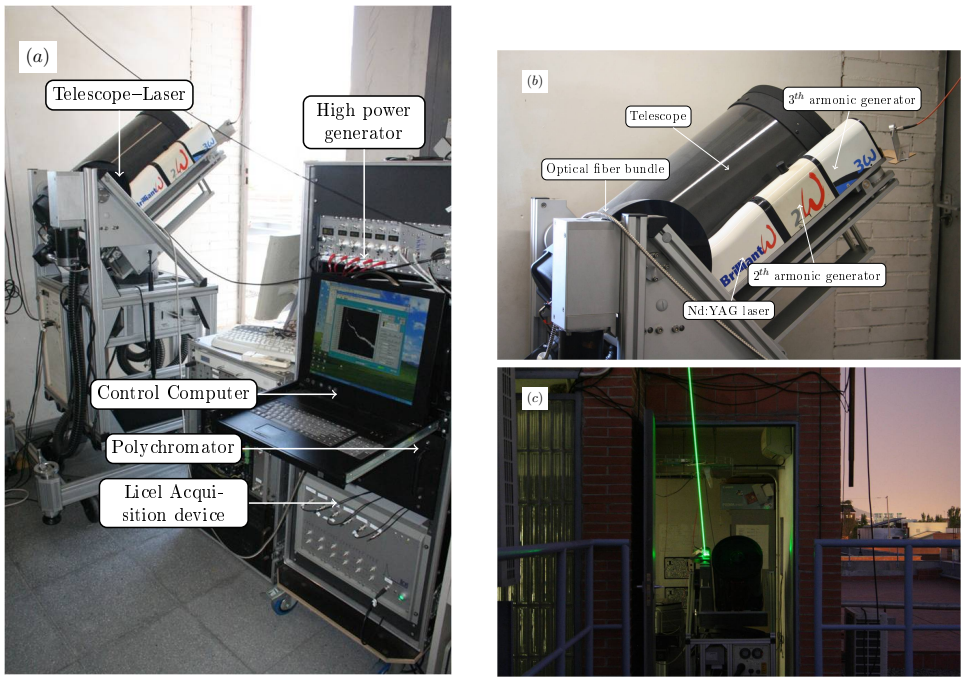

Figure 1.5: The RSLab multi-spectral lidar system (Campus Nord, D3 Building, Barcelona, Spain). (*a*) Photograph of the lidar system showing the scanning telescope–laser unit (right) and the control/acquisition rack unit (left) before integration in the new RSLab automated lidar station (planned July, 2014).(*b*) Detail of the scanning telescope-laser unit. (*c*) Nocturnal operation of the lidar system.

carbon, biomass) [*Ahmed et al.*, 2013]. Over the last twenty years, the MIRSL has developed over a dozen new instruments and methods [*İnce et al.*, 2003; *Pollard et al.*, 2000; *Trabal et al.*, 2013; *Bioucas-Dias et al.*, 2012]. In addition to its own graduate students, MIRSL has hosted several

students from foreign universities (primarily from Germany and Spain) as visiting scholars pursuing projects for their MS or Diploma degrees. *D. Lange has been hosted for a Ph.D. stay from Sept., 2012 to Jan. 2013.*

MIRSL has developed a fleet of novel atmospheric remote sensing systems. These mobile systems participate in field experiments to better understand the dynamics of the lower atmosphere, and in particular, the atmospheric boundary layer. Some active remote sensing examples are: *(i)* meteorological radars operating at microwave frequencies (Fig. 1.6) [*Frasier et al.*, 2008], *(ii)* wind profilers operating at VHF and UHF frequencies [*İnce et al.*, 2003], *(iii)* millimeter-wave cloud radars [*Sekelsky and Clothiaux*, 2002], and *(iv)* infrared and optical lidars for aerosol studies [*Anderson et al.*, 2004]. Passive microwave systems (radiometers) which also measure properties of the atmosphere such as the water-vapour and cloud liquid water content, have been developed by MIRSL [*Scheve and Swift*, 1999].

1.3.1 The MIRSL FMCW radar and lidar ceilometer systems

The MIRSL systems of concern for this Ph.D. are an S–band (2–4 GHz [*Mahafza and Elsherbeni*, 2004]) FMCW radar and a Vaisala CL-31 532-nm lidar ceilometer (Fig. 1.6).

A lidar ceilometer is a low-cost simple backscatter lidar originally devoted to cloud height and extent monitoring. Modern ceilometers such as the Vaisala CL-31 also enable to profile the aerosol structure within the low troposphere [*Vaisala*, 2014].

Figure 1.6: An S-band, FMCW atmospheric profiling radar from MIRSL. It employs separate antennas for transmitting and receiving. A Vaisala CL-31 lidar ceilometer is also contained within the white housing next to the antennas. Source: *MIRSL* [2014].

A FMCW radar usually uses a frequency-modulated instantaneous frequency to retrieve both the range and Doppler shift from a moving target (Sect. 2.3.3). In the context of atmospheric remote sensing and in the S–band the "moving target" is basically Rayleigh scattering from hydrometeors and interferent targets (e.g., insects and birds) and Bragg scattering from refractive index turbulence(Sect. 2.3.2).

Both ceilometer and FMCW radar instruments will be revisited in application Chapter 6.

1.4 Ph.D. motivation

The following motivation topics have been identified from the state-of-art, and the international context:

- *Need to exploit* the UPC multi-spectral Raman lidar system. The importance of aerosol tropospheric profiling in a coordinated basis at continental level (EARLINET) has already been outlined in Sect. 1.2.

- *Atmospheric Boundary Layer Height (ABLH)* estimation. There are several methods to retrieve the ABLH based on remote sensing techniques. These techniques are always based on the detection of a vertical feature from atmospheric variables, which continuously vary with range and time, and having a well defined transition identifiable as an "edge" or "boundary". Height retrieval methods and their accuracy are conditioned to the characteristics of the sensing instrumentation: lidar, sodar, radar wind profilers and RASS among others (see *Seibert et al.* [2000] for an extensive review), either solely or combined [*Emeis et al.*, 2008].

  Elastic backscatter lidars use the backscattered optical power from the atmospheric aerosols to profile the atmospheric structure and benefit from being highly sensitive to the concentration of aerosols, which are used as tracers or proxies of the ABLH.

  Concerning weather radars systems, and despite the disturbing presence of birds and insects in the S–band, they detect variations of the refractive index of the atmosphere, that are in the same order as the wavelength of the sensor [*Stull*, 1988b]. The ABL is often more humid than the FT in certain atmospheric conditions, like fair weather conditions. In these conditions, centimeter-scale eddies on the interface between the ML and the FT create strong echo returns. Within the ML there is a little returned energy in spite of the strong turbulence, because the humidity is low everywhere.

  Optimal estimation [*Stephens and Engelen*, 2001] and adaptive *Kalman filtering (KF)* [*Rocadenbosch et al.*, 1999; *Marchant et al.*, 2010] methods offer the possibility to dynamically track the ABL with minimum mean square error over time, that is, on a statistics basis, and by combining past estimates with present ones to improve the estimation. Besides, they provide "a posteriori" error covariance or inversion error.

  Errors due to the measurement noise (a consequence of the finite and range-dependent SNR in reception) also have a severe impact on the retrieved extinction and backscatter data products, not to mention the impact of the backscatter calibration from the user side [*Klett*, 1981; *Ansmann et al.*, 1992; *Whiteman*, 1999; *Rocadenbosch and Comerón*, 1999; *Rocadenbosch et al.*, 2010a; *Sicard et al.*, 2002, 2009a; *Comerón et al.*, 2004; *Rocadenbosch et al.*, 2012]. These advanced methods, which usually find applications in the context of global space-borne measurements are, however, more complex.

- *Error assessment* for the opto-atmospheric lidar retrieved data products. Backscatter lidars provide only range-resolved profiles of attenuated backscatter signal [*Collis and Russell*, 1976; *Bösenberg and Hoff*, 2007; *Reagan et al.*, 2002]. The lidar equation is inherently undetermined

as it contains two unknowns (the atmospheric extinction, α, and the backscatter coefficient, β) but only a single observable (the optical power returned as a function of time, $P(t)$). This under determination is in contrast to other schemes such as elastic-Raman systems, *High Spectral Resolution Lidars (HSRL)* [*Nishizawa et al.*, 2008], and variational multi-angle backscatter-lidar retrievals [*Sicard et al.*, 2002], all of which enable independent inversion of both aerosol extinction and backscatter coefficients [*Ansmann et al.*, 1992].

Errors in the assumed lidar ratio may result in larger error-propagated errors [*Bösenberg and Hoff*, 2007; *Rocadenbosch et al.*, 2012], especially in situations of a complex layering of aerosols [*Ansmann*, 2006]. *Kunz* [1996] and *Kovalev* [1993, 2003] have proposed alternative variants (not the object of this Ph.D. thesis) allowing trustworthy extinction retrievals, where the far-end calibration is replaced by the optical depth of the sounding path or by a near-end calibration and a nephelometer measurement. The synergetic combination of a backscatter lidar with a sun photometer is also extensively used [*Reba et al.*, 2010].

As far as lidar signal processing is concerned and, particularly, for the UPC elastic/Raman lidar station as a member of the EARLINET community, the following motivation factors have been identified:

- The need to monitor a wide range of environmental phenomena at local, European or global scale, such as aerosol intrusion episodes (e.g., Saharan dust events, volcanic eruption, fire plumes) and CALIPSO satellite overpasses over Barcelona, motivates to exploit the RSLab lidar system in terms of environmental/aerosol transport data interpretation and improved signal-processing raw-data.
- Considering ABLH estimation, low SNR scenarios analysis needs to resort to long time averaging and/or range-smoothing techniques, thus deteriorating the temporal/spatial resolution of the data, respectively.
- Error bounds for the two-component lidar inversion algorithm (retrieval of aerosol extinction and backscatter coefficient profiles) are needed, so that estimated error bounds and, therefore, the inversion quality can be assessed. Aerosol extinction and backscatter are the key optical parameters for subsequent unequivocal inversion of micro-physical parameters when at least 3+2 channels are available [*Böckmann*, 2001].

1.5 Main Objectives

This Ph.D. thesis deals with ***Lidar and S–band radar profiling of the atmosphere: Adaptive processing for Boundary-Layer monitoring, optical-parameter error estimation, and application cases***. Tentative goals are:

1. *Exploitation and dynamic-range enhancement of the UPC multi-spectral lidar system.* This objective comprises system exploitation in the EARLINET context and in support of international cal/val satellite missions, as well as a gluing-data method for dynamic range enhancement elastic lidar signals.

2. *Application of adaptive Kalman Filter (KF) to ABL estimation and tracking using lidar and FMCW radar data.* The Ph.D. is to deal with the atmospheric backscattered signal from these sensors as inputs to Kalman and *Non-Linear least-SQuares estimator (NLSQ)*, their initialization, and error-bound estimates. Besides, the ABLH estimates from these methods will be compared to classic ABLH detection methods.

3. *Assessment of the error bounds in the elastic retrieval of opto-atmospheric parameters, namely, extinction and backscatter coefficients.* This objective is to cover estimates of backscatter error bounds for the elastic two-component lidar inversion algorithm.

To achieve these goals, the RSLab lidar infrastructures and the lidar data processing and inversion platform Link-Detect (1993 – today) developed from the works guided by Dr. Rocadenbosch (M.Sc. thesis from *Molina* [1998],*Aixendri* [1998],*Gilabert* [1998], among others) and integrated in a *GUI (Graphical User Interface)* platform in *Reba* [2010] will be used. A case example is shown in Fig. 1.7. EARLINET and SPALINET lidar networks will provide the European and National consortium framework. Ceilometer and FMCW radar data coming from MIRSL will be also available. The objectives above are respectively detailed in subsequent Sects. 1.5.1 – 1.5.3.

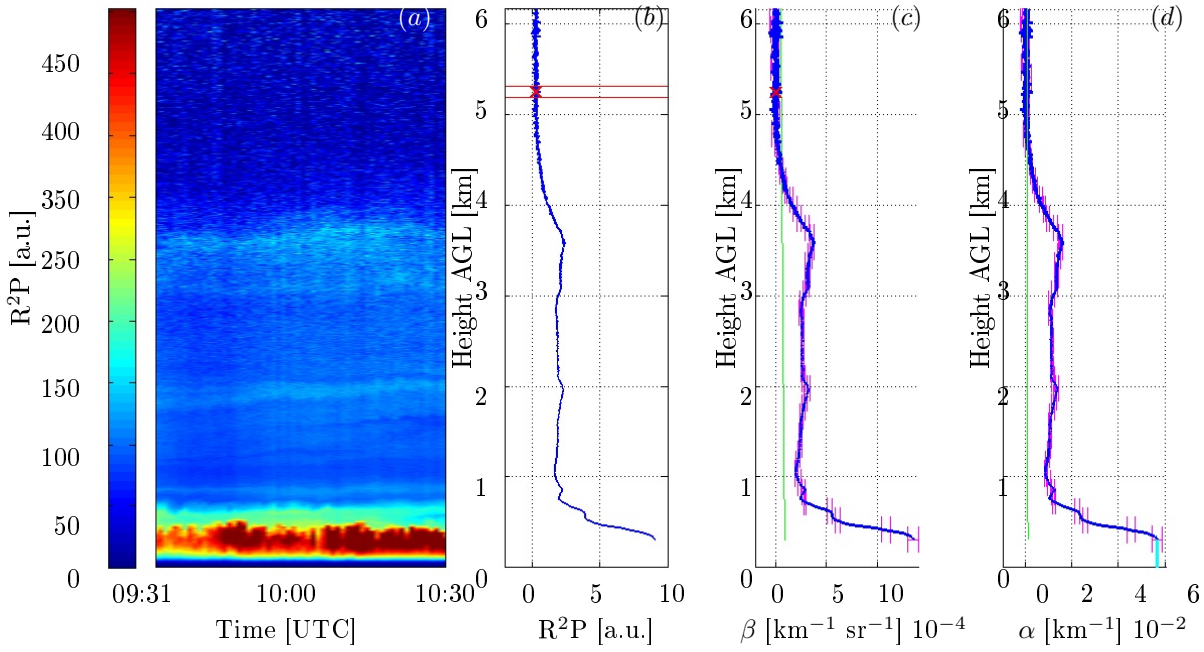

Figure 1.7: Optical atmospheric parameters inversion example (May, 5^{th}, 2011, Barcelona, Spain)), using RSLab lidar data and Link-Detect GUI inversion platform. Klett-Fernald-Sasano method was used [*Klett*, 1985]. Measurement shows a Saharan dust intrusion at several heights (up to 4 km) and inside the ABL. (*a*) Time-height plot of the analog range-corrected lidar signal for the 1064 nm channel. (*b*) Time-averaged range-corrected lidar signal. (*c*) Aerosol (blue) and molecular (green) backscatter coefficients, β_{aer} and β_{mol}, respectively. Error bounds have been computed according to Obj. 3 (Chapter 3). (*d*) Aerosol (blue) and molecular (green) extinction coefficients, α_{aer} and α_{mol}, respectively. The S_{aer} is 50 sr, and the estimated AOT is 0.10 [*Reba et al.*, 2010].

1.5.1 Obj. 1: Exploitation and dynamic-range enhancement of the UPC multi-spectral lidar system

In 2010 the multi-spectral 3+2+1-channel elastic/Raman lidar station started regular operation within EARLINET. This system permits calibrated multi-spectral range-resolved measurement of the extinction and backscatter opto-atmospheric parameters in the UV (ultraviolet, channels at 355 and 387 nm), VIS (visible, 532 and 607 nm), and NIR (near-infrared, 1064 nm) as well as measurement of water-vapor content (407 nm). Retrieval of the atmospheric extinction and backscatter coefficients in the VIS and UV, which is always semi-quantitative using elastic techniques, becomes quantitative thanks to the incorporation of the respective Raman channels (i.e., the Raman return due to the atmospheric nitrogen, the most abundant atmospheric molecular species, is used to calibrate the associated elastic channel).

System exploitation in EARLINET and in support of international calibration/validation satellite missions.- Since the beginning of EARLINET (2000) routine coordinated operation and the establishment of inter-centre measurement alerts in coordination with the rest of the EARLINET stations has allowed monitoring of a wide range of environmental phenomena. Additionally, and with the objective of extending the EARLINET actions to Spain, the RSLab has led the formation of the SPALINET.

This Ph.D. objective is transversally oriented and is aimed at exploiting the RSLab lidar measurements in terms of data interpretation and improvement of related signal-processing techniques. This includes transport and aerosol source analysis, statistics of the ABLH and aerosol layers aloft, and synergies with sun photometers, among others. The latter is of application to the intercomparison of lidar instruments and inversion algorithms level, to the enhancement of the dynamic signal range by means of data gluing (stratospheric measurements) and, more specifically, to Objs. 1.5.2 and 1.5.3.

The scope of lidar measurements in support of this Ph.D. objective comprises:

- Regular coordinated measurements within EARLINET network (3 per week, February 2000 – July 2013).
- CALIPSO measurements (June 2006 – July 2013): 2 to 3 measurements every 16 days (diurnal and nocturnal) in coincidence with overpasses of the CALIPSO satellite.
- SPALINET campaigns: "ad-hoc" measurement campaigns of intercomparison of instruments at different points of Spain and with in-situ cooperative sensors (Madrid, 2010, Fig. 1.4b y c, [*Molero et al.*, 2011, 2012]).
- Monitoring of special events/alerts: Saharan dust, volcanic eruptions, and fire plume outbreaks, measurements of diurnal cycle, cloud height, etc.
- Calibration/validation of RSLab lidar data products, in particular, optical properties of aerosols, cloud height and vertical distribution. This includes the pre-processing of the lidar signals ("raw data" to "clean data") and the inversion and categorization of data (A case example is shown in Fig. 1.7).

It must be noted that since July 2013, the entire system is being improved towards an automated lidar station.

Dynamic-range enhancement: the Gluing method.- Concerning raw data processing in atmospheric lidar remote sensing, the dynamic range of the return power signals can span up to five orders of magnitude. Towards a better exploitation of the RSLab multi-spectral lidar system, dynamic-range enhancement of the reception channels is proposed. Modern acquisition systems such as those based on Licel^{TM} transient recorders combine a dual acquisition mode in which the return signal is recorded simultaneously in both analog (*Analog-to-Digital Conversion, ADC*) and *Photon-Counting (PC)* modes. Although both data records can be analyzed separately, their combination obtained through data gluing technique gives the advantage of the high linearity of the ADC for high light-level signals (especially in the near range) and the high sensitivity of the PC mode for low light-level signals (in the far range) [*Licel*, 2007b].

1.5.2 Obj. 2: Application of adaptive filtering to ABL estimation and tracking

The discrete Kalman filter [*Kalman*, 1960] is an adaptive linear estimator inherited from control system theory that operates recursively using a state-space model formulation [*Brown and Hwang*, 1997]. The filter is based on two models, the state-vector model and the measurement model. The state-vector model is basically a parametrization of the key ABL parameters of interest and the measurement model relates the state-vector to the noisy measurements or "observables".

However poor the "a priori" information or "knowledge" about the atmospheric state-vector model and its statistics may be this information is assimilated by the filter in order to improve its estimation via a recursive process.

When, as is the case of the elastic lidar equation, the measurement model is non linear, a linearization is made around the state-vector trajectory giving rise to the *Extended Kalman Filter (EKF)*. At each successive filter iteration, the state vector, the estimated "a priori" and "a posteriori" error covariance matrices, and the Kalman gain ("projection gain") are recursively updated. By this updating the filter corrects its projection trajectory and improves its estimation.

First EKF implementations to estimate the optical atmospheric parameters have been done by *Rocadenbosch et al.* [1998a] and *Rocadenbosch and Comerón* [1999]. More recently, *Bioucas-Dias et al.* [2004] have applied this method to a calibrated backscatter lidar system. Other relevant applications of the EKF to the extinction retrieval of aerosol load concentrations are the works of *Warren et al.* [2008] and *Marchant et al.* [2010].

In a recent Ph.D. thesis by *Tomás* [2011], an EKF was first applied to estimate the ABLH. In this Ph.D. we tackle its first extension to lidar ceilometer data (low SNR scenarios) and FMCW radar data. The lidar case has given rise to a joint publication and a companion publication is being prepared for the radar case.

The ABL model passed to the filter and the detection of the ABLH (Fig. 1.2) is always based on the detection of a vertical feature in some atmospheric variable identifiable as an edge or boundary. The observed atmospheric variable is the attenuated backscatter signal from aerosols

and molecules in the lidar case (Mie/Rayleigh scattering) and backscattered signal from refractive index turbulence (Bragg scattering) in the radar case. Emphasis is given to filter initialization, a convenient treatment of the observation noise to update the state-noise covariance matrix, and to inter-compare EKF and NLSQ estimators. In turn, these two estimators will be cross-examined with classical methods such as the *Gradient Method (GM)*, the *Threshold Method (THM)*, and the *Inflexion Point Method (IPM)* in short-term fragments of a diurnal cycle.

1.5.3 Obj. 3: Error bounds in the retrieval of the atmospheric optical parameters: Two-component lidar inversion algorithm

This Ph.D. objective has been developed in cooperation with a companion Ph.D. thesis from *Kumar* [2012] and the lidar measurements obtained from Obj. 1 (Sect. 1.5.1). Focus is on the two-component backscatter-coefficient inversion algorithm, the so-called *Klett-Fernald-Sasano's (KFS)* method [*Klett*, 1985], which is widely accepted within EARLINET as a mature algorithm.

Because the elastic lidar equation is inherently undetermined for its contains two unknowns (the total atmospheric extinction and the total backscatter) and a proportionality constant representing the system constant, KFS method requires two critical inputs from the user side: *(i)* a boundary backscatter calibration in a molecular reference range (i.e., a range interval where the aerosol backscatter coefficient is negligible in front of the molecular one) and *(ii)* provision of the range-dependent aerosol lidar ratio, which is defined as the aerosol-extinction-to-backscatter ratio, a most critical input parameter.

In this Ph.D., operational inversions are carried out for the RSLab lidar station of Barcelona, as a part of EARLINET using the two-component inversion algorithm and total-increment error bounds. Two different sets of explicit error bounds are introduced for the optical atmospheric backscatter coefficient: first-order derivative error bounds (approximate) and total-increment error bounds (exact ones) for the dominant error sources.

1.6 Organization of the Ph.D. thesis

This Ph.D. thesis is organized as follows:

Chapter 1 focuses on the motivation and main objectives of this Ph.D. and in relation to the UPC RSLab multi-spectral elastic/Raman lidar system, and to the FMCW weather radar and ceilometer instruments from UMass MIRSL.

Chapter 2 reviews lidar and radar atmospheric remote sensing foundations and presents the RSLab data gluing algorithm aimed at dynamic range enhancement of elastic lidar signals.

Chapter 3 derives the total backscatter-coefficient inversion error bounds for the two-component lidar inversion algorithm in analytical form in response to error sources outlined in Obj. 3 (Sect. 1.5.3).

Chapter 4 gives a perspective of the data-gluing algorithm in line with Obj. 1 (Sect. 1.5.1).

Chapter 5 presents the solution based on a Kalman filter to trace the evolution of the ABLH from elastic-backscatter lidar data, using RSLab's multi-spectral lidar data.

Chapter 6 shows the Kalman filter algorithm applied to radar data from the UMass FMCW weather radar to derive the ABL with time. Emphasis is on both radar data preprocessing and noise treatment. A UMass lidar ceilometer and a classic ABLH detection method are used as validation truth.

Chapter 7 considers two application cases concerning the exploitation of the RSLab lidar: One case concerns to the validation of the RSLab lidar system, and the other, the data–gluing method. In both cases Volcano eruptive events measured by the RSLab multi-spectral lidar system, in synergy with the EARLINET and other lidar networks are discussed.

Chapter 8 gives concluding remarks along with future recommendations.

Chapter 2

Lidar and weather-radar atmospheric remote sensing

This Chapter introduces the basic principles of lidar and radar remote sensing with focus on elastic lidar and FMCW clear-air weather radar as well as an overview of the concept of the ABL and related state-of-the art methods for ABLH detection.

2.1 Introduction

Nowadays, remote sensing techniques are a key component of the atmospheric research. Specifically, lidar and radar systems are the backbones when atmospheric and, more specifically, tropospheric profiling is needed. In both cases, the interaction of the emitted radiation (from natural or artificial sources) with the atmospheric constituents like aerosols, trace gases and clouds can be used to determine physical and environmental variables of interest like, temperature and humidity, the ABL, and to characterize atmospheric processes.

Tropospheric profiling is important because the troposphere, which is the lower layer of the atmosphere, contains approximately 80% of the atmosphere's mass and 99% of its water vapour and aerosols and, in its lowermost part, the ABL, almost all the human processes take place.

Remote sensing technologies such as lidar, radar wind profilers, and *Radio Acoustic Sounding System (RASS)* [*Seibert et al.*, 2000; *Emeis et al.*, 2008] provide *range-resolved* profiles simultaneously for the whole observation range, which greatly improves the temporal resolution of ground instruments to enable a true monitoring of the ABL compared to radiosounding methods [*Sugiyama, G. and Nasstrom, J. S.*, 1999].

Considering the lidar remote sensing of the ABL has been carried out by ground-fixed systems such as backscatter lidars [*Endlich et al.*, 1979], the water-vapor *DIAL (Differential Absorption Lidar)* [*Lammert and Bösenberg*, 2006] or, more recently, ceilometers [*Emeis et al.*, 2009] but also by airborne lidars [*Melfi et al.*, 1985] and scanning lidars in a RHI scan (a vertical section) [*Kunkel et al.*, 1977; *Piironen and Eloranta*, 1995].

Within EARLINET, lidar systems have evolved from the basic elastic backscatter lidar to the more advanced multi-spectral elastic/Raman lidar (3+2 architectures and above). These systems

play an essential role in "ground truth" calibration/validation in support of space missions such as CALIPSO [*Winker et al.*, 2006]. Besides, co-operation between terrestrial lidar networks and satellite-borne lidars requires of quality-assured procedures both at system and algorithm level, usually working in a *Single Calculus Chain (SCC)*. When multi-spectral lidar data is considered, aerosol micro-physical properties inversion (size distribution) can also be achieved [*Böckmann et al.*, 2008].

So far, independent inversion of the opto-atmospheric parameters of interest, namely, aerosol extinction, aerosol backscatter, and lidar ratio, has been tackled by combining at least one elastic and one inelastic Raman channel [*Ansmann et al.*, 1992], multiple zenith-angle elastic signals (assumption of a horizontally stratified atmosphere), *High Spectral Resolution Lidars (HSRL)*, and backscatter lidar measurements combined with sun-photometer measurements [*Reba et al.*, 2010]. An analytical formulation has recently been presented to compute the backscatter range-dependent error bounds for the one- and two-component elastic lidar inversion algorithm [*Rocadenbosch et al.*, 2010a, 2012].

In the field of lidar signal processing the advances made –although sufficient from the operative point of view of the atmospheric observation stations– have comparatively been more modest than those achieved in radar. This is mainly because the bridge between the lidar remote sensing and signal processing disciplines (as inherited from the telecommunications area) is still immature.

Considering the radar, the behavior of refractive index gradients in the ABL has long been of interest in electromagnetic propagation studies. Since the early 1960s, different type of radars have been developed in the VHF, UHF, and lower microwave frequency ranges, so they can measure the backscattered power from refractive index variations in the clear atmosphere and its morphology [*Gossard*, 1990].

FMCW clear-air radars were first introduced in the late 1960s as a means to study the atmospheric boundary layer and lower troposphere. Since then, several such systems have been developed [*Richter*, 1969; *Eaton et al.*, 1995], and virtually all of these radars operate at S–band, near 3 GHz. This frequency enables maximum azimuthal resolution (narrowest beam width) for a given antenna size while still retaining sensitivity to clear-air scattering from refractive index fluctuations with high resolution in height and time [*İnce et al.*, 2003].

2.2 Lidar remote sensing

Despite the lidar principles were introduced in the 1930 decade, when first attempts to measure air density profiles in the upper atmosphere were made by determining the scattering intensity from searchlight beams [*Wandinger*, 2005], first atmospheric observations were published by *Fiocco and Smullin* [1963] using a ruby laser. In the next few decades, the development of optical and electronic technologies lead to improve lidar systems, while new instruments and techniques were designed specifically for them.

Basically, a lidar system consists of transmitter and receiver stages (Fig. 2.1). In the transmitter part, a *laser source* is used to emit light pulses to the atmosphere along the *Line-Of-Sight (LOS)* of the instrument. The short pulse length produced by the laser source (approximately, 20 ns) and

the spectral bandwidth (1 cm^{-1}) allow for highly-resolved ranging measurements with high SNR [*McCormick and Leavor*, 2013]. Laser pulse repetitions can vary from a few to several thousand shots per second. The time resolution is meaningless, since lidar signals are averaged over time intervals of a few seconds to minutes.

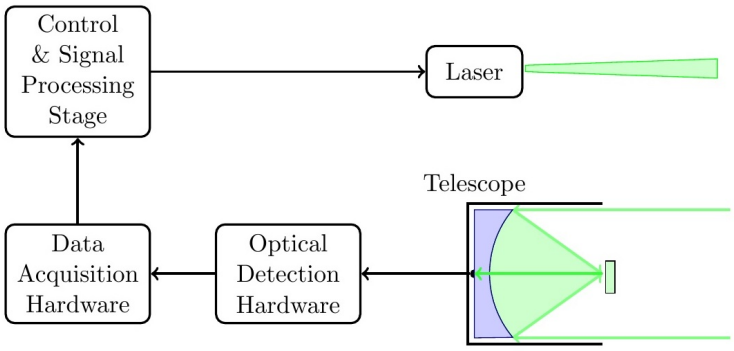

Figure 2.1: Block diagram of a basic lidar setup. Transmitter part: optical transmitter "antenna" (laser source), including perhaps an output beam expander to ensure eye-safety considerations. Receiver part: optical receiver "antenna" (telescope) and the optical detection hardware. The latter includes spectrally selective equipment (an interference filter or a polychromator) depending on the type of lidar configuration and opto-electronic receiver/s, based on APD or PMT detectors. The optical laser return signal is recorded and processed in the control & signal processing stage.

Since the atmospheric extinction is the main design requirement, the emitted laser beam wavelength must lie between the spectral transmission windows of the atmosphere in order not to be severely attenuated. The most useful transparent spectral bands are the *VISible (VIS)* (0.4–0.7 μm), the *Near InfraRed (NIR)* (0.7–1.5 μm), and the windows between 3-5 μm and 9-13 μm. Since the 1980s, high-power excimer and *Nd:YAG* (*Neodymium-doped: Yttrium Aluminum Garnet*) lasers are widely used as a laser source. While excimer lasers produce *UltraViolet (UV)* radiation, Nd:YAG lasers emit in NIR spectral region at 1064 nm. A common setup used along the Nd:YAG lasers is frequency doubling and tripling with nonlinear crystals to convert the primary 1064 nm radiation to 532- and 355 nm, respectively (this is the selected setup for the RSLab multi-spectral lidar system).

In the receiver part, a *telescope* is used as an optical antenna. Its *Field-Of-View (FOV)*, defined as the angle through which a detector is sensitive to electromagnetic radiation, can be chosen as low as a few hundred μrad because laser beams are highly collimated and their divergence is often further reduced [*Wandinger*, 2005]. Typically, Cassegrain telescopes are the chosen ones because their design provides moderate f-numbers (the ratio of the focal length of a lens or a lens system to the effective diameter of its aperture). The FOV is usually determined by a field stop in the focal plane of the receiver optics.

Following Fig. 2.1, laser radiation coming from the laser source is transmitted and scattered or absorbed by atmospheric constituents, such as clouds, aerosols, or molecules. Photons scattered back (i.e., the optical echo) to the receiver are collected by the telescope and then directed to a detector whose signal is analog-to-digitally recorded or counted as a function of altitude or range. The strength of the return signal is related to the physical and optical properties of the scatterers [*McCormick and Leavor*, 2013].

The detector, including a spectrally selective equipment such as an interference filter (in the

simplest case), or a polychromator followed by an opto-electronic receiver stage, carry out the optical analysis of the backscattered photons. A *polychromator* is an optical system equipped with dichroic mirrors that separates the multi-wavelength return radiation into optical paths specific for each wavelength. At the end of each optical path, an opto-electronic receiver is placed to carry out the signal detection. APDs and PMTs are the most common used detectors in opto-electronic receivers. Both detectors can operate in Geiger mode so photons can be counted individually. The type of detector chosen depends on the spectral region of interest, its spectral response, quantum efficiency, gain, and dark-current characteristics. Thus, PMTs are preferred for wavelengths that lie between 200 nm and below 0.8 μm (from UV to NIR bands) because of their high gain and small level of noise [*Measures*, 1992b]. These achieve very good sensitivities for the detection of weak light signals, however, PMTs are susceptible to saturation, usually from background sunlight or from the intense light coming from ranges close to lidar. On the long-wavelength end of the spectrum (above 800 nm) some materials used in the PMT cease to be effective [*Wandinger*, 2005].

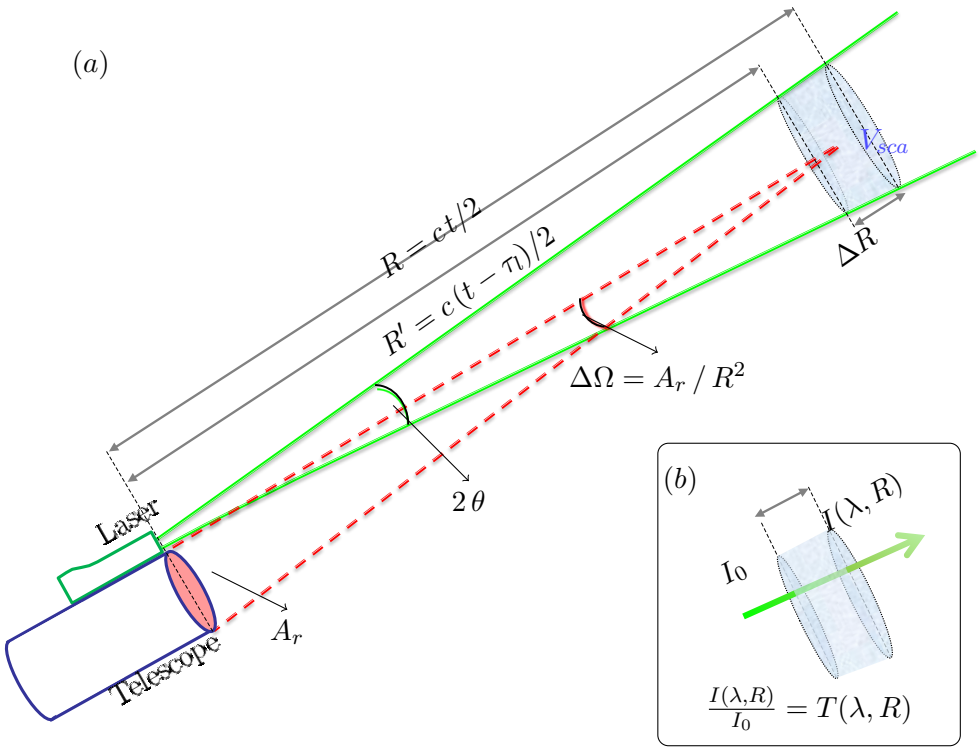

Figure 2.2: Monostatic pulsed lidar setup geometry using a laser–telescope biaxial arrangement. (*a*) Transmitter and receiver parts, with V_{sca}, the scattering volume (or resolution cell), 2θ, the full-angle laser divergence (green solid lines), $\Delta\Omega$, the telescope solid angle subtended to the scattering volume (red dashed lines), A_r, the telescope effective area, $\Delta R = R - R' = c\,\tau_l/2$, the spatial difference between the leading edge and the trailing edge of the laser pulse, τ_l, and R, the range. (*b*) Sketch of the Beer-Bouguer's exponential extinction law. (Light blue volume), the scattering volume, (green fading away arrow) Incident/absorbed/scattered light intensity before/inside/after the scattering volume (light blue volume) (Adapted from *Comerón et al.* [2005]).

Regarding design considerations, lidars may be either monostatic (collocated transmitter and

receiver, the most common configuration) or bistatic (separated transmitter and receiver). Fig. 2.2a shows a monostatic lidar setup geometry. Also operational system conditions are taken in account, such as environmental conditions, day/night time operation, ground based, mobile or aircraft-carried, etc., but the most important design considerations have to do with the type of scattering mechanism from the atmospheric scattering volume back to the instrument (Rayleigh/Mie "elastic" scattering or Raman "inelastic" scattering), in terms of a wavelength-dependent *backscatter coefficient profile,* $\beta(\lambda, R)$ and *extinction coefficient profile,* $\alpha(\lambda, R)$. These two optical parameters respectively model the reflectivity and energy losses associated with laser beam propagation through the atmosphere.

Lidar systems classification is not unique. A first categorization can be done into *elastic* and *inelastic* systems. In the first case, emission and reception wavelengths are the same while in the second case the reception wavelength is shifted from the emitted one due to Raman scattering or fluorescence.

2.2.1 Lidar and atmospheric optical particles

Laser pulses interact with molecules and particles in the atmosphere, which results in light scattering and absorption and leads to the extinction (or attenuation) of the laser beam. Light scattering exhibits angular-dependent behavior and occurs when a portion of the incoming laser pulse dissipates in all directions in which the scattered light intensity varies with the angle between the incoming light and the scattered light [*Lenoble et al.*, 2013]. Physical characteristics of the scatterers (i.e., refractive index, cross section, radii distribution) within the scattering volume determine the scattering intensity in that given angle. On the other hand, light absorption is a result of the change of the internal energy produced by the gaseous or particulate absorbers and, like scattering, the intensity of light absorption depends on the presence of that atmospheric absorbers constituted along the path of the emitted laser pulse (Fig. 2.3) [*Collis and Russell*, 1976].

In the context of lidar, as long as laser light can be considered as a monochromatic light, its scattering can be referred in terms of the size of the optical scatterers from molecules and aerosols which are known as Rayleigh's and Mie's scattering, respectively (for convenience, hereinafter will be referred simply as Rayleigh and Mie scattering).

Rayleigh scattering is always used as a synonym of molecular scattering in which the size of this scatterer is much smaller than the laser wavelength (formally, the incident electromagnetic wave induces an electric dipole moment at the same frequency in the molecule; this dipole emits, according to the classical electromagnetic theory, at the same wavelength, whereas the *Mie scattering* is related to scattering by particulates whose size is comparable to the incident wavelength (formally, describes the scattering of electromagnetic radiation by a sphere; aerosols can be modeled as spheres [*Lenoble et al.*, 2013]). Note that both Rayleigh and Mie scattering are termed elastic scattering since no wavelength shift occurs. Also, the Rayleigh scattering coefficient is proportional to λ^{-4}, known as the *Rayleigh law* . For air molecules, Rayleigh scattering is negligible at $\lambda > 3\mu$m, and for $\lambda < 1\mu$m, air molecules scatters blue light more than red light; that is why the color of the sky is blue. On the other hand, Mie scattering losses decreases rapidly with increasing wavelength (Mie scattering

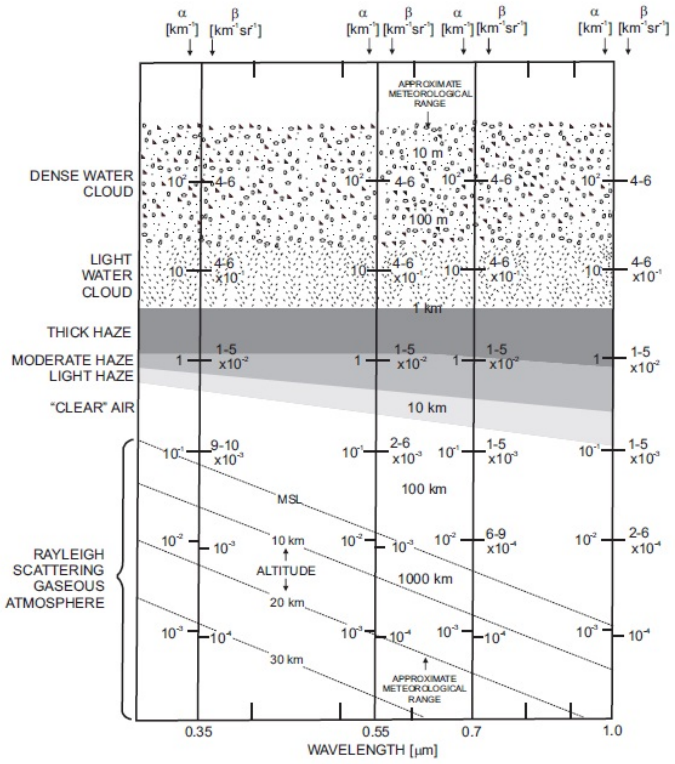

Figure 2.3: Variation of extinction, α, and backscatter coefficients, β, with UV, VIS and NIR wavelength and atmospheric condition. Source: Fig. 4.8 in *Collis and Russell* [1976].

coefficient $\backsim \lambda^{-K}$; $0 \leq \mathrm{K} \leq 2$ typ.); that is the reason why sunset sky appears red [*Andrews*, 2004].

2.2.2 Atmospheric extinction

According to the Beer-Bouguer's exponential extinction law, the spectral intensity of a laser pulse propagating along the range direction ($\vec{r}$) between distances $r = 0$ and $r = R$ in an inhomogeneous medium is given by [*Beer*, 1852; *Collis and Russell*, 1976]

$$\frac{I(\lambda, R)}{I_0} = T(\lambda, R) = \exp\left(-\int_0^R \alpha(\lambda, r)\, dr\right), \tag{2.1}$$

where I_0 is the initial intensity at $r = 0$, I is the intensity [$\mathrm{W\,m^{-2}}$] at $r = R$, λ is the operation wavelength [m] and α is the *total atmospheric extinction coefficient* [$\mathrm{m^{-1}}$] within the transmission range $[0, R]$. Eq. 2.1 gives rise to the *transmission term* (also called *atmospheric transmissivity*), $T(\lambda, R)$ [·]. Fig. 2.2b shows a sketch of the Beer-Bouguer's transmissivity concept.

Strictly speaking, Eq. 2.1 applies only to monochromatic radiation. However, it can also be applied to narrow wavelength intervals over which the intensity and the extinction vary slowly, as is the case of laser radiation for scattering (both molecular and aerosol), aerosol absorption, and ozone absorption, but not for gaseous line absorption [*Lenoble et al.*, 2013].

The total atmospheric extinction coefficient (α) is the sum of three simultaneous attenuation mechanisms: molecular absorption, molecular (Rayleigh) scattering, and aerosol (Mie) scattering, since both molecules and aerosols absorb (radiative energy is transformed into another form of

energy) and scatter (a part of the incident light changes its direction of propagation) radiation. That is

$$\alpha = \alpha_{mol,sca} + \alpha_{aer,sca} + \alpha_{mol,abs} \quad \left[m^{-1}\right], \tag{2.2}$$

where the subscripts *mol*, *aer*, *abs*, and *sca* stand for "molecular" and "aerosol" constituents, and "absorption" and "scattering" mechanisms, respectively [*Rocadenbosch*, 2003b].

According to *Collis and Russell* [1976], the dominant component of the total extinction, α, is the molecular absorption term, $\alpha_{mol,abs}$, which varies strongly with the wavelength in the vicinity of absorption lines of the various atmospheric gases, most frequently in the UV ($\lambda < 300$ nm) and in the IR ($\lambda > 900$ nm) regions of the spectrum, where the effective range of the lidar can be severely limited (Fig. 2.3). For this reason, tropospheric profiling lidars operate in atmospheric transmission windows and out of absorption lines.

On the other hand, the molecular (Rayleigh) scattering extinction, $\alpha_{mol,sca}$ can be defined as

$$\alpha_{mol,sca} = \alpha_{Ray} = N_g \; \sigma_{Ray}(\lambda) \quad \left[m^{-1}\right], \tag{2.3}$$

where N_g is the number density of gas molecules [molecules/m^3] in the atmospheric volume of interest and $\sigma_{Ray}(\lambda)$ is the Rayleigh's scattering cross-section (m^2/*molecule*).

The next component of the total extinction, α, is the aerosol extinction term, $\alpha_{aer,sca}$, which is computed from Mie's scattering models based on homogeneous dielectric spheres with a given radius distribution. Thus, the volumetric aerosol extinction coefficient can be written as

$$\alpha_{aer,sca}(\lambda) = \alpha_{Mie}(\lambda) = \int_0^\infty \pi \, a^2 \, Q_{ext}(x,m) \, N_{aer}(a) \, da \quad \left[m^{-1}\right], \tag{2.4}$$

where a is the *aerosol radius*, Q_{ext} is the *extinction efficiency* (where $Q_{ext} = Q_{sca} + Q_{abs}$ with Q_{sca} and Q_{abs} the *scattering* and *absorption efficiencies*, respectively) $[\cdot]$, x is the *particle size parameter* defined as $x = 2\pi a/\lambda[\cdot]$, m is complex refractive index $[\cdot]$, and $N_{aer}(a)$ is the aerosol number density per unit radius interval [m^{-3}]. The term $\pi a^2 Q_{ext}(x,m)$ directly represents the *extinction cross-section* [m^2] for such a particle of radius a.

The total extinction, α, can also address to a concept that can be used to obtain the lidar performance under certain atmospheric conditions [*Koshmieder*, 1924]. When the particle size is unknown, the *visibility margin* (V_m) [km] for visually clear air can be defined as [*Kruse et al.*, 1963],

$$V_m(\lambda) = \left[\frac{3.91}{\alpha_{aer}(\lambda)\left[km^{-1}\right]}\right]\left[\frac{0.55}{\lambda\left[\mu m\right]}\right]^q \quad \left[km\right]; \quad q = \begin{cases} 0.585 V_M^{1/3} & V_M \leq 6 \; km \\ 1.3 & V_M > 6 \; km \end{cases}, \tag{2.5}$$

or, particularly, for 0.55 μm (maximum sensitivity of the human eye) and considering non-turbid atmospheric conditions, that is, free of aerosol particles [*Collis and Russell*, 1976],

$$V_m = \frac{3.91}{\alpha_{aer}} \quad \left[km\right], \quad \lambda = 0.55 \mu m \, . \tag{2.6}$$

2.2.3 Atmospheric backscatter

Whereas that total extinction, α, gives information about losses (absorption and scattering) in the emitted radiation flux, the *total backscatter coefficient,* β, describes how much light is scattered towards the lidar receiver, and it is the atmospheric parameter that determines the strength of the lidar signal return. It is defined as the volume scattering coefficient for a scattering angle $\theta = \pi$ (i.e. towards the telescope) [*Wandinger*, 2005]. As explained in the previous Section, the total backscatter coefficient is defined as the a sum of contributions from both *molecules,* β_{mol}, and *aerosols* β_{aer}, as

$$\beta = \beta_{mol} + \beta_{aer} \quad \left[m^{-1}sr^{-1}\right], \tag{2.7}$$

In the atmosphere, light scattering properties of particles are difficult to be precisely described, because of their natural variability in shape, composition, and size [*Collis and Russell*, 1976; *Lenoble et al.*, 2013]. Nevertheless, the aerosol backscatter coefficient, β_{aer} can be formulated analogously to Eq. 2.4 as [*Deirmendjian*, 1964, 1969]

$$\beta_{aer}(\lambda) = \beta_{Mie}(\lambda) = \int_0^\infty \pi\, a^2\, Q_{back}(x,m)\, N_{aer}(a)\, da \quad \left[m^{-1}sr^{-1}\right], \tag{2.8}$$

where the term $Q_{back}(x,m)$ is the *backscatter efficiency.* The rest of the variables have been already defined in Eq. 2.4.

As in Eq. 2.3, the molecular backscatter coefficient, β_{mol} due to atmospheric gases is described by Rayleigh scattering theory as

$$\beta_{mol}(\lambda) = \beta_{Ray}(\lambda) = N_g \frac{d\sigma_{Ray}(\pi,\lambda)}{d\Omega} \quad \left[m^{-1}sr^{-1}\right], \tag{2.9}$$

where $d\sigma_{Ray}(\pi,\lambda)/d\Omega$ ($\mathrm{m}^2 sr^{-1}$) is the differential Rayleigh's scattering cross section per solid angle unit in the backward direction. It is characterized by a λ^{-4} wavelength dependency [*Andrews*, 2004] and thus, the molecular backscatter, β_{mol}, in Eq. 2.9 above is insignificant at NIR wavelengths [*Rocadenbosch*, 2003b; *Wandinger*, 2005].

Concerning aerosols, the ratio that relates aerosol extinction and backscatter coefficients (Eq. 2.4 and 2.8) is called *lidar ratio,*

$$S_{aer}(\lambda,R) = \frac{\alpha_{aer}(\lambda,R)}{\beta_{aer}(\lambda,R)} \quad \left[sr\right]. \tag{2.10}$$

As can be observed from Eq. 2.10 above, the lidar ratio contains fundamental information about aerosols, in terms of a wavelength-and-range-dependent parameter, as the density and composition of aerosols typically change from one volume in the atmosphere to another [*Pedros et al.*, 2010; *McCormick and Leavor*, 2013].

Concerning molecules, the equivalent variable to lidar ratio is the *Rayleigh ratio,* S_{mol}, which is known from classic oscillator theory. That is [*Collis and Russell*, 1976],

$$S_{mol}(\lambda,R) = \frac{\alpha_{mol}(\lambda,R)}{\beta_{mol}(\lambda,R)} = \frac{8\pi}{3} \quad \left[sr\right]. \tag{2.11}$$

Unlike S_{aer}, S_{mol} is not range dependent, since the molecular composition of the atmosphere is homogeneous throughout regions used for typical lidar retrievals. This is specially true of aerosol retrievals [*McCormick and Leavor*, 2013].

2.2.4 The elastic lidar equation

The *elastic lidar equation* joins extinction and backscatter parameters with the inherent lidar system parameters (refer to Fig. 2.2).

Considering that the emitted laser pulses have to travel forth and back from the atmosphere, the range information is determined from the two-way-path time of flight of the emitted laser pulses to the scattering target (i.e., aerosols and/or molecules) as

$$R = \frac{ct}{2} \quad [m], \tag{2.12}$$

where R is the *range* (m), t is the *time delay* (s), and c is the *velocity of light* ($\mathrm{m{\cdot}s^{-1}}$).

Regarding the transmitted laser pulse, it is assumed that it has a *rectangular temporal shape* and *finite time duration*, τ_l. Assuming that the lidar signal is detected at an instant time t_0 (unlimited reception bandwidth or equivalently, nil detection time) after the *leading edge* of the laser pulse is emitted, the backscattered light produced by this leading edge arrives from a distance $R = ct/2$. At the same time, the *trailing edge* of the pulse produces backscattered light that comes from a distance $R' = c\,(t - \tau_l)/2$. Therefore, the length of the *scattering volume* from which backscattered light arrives at any instant time t is

$$\Delta R' = R - R' = \frac{c\,\tau_l}{2}, \tag{2.13}$$

where $\Delta R'$ is known as the *effective spatial pulse length* [km] [*Wandinger*, 2005].

In practice, the detection time, τ_d, is not nil and then the detected lidar signal at each time bin of the transient recorder (e.g., an analog acquisition card, photon-counter, or mixed unit) corresponds to the time interval $[t, t + \tau_d]$ rather than to the instant time t. As a consequence, the length of the observation volume contributing backscattered light into a given time bin becomes

$$\Delta R = \frac{c\,(\tau_l + \tau_d)}{2} \approx \frac{c\,\tau_d}{2}, \quad \tau_l \ll \tau_d\,. \tag{2.14}$$

Usually, the duration of the emission laser pulses is comparatively much shorter than the detection time of the signal acquisition unit ($\tau_l \ll \tau_d$) so the effective spatial pulse length reduces to Eq. 2.14 above. If the transient recorder unit operates in analog mode by sampling at a frequency f_s, then the detection period becomes $\tau_d = 1/f_s$ [*Measures*, 1992c].

As explained before, the laser emits a short pulse of time duration τ_l with a full-angle divergence 2θ so that the laser beam actually illuminates a slightly divergent conical volume of space, V_{sca} (light blue volume in Fig. 2.2a), whose length and cross section are $\Delta R'$ and πr^2 $(r = R\theta)$, respectively. The laser operating wavelength is λ_0. Under practical approximation [*Skolnik*, 2001], the scattering volume can be considered cylindrical in shape ($V_{sca} = \pi r^2 \Delta R'$), with R the mean distance. Also, it is assumed that the power distribution of the laser pulse is uniform over the

illuminated cross-section area πr^2, the *incident laser power density* [W·m^{-2}] on the illuminated volume, V_{sca}, can be written as

$$E_{in}(\lambda_0, R) = \frac{P_0}{\pi\, r^2}\, T(\lambda_0, R) \quad \left[W \cdot m^{-2}\right]. \tag{2.15}$$

In Eq. 2.15 above, $T(\lambda_0, R)$ is the one-way transmittance defined by Eq. 2.1 and Eq. 2.2, λ_0 is the elastic wavelength, and P_0 is the *emitted laser power per pulse* at λ_0,

$$P_0 = \frac{E}{\tau_l} \quad \left[W\right], \tag{2.16}$$

where E is the *pulse energy (J)* and τ_l is the *pulse duration* [s]. Neglecting absorption, the one-way transmittance can expressed as

$$T(\lambda_0, R) = \exp\left\{-\int_0^R \left[\alpha_{\lambda_0}^{aer}(r) + \alpha_{\lambda_0}^{mol}(r)\right] dr\right\} \quad [\cdot]. \tag{2.17}$$

The integral term, $\int_0^R \alpha(r)dr$, is referred to as *optical depth (τ)* $[\cdot]$. Because the illuminated volume propagates through the atmosphere, light is scattered isotropically [*Kovalev*, 2004; *McCormick and Leavor*, 2013]. The *backscattered power* (i.e., in the π direction towards the telescope) per solid angle unit is

$$K_{sca}(\lambda_0, R) = \beta(\lambda_0, R)\, E_{in}(\lambda_0, R)\, V_{sca} \quad \left[W\, sr^{-1}\right], \tag{2.18}$$

where $\beta(\lambda_0, R)$ and E_{in} have already been defined in Eqs. 2.7 and 2.15, respectively.

The *backscattered power, $P(\lambda_0, R)$* collected by the telescope is the product of Eq. 2.18, K_{sca}, times the subtended solid angle into which photons are scattered, $\Delta\Omega$, times the atmospheric transmittance, $T(\lambda_0, R)$, along the return path towards the telescope (i.e., from the scattering volume back to the telescope). Besides, the backscattered radiation collected by the telescope must also include a range-dependent geometrical form factor or *overlap factor (OVF)*, $\xi(\lambda_0, R)$, which accounts whether the completeness of the laser-illuminated volume can be imaged on the detector (i.e., falls into the FOV of the telescope) [*Measures*, 1992c; *McCormick and Leavor*, 2013]. Formally,

$$P(\lambda_0, R) = K_{sca}(\lambda_0, R)\, \Delta\Omega\, T(\lambda_0, R)\, \xi(\lambda_0, R) \quad \left[W\right]. \tag{2.19}$$

For a well aligned lidar system the OVF is unity from the range of full overlap (e.g., typically 200-1000 m depending on the system geometry) onwards. The OVF depends on the geometrical separation between the laser and the telescope axes, and on geometrical and optical parameters of the system such as the effective radius of the telescope aperture, laser aperture radius, FOV, imaging properties, and laser divergence. See *Measures* [1992c] for further insight.

Finally, by combining Eqs. 2.15 – 2.18 into Eq. 2.19, the well-known elastic lidar equation under the single-scattering, no-absorption assumption, follows as

$$P_{\lambda_0}(R) = \frac{K}{R^2}\left[\beta_{\lambda_0}^{aer}(R) + \beta_{\lambda_0}^{mol}(R)\right] \exp\left\{-2\int_0^R \left[\alpha_{\lambda_0}^{aer}(r) + \alpha_{\lambda_0}^{mol}(r)\right] dr\right\} \xi(\lambda_0, R) \quad \left[W\right], \tag{2.20}$$

where the *system constant* is defined as

$$K = \frac{E\,c}{2}\,A_r \quad \left[W\,m^3\right]. \tag{2.21}$$

Eq. 2.20 describes the operational capabilities of the lidar system, containing the laser-telescope OVF, $\xi(\lambda_0, R)$ [*Measures*, 1992b], and excluding receiving optics losses such as those associated to lenses or interference filters.

It is usual to state the Eq. 2.20 in range-corrected form,

$$U_{\lambda_0}(R) = R^2\,P_{\lambda_0}(R) = K\left[\beta^{aer}_{\lambda_0}(R) + \beta^{mol}_{\lambda_0}(R)\right]\exp\left\{-2\int_0^R\left[\alpha^{aer}_{\lambda_0}(r) + \alpha^{mol}_{\lambda_0}(r)\right]dr\right\}\xi(\lambda_0, R) \quad \left[W\,km^2\right]. \tag{2.22}$$

2.2.5 The Raman lidar equation

As mentioned in Sect. 2.1, common lidar configurations, as is the case of the RSLab multi-spectral lidar system, include elastic and Raman channels. For the sake of completeness, the Raman lidar equation is explained next. Difference between elastic and Raman interaction is depicted in Fig. 2.4a.

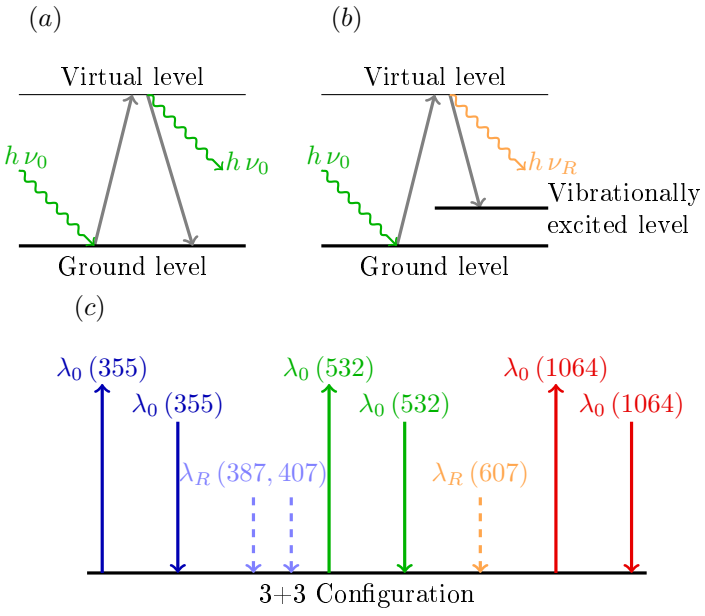

Figure 2.4: Elastic/Raman interaction and 3+3 elastic/Raman configuration. (*a*) Sketch of the elastic scattering for a single photon (green undulated arrow). (*b*) Same as (*a*) for vibrational Raman scattering. h is the Plank constant, ν_0, the incident (and also the scattered in (*a*)) frequency, and ν_R, the Raman frequency. (*c*) The 3+3 elastic/Raman configuration. Elastic interaction (emission and reception wavelength coincide) is depicted in solid arrows. Raman interaction is depicted in dotted lines and close to the corresponding elastic wavelengths. Up arrows indicate emission, down arrows indicate reception. (Adapted from *Measures* [1992a]; *Comerón et al.* [2005]).

In contrast to elastic scattering, the Raman scattering process involves an internal energy transition of the molecular species of interest (atoms and molecules in the atmosphere) and introduces a series of side-band frequencies, $\Delta\nu$, around the *incident frequency*, ν_0 [Hz], in which the amount

of shifting is equivalent to the vibrational-rotational frequencies of the molecules being irradiated. This *frequency shift* can be formulated as *Inaba* [1976]

$$\nu_R = \nu_0 \pm \Delta\nu \quad [Hz]\,. \tag{2.23}$$

The frequencies shifted down ($\Delta\nu = +1$) are called *Stokes lines* while those shifted up ($\Delta\nu = -1$) are called *anti-Stokes* lines. A pure rotational band ($\Delta\nu = 0$) is centered on the incident frequency. Frequency shifts and normalized cross-sections for typical trace molecules present in the atmosphere can be found in the same reference cited above.

If λ_0 is the laser emission wavelength and $\kappa = 1/\lambda$ [m^{-1}] is the *wavelength shift* associated to the molecular species of interest producing the Raman scattering then the Raman return wavelength, λ_R, can be computed as

$$\lambda_R = \frac{\lambda_0}{1 - \lambda_0\,\kappa} \quad [m]\,. \tag{2.24}$$

Because Raman molecular scattering cross-sections are 3-to-4 orders of magnitude weaker than elastic ones, thus, leading to vary faint returns, aerosol-monitoring Raman lidars resort to any abundant atmospheric species such as nitrogen or oxygen to interact with. Besides, Raman lidar require highly energetic laser pulses, larger telescopes, sensitive detectors (PMTs), longer integration times, and are usually limited to night-time operation [*Rocadenbosch*, 2003a; *Kumar et al.*, 2012].

Nitrogen is nearly always the chosen species, since it is the most atmospheric abundant specie (78 % volume concentration) and with a very well-known Raman cross-section. The setup of a cooperative N_2 Raman channel for atmospheric aerosol lidar sensing is of advantage to calibrate the elastic channel and hence, to obtain independent retrievals of both extinction and backscatter atmospheric optical components [*Ansmann et al.*, 1992].

In the case of the RSLab multi-wavelength lidar system emitting at $\lambda_0 = 355$ (UV), 532 (VIS) and 1064-nm (NIR) wavelengths the 3+3 elastic/Raman receiving wavelengths are plotted in Fig. 2.4b.

Raman lidar equation can be explained by comparison to the elastic lidar Eq. 2.20, in which both the optical emission and return path were operating at the same wavelength, λ_0. In the Raman case, the emission path continues to be at λ_0 but the return path is at λ_R, therefore the two-way path Raman transmittance takes the form,

$$T_0(\lambda_0, R)\,T_R(\lambda_R, R); \qquad T(\lambda_i, R) = \exp\left\{-\int_0^R \left[\alpha_{\lambda_i}^{aer}(r) + \alpha_{\lambda_i}^{mol}(r)\right] dr\right\}. \tag{2.25}$$

Eq. 2.25 is in contrast to the two-way path elastic transmittance given by $T(\lambda_0, R)^2$.

The *Raman backscatter coefficient* can be computed as

$$\beta_{\lambda_R}(R) = N_R(R)\,\frac{d\sigma_{\lambda_R}(\pi)}{d\Omega} \quad \left[m^{-1}sr^{-1}\right], \tag{2.26}$$

where $N_R(R)$ is the nitrogen molecule number density at λ_R and $d\sigma_{\lambda_R}(\pi)/d\Omega$ is the range-independent nitrogen Raman backscatter cross-section per solid angle unit. Accordingly, the Raman lidar equa-

tion can be written as

$$P_{\lambda_R}(R) = \frac{K}{R^2}\left[N_R(R)\,\frac{d\sigma_{\lambda_R}(\pi)}{d\Omega}\right]\exp\left\{-\int_0^R\left[\alpha^{aer}_{\lambda_0}(r)+\alpha^{mol}_{\lambda_0}(r)+\alpha^{aer}_{\lambda_R}(r)+\alpha^{mol}_{\lambda_R}(r)\right]dr\right\}\xi(\lambda_R,R)\quad\left[W\right], \tag{2.27}$$

where atmospheric absorption effects have been neglected. In order to compute Eq. 2.27, $N_R(R)$ and $\alpha^{mol}_{\lambda_0,\lambda_R}(r)$ profiles are approximated from a US-standard atmosphere model along with temperature/pressure ground-level conditions or from temperature/pressure radiosounding measurements [*Bodhaine et al.*, 1999].

2.2.6 Review of the Klett-Fernald-Sasano two component elastic inversion algorithm review

This section is introduced with a view to Chapter 3. The elastic lidar equation (Eq. 2.20) is inherently under-determined as it contains two unknowns (i.e., the atmospheric extinction, α and the backscatter coefficient, β) but only a single observable (the backscattered power $P_{\lambda_0}(R)$) because, as it has been shown, backscatter lidars provide only range-resolved profiles of attenuated backscatter signal [*Bösenberg and Hoff*, 2007]. This under-determination is in contrast to other schemes such as elastic-Raman systems, HSRL [*Nishizawa et al.*, 2008], and variational multi-angle backscatter-lidar retrievals [*Sicard et al.*, 2002], all of which enable independent inversion of both aerosol extinction and backscatter coefficients [*Ansmann et al.*, 1992].

In 1981, *Klett* [1981] presented a stable inversion algorithm to invert the elastic single-scattering lidar equation assuming a one-component atmosphere where there is no separation between aerosol and molecular components. In 1984, *Fernald* [1984] presented the two-component version of the algorithm , which *Klett* [1985] reformulated in a unified approach. Both *Klett's one-component (KLT)* and Fernald's two-component algorithm (also known as *Klett-Fernald-Sasano's method, KFS*) require additional inputs to resolve the under-determination of the lidar equation. They are, provision of (1) a boundary condition and (2) a range-dependent extinction-to-backscatter ratio.

The *boundary condition* usually consists on a known or presumed value of the extinction or backscatter coefficient at the far-end of the range profile. This value is used as an absolute calibration for retrieving extinction or backscatter coefficients at lesser ranges. The *extinction-to-backscatter ratio* can be expressed as the ratio of total (aerosol plus molecular) components or aerosol components only. Today, the term *lidar ratio* is widely accepted to refer to the aerosol-only extinction-to-backscatter ratio. In what follows, the distinction between "total" lidar ratio (including molecular component) and the "lidar ratio" (aerosol-component only) will be made when necessary.

Backscatter-coefficient retrieval.- Though historically this was not the case, today both one- and two-component inversion algorithms are usually formulated in backscatter-coefficient form. Backscatter coefficient is always the preferred quantity for retrieval as the aerosol extinction coefficient is estimated by multiplying the profile of the aerosol backscatter coefficient by the assumed aerosol lidar ratio, S_{aer}, profile used as input to the retrieval [*Sasano et al.*, 1985].

Solution form.- In the two-component KFS the relevant variable to be solved is the total backscatter coefficient (Eq. 2.7), given the ideal range-corrected backscatter power (Eq. 2.22 excluding the OVF non-ideal term), the user-input lidar ratio, $S_{aer}(R)$ (Eq. 2.10), the molecular lidar ratio, S_{mol} (Eq. 2.11) and a backscatter calibration at a reference range R_0,

$$\beta_{tot}(R_0) = \beta_{aer}(R_0) + \beta_{mol}(R_0) \quad \left[m^{-1}sr^{-1}\right], \tag{2.28}$$

The mathematical development next follows Sect. IV in *Klett* [1985], and is further detailed in Chapt. 4 in *Reba* [2010].

The first step is to reformulate the two-component lidar equation in differential form [*Klett*, 1981]. Towards this end, Eqs. 2.10 and 2.11 are substituted into the range-corrected power form of the Eq. 2.22 to yield,

$$U(R) = R^2\,P(R) = K\,\beta_{tot}(R)\exp\left\{-2\int_0^R \left[S_{aer}(r)\,\beta_{aer}(r) + S_{mol}\,\beta_{mol}(r)\right] dr\right\}. \tag{2.29}$$

where subscript λ_0 has been omitted for brevity.

By multiplying both sides of Eq. 2.29 by $\left[-2\int_0^R S_{aer}(r)\,\beta_{mol}(r)\,dr + 2\int_0^R S_{mol}\,\beta_{mol}(r)\,dr\right]$ (compare with Eq. 20 in *Klett* [1985]) and introducing Eq. 2.28, Eq. 2.29 can be rewritten as

$$K\,\beta_{tot}(R)\,\exp\left[-2\int_0^R S_{aer}(r)\,\beta_{tot}(r)\,dr\right] = U(R)\,\exp\left\{-2\int_0^R \left[S_{aer}(r) - S_{mol}\right]\beta_{mol}(r)\,dr\right\}. \tag{2.30}$$

Eq. 2.30 can be rearranged in a more readable form by taking the logarithm on both sides of the equation and by defining the *modified logarithmic* range-corrected signal,

$$D'(R) = \ln\left[U(R)\,\exp\left\{-2\int_0^R \left[S_{aer}(r) - S_{mol}\right]\beta_{mol}(r)\,dr\right\}\right]. \tag{2.31}$$

Therefore, Eq. 2.30 reads as,

$$\ln\left[K\,\beta_{tot}(R)\right] - 2\int_0^R S_{aer}(r)\,\beta_{tot}(r)\,dr = D'(R)\,. \tag{2.32}$$

The two-component differential lidar equation is obtained in system-independent form, by differentiating Eq. 2.32 with respect to R as follows

$$\frac{1}{\beta_{tot}(R)}\,\frac{d\,\beta_{tot}(R)}{d\,R} - 2\,S_{aer}(R)\,\beta_{tot}(R) = \frac{d\,D'(R)}{d\,R}\,. \tag{2.33}$$

The solution of Eq. 2.33 has the elementary structure of the Bernoulli or homogeneous Ricatti equation, which introducing as boundary condition the total backscatter calibration at the reference range R_0, $\beta_{tot,0} = \beta_{tot}(R_0)$ (Eq. 2.28), and power boundary condition $D'_0 = D'(R_0)$ (Eq. 2.31), has

the well-known solution (compare with Eq. 22 in *Klett* [1985]),

$$\beta_{tot}(R) = \frac{\exp\left[D'(r) - D'_0\right]}{\frac{1}{\beta_{tot,0}} + 2\int_R^{R_0} S_{aer}(r)\,\exp\left[D'(r) - D'_0\right] dr} \tag{2.34}$$

From the previous equations, Eq. 2.34 can be written in expanded form as

$$\beta_{aer}(R) = \frac{\left[R^2\,P(R)\right]\,\exp\left\{2\int_R^{R_0}\left[S_{aer}(u) - S_{mol}\right]\beta_{mol}(u)\,du\right\}}{\frac{\left[R_0^2\,P(R_0)\right]}{\beta_{aer}(R_0)+\beta_{mol}(R_0)} + 2\int_R^{R_0} S_{aer}(u)\left[u^2\,P(u)\right]\,\exp\left\{2\int_u^{R_0}\left[S_{aer}(v) - S_{mol}\right]\beta_{mol}(v)\,dv\right\}du} - \beta_{mol}(R) \quad \left[m^{-1}sr^{-1}\right], \tag{2.35}$$

The solution to Bernoulli differential equation, Eq.2.35 expresses aerosol, β_{aer}, and molecular backscatter, β_{mol}, at range R, as a function of the range-corrected lidar return, R^2P, the molecular lidar ratio, S_{mol}, and the aerosol lidar ratio, S_{aer}. This last term is usually assumed as known, using previous knowledge of the type os aerosol to be measured [*Pedros et al.*, 2010; *Wandinger et al.*, 2002; *Mattis et al.*, 2004]. The range reference can be taken as an upper molecular-only region, and the integral evaluated towards the laser [*McCormick and Leavor*, 2013].

In practice, the molecular backscatter is estimated from local temperature/pressure radiosounding measurements or a US-standard atmosphere model given ground-level temperature and pressure data [*Bodhaine et al.*, 1999].

2.3 Radar remote sensing

Propagation of electromagnetic radiation in the atmosphere is influenced by its physical properties. In the case of most common radar applications, atmospheric effects are avoided or minimized as much as possible. However, in the weather-radar case, those effects are maximized for observing the atmosphere behavior, and the solid targets are treated as noise.

The study of the scattering of electromagnetic waves by turbulent media has been approached by many authors. Among these, *Tatarski'i* [1961] has a general account of the theoretical results that served as a basis for interpreting a variety of experimental studies. This made possible to define the relationship between the concepts used to describe the phenomena and the measurable quantities characterizing atmospheric turbulence. See e.g., *Ottersten* [1969] for a summary.

Classification.- Regarding radar categorization, they can be classified by the type of waveforms they use, or by their operating frequency.

In the first case, radars can be *Pulsed (PR)* or *Continuous Wave (CW)* radars. PR transmit and receive a train of modulated pulses, and range information is extracted from the two-way time delay between a transmitted and received pulse. On the other hand, CW radars continuously emit electromagnetic energy, and use separate transmit and receive antennas (or a single Tx/Rx antenna and a circulator). The transmitted signal is constant in amplitude and frequency and the echo signal is received and processed permanently. While CW radars without modulation can accurately measure target radial velocity (due to Doppler shift) and angular position, target range

information cannot be extracted without utilizing some form of modulation, because lack of pulses [*Mahafza and Elsherbeni*, 2004]. This CW disadvantage can be corrected using frequency shifting methods. Thus, a signal that constantly changes in frequency around a fixed reference is used to detect stationary targets. When an echo signal is received the frequencies can be examined, and compared with time in the past that particular frequency was sent out. This principle permits a range calculation similar to using a train of pulses. This specific type of radar is know as *Frequency-Modulated Continuous Wave (FMCW)* radar, which use a smoothly varying ramp of frequencies up and down instead of random frequencies.

Table 2.1: Radar frequency band classification [*Mahafza and Elsherbeni*, 2004].

Letter designation	**Frequency range (GHz)**
HF (High Frequency)	0.003 – 0.03
VHF (Very High Frequency)	0.03 – 0.3
UHF (Ultra High Frequency)	0.3 – 1.0
L–band	1.0 – 2.0
S–band	2.0 – 4.0
C–band	4.0 – 8.0
X–band	8.0 – 12.5
Ku–band	12.5 – 18.0
K–band	18.0 – 26.5
Ka–band	26.5 – 40.0
MWF	$>$ 34.0

Weather radar.- According to operating frequency, radar classification is shown in Table 2.1. Most weather radar systems use either S–band or C–band [*Mahafza and Elsherbeni*, 2004].

Historically, while rain precipitation were detected using radars since the early beginning of the technology (as a serious thread for surveillance systems during the World War II), and the first meteorological observations exploiting radar were made in 1941, it was not until the early 1970s that Doppler radar provided meteorological research with full efficiency [*Sauvageot*, 1992b]. Also in the early 1970s, VHF and UHF radar systems (Table 2.1) lead to the appearing of the *clear air detection* techniques, allowing the observation of the atmosphere permanently, and not only when rain precipitation was present. Weather-radar systems are remote sensing systems that detect variations of the refractive index of the atmosphere that are in the same order as the wavelength of the sensor [*Stull*, 1988a], which is an advantage to detect the ABLH.

In *clear-air* radar, refractive index gradients give rise to Bragg scattering [*Contreras and Frasier*, 2008], which is the signal component –that is–, the component of interest. On the other hand, Rayleigh scattering due to hydrometeors and hydrometeors-like scatterers like insects and birds are considered the noise component in addition to usual thermal noise. To remove the contribution of such interferent scatterers different techniques have been tackled: *Angevine et al.* [1993]; *Angevine* [1997] have based their method on the elimination of the spatial samples or "outliers" characterized by a SNR, speed or spectral width exceeding a predetermined standard-deviation threshold (usually 2-3 σ) computed over 1-h measurements. Out-of-threshold signal levels are discarded hence preserving information on the measured turbulence intensity from the radar signal. *Merritt* [1995] has proposed a statistical averaging technique in which, in contrast to classic Doppler-radar spectral

estimators, signals from different objects are identified and separated before the average spectral estimate is made.

In fair weather conditions, the ABL is often more humid than the FT and centimeter-scale eddies on the interface between the mixed layer and the free atmosphere create strong returns. Within the ML there is a little returned energy in spite of the strong turbulence, because the humidity is low everywhere.

2.3.1 Radar equation

In terms of the radar equation, and according to the antenna configuration, radar systems can be classified as monostatic and biestatic radars. The first one uses the same antenna for both transmission and reception stages, while the latter uses one antenna for each stage, and both antennas are usually located in different places. Although CW and FMCW radars use separate transmit and receive antennas, they are considered as monostatic, unless the distance between the antennas is considerable [*Mahafza and Elsherbeni*, 2004].

The monostatic radar equation (i.e., with collocated emitter and receiver antennas or with a single emitter/receiver antenna) can be expressed as

$$P_r = \frac{P_t}{4\pi R^2} G \frac{1}{4\pi R^2} \left(\frac{\lambda^2}{4\pi} G \right) \sigma, \tag{2.36}$$

where P_r [W] is the *received power*, P_t [W] is the *transmitted power*, R [km] is the range along the radar LOS, G [·] is the antenna gain, λ [m] is the radar wavelength and σ [m^2] is the effective *radar cross section (RCS)* of the observation volume at a range R. The observation volume, $V = \Delta R \Delta S$ [m^3], can be defined as the product of the radar spatial resolution, ΔR, times the antenna "projected-reading area" at the range, R, $\Delta S = R^2 \Delta\theta \Delta\phi$, with $\Delta\theta$, $\Delta\phi$ the angular E– and H–plane *Half Power BandWidth (HPBW)* of the antenna pattern. ΔR is derived from the resolution of the frequency estimator used by the FMCW in the detection process. Fig. 2.5a shows the radar geometry used to describe the monostatic radar equation.

In Eq. 2.36, the following terms are explained for physical significance: *(i)* the term $\left(\frac{P_t}{4\pi R^2} \right)$ is the power density [W/m^2] incident on the target observation volume at a range, R, assuming an isotropic antenna; *(ii)* $\left(\frac{P_t}{4\pi R^2} G \right)$ is the power density incident at the range, R, including the antenna gain G; *(iii)* $\left(\frac{P_t}{4\pi R^2} G \sigma \right)$ is the collected power [W] in the observation volume, V; *(iv)* $\left(\frac{P_t}{4\pi R^2} G \frac{1}{4\pi R^2} \sigma \right)$ is the backscattered power density from the observation volume, V and received at the radar location; and *(v)* $\left(\frac{\lambda^2}{4\pi} G \right)$ is the effective area [m^2] of the antenna in reception according to the antenna reciprocity theorem assuming an ideal antenna [*Balanis*, 2005]. Therefore, the product of terms *(iv)* and *(v)* gives the received power P_r [W].

2.3.2 Weather-radar and atmospheric radar reflectivity

Because of the limited radar spatial resolution, the observation volume, V can be though as filled with a homogeneous distribution of targets (or meteorological scatterers) with randomly distributed phases [*Sauvageot*, 1992a], so that σ in Eq. 2.36 above must be replaced with the sum of the RCSs of all these scatterers inside the observation volume, V. That is,

$$\sigma = \sum_V \sigma_i = V\left(\frac{\sum_V \sigma_i}{V}\right) = V\eta \ , \tag{2.37}$$

where $(1/V)\sum_V \sigma_i$ [m^2 m^{-3}] is the average RCS of the scatterers per unit volume, and is called the *volume radar reflectivity,* η. In what follows it will be addressed as the "reflectivity" and will be computed in decibels ($\eta(dB) = 10\ log\ \eta$).

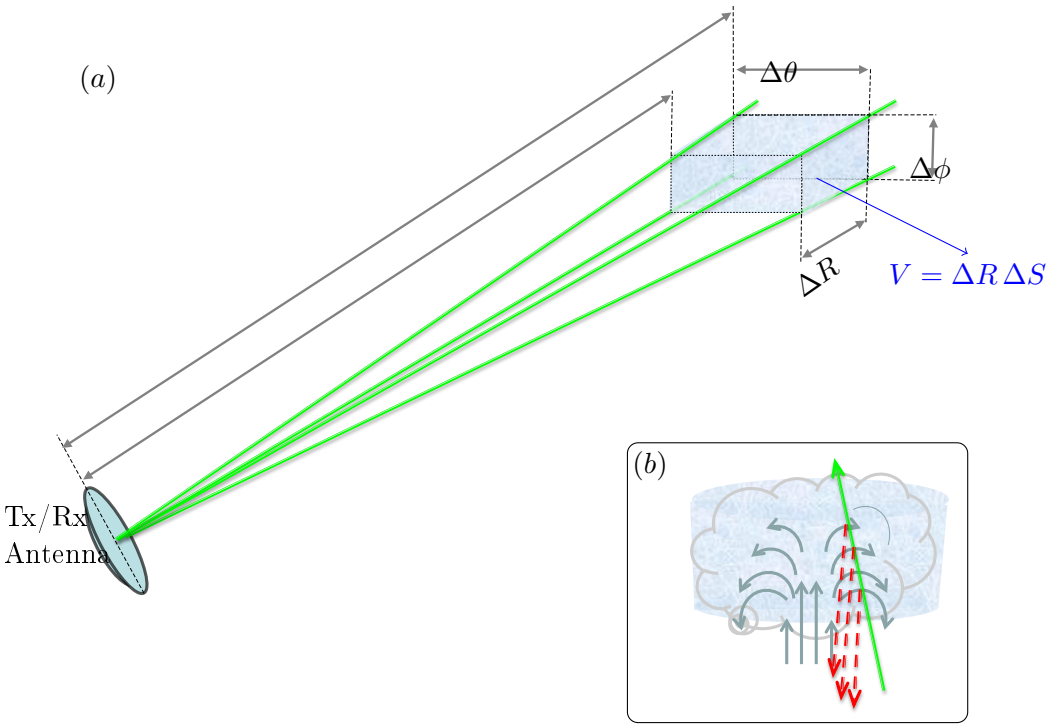

Figure 2.5: Monostatic radar setup geometry used to derive the radar equation. (a) Transmitter and receiver parts, V is the scattering volume or resolution cell, $\Delta\theta$ and $\Delta\phi$ are the angular E– and H–plane HPBW of the Tx/Rx antenna pattern respectively, R is the range, and ΔR is the radar spatial resolution. Green solid lines mark off the idealized antenna beam pattern (same in transmission and reception). (b) Sketch showing the Bragg scattering (red dashed arrows) due to turbulences (gray solid arrows), when incident power density (green solid arrow) interacts with atmosphere inside the scattering volume (light blue volume).

When *clouds* and *precipitation* are considered (σ_i much smaller than the radar wavelength) the prevailing scattering mechanism is Rayleigh, which is characterized by a size parameter, $x = D/\lambda \ll 1$ (D the scatterers' diameter, e.g., a raindrop), and a scattered power proportional to the reciprocal of the fourth power of the wavelength and to the sixth power of the scatterers' diameter

[*Sauvageot*, 1992a],

$$\sigma_i = \frac{\pi^5}{\lambda^4}|K|^2 D_i^6 \,. \tag{2.38}$$

In Eq. 2.38, $|K|^2$ is a factor depending on the dielectric constant of the scattering medium ($K = (\varepsilon - 1)/(\varepsilon + 2)$, 0.934–$j$0.011 for water at 0 °C and λ =10 cm) and subindex i stands for i-th scatterer. When, as is the case in practice, a particle size distribution is considered, η can be written as

$$\eta = \frac{\pi^5}{\lambda^4}|K|^2 \int_{D_{min}}^{D_{max}} D^6 N(D) dD = \frac{\pi^5}{\lambda^4}|K|^2 Z, \tag{2.39}$$

where $N(D)$ is the particle size distribution (particles per unit volume with diameter between D and $D + dD$) and Z is the *radar reflectivity factor*. However, when the observed scattering volume,V, does not satisfy the size-parameter conditions of the Rayleigh approximation ($x = D/\lambda \ll 1$), it is common to use an equivalent reflectivity factor, Z_e, instead Z, which is equal to the reflectivity factor of a population of spherical and liquid particles satisfying the Rayleigh approximation and producing a signal of the same power [*Sauvageot*, 1992a],

$$\eta = \frac{\pi^5}{\lambda^4}|K|^2 Z_e. \tag{2.40}$$

Insects and *birds* are Rayleigh-like scatterers at radar wavelengths ($x \ll 1$) that will be treated as "corrupting noise" additive to the radar return signal. The motivation for that is twofold:

First, insects have typical sizes much smaller than the sounding wavelength and a significant proportion of water, approximately 50 to 70% of the total weight of their bodies, which cause a significant backscattering cross section easy to be detected.

Second, insects are not good "tracers" of the ABL [*Contreras and Frasier*, 2008]. In *Achtemeier* [1991], a dual-polarized S-band radar was used to evaluate insects as a tracer of the ABL motion. It was inferred that insects were reorienting themselves in response to air motion, to avoid temperatures less than 10-15°. So insects are not passive tracers, and cannot be used to estimate the ABLH. Moreover, insects are effective tracers of horizontal wind velocities during summer daylight hours [*Angevine*, 1997; *Kusunoki*, 2002]. Birds, which also form part of the second main cause of radar echoes, have their own velocity of movement (10–20 [ms^{-1}]) and they will be treated like insects [*Sauvageot*, 1992a].

In clear-air conditions, Bragg and Rayleigh scattering (the latter mostly due to birds and insects) are the prevailing scattering mechanisms. Bragg scattering at the radar frequencies of interest (C-band and S-band mainly) is due to very strong gradients and random fluctuations of the refractive index associated with discontinuities and/or turbulences of the atmosphere. A sketch showing Bragg scattering can be found in Fig. 2.5b.

The *refractive index* n of the atmosphere is a function of the *atmospheric pressure*, p [hPa], temperature, T [K], and *partial pressure of water vapour*, e [hPa], which is formally expressed in

terms of the *radioelectric refractivity* or *refractivity*, N as [*Sauvageot*, 1992b]

$$N = (n-1)\cdot 10^6 = \left(\frac{77.6}{T}\right)\left(\frac{p+4810e}{T}\right) \quad [\cdot]. \tag{2.41}$$

Atmospheric random fluctuations of the refractive index can be related to the reflectivity by means of spectral power-density function of the refractive index in space, $\phi_n(k)$, where k is the wave-number vector (equivalently, ϕ_n is the Fourier transform of the autocorrelation function of the refractive index). *Tatarski'i* [1961] showed that the reflectivity can be related to the random fluctuations of the refractive index as [*Sauvageot*, 1992a]

$$\eta(\mathbf{k}) = \frac{\pi^2}{2} k^4\, \phi_n(\mathbf{k}), \tag{2.42}$$

where k is the wave-number vector in the radar propagation direction, with $|k| = 4\,\pi/\lambda$. Although $\phi_n(k)$ is defined for the entire space of the wave numbers, only spatial fluctuations whose scale, following the direction of propagation, is close to $\lambda/2$ produce additive phases and are perceived by the radar (Bragg scattering); however, detection takes place only if there is sufficient spectral energy on the $\lambda/2$ scale, which is selectively observed by the radar [*Sauvageot*, 1992a].

Under these conditions, η is commonly related to the *refractive index structure function parameter*, C_n^2, [*İnce et al.*, 2003; *Tatarski'i*, 1961] by

$$\eta = 0.38\; C_n^2\; \lambda^{-1/3}. \tag{2.43}$$

In terms of frequency, Bragg scattering composes a substantial part of the backscatter for frequencies below 3 GHz [*Riley*, 1985; *Vaughn*, 1985], while Rayleigh scattering tends to dominate for higher frequencies [*Contreras and Frasier*, 2008].

2.3.3 FMCW radar foundations

FMCW radars have been used to monitor the atmosphere (the ABL and the FT) since late 1970s [*Richter*, 1969; *Eaton et al.*, 1995]. The strength of this type of radars lies in its ability to monitor the atmospheric refractive-index structure parameter, C_n^2, with high resolution in height and time, by adding Doppler capability [*İnce et al.*, 2003]. In that respect, S–band FMCW radars marked the beginning of a new research field [*Gossard*, 1990]. Some examples of this type or radars can be found in *Richter* [1969]; *Strauch et al.* [1976]; *Eaton et al.* [1995].

FMCW radars may be thought as a limiting case of the pulse-compression radars where the duty cycle of the transmitted waveform approaches 100 %. While pulse-compression radars operate by emitting a complex, long coded waveform of bandwidth B and duration T (e.g. a chirp signal), FMCW radars use a simple linear frequency modulation with period $T = T_m$ [*İnce et al.*, 2003].

Fig. 2.6 shows the principle of operation of a FMCW radar considering triangular-wave frequency modulation with *period*, T_m, and *sweep frequency*, Δf, over a *carrier frequency*, $f_r(t)$, enables to estimate range and radial speed of the target.

Because the improvement factor if compression-gain radars over PRs of equivalent range resolution is given by the time-bandwidth product, BT, the so-called *compression gain*, in FMCW

radars this gain can be very large, exceeding 60 dB. Not to mention that FMCW radars rely on the same radar equation as PRs.

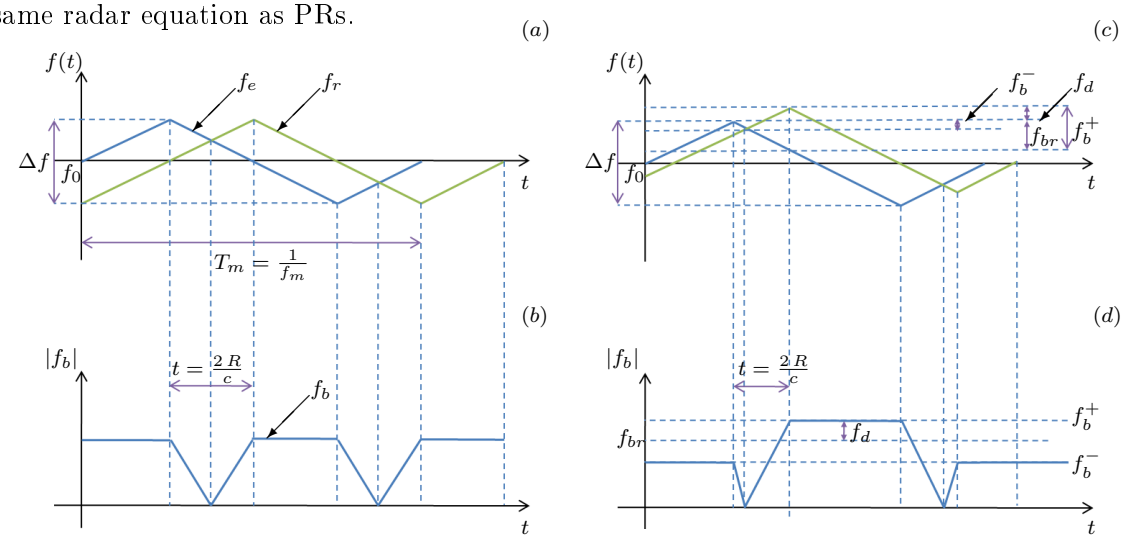

Figure 2.6: Principle of operation of a FMCW radar,using triangular-wave frequency modulation. (*a*) Stationary target detection located at a distance R. f_e is the instantaneous emission frequency, f_r, is the instantaneous reception frequency, f_m is the modulation frequency, f_0 is the carrier frequency, and Δf is the sweep frequency. (*b*) Instantaneous beat frequency (absolute values). f_b for stationary target case (*a*). (*c*) Moving target detection located at a distance R. The maximum value of the f_b, f_b^+, is the beat frequency plus the Doppler shift caused by the moving target in the rising edge of the receiver frequency, $f_b^+ = f_{br} + f_d$. Likewise, the minimum value of the f_{br}, f_b^-, is $f_b^- = f_{br} - f_d$. Thus, $f_{br} = (f_b^+ + f_b^-)/2$. (*d*) Same as (*b*) for the moving target case of (*c*).

To illustrate the principles of FMCW range/radial - velocity estimation, two cases can be considered next: (1) A stationary target at range R, and (2) a moving target at range R with radial speed, the speed component of the target which acts towards or away the radar (Fig. 2.6c-d).

Stationary target.- A delay will shift the echo signal from the atmospheric target in time, which is essentially a delayed, attenuated, and possibly Doppler-shifted replica of the transmitted signal (green trace in Fig. 2.6a). This results in a frequency difference between the actual frequency, f_e, and the delayed echo signal, f_r (blue trace in Fig. 2.6b), which is a measure of the distance of the atmospheric target, namely, the *beat frequency*, f_b, in Fig. 2.6b. For stationary targets, the beat frequency and the target distance are related through

$$f_b(R) = \frac{\Delta f}{T_m}\, t = \frac{\Delta f}{T_m}\,\frac{2\,R}{c} = \frac{4\,\Delta f\, R\, f_m}{c} \quad \left[Hz\right], \tag{2.44}$$

and therefore, the target distance can be computed as

$$R = \frac{c\, f_b}{4\,\Delta f\, f_m} \quad \left[m\right]. \tag{2.45}$$

Resolving in range is done through frequency analysis of the sampled waveform, most often through a *Discrete Fourier Transform (DFT)*.

Moving target.- When the target (or aerosol target) moves, the Doppler shift moves the frequency of the entire echo signal either up (moving towards the radar) or down (moving away from the radar). Fig. 2.6c-d shows a target moving towards the radar, where the beat frequency is represented as

f_{br}, to distinguish it from the stationary target case. The maximum value of f_b, f_b^+, is the beat frequency plus the Doppler shift, f_d, caused by the moving target in the rising edge of the receiver frequency, and can be computed as $f_b^+ = f_{br} + f_d$. Likewise, the minimum value of the f_{br}, f_b^-, can be computed as $f_b^- = f_{br} - f_d$. Thus, $f_{br} = (f_b^+ + f_b^-)/2$, as can be seen in Fig. 2.6c-d. The range can be estimated by mixing the echoes with a portion of the transmitted signal with the same frequency (available from the VCO "block" in Fig. 2.7). For moving targets, the mean beat frequency, f_{br}, and the target distance, R, are related through

$$f_{br}(R) = \frac{f_b^+ + f_b^-}{2} = \frac{4\,\Delta f\,R\,f_m}{c} \quad \left[Hz\right]. \tag{2.46}$$

Note that the mean beat frequency, f_{br}, in Fig. 2.6d corresponds to f_b in Fig. 2.6b.

From Eq. 2.44 above, target distance can be computed as

$$R = \frac{f_{br}\,c}{4\,\Delta f\,f_m} \quad \left[m\right]. \tag{2.47}$$

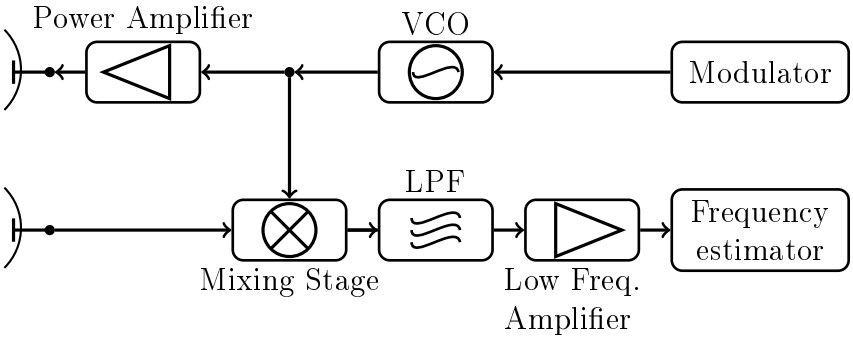

Figure 2.7: Block diagram of a FMCW radar setup. Transmitter part: The Modulator converts digital control words implementing a modulation into an analog control voltage for the next stage, the *Voltage Controlled Oscillator (VCO)*, that generates the high frequency signal, which is amplified before the transmitter antenna. Receiver part: receiver antenna, the mixing stage, which down converts the received high frequency signal to the baseband signal, a low-pass filter, that blocks unwanted mixed frequencies. An amplifier is needed because the echo signals are weak. Finally, the Frequency estimator converts the analog voltage into a digital signal.

2.4 The Atmospheric Boundary Layer

The ABL (also called *Planetary Boundary Layer, PBL*) is the lowest part of the troposphere that is directly influenced by the ground and whose changes are shown in less than one hour [*Stull*, 1988a]. The ABL vertical extent varies from a few tens of meters to several kilometers.

Factors related to the orography, the season, the daytime or the weather act over the ABL and change its structure both spatially and temporally. Temperature, pressure and density variations can be clearly seen inside the ABL (lower troposphere), while they are not evident at greater altitudes (upper troposphere or FT). Processes that cause those variations are related to the thermodynamic equilibrium between the atmosphere and the ground, which warms and cools in response

to the incoming radiation from the sun during the daytime, and cools during nighttime. They also depend on altitude and weather [*Blaunstein et al.*, 2010]. So, ABL changes are forced due to these variations via transport processes [*Stull*, 1988a]. One of the most important transport processes is turbulence. From the radar point-of-view, turbulent variations in the refractive index of air (eddies) are tracers of the ABL behavior [*Sauvageot*, 1992a].

Considering *refractive index* of the air, small-scale atmospheric dynamic perturbations produce local modifications to its field. In fact, during a turbulent mixing process, "air particles" in a turbulent volume are rapidly displaced from each other and do not immediately mix in a complete and homogeneous manner; they temporarily preserve their identity: the pressure is equal to that of the environment but the potential temperature and the specific humidity are maintained. The higher the average initial gradients and the greater the displacement (i.e., the stronger the turbulence) the more marked are the local variations in these variables at the boundary of the air particles (Fig. 1.3a) [*Sauvageot*, 1992b].

The ABL is characterized by the presence of aerosols, which are air-borne solid particles from both natural and anthropogenic origins. Aerosols have an important role in the processes of optical dispersion and therefore, they have a significant contribution in the Earth radiative budget, in cloud formation and in climate understanding. From the lidar point-of-view, aerosols inside the ABL are tracers of its behavior, since ABL usually has a much higher concentration than the FT, therefore, lidar returns from the ABL are stronger compared with those coming from the FT (Fig. 1.3b) [*Stull*, 1988a].

2.5 ABLH detection methods

The ABL profile typically presents a sharp decrease at some height inside the EZ, henceforth called the ABL local transition. The buoyancy-driven updrafts tends to narrow this local transition, while in the case of downdrafts the transition widens [*Hägeli et al.*, 2000]. This simple assumption is often distorted by several factors such as multi-layer scenarios (transported layers, stratified layers, lateral entrainment or the residual layer), and non-linear effects of moisture distribution in the aerosol concentration. The influence of all these effects is different depending on which method of ABL height detection and which type of remote sensing system are chosen. Thus, active research in terms of inter-comparison is still under way [*Pal et al.*, 2010; *Haeffelin et al.*, 2012; *Lange et al.*].

Two different approaches to estimate the ABLH from lidar signals can be outlined:

- The *geometrical approach* uses the fact that the EZ region usually appears in the individual lidar signal profiles as a sharp decrease between the two air masses (this is due to the lack of aerosols and moisture in the free troposphere), all of which causes a strong signature in the range-corrected backscatter lidar return. Geometrical-based ABL-detection methods rely on the detection of a meaningful transition, usually by some sort of edge-detection analysis, by means of a threshold criterion [*Melfi et al.*, 1985; *Boers and Eloranta*, 1986; *Batchvarova et al.*, 1999] or gradient detection [*Endlich et al.*, 1979; *Sicard et al.*, 2006] applied to time-averaged profiles. When high-SNR and temporal resolution is available from the lidar sensor,

geometrical methods are able to retrieve the instantaneous ABLH (the term h_{ABL} will be used indistinctly), which is identified as the instantaneous ABL top.

- The *statistical approach* uses the high variability in the return signal caused by the mixing processes in the EZ between cells in the EZ and cells in the FT above or in the mixing layer below. This approach requires the analysis of a set of profiles to produce a statistically significant estimate of the mixing-layer depth, taken as the mean ABLH ($\bar{h}_{ABL}$).

Next, some of the most common methods used to trace the ABLH are revisited. They are the *Threshold Method (THM)*, derivative methods and the *Centroid/Variance Method (VCM)*. The THM and the derivative methods are based on the geometrical morphology of the returned backscatter lidar signal, while the last one falls into the statistic analysis class of methods.

Threshold method.- Also known as "critical backscatter" method, the THM is a simple method useful to detect sharp lidar signal transitions with well known levels, usual in the *Convective Boundary Layer (CBL)* [*Melfi et al.*, 1985; *Batchvarova et al.*, 1999]. An arbitrary threshold value (set by trial and error) is applied to the range-corrected profile to differentiate between a high-level backscatter region (the ML in Fig. 1.2) and a low-level backscatter region (the FT in Fig. 1.2). The ABL height is computed as the lowest height whose backscatter value coincides with the threshold. Some issues of this method are the arbitrary threshold value itself, and the noise-contamination signal that could induce a biased detection, unless a range-smoothing and/or a pulse averaging window is applied.

Derivative methods.- Among the derivative methods, the *Gradient Method (GM)* seeks for the range position corresponding to the *absolute minimum* of the first derivative,

$$h_{bl,GM} = \min\left[\frac{dU(R)}{dR}\right], \tag{2.48}$$

which is the maximum local slope of the lidar profile (Fig. 2.8). In Eq. 2.48 above, $U(R)$ is the range-corrected lidar signal, $U(R) = R^2\,P(R)$. Since the measured lidar signal is noise-corrupted and the atmosphere is particularly variable when reaching the ML, the derivative of the signal can present several small negative peaks. There are several solutions commonly used together to reduce the noise.

As in the THM, a time-averaging over a set of lidar profiles can be applied in order to obtain a less noisy lidar signal. A range-smoothing moving-average window can also be applied to the lidar profile and its derivative to suppress noise peaks, e.g. *Wavelet method (WM)* in *Cohn and Angevine* [2000], which finds the peak in range-corrected SNR. All of these solutions lead to a reduction of the temporal and/or spatial resolution.

A further approach to detect the ABLH is to compute the derivative of the logarithm of the range-corrected lidar signal [*Martucci et al.*, 2003], which is proportional to the aerosol extinction gradient, and detect the largest negative gradient,

$$h_{bl,LGM} = \min\left[d\ln U(R)/dR)\right]. \tag{2.49}$$

The derivative of the logarithm (*Logarithm Gradient Method, (LGM)*), enhances the aerosol

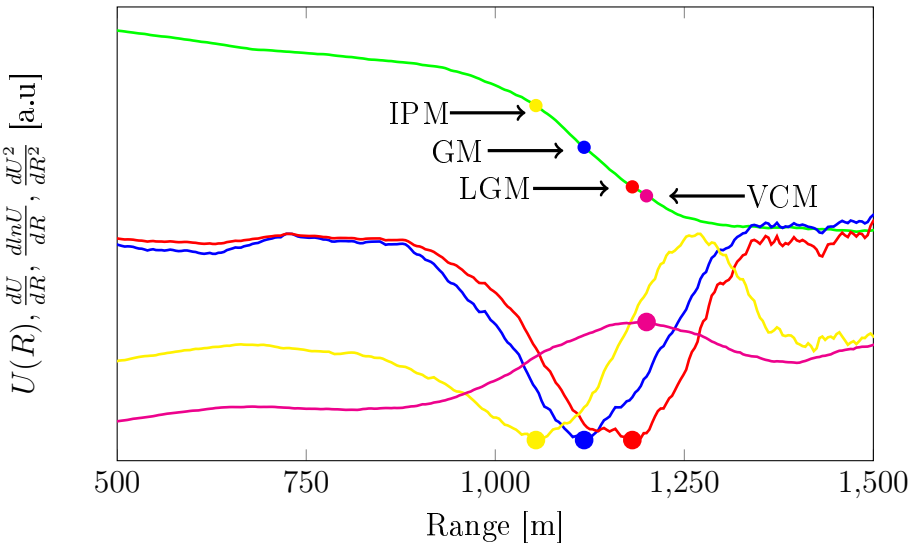

Figure 2.8: Cross-examination of four classic ABL estimation methods (VCM, LGM, GM, and IPM). The green line represents the measured time-averaged range-corrected lidar profile. The blue line corresponds to the first derivative of the range-corrected lidar signal, $\frac{dU(R)}{dR}$, the red line to the derivative of the logarithm, $\frac{d\ln U(R)}{dR}$, and the yellow line to the second derivative, $\frac{d^2U(R)}{dR^2}$. The magenta line is the range-dependent variance of the lidar measurement set. Because all the plots have different scales, they have been arbitrarily normalized so that they can be plotted on the same scale for visual purposes (adapted from *Lange et al.* [2013]).

contrast [*Martucci et al.*, 2003] but also the noise contamination is amplified.

Another usual derivative method is the *Inflection Point Method (IPM)* [*Sicard et al.*, 2006]. Instead of using the first derivative of the range-corrected lidar signal, the IPM computes the minimum of the second derivative to find the inflection points of the range-corrected lidar profile,

$$h_{bl,IPM} = \min\left[\frac{d^2U(R)}{dR^2}\right]. \tag{2.50}$$

The time-averaged profile of the noise-corrupted lidar profile has its best estimator in the IPM solution as an average height identified with the middle of the EZ [*Menut et al.*, 1999; *Sicard et al.*, 2006]. Because the IPM method differentiates two times the range-corrected corrected lidar signal, and, as mentioned before, noise corrupts computation of the signal derivatives, a more stringent smoothing has to be applied to the raw-lidar signal. As a result, the IPM method yields a poorer resolution than GM and LGM methods.

To illustrate the behavior of these methods, Fig. 2.8 shows a measured range-corrected profile from the RSLab lidar system (green line) along with the computed first and second-order derivatives (blue and yellow line, respectively). The first derivative has been computed by averaging 10^4 lidar vertical profiles (PRF = 20 Hz, λ = 1064 nm) in combination with a range-smoothing rectangular sliding-window over the lidar signal (the spatial window length is 25 samples and the raw data spatial resolution is 3.75 m/sample). This yields a temporal resolution of Δt_{GM} $\sim 6{\cdot}10^2$ s and ΔR_{GM} $\sim$100 m in the determination of the ABLH. The first derivative of the logarithm of the ABLH has been computed by using the same smoothing parameters as for the GM. To compute

the second derivative for the IPM a larger range-smoothing has been used ($\Delta R_{IPM} \simeq 150\ m$), which leads to a slightly worse range resolution. Because – as mentioned – the THM method uses an threshold value set from the user side, the ABLH can be located anywhere in the transition range from 1000 m to 1250 m.

The estimated ABLH for each of derivative methods is marked with a dot (GM, red dot; LGM, yellow dot; IPM, black dot). The GM and LGM give slightly larger values than the IPM method. To better inter-compare the derivative methods presented, the original signals in Fig. 2.8 have been normalized in such a way that they can be compared in the same scale.

Variance/Centroid method.- In the EZ, small-scale turbulent motions found between the aerosol-loaded updrafts and the downdrafts of clean air determine a region of high variability in concentration, which is reflected in the lidar signal received. The average ABL "centroid" height is defined as the lowest range position of a local maximum of the variance profile [*Hooper and Eloranta*, 1986],

$$\max(\mathrm{Var}(R));\ \ \mathrm{Var}(R) = \frac{1}{N-1}\sum_{i=1}^{N}\Big[U(R,t_i) - \overline{U}(R)\Big]^2, \tag{2.51}$$

where the horizontal top bar indicates time average.

The VCM method is often mislead by shear-induced turbulence in urban environments and tends to yield overestimates with respect to the IPM. Nevertheless, the VCM is a good method to sense the residual layer in urban environments, whereas in rural environments this method is indicated to track the sedimented layer [*Menut et al.*, 1999].

A good performance is found when both VCM and GM methods are combined into a constrained detection method [*Lammert and Bösenberg*, 2006]. Because in Eq. 2.51, the variance must be computed over the ensemble of temporal realizations for each range cell, a large number of profiles is needed to compute a statistically significant variance. This leads to a low temporal resolution method. In Fig. 2.8, the time resolution of the variance profile (green line) is $\Delta t \simeq 4.5{\cdot}10^3\ s$ as compared to $\Delta t \simeq 6{\cdot}10^2\ s$ of the derivative methods. Range smoothing and time averaging are enough to ensure sufficient SNR in the applicability of the classic methods presented so far. However, these often give biased results and, definitely, a reduced resolution [*Sicard et al.*, 2006].

As a common trait, the nearly totality of the methods lack in some degree the requirements to operate in an unattended, real-time basis to monitor the ABL. Whereas statistical methods like the VCM cannot follow the fast time resolution of the lidar profiles to track the time evolution of the ABL, non-adaptive geometrical methods do not have the capability to assimilate past ABL estimates to enhance their ABL estimation with time.

The applicability of these methods and in particular, the THM, to the radar case will be further explored in Chap. 6.

In the state-of-the-art, *Angevine et al.* [1994] have applied a peak-locating algorithm to estimate the ABLH from radar wind profilers. This method finds a peak in the range-corrected SNR by integrating 30-s profiles into 1 h estimates, consequently, degrading the temporal resolution. According to *Cohn and Angevine* [2000], results are in good agreement with those obtained by applying the WM to HRDL backscatter profiles.

Chapter 3

Total backscatter-coefficient inversion error bounds

Total backscatter-coefficient inversion error bounds for the two-component lidar inversion algorithm (the so-called Fernald's or Klett-Fernald-Sasano's method) are derived in analytical form in response to three error sources: (i) the measurement noise, (ii) the user uncertainty in the backscatter-coefficient calibration, and (iii) in the aerosol extinction-to-backscatter ratio.
Two different types of error bounds are presented: Approximate error bounds using first-order error propagation and exact error bounds using a total-increment method. Both error bounds are formulated in explicit analytical form, which is of advantage for practical physical sensitivity analysis and computational implementation. A Monte Carlo approach is used to validate the error bounds at 355-, 532-, and 1064-nm wavelengths.

This paper was published in IEEE Transac. Geosc. Rem. Sensing journal and is made available as an electronic reprint with te permission of IEEE. The paper can be found at the following URL on the IEEE website: `http://ieeexplore.ieee.org/xpl/articleDetails.jsp?tp=&arnumber=6205622&queryText%3D10.1109%2FTGRS.2012.2194501`.

3.1 Introduction

The boundary condition usually consists on a known or presumed value of the extinction or backscatter coefficient at the far-end of the range profile. This value is used as an absolute calibration for retrieving extinction or backscatter coefficients at lesser ranges. Henceforth, it is referred simply as the calibration. The extinction-to-backscatter ratio may include both molecular and aerosol effects, or it may include aerosol effects only. Many authors use the term "lidar ratio" to refer to the aerosol-only extinction-to-backscatter ratio. The distinction between the "total" lidar ratio (including molecular effects) and the aerosol-only lidar ratio is noted when necessary.

Methods to assess the calibration for Klett's one-component inversion algorithm were proposed by *Klett* [1983, 1986] himself and for the two-component algorithm by *Sasano and Nakane* [1987].

Several authors have since carried out sensitivity studies concerning uncertainties in the lidar ratio [*Sasano and Nakane*, 1984], the impact of assuming a range-independent lidar ratio [*Sasano et al.*, 1985], uncertainties in the calibration [*Bissonnette*, 1986; *Matsumoto and Takeuchi*, 1994], and the forward/backward stability of these inversion methods as function of the optical depth [*Qiu*, 1988].

Errors in the assumed lidar ratio may result in larger error-propagated errors [*Bösenberg and Hoff*, 2007], especially in situations of a complex layering of aerosols [*Ansmann*, 2006]. *Kunz* [1996] and *Kovalev* [1993, 2003] have proposed alternative variants (not the object of this Ph.D. thesis) allowing trustworthy extinction retrievals, where the far-end calibration is replaced by the optical depth of the sounding path or by a near-end calibration and a nephelometer measurement. The synergistic combination of a backscatter lidar with a sun photometer is also extensively used [*Reba et al.*, 2010]. Furthermore, optimal estimation [*Stephens and Engelen*, 2001] and adaptive filtering [*Rocadenbosch et al.*, 1999; *Marchant et al.*, 2010] methods offer the possibility to incorporate different relevant information (such as optical thickness or spectral radiance measurements [*Huneeus and Boucher*, 2007]) into the lidar inversion problem and to provide inversion-error indicators. These advanced methods, which usually find applications in the context of global space-borne measurements are, however, more complex.

Despite the fact that from a purely mathematical analysis both the one- and the two-component algorithms yield equivalent solutions, the two-component algorithm is always the preferred one. This is because the KFS algorithm enables use of the aerosol-only lidar ratio, a parameter characterizing the microphysical aerosol properties [*Böckmann et al.*, 2008]. In contrast, the KLT requires a total lidar ratio including molecular effects. From a physical point of view, the assumption of a constant total lidar ratio is not justified under relatively clear atmospheres. However, for optically thick atmospheres the aerosol component becomes dominant, and the total lidar ratio reduces to the aerosol lidar ratio, which gave rise to the first applications of the one-component algorithm in the 1980's.

This Chapter concentrates on the two-component backscatter-coefficient inversion algorithm and is the fifth in a series [*Rocadenbosch and Comerón*, 1999; *Comerón et al.*, 2004; *Rocadenbosch et al.*, 2010a; *Sicard et al.*, 2009a] from the RSLab related to study the behavior and error sensitivity of the one- and two-component algorithms. The work presented here first contributes a comprehensive analytical approach in explicit mathematical form merging into a single body all the main error sources involved in the KFS inversion of the aerosol backscatter coefficient. These include: (1) systematic errors due to uncertainties in the calibration, (2) systematic errors due to a range-dependent aerosol lidar ratio, and (3) random errors due to finite SNR in the opto-electronic receiver of the lidar system at all ranges except that of the calibration, and 4) random errors due to finite SNR at the calibration range. The latter two sources of error are considered separately as it was shown in [*Comerón et al.*, 2004] that source (4) dominates.

Errors in the *backscatter-coefficient calibration* (error source 1) and in the assumed lidar ratio (error source 2) are systematic errors, as they induce biases in the retrieval of the backscatter coefficient once they are encountered. These are in contrast to the random errors induced by noise (error sources 3 and 4). While it is common to treat the random errors as drawn from independent Gaussian distributions with standard deviations adding in mean-square, the systematic errors must

be treated separately. These errors in the input parameters to the retrieval are more appropriately described by a worst-case deviation from their nominal value with the assumption that input errors may be uniformly distributed between these worst-case limits. A similar approach for the Raman lidar inversion algorithm is described in [*Groß et al.*, 2011].

This Chapter finds the backscatter-coefficient error bounds for the KFS algorithm explicitly in both approximate and exact forms. Two different sets of explicit error bounds are introduced: first-order derivative error bounds (approximate), which are the KFS counterpart of those found for the KLT algorithm in *Rocadenbosch et al.* [2010a]) and, total-increment error bounds (exact ones) for the dominant error sources (1, 2 and 4 above). These characteristics are new to the state of the art in the lidar community.

This Chapter is organized as follows: In Sect. 3.2 the KFS inversion algorithm is reviewed and reformulated in both backward and forward form. In Sect. 3.3 first-order error bounds are presented. Following this, in Sect. 3.4 total-increment (i.e., exact) error bounds are obtained for the dominant error sources. In Sect. 3.5, both first-order and total-increment error bounds are cross-examined and validated using a Monte Carlo method for the random component at 355-, 532-nm , and 1064-nm wavelengths. Finally, concluding remarks are given in Sect. 3.6.

3.2 KFS two component algorithm

3.2.1 Modified backward KFS form

Considering KFS 's inversion algorithm is formulated in backward backscatter-coefficient form as Eq. 2.35, the aerosol and the molecular backscatter coefficients are assimilated into the total backscatter coefficient, $\beta(R) = \beta^{aer}(R) + \beta^{mol}(R)$, and errors on the molecular backscatter coefficient are neglected so that

$$d\beta^{aer}(R) = d\beta(R). \tag{3.1}$$

This is justified because the molecular component can be assumed to be very well known (Sect. 2.2.6). Therefore, when calibrating in an atmospheric layer dominated by molecular scattering,

$$\beta_N = \beta(R_N) = \beta^{aer}(R_N) + \beta^{mol}(R_N) \approx \beta^{mol}(R_N). \tag{3.2}$$

By introducing the discrete range, $R_j = R_{\min} + (j-1)\Delta R, \quad j = 1..N$, with ΔR the spatial resolution of the lidar data and N the number of range samples (or cells) to be inverted, Eq. 2.35 can be rewritten in discrete form as

$$\beta_j\left(\beta_N, \vec{S}, \vec{U}\right) = \frac{\beta_N U_j F_j\left(\vec{S}\right)}{U_N + 2\beta_N H_j\left(\vec{S}, \vec{U}\right)}, \tag{3.3}$$

where U_j, F_j and H_j are shorthand for $U(R_j)$, $F(R_j)$ and $H(R_j)$, which are auxiliary functions evaluated for each range, and the vector $\vec{S}$ is the range-dependent aerosol lidar ratio, $S^{aer}(R_j)$.

The auxiliary functions U_j, F_j and H_j are defined as

$$U_j = R_j^2 P\left(R_j\right), \tag{3.4}$$

$$F_j\left(\vec{S}\right) = \exp\left[2G_j\left(\vec{S}\right)\right], \tag{3.5}$$

where

$$G_j\left(\vec{S}\right) = \begin{cases} \sum_{i=j}^{N} w_i \left(S_i^{aer} - S_i^{mol}\right) \beta_i^{mol} & j < N \\ 0 & j = N \end{cases}, \tag{3.6}$$

and

$$H_j\left(\vec{S},\vec{U}\right) = \sum_{i=j}^{N} w_i S_i^{aer} U_i F_i\left(\vec{S}\right). \tag{3.7}$$

In Eqs. 3.6-3.7, the $w_i, \quad i = 1..N$ denote generic integration weights (e.g., $w_i = h = 1, i = 1..N-1; w_N = 0$ in the case of rectangle integration, which requires $N \geq 2$ points). The notation $\beta_j\left(\beta_N, \vec{S}, \vec{U}\right)$ is a reminder that the total backscatter coefficient inverted at the range cell, R_j, depends upon the total backscatter coefficient at the far-range calibration range, β_N, the user-input range-dependent aerosol lidar ratio, $\vec{S}$, and the range-corrected power, $\vec{U}$. In what follows superscript "aer" for the aerosol lidar ratio is omitted so that $\vec{S}$ refers to $\vec{S}^{aer}$, and the "aerosol lidar ratio" is simply addressed as "the lidar ratio".

3.2.2 Comparison with Klett's one-component algorithm

When comparing KLT versus KFS equations (Eqs.5-6) in *Rocadenbosch et al.* [2010a] with Eqs. 3.3, 3.5 and 3.7 above, the KLT-to-KFS correspondence Table 3.1 is obtained. The U_j into $U_j F_j\left(\vec{S}\right)$ relationship agrees with previous published results (Table1 in [*Sicard et al.*, 2009a]) and the $G_j\left(\vec{S},\vec{U}\right)$ into $H_j\left(\vec{S},\vec{U},\vec{F}\right)$ is a new relationship completing the transformation.

3.2.3 Forward case

In the forward-integration form of the KFS algorithm (i.e., calibration range located at the near end of the inversion range) the far-end calibration at $R = R_N$ is replaced by the near-end calibration $R = R_1$, (i.e., $\beta_N \rightarrow \beta_1$) in Eq. 3.3, and $\sum_{i=j}^{N}(.)$ is replaced by $-\sum_{i=1}^{j}(.)$ in all subsequent formulas. In so doing, Eq. 3.3 for the forward case becomes

$$\beta_j\left(\beta_1, \vec{S}, \vec{U}\right) = \frac{\beta_1\, U_j F_j^F\left(\vec{S}\right)}{U_1 + 2\beta_1\, H_j^F\left(\vec{S},\vec{U}\right)}, \tag{3.8}$$

where $F_j^F\left(\vec{S}\right) = \exp\left(2G_j^F\right)$ after Eq. 3.5 and G_j^F and H_j^F are defined following Eqs. 3.6- 3.7 above but replacing $\sum_{i=j}^{N}(.)$ by $-\sum_{i=1}^{j}(.)$, as mentioned. This leads to the well-known classic forward form including a minus sign in front of the factor of 2 in the denominator and in the exponential arguments of Eq. 2.35. Note also that the minus sign arising from the change of summations

above is algebraically equivalent to substituting $S^{aer} \rightarrow -S^{aer}$ and $S^{mol} \rightarrow -S^{mol}$ into the KFS backward form of Eq. 3.3. This also accounts for the opposite signs of the backscatter-to-lidar-ratio derivatives of the forward/backward forms (Sect. 3.4.2).

3.3 First-order backscatter coefficient error bounds

This Section parallels Sect. 3 of *Rocadenbosch et al.* [2010a] where the backscatter-coefficient error bounds are computed from the superposition of error sources 1-4 (Sect. 3.1) using a first-order derivative approach. Following Eq. 7 in that work,

$$\begin{cases} |d\beta_j| = \left|\frac{\partial\beta_j}{\partial\beta_N} d\beta_N\right| + \sum_{k=1}^{N} \left|\frac{\partial\beta_j}{\partial S_k} dS_k\right| + \sum_{k=1}^{N-1} \left|\frac{\partial\beta_j}{\partial P_k} dP_k\right| + \left|\frac{\partial\beta_j}{\partial P_N} dP_N\right|; & j < N \\ |d\beta_j| = |d\beta_N|; & j = N \end{cases}, \tag{3.9}$$

where $d\beta_j$ is the total backscatter coefficient error at range, R_j, and $d\beta_N$, dS_k, dP_k, and dP_N, respectively stand for error sources 1-4.

For the case $j < N$ the terms $\frac{\partial\beta_j}{\partial\beta_N}$, $\frac{\partial\beta_j}{\partial P_k}$ and $\frac{\partial\beta_j}{\partial P_N}$ can be computed from *Rocadenbosch et al.* [2010a] and the function substitutions indicated in the KLT-to-KFS transformation (Table 3.1). Yet, this procedure cannot be followed when computing the errors due to the lidar ratio, $\frac{\partial\beta_j}{\partial S_k}$, as the KFS auxiliary functions F_j and H_j (Eqs. 3.5, 3.7) also depend on the lidar ratio.

Table 3.1: KLT-to-KFS transformation relationships. Notation: In both algorithms, β_j stands for total (aerosol plus molecular) backscatter coefficient at the range cell R_j.

KLT	**KFS**
$\beta_j\left(\beta_N, \vec{S}, \vec{U}\right) = \frac{\beta_N U_j}{U_N + 2\beta_N G_j\left(\vec{S},\vec{U}\right)}$	$\beta_j\left(\beta_N, \vec{S}, \vec{U}\right) = \frac{\beta_N\, U_j F_j\left(\vec{S}\right)}{U_N + 2\beta_N\, H_j\left(\vec{S},\vec{U}\right)}$
$\vec{S}$ stands for the total lidar ratio, $\vec{S}^{tot}$	$\vec{S}$ stands for the aerosol lidar ratio, $\vec{S}^{aer}$
U_j	$U_j F_j\left(\vec{S}\right)$
$G_j\left(\vec{S},\vec{U}\right)$	$H_j\left(\vec{S},\vec{U},\vec{F}\right)$

The case $j = N$ in Eq. 3.9 expresses the assumed error on the backscatter-coefficient calibration. Finally, the terms comprising Eq. 3.9 and denoted $\varepsilon_{j,1-4}$ are detailed in Table 3.2.

The treatment of systematic and random errors is as follows: The relationship between the backscatter-coefficient retrieval error ($\delta_{\varepsilon_{j,1}}$) due to the calibration error (δ_{β_N}) shown in Eq. 3.26 is a straightforward modification of Eq. 3.10 where lowercase deltas have been used to denote systematic errors. The relationship between the retrieval error ($\sigma_{\varepsilon_{j,3}}$) due to noise in range cells 1..N-1 (σ_{U_k}) shown in Eq. 3.31 is obtained from Eq. 3.15 by treating the range-corrected random noises (dU_k) as independent Gaussian random variables with standard deviation σ_{U_k}. The retrieval error due to noise in the calibration cell is given by Eq. 3.33 and is derived similarly using the approximation shown, in *Rocadenbosch et al.* [2010a]. At this point, note that $G_N = 0$ and $F_N = 1$ (Eqs.(3.5-3.6) and that, when considering error sources 3 and 4, $d\left(U_k F_k\right) = F_k dU_k$, $k = 1..N$, because the only "fluctuating" variable due to noise is the range-corrected power, U_k. At this point

Table 3.2: Total backscatter-coefficient error-propagated terms for the KFS backward inversion algorithm in response to error sources 1-4 (see Sect. 3.3). For the case $j = N$, the total backscatter-coefficient error is directly the calibration error. For the KFS forward algorithm consider Sect. 3.2.3 changes.

Concept	Equation
Total backscatter-coefficient error (case $j < N$) where	$\lvert d\beta_j\rvert = \left\lvert\frac{\partial\beta_j}{\partial\beta_N}d\beta_N\right\rvert + \sum_{k=1}^{N}\left\lvert\frac{\partial\beta_j}{\partial S_k}dS_k\right\rvert + \sum_{k=1}^{N-1}\left\lvert\frac{\partial\beta_j}{\partial P_k}dP_k\right\rvert + \left\lvert\frac{\partial\beta_j}{\partial P_N}dP_N\right\rvert ;\ j < N$ (1.10)
1. Error due to the backscatter-coefficient calibration	$\varepsilon_{j,1} = \frac{\partial\beta_j}{\partial\beta_N}d\beta_N = \left(\frac{\beta_j}{\beta_N}\right)^2\frac{U_N}{U_jF_j}d\beta_N$ (3.10)
2. Error due to the (range-dependent) lidar ratio	$\varepsilon_{j,2} = \sum_{k=1}^{N}\frac{\partial\beta_j}{\partial S_k}dS_k = 2\beta_j dI_{j,1} - \frac{2\beta_j^2}{U_jF_j}dI_{j,2} - \frac{4\beta_j^2}{U_jF_j}dI_{j,3}$ (3.11)
where	$dI_{j,1} = \sum_{k=j}^{N} w_k\beta_k^{mol}dS_k$ (3.12)
	$dI_{j,2} = \sum_{k=j}^{N} w_kU_kF_kdS_k$ (3.13)
	$dI_{j,3} = \sum_{k=j}^{N} w_kS_kU_kF_kdI_{k,1}$ (3.14)
3. Error due to the measurement noise (range cells 1..N-1)	$\varepsilon_{j,3} = \sum_{k=1}^{N-1}\frac{\partial\beta_j}{\partial P_k}dP_k = \frac{\beta_j}{U_j}dU_j - \frac{2\beta_j^2}{U_jF_j}\sum_{k=j}^{N} w_kS_kF_kdU_k$ (3.15)
4. Error due to the measurement noise at the calibration cell (range cell N)	$\varepsilon_{j,4} = \frac{\partial\beta_j}{\partial P_N}dP_N = -\frac{\beta_j^2}{\beta_NU_jF_j}dU_N - \frac{2\beta_j^2}{U_jF_j}w_NS_NdU_N$ (3.16)
Total backscatter-coefficient error (case $j = N$, calibration point)	$\lvert d\beta_j\rvert = \lvert d\beta_N\rvert ;\qquad j = N$

a few comments are in order:

First, the relative impacts on the retrieval of the backscatter-coefficient calibration error ($\delta_{\varepsilon_{j,1}}$) and the standard deviation of the noise at the calibration cell ($\sigma_{\varepsilon_{j,4}}$) may be compared by evaluating their ratio,

$$\frac{\delta_{\varepsilon_{j,1}}}{\sigma_{\varepsilon_{j,4}}} \approx \left|\frac{U_N}{\beta_N}\right| \frac{\delta_{\beta_N}}{\sigma_{U_N}} = \mathrm{SNR_N} \varepsilon_r^{\beta_N} \ . \tag{3.17}$$

Here, $\varepsilon_r^{\beta_N} = \delta_{\beta_N}/\beta_N$ is the relative error in the backscatter-coefficient calibration, and SNR_N is the SNR at the calibration range, $R = R_N$. Thus it is not necessary to carry out separate simulations to evaluate the separate impacts of error sources 1 and 4. Although it was shown in that the relative impacts of these different error sources are related by an equation analogous to Eq. 3.17, it should not be interpreted that a systematic error can be derived from the random error or vice versa.

Second, regarding errors due to the measurement noise ($\sigma_{\varepsilon_{j,3}}$ and $\sigma_{\varepsilon_{j,4}}$), from Eq. 3.31 the backscatter-coefficient error on the j-th range cell is inversely proportional both to the SNR at that cell, $SNR_j = U_j/\sigma_{U_j}$, and to a "cross-cell SNR" defined as $SNR_{j,k} = U_j/\sigma_{U_k}$. A similar dependence was found in *Comerón et al.* [2004] and *Rocadenbosch et al.* [2010a] and earlier by Knauss [*Knauss*, 1982], who predicted an inverse SNR sensitivity. Concerning $\sigma_{\varepsilon_{j,4}}$, Eq. 3.33 can be rewritten as $\sigma_{\varepsilon_{j,4}} \approx \left|\frac{\beta_j^2 U_N}{\beta_N U_j F_j}\right| \frac{1}{SNR_N}$ [*Rocadenbosch et al.*, 2010a]. It emerges that a finite SNR at the calibration range propagates errors to all the range cells.

Regarding error due to a range-dependent lidar ratio ($\delta_{\varepsilon_{j,2}}$), as a first approximation we define a systematic lidar-ratio relative error, p relating the lidar-ratio error to the true range-dependent atmospheric lidar ratio as *Rocadenbosch et al.* [2010a]

$$dS(R) = pS\left(R\right) \Leftrightarrow dS_k = pS_k. \tag{3.18}$$

Equivalently, the atmospheric lidar ratio is assumed to lie within $S\left(R\right)\left(1 \pm |p|\right)$. Error bound computation uses first-order series expansion of Eq. 3.3 around p. Towards this end Eq. 3.3 is rewritten as a function of lidar-ratio perturbation p as

$$\beta_j\left(p\right) = \frac{\beta_N \, U_j F_j\left(p\right)}{U_N + 2\beta_N \, H_j\left(p\right)}, \tag{3.19}$$

where the incremental auxiliary function $F_j\left(p\right)$ is related to $G_j\left(p\right)$ via Eq. 3.5, and $G_j\left(p\right)$ and $H_j\left(p\right)$ from Eqs. 3.6-3.7 become

$$G_j\left(p\right) = \begin{cases} \left(1+p\right) I_{j,1} - K_j; & j < N \\ 0 & j = N \end{cases} \ , \tag{3.20}$$

where

$$I_{j,1} = \sum_{i=j}^{N} w_i \beta_i^{mol} S_i^{aer}, \quad K_j = \sum_{i=j}^{N} w_i \beta_i^{mol} S_i^{mol}, \tag{3.21}$$

and

$$H_j(p) = (1+p)\sum_{i=j}^{N} w_i S_i^{aer} U_i F_i(p). \tag{3.22}$$

From Eqs. 3.20- 3.21 above Eq. 3.5, $F_j(p)$ takes the form

$$F_j(p) = \exp[2G_j(p)] = F_j(0)\exp(2pI_{j,1}). \tag{3.23}$$

Finally, the backscatter-coefficient error is obtained after first-order series expansion as

$$\delta_{\varepsilon_{j,2}} \approx \left| \left(\left. \frac{\partial \beta_j}{\partial p} \right|_{p=0} \right) p \right|, \tag{3.24}$$

where superscript "S" denotes "due to the lidar ratio". Eq. 3.24 is computed by substituting the proportionality condition of Eq. 3.18 into the general expression of the propagated lidar-ratio error, $\varepsilon_{j,2}$ (Eqs. 3.11- 3.14). The result is summarized in Table 3.3 and yields symmetrical error bounds.

3.4 Total increment backscatter coefficient error bounds

Total-increment error bounds stand for infinite order, or equivalently, exact error bounds. The procedure is conceptually simple for it reduces to compute the total error, $\beta_j(x \pm \Delta x) - \beta_j(x)$, where x is the variable of interest. In what follows, Δx refers to a generic input error, which may be large and is therefore not expressed as a differential amount, $\Delta\beta_N$ (backscatter-coefficient calibration error), ΔS_k (lidar-ratio error) or ΔU_k, $k = 1..N$ (range-corrected noise-induced error, Sect. 3.3).

The first-order error propagation approach of Table 3.2 is just a perturbational approach simply scaling the input errors by partial derivatives to estimate the total backscatter-coefficient error. In contrast, under low SNRs and/or when the user's uncertainty of the algorithm inputs ($[x - \Delta x, x + \Delta x]$) is comparatively large, first-order derivative error bounds fail to correctly estimate the backscatter-coefficient error. Therefore, total-increment error bounds provide a convenient way to compute exact upper and lower error bounds (usually with asymmetrical amplitudes around the true backscatter value) in explicit form.

3.4.1 Error source 1: Error due to the backscatter-coefficient calibration

From Eq. 3.10 it emerges that the derivative of the inverted backscatter coefficient with respect to the backscatter-coefficient calibration is always positive, $\frac{\partial \beta_j}{\partial \beta_N} > 0$, since $\beta_j, \beta_N, U_j, U_N$ and F_j are positive-defined magnitudes. As a result, $\beta_j(\beta_N \pm \Delta\beta_N) = \beta_j \pm \Delta\beta_j$ (plus and minus signs are one-to-one maintained) and the total-increment error bounds of Eq. 3.39 result.

Table 3.3: First-order error bounds for the KFS backward inversion algorithm in response to error sources 1-4 (see Sect. 3.3). For the case $j = N$, the backscatter-coefficient error bound is directly the calibration error bound. "sys" and "rand" stand for "systematic" and "random" errors, respectively. For the KFS forward algorithm consider Sect. 3.2.3 changes.

Concept	Formula
Total backscatter-coefficient error bounds (case $j < N$) where	$\delta_{\beta_j}^{sys} = \left\|\delta_{\varepsilon_{j,1}}\right\| + \left\|\delta_{\varepsilon_{j,2}}\right\|, \sigma_{\beta_j}^{rand} = \left(\sigma_{\varepsilon_{j,3}}^2 + \sigma_{\varepsilon_{j,4}}^2\right)^{\frac{1}{2}}$ (3.25)
1. Systematic error due to the backscatter-coefficient calibration	$\delta_{\varepsilon_{j,1}} = \left\|\left(\frac{\beta_j}{\beta_N}\right)^2 \frac{U_N}{U_j F_j}\right\| \delta_{\beta_N}$ (3.26)
2. Systematic error due to the (range-dependent) lidar ratio	$\delta_{\varepsilon_{j,2}} = \|p\| \left\|2\beta_j I_{j,1} - \frac{2\beta_j^2}{U_j F_j} I_{j,2} - \frac{4\beta_j^2}{U_j F_j} I_{j,3}\right\|$ (3.27)
where	$I_{j,1} = \sum_{k=j}^{N} w_k \beta_k^{mol} S_k$ (3.28)
	$I_{j,2} = \sum_{k=j}^{N} w_k U_k F_k S_k$ (3.29)
	$I_{j,3} = \sum_{k=j}^{N} w_k S_k U_k F_k I_{k,1}$ (3.30)
3. Random error due to the measurement noise (range cells 1..N-1)	$\sigma_{\varepsilon_{j,3}} = \left[\left(\frac{\beta_j}{U_j}\right)^2 \sigma_{U_j}^2 + \left(\frac{2\beta_j^2}{U_j F_j}\right)^2 \sigma_{HU,j}^2\right]^{\frac{1}{2}}$ (3.31)
where	$\sigma_{HU,j}^2 = \sum_{k=j}^{N} \left(w_k S_k F_k\right)^2 \sigma_{U_k}^2$ (3.32)
4. Random error due to the measurement noise at the calibration cell (range cell N)	$\sigma_{\varepsilon_{j,4}} = \left(\left\|\frac{\beta_j^2}{\beta_N U_j F_j}\right\| + \left\|\frac{2\beta_j^2}{U_j F_j} w_N S_N\right\|\right) \sigma_{U_N} \approx \left\|\frac{\beta_j^2}{\beta_N U_j F_j}\right\| \sigma_{U_N}$ (3.33)
Total backscatter-coefficient error bound (case $j = N$, calibration point)	$\delta_{\beta_j}^{sys} = \delta_{\beta_N}$ (3.34)

3.4.2 Error source 2: Error due to the range-dependent lidar ratio

From Eq. 3.3 the incremented backscatter-coefficient function can be expressed as

$$\beta_j\left(\vec{S}+\Delta\vec{S}\right)=\frac{\beta_N\,U_jF_j\left(\vec{S}+\Delta\vec{S}\right)}{U_N+2\beta_N\,H_j\left(\vec{S}+\Delta\vec{S},\vec{U}\right)}\overset{\Delta\vec{S}=p\vec{S}}{\longrightarrow}\beta_j\left(p\right)=\frac{\beta_N\,U_jF_j\left(p\right)}{U_N+2\beta_N\,H_j\left(p,\vec{U}\right)}. \tag{3.35}$$

The lidar-ratio increment $\Delta\vec{S}$ is related to the lidar ratio $\vec{S}$ via the relative error p so that $\Delta\vec{S}=p\vec{S}$ (Eq. 3.18). As a result, the incremental term $\left(\vec{S}+\Delta\vec{S}\right)$ (equivalently, $\vec{S}\left(1+p\right)$) becomes only a function of the scalar relative error p and Eq. 3.35 reduces to Eq. 3.19. Incremental auxiliary functions $F_j\left(p\right)$ and $H_j\left(p,\vec{U}\right)$ can be computed from Eqs. 3.5 and 3.7, respectively.

The sign of the backscatter-coefficient's derivative with respect to the lidar-ratio relative error, $\frac{\partial\beta_j}{\partial p}$, at each particular range R_j determines whether the upper and lower backscatter-coefficient error bounds at each range cell are respectively obtained from $\beta_j\left(p\right)$ (i.e., $\beta_j\left(\vec{S}+\Delta\vec{S}\right)$) and $\beta_j\left(-p\right)$ (i.e., $\beta_j\left(\vec{S}-\Delta\vec{S}\right)$) or with opposite signs. For the backward integration case this derivative is obtained following a somewhat lengthy but similar development to that of $\left.\frac{\partial\beta_j}{\partial p}\right|_{p=0}$ in Eqs. 3.24 and 3.27. Formally,

$$\frac{\partial\beta_j^B}{\partial p}=2\beta_j^B\left(p\right)I_{j,1}^B-\frac{2\beta_j^B\left(p\right)^2}{U_jF_j^B\left(p\right)}\left[I_{j,2}^B\left(p\right)+2\left(1+p\right)I_{j,3}^B\left(p\right)\right],\quad j<N, \tag{3.36}$$

where $I_{j,1-3}^B$ is given by Eqs. 3.28-3.30 in Table 3.3. The result is identical for the forward integration case ($j>1$) with superscripts "F" (forward) instead of "B" (backward). Note that forward integrals $I_{j,1-3}^F$ must include a minus sign according to Sect. 3.2.3.

Note that a more elegant and physically-rooted way to identify the sign of the backscatter-coefficient derivative to the lidar-ratio relative error is to recall that in forward (backward) integration the inverted backscatter coefficient at any range increases (decreases) with the lidar ratio (Fig. 3.1). This property is the basis of the two-point lidar-ratio estimation method in an aerosol layer aloft using combined forward/backward integration [*Ansmann et al.*, 1992] and detailed in *Rocadenbosch et al.* [2010b]). The derivative of the backscatter coefficient with respect to the lidar ratio is zero at the calibration point. In summary,

$$\frac{\partial\beta_j^F}{\partial p}>0,\ \frac{\partial\beta_j^B}{\partial p}<0,\quad\forall p,j,\qquad\left.\frac{\partial\beta_j^F}{\partial p}\right|_{j=1}=0,\ \left.\frac{\partial\beta_j^B}{\partial p}\right|_{j=N}=0,\quad\forall p, \tag{3.37}$$

which is a condition applying to any range R_j. Therefore, $\beta_j\left(\vec{S}\pm\Delta\vec{S}\right)=\beta_j\pm\Delta\beta_j$ in the forward case whereas $\beta_j\left(\vec{S}\pm\Delta\vec{S}\right)=\beta_j\mp\Delta\beta_j$ in the backward case (Table 3.4).

3.4.3 Error sources 3-4: Errors due to the measurement noise

As discussed in Sect. 3.1, the impact of measurement noise in the KFS algorithm has been studied in *Sicard et al.* [2009a]. In spite of the fact that exact backscatter-coefficient error bounds satisfying a constant confidence level are given analytically, its formulation is in implicit form. This means

Table 3.4: Total-increment error bounds for the KFS backward inversion algorithm in response to error sources 1-4 (see Sect. 3.4). Superindexes "u" and "l" stand for "upper" and "lower" error bound, respectively. $\varepsilon^{u}_{j,1-4}$ and $\varepsilon^{l}_{j,1-4}$ are positive-defined error amplitudes. For the case $j = N$, the upper/lower backscatter-coefficient error bounds are directly given by those of the calibration error. "sys" and "rand" stand for "systematic" and "random" errors, respectively. For the KFS forward algorithm consider Sect. 3.2.3 changes.

Concept	Formula
Total backscatter-coefficient error bounds (case $j < N$) where	$\varepsilon^{u/l}_{sys,j} = \lvert\varepsilon_{j,1}\rvert + \lvert\varepsilon_{j,2}\rvert\,, \quad \varepsilon^{u/l}_{rand,j} = \left(\varepsilon^{2}_{j,3} + \varepsilon^{2}_{j,4}\right)^{\frac{1}{2}}$ (3.38)
1. Systematic error due to the backscatter-coefficient calibration $\frac{\partial \beta_j}{\partial \beta_N} > 0$, (Eq. 3.10)	$\varepsilon^{u}_{j,1} = \beta_j\left(\beta_N + \Delta\beta_N\right) - \beta_j\left(\beta_N\right) \varepsilon^{l}_{j,1} = -\beta_j\left(\beta_N - \Delta\beta_N\right) + \beta_j\left(\beta_N\right)$ (3.39)
2. Systematic error due to the (range-dependent) lidar ratio	$\beta_j\left(p\right) = \dfrac{\beta_N\, U_j F_j\left(p\right)}{U_N + 2\beta_N\, H_j\left(p, \vec{U}\right)}$ $\beta_j\left(p\right)$ stands for $\beta_j\left(\vec{S} + \Delta\vec{S}\right)\,,\ \Delta\vec{S} = p\vec{S}$ (3.40)
Case FORWARD $\frac{\partial \beta_j}{\partial p} > 0$, Sect. 3.2	$\varepsilon^{u}_{j,2} = \beta_j\left(\vec{S} + \Delta\vec{S}\right) - \beta_j\left(\vec{S}\right) \varepsilon^{l}_{j,2} = -\beta_j\left(\vec{S} - \Delta\vec{S}\right) + \beta_j\left(\vec{S}\right)$ (3.41)
Case BACKWARD $\frac{\partial \beta_j}{\partial p} < 0$, Sect. 3.2	$\varepsilon^{u}_{j,2} = \beta_j\left(\vec{S} - \Delta\vec{S}\right) - \beta_j\left(\vec{S}\right) \varepsilon^{l}_{j,2} = -\beta_j\left(\vec{S} + \Delta\vec{S}\right) + \beta_j\left(\vec{S}\right)$ (3.42)
3. Random error due to the measurement noise (range cells 1..N-1)	(not available) Use $\varepsilon^{u/l}_{j,3} \approx 3\sigma_{\varepsilon_{j,3}}$, 3-$\sigma$ first-order error approx. (3.43)
4. Random error due to the measurement noise at the calibration cell (range cell N) $\frac{\partial \beta_j}{\partial P_N} < 0$, (Eq. 3.16)	$\varepsilon^{u}_{j,4} = \beta_j\left(U_N - \Delta U_N\right) - \beta_j\left(U_N\right)$ $\varepsilon^{l}_{j,4} = -\beta_j\left(U_N + \Delta U_N\right) + \beta_j\left(U_N\right)$ $\left(\Delta U_N = 3\sigma_{U_N} \text{ for } 3-\sigma \text{ level}\right)$ (3.44)
Total backscatter-coefficient error bound (case $j = N$, calibration point)	$\varepsilon^{u/l}_{sys,j} = \varepsilon^{u/l}_{\beta_N}$ (3.45)

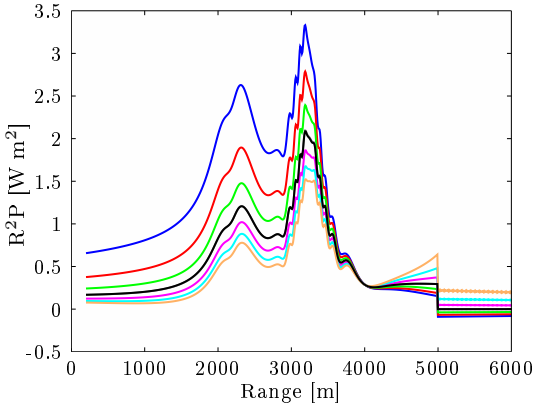

Figure 3.1: Behavior of the forward and backward forms of the KFS-inverted backscatter coefficient for several values of the aerosol lidar ratio. Lidar ratios vary from 20 sr to 80 sr (in steps of 10 sr) in a simulated backscatter profile of an elevated dust layer. Calibration range is at 4 km. For $R < R_{cal}$ inversion is via backward integration and the upper (lower) profile corresponds to the smallest (largest) lidar ratio. For $R > R_{cal}$, inversion is via forward propagation and the upper (lower) profile corresponds to the largest (smallest) lidar ratio. Simulation wavelength: 355 nm.

that given a confidence level, two auxiliary integrals and two integral equations [*Sicard et al.*, 2009a] must be solved for each range of interest. This yields two error bounds, which are later used to compute the upper and lower backscatter-coefficient error bounds.

Explicit formulation of total-increment error bounds is hampered by the fact that the measurement noise is usually uncorrelated with range, i.e., each range cell along the inversion range contributes independent error amounts $\Delta U_j, j = 1..N-1$. This leads to the superposition of $N-1$ noise sources, that is, to an $(N-1)$-dimensional problem impeding any explicit formulation of the total-increment error bounds in Table 3.4.

However, because of the comparatively larger impact of error source 4 (see NIR grounds in *Sicard et al.* [2009a] and results in Sect. 3.5.1.3) the first-order error bound, $\sigma_{\varepsilon_{j,3}}$, given by Eq. 3.31, represents a very good approximation of an already small quantity. A final remark is that the first term of the error-propagated backscatter-coefficient derivative, $\varepsilon_{j,3} \approx \frac{\beta_j}{U_j} dU_j$ (Eq. 3.15) does represent the total increment $\beta_j\left(\vec{U}+\Delta\vec{U}\right) - \beta_j\left(\vec{U}\right)$ if $H_j\left(\overrightarrow{S},\overrightarrow{U}\right)$ (Eq. 3.7) is assumed to be nearly independent of fluctuations in $\vec{U}$. This is indeed the case, because range-corrected power fluctuations tend to smooth out with range during forward/backward integration.

Finally, the error due to the measurement noise at the calibration cell is analogous to that of Sect. 3.5.2, except for the fact that now the derivative of the inverted backscatter coefficient to the power at the calibration range is always negative, $\frac{\partial\beta_j}{\partial P_N} < 0$ (Eq. 3.16). The error bounds are given in (Eq. 3.44), Table 3.4.

3.5 Discussion

First-order error bounds (Table 3.3) and total-increment error bounds (Table 3.4) are validated here using a multi-wavelength *Monte Carlo (MC)* approach at 355-, 532-, and 1064-nm wavelengths. In the MC simulation, for each wavelength, a set of 100 profiles of the aerosol backscatter coefficient has

been inverted given 100 noisy lidar power returns realized from a synthetic backscatter atmospheric profile and a range-dependent SNR profile (Fig. 3.2).

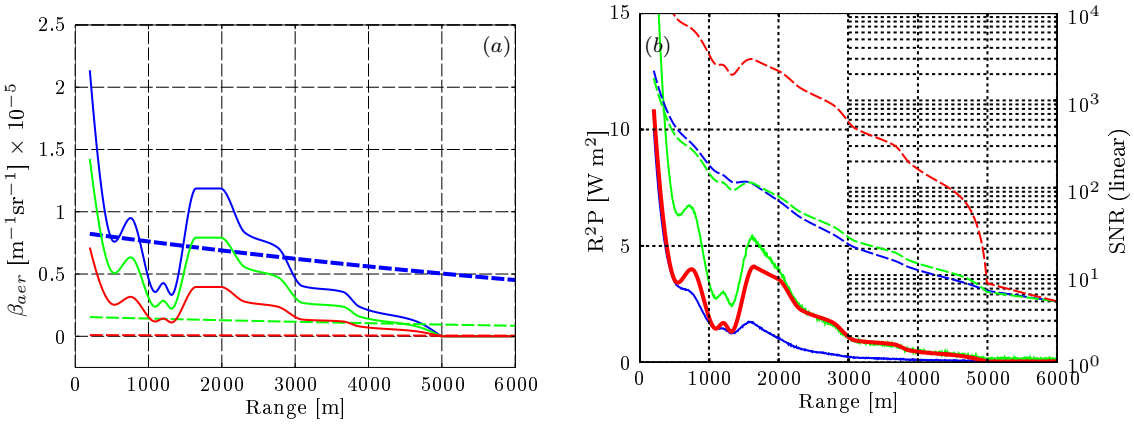

Figure 3.2: Simulated lidar signals. (*a*) Aerosol backscatter-coefficient atmospheric profiles (solid trace) and related molecular (Rayleigh) levels (dashed). (*b*) Noisy range-corrected power returns (solid) and related SNR profiles for each channel. UV (355 nm, blue), VIS (532 nm, light green), and NIR (1064 nm, red).

To make the simulation more realistic, the shape of the profile of the aerosol backscatter coefficient has been obtained from a 532-nm inversion of a measurement record obtained with the RSLab lidar (slant path, 54-deg elevation angle). The 355- and 1064-nm aerosol backscatter components have been extrapolated from the inverted one at 532 nm assuming a λ^{-1} spectral dependency. The molecular backscatter component follows a U.S. standard atmosphere model [*Bodhaine et al.*, 1999] (15°C and 1013.15 hPa ground-level conditions) and a λ^{-4} spectral dependency. A mean total extinction, $\bar{\alpha} \approx 2 \times 10^{-4} m^{-1}$ at 532 nm, corresponding to a total optical depth, $\tau \approx 1.2$, over the slant sounding path, is simulated. In order to study error sources 1-4 in identical simulation conditions, a wavelength-independent lidar ratio, $S^{aer} = 50sr$ is used, and the simulated measurement noise level is adjusted so as to ensure a SNR of 5 at the maximum range (a relatively modest figure in practice), in all three lidar channels. The inversion interval ranges from $R_{\min} = 0.2km$ to a maximum range, $R_{\max} = 6km$. The calibration range is chosen at $R_{cal} = R_{\max} = 6km$, where the lidar return is dominated by molecular scattering. The atmospheric boundary layer, characterized by significant aerosol backscatter, ends at approximately 5 km range.

Lidar system parameters used for the simulation are based on the RSLab multi-spectral lidar system (Table 1.2)

Backscatter-coefficient plots are *visible-wavelength normalized (VIS-normalized)* to aid intercomparison at the three wavelengths. Thus, UV and NIR profiles of the inverted backscatter coefficient are scaled by $(\lambda_{532}/\lambda_{355})^{-1}$ and $(\lambda_{532}/\lambda_{1064})^{-1}$ factors, respectively. A VIS-normalized Fig. 3.2a would appear with UV, VIS and NIR traces all coincident (figure not shown).

3.5.1 Error sources 3-4: Errors due to the measurement noise

3.5.1.1 Noise in all range cells except the calibration cell

According to the superposition principle the simulation runs with $SNR(R)\ for\ R \neq R_{cal}$, Fig. 3.2b, and all other error sources inactive. That is, $SNR(R_{cal}) \to \infty$ (no noise on the return power at the calibration cell, error source 4), perfect backscatter-coefficient calibration (error source 1), and known atmospheric lidar ratio (error source 2).

Fig. 3.3a plots the envelopes of the family of the MC-inverted profiles of the aerosol backscatter coefficient along with first-order error bounds (Eq. 3.31, Table 3.3) computed at 3σ (error bounds are plotted as vertical bars centered in the input "true" profile of the atmospheric backscatter coefficient) while Fig. 3.3b compares their error amplitudes. The error amplitudes represent the difference between the upper and lower backscatter-coefficient error bounds and the true profile of the atmospheric backscatter coefficient. In Fig. 3.3b, upper and lower MC error bounds superimpose and appear as a single noisy trace -at each wavelength-. Because of the first-order series expansion, first-order error bounds are always symmetric. Besides, Fig. 3.3b shows perfect agreement between both MC and first-order error bounds at all wavelengths. This is of advantage in order to approximate the total-increment error bound $\varepsilon_{j,3}^{u/l}$ (not found for this error source) as $\varepsilon_{j,3}^{u/l} \approx 3\sigma_{\varepsilon_{j,3}}$ in Table 3.4.

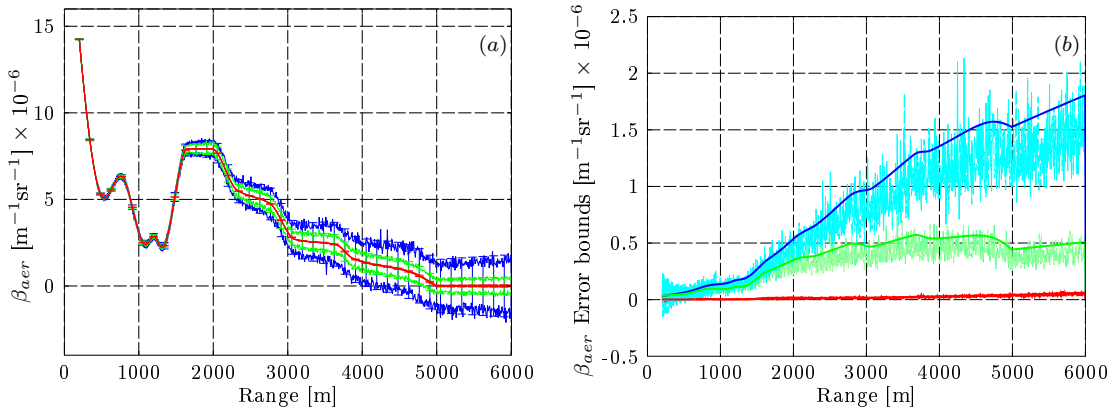

Figure 3.3: Analysis of noise corrupting all range cells except the calibration cell (error source 3) for SNR profile in Fig. 3.2b. (*a*) Envelopes of the aerosol backscatter coefficient from MC inversion (100 realizations) with superimposed first-order error bounds (vertical error bars) at 3σ. (*b*) Amplitude of the backscatter-coefficient error bound as a function of range: Comparison between MC error bounds (noisy traces) and first-order error bounds (solid traces). Both (*a*) and (*b*) are VIS-normalized. UV (355 nm, blue), VIS (532 nm, light green), and NIR (1064 nm, red).

Fig. 3.3 shows that errors increase with range in response to a progressively decreasing range-dependent SNR (Fig. 3.2b) and also increase towards the UV. An explanation for that is that the $\sigma_{\varepsilon_{j,3}}$ term $(\beta_j/U_j)\,\sigma_{U_j} = \beta_j/SNR_j$ in Eq. 3.31, Table 3.3 is inversely proportional to the SNR and directly proportional to the backscatter coefficient. Towards the UV, $\sigma_{\varepsilon_{j,3}}$ increases due to the higher scattering in this band and a lower SNR (Fig. 3.2b). As mentioned in Sect. 3.4.3, the term $\sigma_{HU,j}$ (Eq. 3.32) becomes numerically much lower because noise averages out when integrating.

3.5.1.2 Noise in the calibration cell

Simulation conditions are analogous to those used for the error source 3 above except that now $SNR(R_{cal}) = SNR_N = 5$ and $SNR(R) \rightarrow \infty$, $R \neq R_{cal}$. Fig. 3.4a shows that the effects of the measurement noise at the calibration cell propagate down to all the inversion cells and are comparatively larger in the NIR. Thus, while in the NIR, errors tend to amplify progressively backwards with range (up to 1.8 km approximately), in the UV, they reduce backwards with range (see analogous behavior for error source 1, Sect. 3.5.2). Fig. 3.4b shows fairly good agreement between first-order error bounds ($\sigma_{\varepsilon_{j,4}}$ in Table 3.3) and MC error bounds, evidenced by the former falling in between upper and lower MC error bounds.

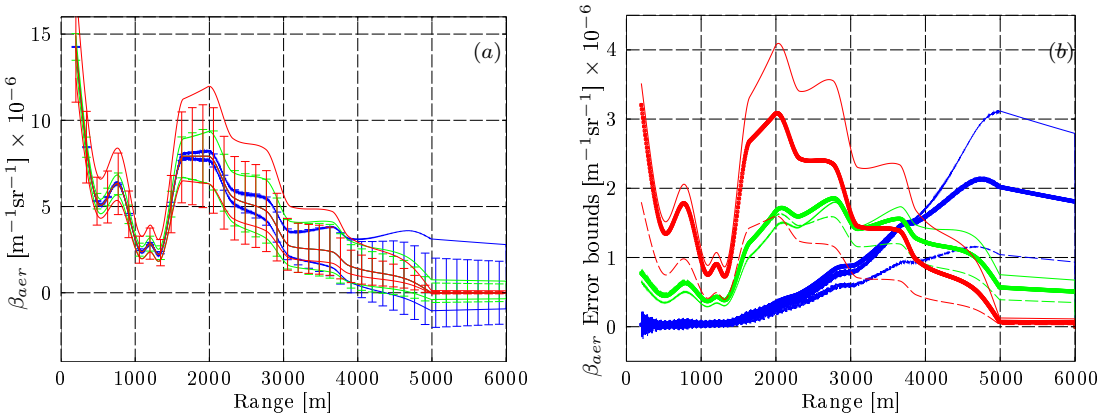

Figure 3.4: Analysis of noise at the calibration range (error source 4) for $SNR(R_{cal}) = 5$, $SNR(R) \rightarrow \infty$, $R \neq R_{cal}$. (a) As in Fig. 3.3a. (b) First-order error-bound amplitudes at 3σ (thick traces), and asymmetrical MC error-bound amplitudes (thin traces), where solid/dashed traces correspond to upper/lower MC error bounds, respectively. Total-increment error bounds perfectly match upper and lower MC error bounds and superimpose with them. Both (a) and (b) are VIS-normalized. UV (355 nm, blue), VIS (532 nm, green), and NIR (1064 nm, red).

In contrast to what happened when studying the error source (Eq. 3.19), MC error bounds are no longer symmetric. An explanation for that is that noise at the calibration range tends to be the dominant error source ($\sigma_{\varepsilon_{j,4}} \geq \sigma_{\varepsilon_{j,3}}$ over the whole inversion range), hence causing that larger backscatter-coefficient errors cease to be Gaussian distributed [*Comerón et al.*, 2004]. By comparing Fig. 3.4b and Fig. 3.3b, the impact of noise at the calibration range is more prominent towards the NIR. Thus, in the UV, $\sigma_{\varepsilon_{j,4}} \approx \sigma_{\varepsilon_{j,3}}$ (this distinguishing feature was not identified in earlier work as it was conducted at 1064 nm). A mathematical hint for that comes from the ratio between these two noise-induced error sources, $\frac{\sigma_{\varepsilon_{j,4}}}{\sigma_{\varepsilon_{j,3}}} \approx \frac{\beta_j}{\beta_N}\frac{1}{F_j}\frac{\sigma_{U_N}}{\sigma_{U_j}}$ (Eqs. 3.31- 3.33), where -by experiment- it has been found that $\left(\frac{2\beta_j^2}{U_j F_j}\right)^2 \sigma^2_{HU,j} << \left(\frac{\beta_j}{U_j}\right)^2 \sigma^2_{U_j}$ in Eq. 3.31. Because of the higher molecular component in the UV, the ratio β_j/β_N (recall that β stands for the "total" backscatter coefficient and that β_N is calibrated in a purely molecular reference range, Sect. 2.2.6) is much smaller in the UV than in the NIR, thus enabling $\sigma_{\varepsilon_{j,3}}$ and $\sigma_{\varepsilon_{j,4}}$ to become comparable in the UV. Total-increment error bounds $\varepsilon^{u/l}_{j,4}$ at 3σ (Table 3.4) perfectly match upper and lower MC error bounds in Fig. 3.4a and superimpose with them.

3.5.1.3 Superposition of error sources 3-4

First-order error bounds ($\sigma_{\varepsilon_{j,3-4}}$) and total-increment error bounds ($\varepsilon^{u/l}_{j,3-4}$) are compared with the implicit integral ones from previously published results (Sect. 3.4.3). All three types of error bounds are computed at 3σ ($p = 99.73\%$ probability that an inverted backscatter-coefficient realization falls within the error bounds). To compute first-order error bounds $3\sigma_{\varepsilon_{j,3-4}}$, Table 3.3 is used. To compute total-increment error bounds, $\varepsilon^{u/l}_{j,3}$, Eq. 3.43 approximation, Table 3.4 is used and, obviously, the exact Eq. 3.44 with $\Delta U_N = 3\sigma_{U_N}$ is used to compute $\varepsilon^{u/l}_{j,4}$.

Because upper and lower integral error bounds must be solved for each range cell and the solutions become numerically ill-conditioned for dense atmospheres ($\tau > 2$, approximately), they have only been computed for a discrete set of six ranges, from 1 to 6 km, equi-spaced 1 km. In nearly all the simulation runs the upper and lower MC error bounds computed with 100 lidar signal realizations coincided with the integral error bounds (i.e., the exact theoretical reference). Thus, the MC error bounds can be considered reliable bounds of the 3-σ inverted backscatter-coefficient population and, therefore, equivalent trustworthy extrapolations of the integral "exact" error bounds over all the range cells.

Multi-wavelength performance of both first-order and total-increment error bounds with reference to the implicit integral error bounds is shown in Fig. 3.5. Fig. 3.5a shows a comparatively poorer but still fairly good performance of the first-order error bounds, which give error bound amplitudes in between those of the MC error bounds or slightly closer to the MC lower error bound (the upper MC error bound in the NIR falls below the implicit integral error bound as a consequence of the natural statistical dispersion in this specific simulation run and wavelength). Fig. 3.5b shows that total-increment error bounds give virtually identical estimates that the implicit-integral error bounds with the advantage of being formulated in explicit form, being simpler to compute, and providing range-resolved information. The mean backscatter-relative error between both types of error bounds is below 1.7% in the UV, 0.6 % in the VIS, and 0.5% in the NIR, this difference being only due to Eq. 3.43 approximation. The spectral behaviour of Fig. 3.5 is analogous to that of Fig. 3.4b.

3.5.2 Errors due to the backscatter-coefficient calibration

By virtue of the relationship established in Eq. 3.17, the behaviour of this error source is qualitatively similar to that of the noise at the calibration range (error source (4), Fig. 3.4) – hence, analogous plots are retrieved (figure not shown), which are scaled by a multiplicative factor. For example, a relative backscatter calibration error of $\delta_{\beta_N} = 0.1\beta_N$ yields the plot of Fig. 3.4a ($SNR_N = 5$) scaled by a factor 0.5/3 (the dividing factor 3 is due to the fact that in Fig. 3.4b error envelopes are plotted at 3σ). Therefore, similar simulation conclusions apply, specifically, that the backscatter-coefficient calibration error becomes dominant in the NIR. This is best corroborated in Fig. 3.6, which uses a step-function atmospheric backscatter-coefficient profile with a 1-km falling edge between 4-5 km simulating the end of the boundary layer, and an error strength, $\varepsilon_r^{\beta_N} = 0.1$. In the mixing layer (0.2-4-km range) the error bound amplitudes can be ranked NIR > VIS > UV, as expected.

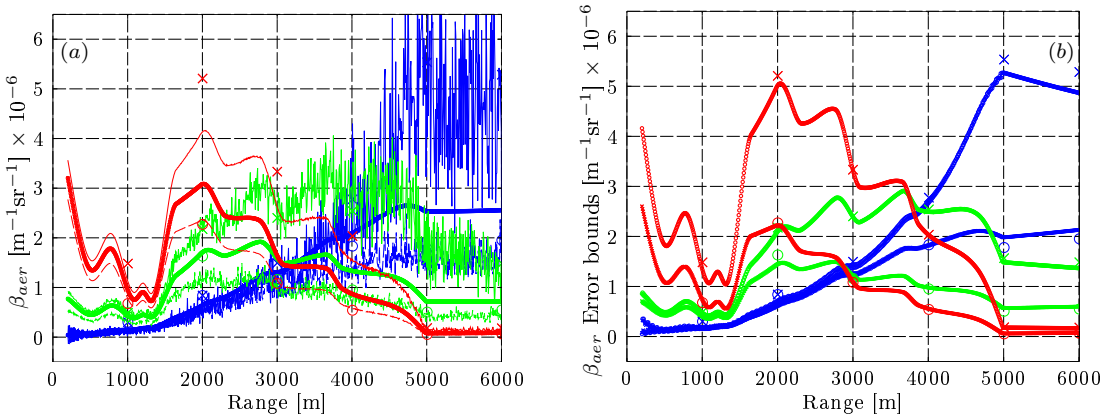

Figure 3.5: Superposition of error sources 3 and 4. Error amplitude plots comparing total-increment and first-order error bounds with implicit integral error bounds. (a) Performance of first-order error bounds: Crosses and circles denote implicit-integral upper and lower error-bound amplitudes at 3σ, respectively, noisy thin solid/dashed traces denote MC upper/lower error amplitudes, respectively, and solid thick traces denote first-order error-bound amplitudes at 3σ. (b) Performance of total-increment error bounds: Crosses and circles denote implicit-integral upper and lower error-bound amplitudes at 3σ, respectively, solid lines denote MC upper and lower error-bound amplitudes. Total-increment error bounds perfectly match MC error bounds and superimpose with them. (a) and (b) plots are VIS-normalized. UV (355 nm, blue), VIS (532 nm, light green), and NIR (1064 nm, red).

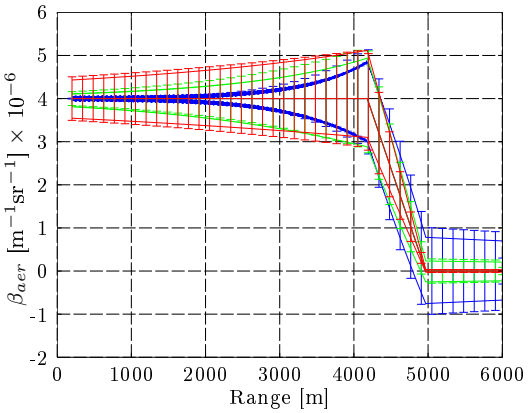

Figure 3.6: Analysis of aerosol backscatter-coefficient calibration error (error source 1). Same description as in Fig. 3.3a. The family of inverted backscatter-coefficient profiles is in response to a step-function profile of the atmospheric aerosol backscatter coefficient simulating the atmospheric boundary layer ($R \leq 5km$). Calibration errors in the range $\pm 30\%$ over the nominal backscatter Rayleigh level at the calibration range ($R_{cal} = R_{\max} = 6km$). Plots are VIS-normalized. UV (355 nm, blue), VIS (532 nm, light green), and NIR (1064 nm, red).

3.5.3 Errors due to the lidar ratio

Simulation conditions for this case assume noiseless power lidar returns ($SNR(R) \to \infty$ in all range cells), perfect backscatter-coefficient calibration, and lidar-ratio errors defined by a relative error figure, p. During the tests, Eqs. 3.36 and 3.37 gave always the same signs, as expected.

Fig. 3.7 shows the performance of the total-increment error bounds, which perfectly match the simulated error deviations. For small-to-moderate errors (p=±30%, figure not shown) the total-increment upper and lower error bounds tend to distribute symmetrically around the "true" atmospheric backscatter coefficient, that is, which similar upper and lower error amplitudes. This is no longer the case for large errors (p=±90%). The inverted backscatter-coefficient error bounds and their asymmetry increases towards the UV, which reinforces the fact that lidar ratio uncertainties become more critical towards the UV.

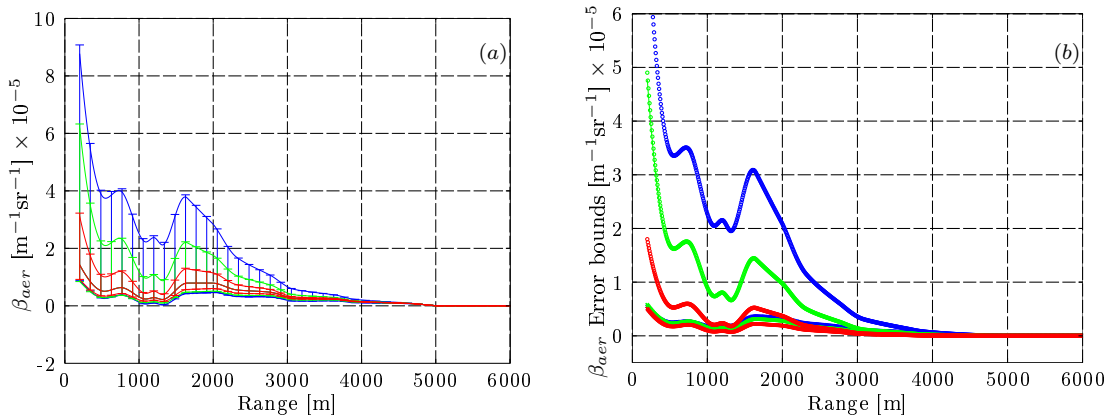

Figure 3.7: Analysis of lidar-ratio errors (error source 2). (a) Aerosol backscatter-coefficient envelopes with superimposed total-increment error bounds (vertical error bars). Error strength, $p = \pm 90\%$. Constant relative deviation over the nominal lidar ratio. (b) Backscatter-coefficient error-bound amplitudes associated with (a). Solid trace denotes upper/lower error-bound amplitudes. Total-increment error bounds perfectly match error bounds and superimpose with them. Both (a) and (b) are VIS-normalized. UV (355 nm, blue), VIS (532 nm, light green), and NIR (1064 nm, red).

3.6 Conclusions

Two different types of backscatter-coefficient inversion error bounds have been formulated: first-order error bounds (Sect. 3.3) and total-increment error bounds (Sect. 3.4). Both have been formulated analytically in explicit form for the two-component KFS lidar inversion algorithm subject to error sources 1-4. The error bounds have been validated using a MC method.

First-order error bounds are obtained using the classic error-propagation approach. They are symmetric about the true value with an amplitude lying between those of the upper and lower MC error bounds. Their amplitudes encompass most of the inverted backscatter profiles in practical situations ($SNR \geq 5$, lidar-ratio relative error strength, $p \leq 30\%$, Sect. 3.5). Yet, strictly speaking, first-order error bounds are still approximate. With larger errors (lower SNRs and/or higher uncertainties), upper and lower MC error bounds become progressively asymmetric, a property that

first-order error bounds cannot reflect.

It has been shown that when the random error source follows a Gaussian distribution, total-increment error bounds computed at 3σ coincide with 3-σ statistical confidence levels and, therefore, provide the exact result in explicit analytical form. The total-increment error bound associated with error source 3 was not found explicitly because of the multi-dimensionality of the problem. However, it is well approximated by the 3-σ first-order error bound as $\varepsilon_{j,3}^{u/l} \approx 3\sigma_{\varepsilon_{j,3}}$. Similarly, when the uncertainty of a systematic error source is assumed to be uniform (the usual case for error sources 1-2 when no further "a priori" information is available) the total-increment error bound gives the total error span on the inverted-backscatter profiles.

As in the KLT algorithm, the effect of noise at the calibration cell dominates (particularly towards the NIR) over the effect of the noise from all other range cells. Though fundamentally different, error sources 1 and 4 yield similar effects on the retrieval via Eq. 3.17, thus error sources 2 and 4 are of most concern. Concerning their spectral behavior, uncertainties in the lidar ratio largely dominate the UV error bounds while the backscatter-coefficient calibration is the dominant error source in the NIR. The explicit analytical error bound formulation summarized in Table 3.3 and Table 3.4 is -to the best of our knowledge- new in the state of the art of lidar inversion algorithms.

Chapter 4

Enhanced data-gluing algorithm for mixed analog/photon-counting lidar signals

Because of the large dynamic range of the backscatter lidar signal, data-gluing algorithms are used to combine simultaneously-acquired analog and photon-counting records into a single distortionless wide-dynamic-range data record. From this perspective, this Chapter departs from an overview of Licel's gluing algorithm and presents an enhanced version of it, which automatically finds the best spatial fitting range. Two applications of the gluing procedure are presented: First, a case example based on time series monitoring of the aerosol load from Nabro's volcanic event. Second, a prospective application to calibrate the signal gain and optical losses of the receiving chain. The contents presented in this Chapter are a compilation of two proceedings, Lange et al. [2012b] (Sect. 4.2 and 4.3) and Lange et al. [2012a] (Sect. 4.4).

4.1 Introduction

The data-gluing presented next provides a convenient way to deal with the large dynamic range of the lidar power return signals, which can span up to five orders of magnitude.

The RSLab multi-spectral lidar system is based on Licel transient recorders, which combine simultaneous analog and photon-counting acquisition modes. Both modes have advantages, namely, ADC has a better linearity for high light-level signals occurring especially in the near range, while PC mode has a better sensitivity for low light-level signals in the far range [*Licel*, 2007a]. Combination of both modes, each of them in the range where it is advantageous, in a process called *data-gluing*, allows to exploit the lidar signal in all its range extension.

Applications that can benefit from the data-gluing are events that combine aerosols loads in the whole troposphere and/or the stratosphere. Examples of them are as eruptive events with a high aerosol load in the upper troposphere and/or the stratosphere, dust events that carry a large amount of dust both inside the ABL or in the upper troposphere, and fire plumes. Eruptive events such as Eyjafjallajökull (Iceland) in 2010, Grímsvötn (Iceland), Puyehue (Argentina), Nabro

(Eritrea) and Mount Lokon (Indonesia) in 2011 have yielded emergency situations with a strong economical cost due to human evacuation and/or air traffic interruption. Volcanic aerosols are first injected in the troposphere and often reach the stratosphere where they can reside for several years.

This Chapter is organized as follows: Sect. 4.2 introduces the basic- and the enhanced- data-gluing algorithm, while Sect. 4.3 shows a case example for the enhanced version. Sect. 4.4 presents a prospective application, Finally, concluding results are presented in Section 4.5.

4.2 Enhanced data-gluing algorithm

Basic version.- The basic gluing algorithm proposed in *Licel* [2007a] by Licel, combines the analog- and PC-recorded signals in a "fixed" fitting range interval $[R_A, R_B]$, where both analog and dead-time-corrected PC signals are valid and have a high SNR.

Data-gluing minimizes the error norm between the dead-time-corrected photon-counted (PC) signal, $\overrightarrow{V_{pc}}$ [counts-per-second units, cps], and a scaled and offset version of the analog voltage signal, $\overrightarrow{V_a}$ [V], for solving parameters a (scaling) and b (offset) in the fitting interval, $[R_A, R_B]$. Formally, this can be expressed as

$$\min\left\{\|\overrightarrow{\varepsilon_I}\|^2\right\}_{a,b} = \min\left\{\left\|\overrightarrow{V_{pc}} - \left(a\overrightarrow{V_a} + b\overrightarrow{1}\right)\right\|^2\right\}_{a,b} \quad I \in [R_A, R_B]\ . \tag{4.1}$$

The error vector, $\overrightarrow{\varepsilon_I}$ can be defined as

$$\overrightarrow{\varepsilon_I} = \overrightarrow{V_{pc}} - \left(a\overrightarrow{V_a} + b\overrightarrow{1}\right), \tag{4.2}$$

with $\overrightarrow{V_a'} = a\overrightarrow{V_a} + b\overrightarrow{1}$, the scaled-and-offset analog signal.

For a typical mini-PMT the fitting interval corresponds to the range interval where the PC signal is in the 0.5-to-10-MHz region. In Eq. 4.1 the residual error norm $\|\overrightarrow{\varepsilon_I}\|^2$ is an indicator of the quality of the fitting. Besides, it has been found by experiment [*Lange et al.*, 2012a] that $\left\|a\overrightarrow{V_a}\right\| >> b$ so that the scaling parameter a is the dominant parameter in the error norm.

Enhanced version.- The enhanced gluing method proposes a fine-tuning automatic-search algorithm to find the best fitting range interval I ensuring minimum residual error norm. Towards this goal a two-step procedure is followed:

1) First, the central point of the best fitting range interval, I_i, is obtained. To do that, the modified form of Eq. 4.1 above,

$$\min\left\{\|\overrightarrow{\varepsilon_{I_i}}\|^2\right\}_{a_i,b_i} = \min\left\{\left\|\overrightarrow{V_{pc}} - \left(a_i\overrightarrow{V_a} + b_i\overrightarrow{1}\right)\right\|^2\right\}_{a_i,b_i} \quad in\ I_i \tag{4.3}$$

is solved for $\overrightarrow{x_i} = (a_i, b_i)$ along successive adjacent fitting range intervals $I_i \in \left(R_A^i, R_B^i\right)$ of constant length ($\Delta R_I = 100$ m) centered at the range R_i. In practice, R_i is incremented in steps of ΔR_I along the measurement range. This is to say that for each range R_i, a relationship $(a_i, b_i) \longleftrightarrow \|\overrightarrow{\varepsilon_{I_i}}\|$ is obtained, meaning that the solution $\overrightarrow{x_i} = (a_i, b_i)$ is associated to the error norm figure, $\|\overrightarrow{\varepsilon_{I_i}}(\overrightarrow{x_i})\|$. Because $\left\|a_i\overrightarrow{V_a}\right\| >> b_i$, one can biunivocally relate $a_i \longleftrightarrow \|\overrightarrow{\varepsilon_{I_i}}\|$.

By experiment, the intercept point, R_{opt}, yielding the best fitting range interval, I_{opt}, is found as the point where the difference between the photon-counting signal and the a-scaled analog signal is a minimum. Formally, this distance (in what follows, the *gluing-error distance*) is defined as

$$\varepsilon_g(R) = |V_{pc}(R) - a_i^s\, V_a(R)|\,, \tag{4.4}$$

where a_i^s is a smoothed version of the range-dependent parameter a_i obtained from Eq. 4.3. $V_{pc}(R)$ and $a_i^s\, V_a(R)$ are plotted in the example of Fig. 4.1a. a_i and a_i^s as a function of range are plotted in Fig. 4.1b, and the gluing error distance according to Eq. 4.4 above is represented in Fig. 4.1c. Each step ladder in a_i corresponds to an interval, I_i. From Fig.4.1c, the minimum gluing-error distance, $\varepsilon_g(R)$, is obtained at R_{opt}=3.2 km LOS, which corresponds to $a_{opt}^s = a(R_{opt})$=5.3×10^{10} cps/V.

2) Once the best fitting interval, I_{opt}, has been determined from Eq. 4.4 (Fig. 4.1), the end points of this range interval, R_A^{opt} and R_B^{opt} (i.e., left and right to the central point, R_{opt}) are computed from the photon-counting voltage record, $V_{pc}(R)$ [cps], and a threshold level 10% above and below the counts per second at R_{opt}, $V_{pc}(R_{opt})$, see Fig. 4.1d. After that, the corresponding R_A^{opt} and R_B^{opt} are found. The 10% criterion has been determined by experiment and yields a typical fitting length, $R_B^{opt} - R_A^{opt}$, of less than 1 km, smaller than the length obtained from the basic gluing algorithm of Eq. 4.1 (around 7 km), where the fitting interval is predefined from the beginning. Larger fitting ranges lead to situations characterized by a lower SNR and, consequently, a higher noise level.

Finally, the glued signal is formed as,

$$V_{glued}(R) = \begin{cases} a_{opt}^s\, V_a(R)\,, & R \le R_{opt} \\ V_{pc}(R)\,, & R > R_{opt} \end{cases}\,. \tag{4.5}$$

From Fig. 4.1d it is seen that R_{opt} falls approximately at 3.2 km, which corresponds to a PC signal level of 19 Mcps (19 MHz). The fitting range interval, I_{opt}, ranges from 3.0- to 3.4-km or, equivalently, 21- to 17-MHz, respectively. Though Licel's gluing range goes from 10 to 0.5 Mcps, the optimal range interval obtained above also avoids the noisier ranges in the far range. (Fig. 4.1d).

Regarding *dead-time correction*, the photon-counting unit part of Licel's transient recorder equipping the RSLab lidar are non-paralyzable. This means that an event (understood as a *single pulse of photo-induced charge* of great enough amplitude that arrives at the discriminator) will not be recorded when the time interval between its occurrence and the occurrence of the last recorded event is smaller than some given interval, τ_{dead}. Following *Donovan et al.* [1993], τ_{dead} often characterizes the length of time after the occurrence or the detection of an event that the detection system is dead, so it is often referred to as the *dead time*.

The dead-time corrected count rate is computed as *Whiteman* [2003],

$$N_{real} = \frac{N_{meas}}{1 - \tau_{dead}\, N_{meas}}\,, \tag{4.6}$$

where N_{meas} [cps] is the observed or measured "raw" count rate, N_{real} [cps] is the dead-time

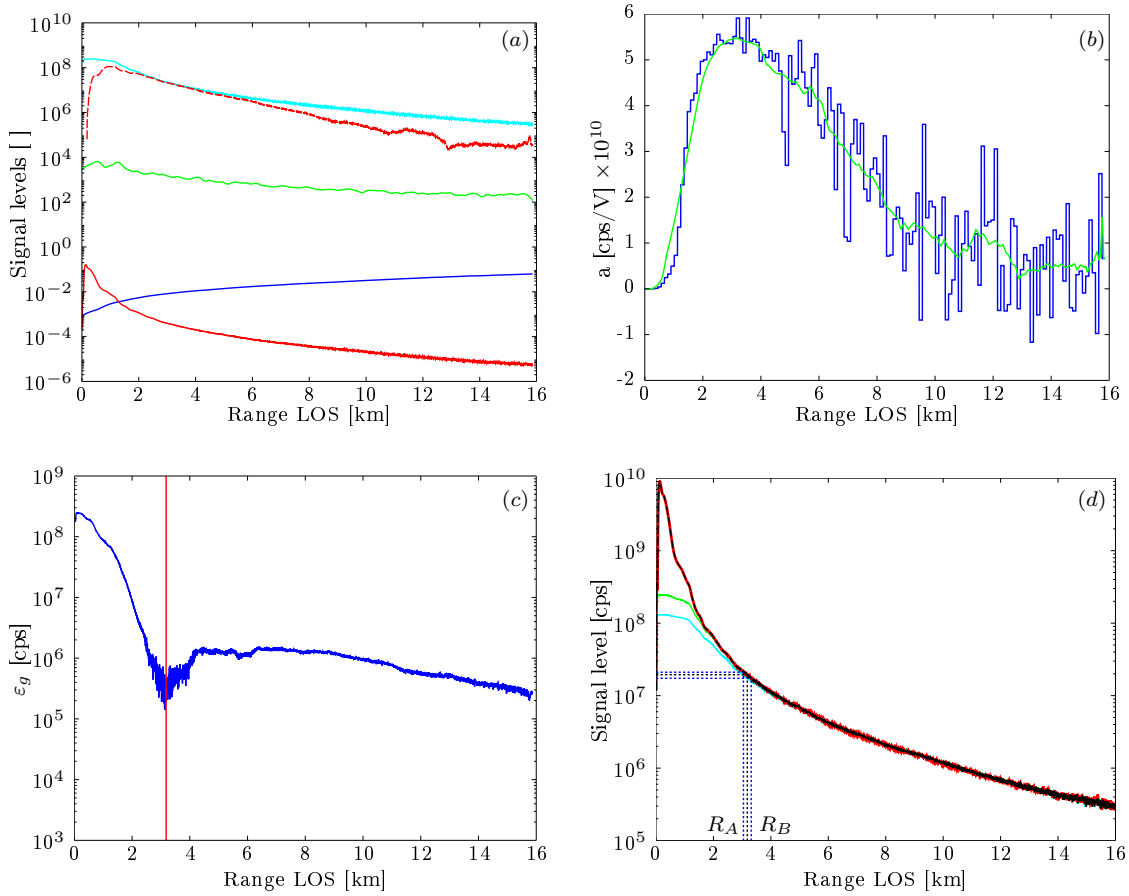

Figure 4.1: The enhanced gluing algorithm. (a) Relevant signals and indicators of the fitting process. (Cyan) Dead-time corrected, photon-counting signal, $V_{pc}(R)$. (Red) Analog signal, $V_a(R)$. (Dashed red) a-scaled analog signal, $a_i^s(R)\,V_a(R)$. (Green) Normalized error norm, $1/\sqrt{N}\;\|\varepsilon_{I_i}\|$, Eq. 4.3. (Blue) Inverse analog SNR, $\mathrm{ISNR}_a(R)$. (b) Fitting parameter a_i (Eq. 4.3) as a function of range. (Blue ladder) $a_i(R)$. (Green) Smoothed version (400-sample span, or 1500 m), $a_i^s(R)$, used in Eq. 4.4. (c) Gluing error distance, $\varepsilon_g(R)$ [cps], Eq. 4.4. Algorithm step 1: The central point R_{opt}, of the best interval, I_{opt}, is determined as the minimum of $\varepsilon_g(R)$ (red vertical line). (d) Algorithm step 2: End points of the best fitting interval, R_A^{opt} and R_B^{opt} (dotted blue lines), are computed as the ranges associated to $\pm 10\%$ the count number for R_{opt} (dotted black line). (Green) Dead-time-corrected photon-counting signal. (Cyan) Non-dead-time-corrected signal. (Red) a_{opt}-scaled $a_{opt}^s\,V_a(R)$. (Black) Final glued signal, Eq. 4.5.

corrected or "true" count rate, and τ_{dead} [s] is the dead time.

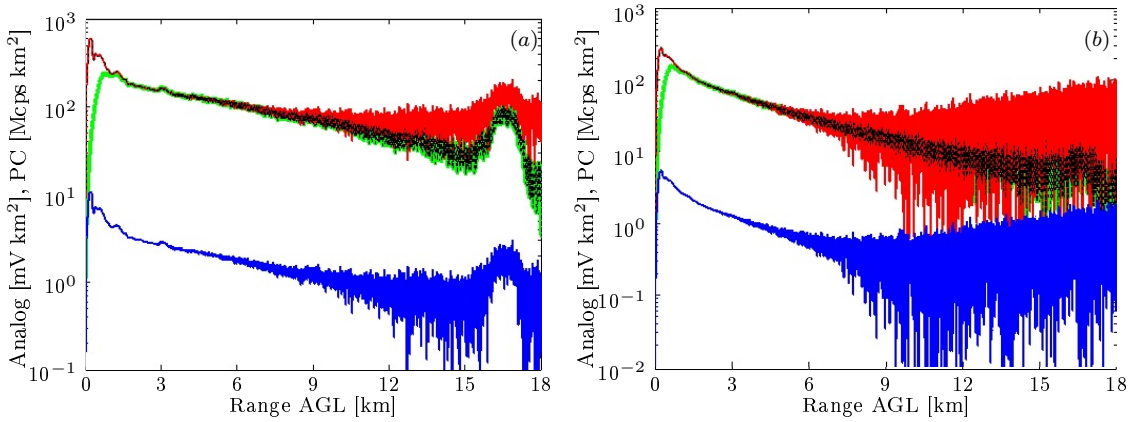

Figure 4.2: Comparison among analog, PC, and glued range-corrected signals (Barcelona UPC, Campus Nord, June, 27^{th}, 2011). (a) 532-nm range-corrected channel measurement for the Nabro volcanic event shown Fig. 4.3. (b) 355-nm range-corrected channel (same measurement case). (Blue) Analog raw signal, $\overrightarrow{V_a}$. (Red) Scaled-and-offset analog signal, $\overrightarrow{V_a'} = a\overrightarrow{V_a} + b\overrightarrow{1}$. (Green) Dead-time corrected photon counting signal. (Black) Glued analog-PC signal. Black trace superimposes the red one in the near range, and the green one in the far range.

4.3 Case example

A case scene showing volcanic aerosols from Nabro' volcanic event (Eritrea, 2011) in the stratosphere and, simultaneously, Saharan dust in the troposphere is presented. The scene was captured by the RSLab multi-spectral lidar over UPC, Campus Nord, Barcelona during the period 27 June - 1 July, 2011.

Saharan dust intrusion episodes are frequent in the Iberian Peninsula [*Pérez et al.*, 2006]and occur at low-troposphere heights. Because of the high intensity of the lidar returns in the near-range range, these dust episodes are nicely recorded by the analog channel and poorly recorded by the PC channel, which saturates due to the large number of counts in the near-range. The opposite situation occurs when monitoring volcanic eruptions [*Guerrero-Rascado et al.*, 2010; *Sawamura et al.*, 2012; *Pappalardo et al.*, 2013], that inject volcanic aerosols and ashes up in the stratosphere. At such heights, the lidar returns are too faint to be properly recorded within the sensitivity of the analog channel (only a few ADC levels are "moved" and with a very poor SNR).

In Fig. 4.2, 532- and 355-nm lidar measurements are shown. In both cases, the analog signal is very noisy around 17 km so that Nabro volcanic aerosols cannot be distinguished from noise, specially for the 355-nm case. This case example is also shown in Sect. 7.2.4. The PC signal fails to show aerosol layers below about 3 km in both cases. In contrast, the glued signal profile in Fig. 4.2 and its time series in Fig. 4.3 and Fig. 4.4 evidences, with a good SNR, both Saharan dust layers in the 0–4 km subplot (low range) and volcanic aerosols in the 15–18 km subplot (high range), for the 532-nm case.

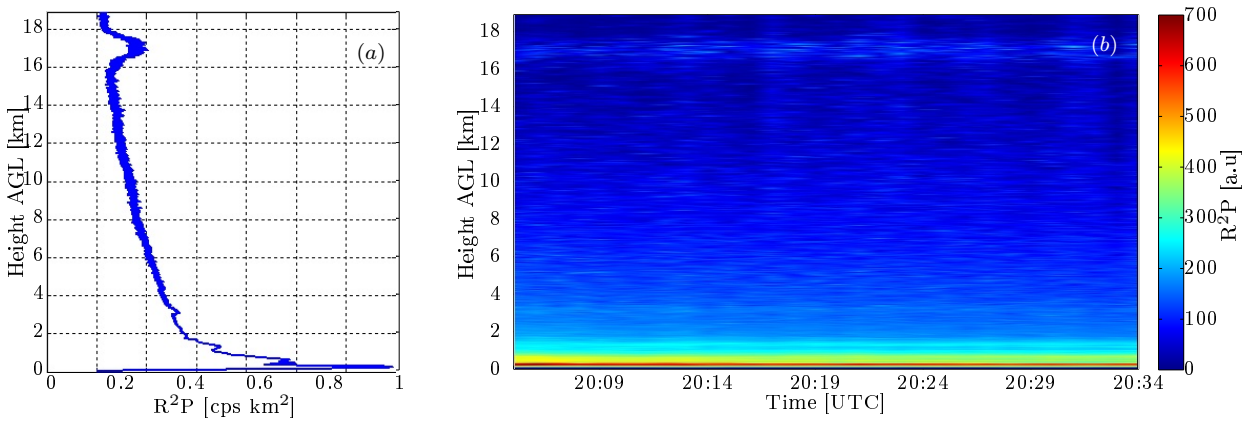

Figure 4.3: Time series monitoring the evolution of a vertical profile of volcanic aerosols in the stratosphere (about 17 km) and Saharan dust layers in the troposphere (below 3.5 km), 532-nm channel, same case as Fig. 4.2a. (*a*) Range-corrected profile of the glued analog-PC signal. (*b*) Glued analog-PC signal time series. 0–4 km and 15–18 km range intervals are zoomed-in in Fig. 4.4.

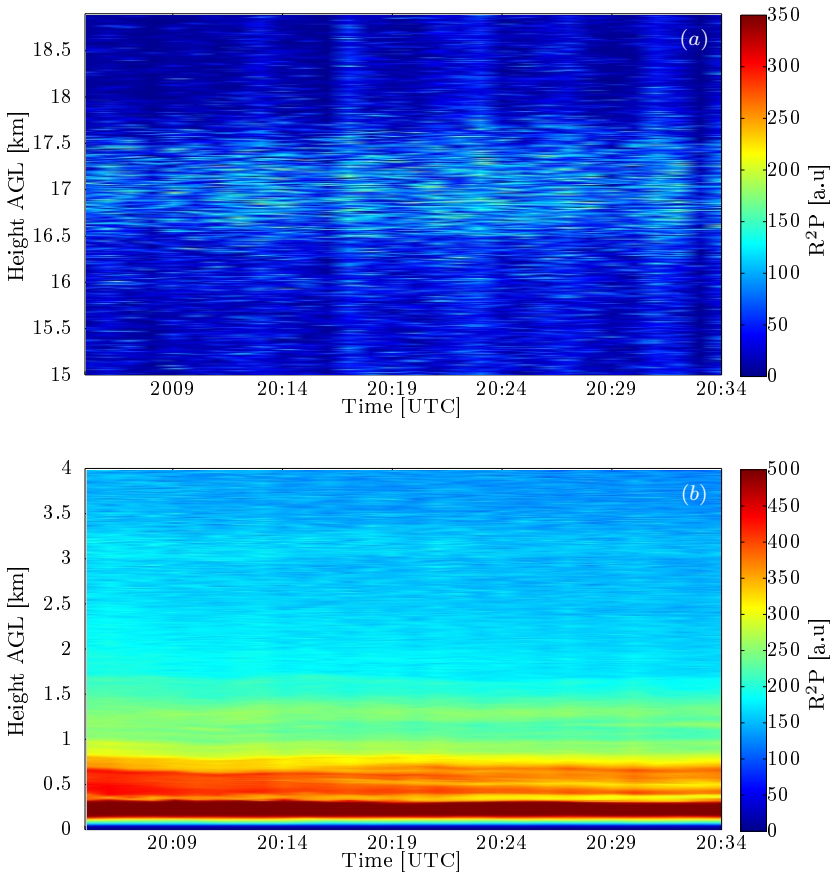

Figure 4.4: Glued analog-PC signals from the Fig. 4.3 zoomed-in in the low range (0–4 km) and in the far range, 15–18 km.

4.4 Prospective application: Lidar calibration

4.4.1 Receiving channel calibration

Another interpretation of the concept of calibration has to do with relating the measured voltage levels at the lidar receiver output to the backscattered optical power levels at the telescope input via the *net voltage responsivity*. This is of importance to cross-examine the measured optical levels with the predicted ones arising from energy link-budged studies at the design stage of the tropospheric lidar system [*Kumar et al.*, 2012]. As a result, a rough estimate of the optical losses of the reception chain can be obtained.

The method is presented next with two different levels of approximation: At level 1, only a rough estimate of the net voltage responsivity is obtained. At level 2, a rough estimate of the *optical losses* is derived as well. To achieve this second level of approximation, the method assumes simultaneous analog and photon-counting acquisition by using PMT- and APD-based detectors and e.g., Licel transient recorders [*Licel*, 2007b].

4.4.2 Calibration method

Net responsivity calibration.- Calibration of the optical power levels in return can be done in one or two steps of progressive refinement. Step 2 being an improvement of Step 1 as it enables to approximately estimate the optical transmissivity of the receiving chain (Fig. 4.5).

Step 1 (level-1 approximation).- First, a Rayleigh fit is used to determine the *scaling factor*, K'_{aer}, between a purely molecular range-corrected power signal [*Collis and Russell*, 1976],

$$R^2 P_{Ray}(R) = \beta_{mol}(R) \exp\left[-2\int_0^R \alpha_{mol}(r)\, dr\right], \tag{4.7}$$

and the measured voltage signal,

$$V(R) = R'_v\, P(R) \quad [V], \tag{4.8}$$

where R'_v [V/W] is the *net voltage responsivity* (i.e., including optical losses) of the reception channel (Fig. 4.5), and $P(R)$ is the elastic lidar equation (Eq. 2.20) excluding OVF effects,

$$P(R) = \frac{K}{R^2}\left[\beta_{aer}(R) + \beta_{mol}(R)\right] \exp\left\{-2\int_0^{R_{bl}} \alpha_{aer}(r)\, dr\right\} \exp\left\{-2\int_0^R \alpha_{mol}(r)\, dr\right\} \quad [W]. \tag{4.9}$$

In Eq. 4.7-4.9, α_{mol} and β_{mol} are the atmospheric molecular extinction and backscatter coefficients, respectively, α_{aer} and β_{aer} are the atmospheric aerosol extinction and backscatter coefficients, respectively, R is the range, and K is the lossless instrument constant of the lidar (Eq. 2.21).

When fitting Eq. 4.8 to Eq. 4.7 it can be shown that the Rayleigh's fit is given by the scaling

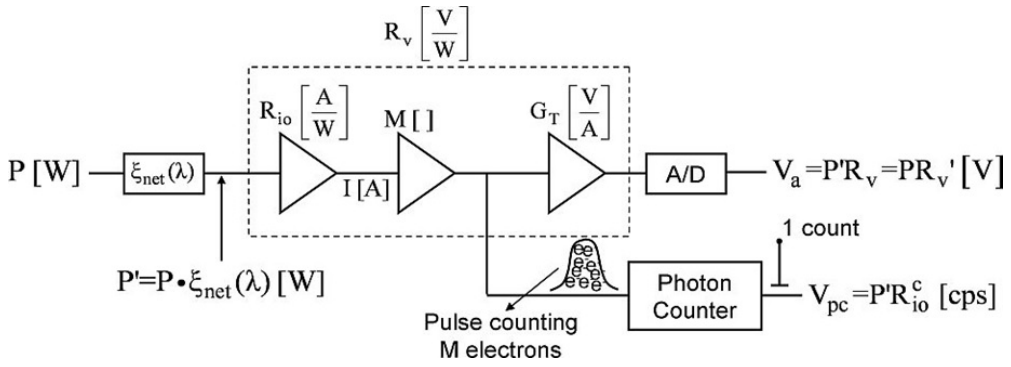

Figure 4.5: Generalized block diagram of a lidar reception channel combining simultaneous analog/photon-counting acquisition. P is the backscattered optical power in reception, $\xi_{net}(\lambda)$ is the optical transmissivity of the receiving chain, R_v is the receiver voltage responsivity excluding losses, and A/D stands for analog-to-digital converter. Both A/D and "photon counter" blocks are included into the transient recorder unit. V_a is the analog voltage signal [V], V_{pc} is the PC signal in counts-per-second units (cps), and $R^c_{io} = R_{io}/q$ [cps/W] with q the electron charge. For an APD-based reception channel, G_T is the preamplifier gain, for a PMT-based channel, G_T is directly the input impedance of the transient recorder (50Ω)

factor,

$$K'_{aer} = KR'_V T^2_{ABL,aer}, \tag{4.10}$$

In Eq. 4.10 above, $T^2_{ABL,aer} = \exp(-2\int_0^{R_{bl}} \alpha_{aer}(r)\, dr)$ is the two-way path atmospheric aerosol transmittance up to the end of the ABL due to the aerosol load (Eq. 2.17) and it has been used that $\beta_{aer}(R) \simeq 0$ for $R > R_{bl}$ in Eq. 4.9.

Because the lossless instrument constant, K, and the aerosol transmittance, $T^2_{ABL,aer}$, can be known with relatively low uncertainties, the net responsivity R'_v can be estimated from Eq. 4.10 as

$$R'_v = K'_{aer} / \left(KT^2\right), \tag{4.11}$$

where T^2 is shorthand notation for $T^2_{ABL,aer}$. Following Sect. 2.2.4, the aerosol transmittance can be estimated from a cooperative Raman channel or from the slope method applied to the ABL of the measured lidar signal [*Kunz and de Leeuw*, 1993]. In the latter case, the assumption of a homogeneous mixture of aerosols inside the ML is needed. Once R'_v has been estimated it is possible to convert the measured backscattered voltage levels into optical power levels, hence quantifying the deviation between the measured ones and the predicted ones via lidar-design link-budget studies.

Given uncertainties, ΔK and ΔT, associated to the lidar system constant and aerosol transmissivity, the upper and lower error bounds for the estimated net responsivity become

$$\begin{cases} \Delta R'^{+}_v = R'_v - \frac{K'_{aer}}{(K+\Delta K)(T^2+\Delta T^2)} \\ \Delta R'^{-}_v = \frac{K'_{aer}}{(K-\Delta K)(T^2-\Delta T^2)} - R'_v \end{cases}, \tag{4.12}$$

where superscripts "+" and "-" denote upper and lower bounds.

Step 2 (level-2 approximation).- For the UV and VIS elastic channels of the RSLab lidar, which provide both analog and PC records of the measured lidar signal, a calibration method to quantify

the signal gain of the elastic channel (i.e., the product $M\,G_T$ in Fig. 4.5, where M is the *detector multiplication factor*, and G_T is the *preamplifier gain*) is carried out as follows:

The analog/PC data-gluing procedure explained in Sect. 4.2 is used to estimate the signal gain in the range interval where both analog and PC signals are valid.

Departing from Eq. 4.1 and Fig. 4.5, imposing the condition that both analog and PC records are proportional, the condition $\overrightarrow{V_{pc}} = a\overrightarrow{V_a}$ leads to $P'\,R_{io}^c$ [cps] $= a\,P'\,R_v$ [cps], or, equivalently, $a = R_{io}^c/R_v$. Introducing the definition of *voltage responsivity*, as $R_v = R_{io}\,M\,G_T$ (dashed box in Fig. 4.5), the fitting parameter a can be expressed from receiving-chain system parameter as

$$a \simeq \frac{1}{q\,M\,G_T} \quad \left[\frac{cps}{V}\right]. \tag{4.13}$$

which yields the *signal gain*, $M\,G_T \simeq 1/(q\,a)$ once a is solved from Eq. 4.13 above.

Because for the NIR channel of the RSLab lidar only analog acquisition is available (APD-based channel), the analog/PC gluing technique cannot be applied and the signal gain is estimated with larger uncertainties based only on manufacturer's specs for M, and G_T.

Finally, given (i) the signal gain $M\,G_T$ obtained from step 2 above, (ii) the net voltage responsivity, R'_v, from step 1, and (iii) the detector intrinsic responsivity, R_{io}, the *optical transmissivity* of the receiving chain can be estimated as (Fig. 4.5),

$$\xi_{net}(\lambda) = \frac{R'_v}{R_{io}\,M\,G_T} \quad [\cdot]\,. \tag{4.14}$$

Though experimentation with the proposed calibration method is still in progress, Fig. 4.6 shows how link-budget design studies are validated assuming ± 5% cumulative loss deviations in all optical elements in reception.

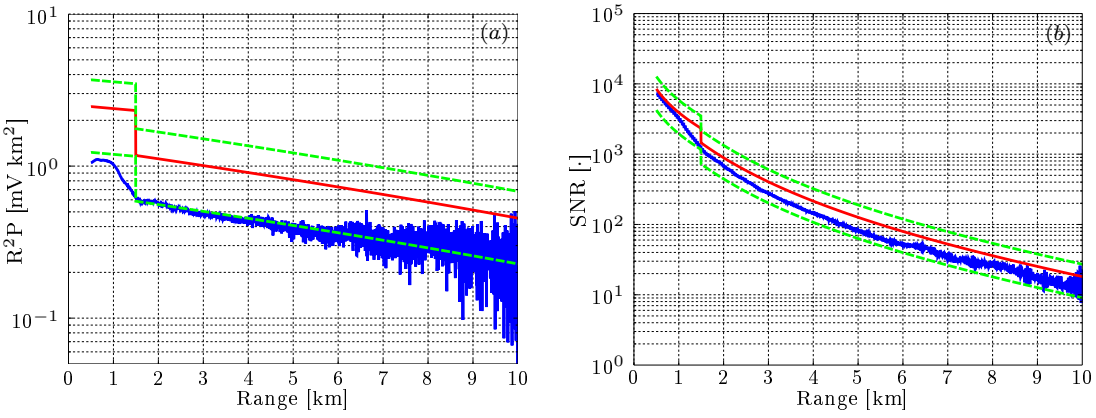

Figure 4.6: Validation of the backscattered return signal and SNR levels in reception (1064-nm channel). (a) Range-corrected voltage level as a function of range. (Red) Theoretical level expected assuming manufacturer's transmissivities for the receiving optical elements and a homogeneous atmosphere in the boundary layer ($R_{bl} = 1.5\,km$). (Dashed green) Theoretical levels assuming cumulative ±5% deviations in all optical elements in reception. (Blue) Measured signal level. (b) Signal-to-noise ratio. Trace description as in (a).

4.5 Conclusions

It has been shown that data-gluing algorithms, which combine analog with photon-counting data records from fast Licel lidar transient recorders, provide an effective way to enhance the dynamic range of the receiving lidar channel. The mixed analog/photo-counting acquisition approach is particularly suitable for the detection of volcanic aerosols in both the troposphere (near/mid range) and the stratosphere (far range). To glue both signals, the PC channel must also be dead-time corrected [*Whiteman*, 2003; *Hamamatsu*, 1998].

While existing gluing algorithms solve the fitting coefficients by matching both analog and PC data over a predefined spatial range depending on which kind of photo-detector is being used [*Licel*, 2007a], the enhanced data-gluing algorithm presented automatically finds the spatial range where both analog and photon-counting signals are more similar. The method is based on Euclidean distance minimization over piece-wise range intervals along the whole acquisition spatial range.

A prospective application of the data-gluing calibration method to estimate the signal gain, $M\,G_T$, and optical transmissivity, $\xi_{net}(\lambda)$, of the lidar receiving chain has been proposed. The method has been formulated in two steps of progressive approximation. The first step estimates the net voltage responsivity (i.e., including optical losses in the receiving chain) and the second step requires analog/PC data gluing and provides an estimate of the receiving chain optical losses. This is to serve the purpose of validating link-budget studies.

Chapter 5

ABLH monitoring using a Kalman filter and backscatter lidar returns

A solution based on a Kalman filter to trace the evolution of the ABL sensed by a ground-based elastic-backscatter tropospheric lidar is presented. An erf-like profile is used to model the mixing layer top and the entrainment zone thickness. The EKF enables to retrieve and track the ABL parameters based on simplified statistics of the ABL dynamics and of the observation noise present in the lidar signal. This adaptive feature permits to analyze atmospheric scenes with low SNRs without the need to resort on long time averages or range-smoothing techniques, as well as to pave the way for future automated detection solutions. First EKF results based on oversimplified synthetic and experimental lidar profiles are presented and compared with classic ABL estimation quantifiers for a case study with different SNR scenarios.

5.1 Introduction

A significant advantage of backscatter lidar remote sensing instruments is that they are able to gather a range-resolved profile of the ABL simultaneously for the whole observation range, which greatly improves the temporal resolution of in-situ sensors and radiosoundings.

The lidar signal shows this relative distribution of aerosols and moisture along the troposphere in terms of the background-subtracted range-corrected power $U(R) = R^2P(R)$, with $P(R)$ the single scattering return power as *Kovalev* [2004]

$$\begin{aligned} U(R) = &\quad K\Big[\beta_{mol}(R) + \beta_{aer}(R)\Big]T^2(R), \\ T^2(R) = &\quad e^{-2\int_0^R \Big[\alpha_{aer}(u) + \alpha_{mol}(u)\Big]du}, \end{aligned} \tag{5.1}$$

where R [km] is the range along the lidar LOS (R is related to height z as $z = R\sin(\theta)$, where θ is the LOS elevation angle), K [W km^3] is the system constant, and $\beta(R)_{mol}$ and $\beta_{aer}(R)$ [km^{-1} sr^{-1}] are the range-dependent molecular and aerosol optical backscatter coefficients, respectively. β_{aer} is defined as $\beta_{aer}(R) = N_{aer}(R)\frac{d\sigma_{aer}(\pi)}{d\Omega}$, that is, the product of the aerosol number concentration, $N(R)_{aer}$ [km^{-3}], and the average differential backscatter cross-section of the aerosol mixture, $\frac{d\sigma_{aer}(\pi)}{d\Omega}$ [km^2 sr^{-1}], which includes the effects of aerosol type and moisture. The molecular component, $\beta_{mol}(R)$, can be computed from the US standard atmosphere model [*Bodhaine et al.*, 1999] or radiosoundings.

Finally, $T^2(R)$ represents the two-way path atmospheric transmittance affecting the optical pulse, with α_{mol} and α_{aer} the atmospheric extinction coefficient due to aerosols and molecules, respectively.

The transmittance factor can be included into the total backscatter by defining the attenuated total backscatter as

$$\beta_{atten}(R) = \beta(R)T^2(R), \tag{5.2}$$

where $\beta(R) = \beta_{mol}(R) + \beta_{aer}(R)$. Inside the ML and, particularly, towards the NIR or in relatively optically dense atmospheres, the aerosol backscatter component dominates, so that $\beta_{aer}(R) >> \beta_{mol}(R)$ and $\beta(R) \approx \beta_{aer}(R)$. This simplification makes the range-corrected lidar signal, $U(R)$, almost proportional to the aerosol number concentration profile, $N_{aer}(R)$. In contrast, in the free troposphere (FT) the aerosol contents is virtually nil (with the exception of e.g., unstable dust layers or dust intrusions [*Pérez et al.*, 2006] and hence, $\beta(R) \approx \beta_{mol}(R)$. As a result, in the FT the lidar signal, $U(R)$, becomes proportional to the profile of the molecular number concentration, $N_{mol}(R)$ (Fig. 1.2).

In this Chapter, a trade-off between geometrical and statistical approaches (Sect. 2.5) by using an adaptive filter solution based on the EKF is presented, which estimates the time-dependent ABLH, the approximate EZ thickness, and auxiliary atmospheric backscatter-coefficient parameters. A preliminary study on the problem has been outlined in *Tomás et al.* [2010], from the RSLab. Because the filter adaptively fits a model shape function to the lidar-measured data and minimizes the mean-squared error over time in a statistical sense, it provides convenient estimates. The filter thus makes the most from the high temporal resolution of curve-fitting geometrical models and the physically significant estimates output by statistical methods.

In the concept-design implementation of the filter presented here multi-layer scenes are not considered. In contrast, the paper focus on the impact that noise has on the filter estimates, particularly, for different SNR scenarios.

This Chapter is organized as follows: Section 5.2 formulates the non-linear adaptive estimator based on Kalman filter theory with which ABL parameters can sensibly be estimated. Section 5.3 presents the results of applying the EKF approach to experimental lidar backscatter data under two different SNR scenarios (high- and low- SNR). Results are also compared with well-known classical ABL detection methods in the literature. Finally, concluding results are presented in Section 5.4.

5.2 ABL adaptive detection method

An EKF is applied to adaptively fit an erf-like function modeling the EZ lidar-signal transition curve to the range-corrected lidar measurements. The erf curve-fitting method [*Steyn et al.*, 1999] is chosen because it is a robust approach which involves the bulk of the lidar profile. Later studies have been given by *Hägeli et al.* [2000] and *Mok and Rudowicz* [2004] mostly on the CBL.

Application of the EKF to the field of lidar signal processing to estimate the atmospheric optical parameters departs from previous works from *Rocadenbosch et al.* [1998a, 1999]. On the other hand, *Mukherjee et al.* [2002] has applied a scalar Kalman filter to estimate the ABL height from sodar signals.

5.2.1 The Extended Kalman Filter approach

The discrete Kalman filter is an adaptive linear estimator inherited from control system theory that operates recursively using a state-space model formulation. The filter is based on two models: (*i*) The measurement model (Sect. 5.2.4), which relates the atmospheric state-vector unknowns (to be estimated) to the observation measurements (i.e., the range-corrected lidar backscatter signals), and (*ii*) the state-vector model (Sect. 5.2.4), which approximately describes the temporal projection of the unknowns and its associated statistics (Eq. 5.5). However poor this "a priori" information about the atmospheric state vector and its statistics may be, this information is of advantage to the filter in order to improve its estimates by combining the actual estimation with the statistical behavior from past estimates. In what follows "a priori" and "a posteriori" stands for "before" and "after" assimilating the information from the present measurement at discrete time t_k.

When, as is the case of Eq. 5.1, the measurement model is non-linear, a linearization is made around the state-vector trajectory, which is updated at each successive iteration of the filter once a new measurement $\mathbf{z}_k$ is assimilated in what is called the extended Kalman filter. Likewise, at each filter iteration, the state vector, $\mathbf{x}_k$, the estimated a priori and a posteriori error-covariance matrices, $\mathbf{P}_k^-$ and $\mathbf{P}_k$ respectively, and the Kalman gain, $\mathbf{K}_k$ are recursively updated (see e.g., *Brown and Hwang* [1997], and *Rocadenbosch et al.* [1999]). By the recursive procedure, the filter corrects its projection trajectory of the ABL atmospheric variables and improves its estimation of the ABL parameters via a new atmospheric state-vector $\hat{\mathbf{x}}_k$ being estimated. By means of this convenient adaptive behavior, tracking the state-vector components appears as a natural and desirable feature of the filter.

For a M-component state vector ($M = 4$ in the case of the ABL estimation model described in Sect. 5.2.4), the number of observation samples in the ABL transition (N) must obviously be $N \geq M$ for data sufficiency. In practice, a much larger number of samples - as it is always the case - conveys the extra benefit of enhanced robustness to noise (this is equivalent to an over-determined system of equations in classic algebra theory).

5.2.2 ABL Problem formulation

For moderate to clear-air atmospheres and lidar sounding ranges roughly below 3 km ($R \leq 3$[km]), the optical thickness, $\tau = \int_0^R [\alpha_{aer}(u) + \alpha_{mol}(u)]du$, can be considered low enough ($\tau < 1$) to disregard the effects of the atmospheric transmissivity term $T(R)$ in Eq. 5.1. Under these conditions usually found in practice, the range-corrected lidar signal, $U(R)$, is proportional to the total backscatter coefficient in Eq. 5.1,

$$U(R) \simeq K\beta(R), \tag{5.3}$$

with $\beta(R) = \beta_{aer}(R) + \beta_{mol}(R)$. As a result, $U(R)$ can be considered a surrogate for the total backscatter coefficient $\beta(R)$, which is representative of the average aerosol and molecular concentration of the atmospheric mixture aloft.

In Fig.5.1, the conceptual block diagram of the EKF is shown. Each block is being explained next.

The range-corrected lidar signal exhibits a transition curve from high concentrations inside the ABL to lower concentrations (molecular background level) as the height increases. The ABL transition model proposed here follows a similar formulation to that of *Steyn et al.* [1999] but for the total backscatter coefficient. The erf-like total backscatter-coefficient model (Fig.5.1) is formulated in terms of four characteristic parameters, R_{bl}, a, A, and c as

$$h(R; R_{bl}, a, A, c) = \frac{A}{2}\Big\{1 - \mathrm{erf}\Big[\frac{a}{\sqrt{2}}(R - R_{bl})\Big]\Big\} + c, \tag{5.4}$$

where R_{bl} is the range position that marks the instantaneous ABL height, defined as the inflection point where the function h changes from convex to concave (equivalently, the point where h has minimum gradient), a is a scaling factor related to the transition thickness, A is the total backscatter-coefficient transition amplitude (equivalently, the difference between the upper and lower asymptotical levels of h, or between the ML and FT backscatter-related values), and c is an offset term modeling the FT molecular-backscatter level. Equation 5.4 models an idealized convective boundary-layer profile consisting of a single transition structure between the ML and the FT within the range interval $[R_1, R_2]$ (Fig. 1.2b).

In Eq. 5.4 above, the key parameters of interest are R_{bl} and a for they are directly related to the measurements of the ML depth and to the EZ thickness [*Hägeli et al.*, 2000]. The instantaneous ML top is identified as the minimum-gradient model parameter, R_{bl} [*Flamant et al.*, 1997]. For an erf-based ABL transition its derivative is a Gaussian curve whose full-width half maximum, σ_{bl}, is related to a as $a^{-1} = \sqrt{2}\sigma_{bl}$ (Fig. 1.2). Following *Steyn et al.* [1999] the 95-to-5% falling transition thickness is $2.77a^{-1}$.

From the physical point of view, the variation of the local-transition scale factor a with time comes as a function of the variation of the EZ thickness (i.e., a varies as the local transitions caused by updrafts and downdrafts). The variability of the amplitude of the ML with respect to the molecular level (A in Eq. 5.19) is caused by the entrainments of aerosol structures as they cross the lidar beam and is dependent of the normalized backscatter values of these structures, their size, their advection velocity, and the time resolution of the lidar acquisition.

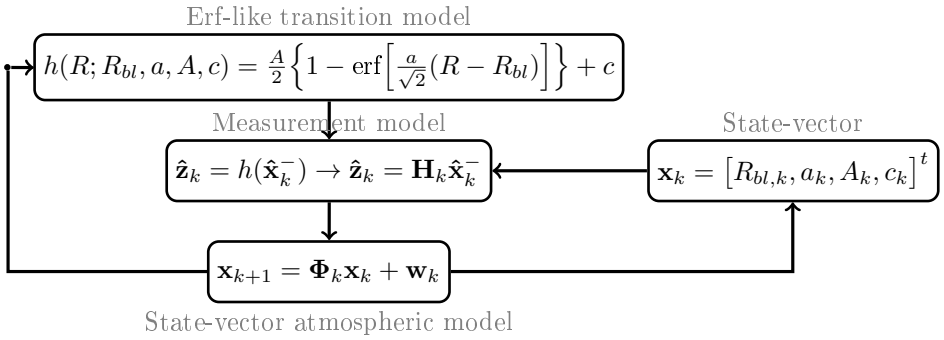

Figure 5.1: Conceptual block diagram of the Extended Kalman filter approach.

In the adaptive approach proposed next, the EKF filter considers the four characteristic parameters of the Eq. 5.4 model as time-variant stochastic processes forming the *state vector* to be estimated at each time t_k,

$$\mathbf{x}_k=\left[R_{bl,k},a_k,A_k,c_k\right]^t, \tag{5.5}$$

here given in transposed form (Fig.5.1).

The EKF observation vector, $\mathbf{z}_k$, is related to the state vector, $\mathbf{x}_k$, via the *measurement model*,

$$\mathbf{z}_k=h(\mathbf{x}_k)+\mathbf{v}_k, \tag{5.6}$$

where h is the ABL transition model of Eq. 5.4 and $\mathbf{v}_k$ is the observation noise at time t_k (including both lidar instrument noise and modeling errors) with associated noise covariance matrix $\mathbf{R}_k$ (*Brown and Hwang* [1997]). In Eq. 5.6 above, the observation vector $\mathbf{z}_k$ (i.e., the lidar measurements at each time t_k) is the measured noise-corrupted version of $h(R)$ in the range interval $[R_1,R_2]$ (Fig.5.1).

As mentioned in Sect. 5.2.2, under moderate-to-low optical thickness ($\tau<1$) the range-corrected lidar signal $U(R)$ is basically proportional to the total backscatter coefficient.

For better numerical conditioning and physical significance, the observation vector $\mathbf{z}_k$ presented to the filter is a molecular-normalized version of $U(R)$, $\mathbf{z}_k=U_n(R_k)$, as described in Sect. 5.2.3.

This is basically saying that $U_n(R)\simeq\beta_{mol}(R)+\beta_{aer}(R)$ in Eq.5.1, which is in accordance to Fig.1.2 (in $[R_1,R_1']$ $h(R)$ tends to $\beta_{mol}+\beta_{aer}$, in $[R_2',R_2]$ $h(R)$ tends to β_{mol}).

5.2.3 Normalization of the range-corrected lidar signal

The lidar signal of Eq. 5.1 can be written in expanded form as

$$U(R)=\begin{cases} K\left[\beta_{mol}(R)+\beta_{aer}(R)\right]e^{-2\int_0^R\left[\alpha_{aer}(u)+\alpha_{mol}(u)\right]du} & \text{if } R\leq R_0 \\ K'_{aer}\beta_{mol}(R)e^{-2\int_0^R\alpha_{mol}(u)du} & \text{if } R>R_0 \end{cases}. \tag{5.7}$$

where

$$K'_{aer}=Ke^{-2\int_0^{R_0}\alpha_{aer}(u)du} \tag{5.8}$$

and R_0 is the end of the ABL (equivalently, the starting range of the FT containing only molecules, R_2' in Fig. 1).

Because the lidar system constant K is undetermined in practice (or known with large errors) and the lidar signal is corrupted with different background offsets of natural and instruments origins, a molecular reference range (e.g., $[R_2^{'}, R_2]$ in Fig. 1.2) in the FT is used to calibrate the lidar signal [*Bösenberg and Hoff*, 2007; *Lange et al.*, 2012a].

In a molecular reference range, $\alpha_{mol}(R)$ and $\beta_{mol}(R)$, the molecular extinction and backscatter profiles, respectively, are known from a US-standard atmospheric and ground-level temperature and pressure conditions from radiosounding data.

Because the ABL transition model of Eq. 5.4 (Fig. 1.2) is formulated in terms of the total backscatter coefficient, $\beta(R)$, a normalization factor for (Eq. 5.7) must be derived.

Assuming a ground-based backscatter lidar and considering as molecular reference range the region $R > R_2'$ in Fig.1.2, Eq. 5.7 fits $\beta_{mol}(R)$ when Eq. 5.7 is multiplied by a scaling factor

$$\zeta = \frac{1}{K'_{aer}} e^{2\int_0^R \alpha_{mol}(u)du} \tag{5.9}$$

.

This yields the sought-after molecular-normalized version of $U(R)$, $U_n(R)$. In expanded form

$$U_n(R) = \begin{cases} [\beta_{mol}(R) + \beta_{aer}(R)] e^{2\int_R^{R_0} \alpha_{aer}(u)du} & R \leq R_0 \\ \beta_{mol}(R) & R > R_0 \end{cases} . \tag{5.10}$$

At this point it is interesting to see that for $R < R_0$ and assuming low optical thickness ($e^{2\int_R^{R_0}} \simeq 1$),

$$U_n(R) \simeq \begin{cases} \beta_{mol}(R) + \beta_{aer}(R) & R \leq R_0 \\ \beta_{mol}(R) & R > R_0 \end{cases} , \tag{5.11}$$

which is in accordance to the model of Eq. 5.4 and Fig. 1.2.

The observation vector, $\mathbf{z_k}$, is computed from the measured lidar signals at each time t_k as

$$\mathbf{z}_k = \zeta Z_k(R), \tag{5.12}$$

where $Z_k(R) = U_k(R) + \mathbf{v}_k(R)$ is the discrete range-corrected measured lidar signal at time t_k, with $U_k(R)$ being the noiseless range-corrected backscatter power of Eq. 5.1, and $\mathbf{v}_k$ is the additive range-corrected instrumental noise.

5.2.4 Filter Models

Measurement model.- In the EKF approach, at each successive time t_k, the filter compares the actual observable $\mathbf{z_k}$ formed from the measured normalized lidar signal (Eq. 5.12) with a linearized version of the observation model, $\mathbf{H}_k$. The latter is based on the partial derivatives of the measurement model function $h(R)$ (Eq. 5.4) evaluated at the "a priori" estimate of the state vector, $\hat{\mathbf{x}}_k^-$,

$$\hat{\mathbf{z}}_k = h(\hat{\mathbf{x}}_k^-) \rightarrow \hat{\mathbf{z}}_k = \mathbf{H}_k \hat{\mathbf{x}}_k^-, \tag{5.13}$$

where $\hat{\mathbf{z}}_k$ is the estimated observation vector, in turn, used to update the estimation of the state-vector $\hat{\mathbf{x}}_k$,

$$\hat{\mathbf{x}}_k = \hat{\mathbf{x}}_k^- + \mathbf{K}_k(\mathbf{z}_k - \hat{\mathbf{z}}_k) = \hat{\mathbf{x}}_k^- + \mathbf{K}_k(\mathbf{z}_k - \mathbf{H}_k\hat{\mathbf{x}}_k^-) \tag{5.14}$$

In Eq. 5.14 above K_k is the so-called Kalman filter gain or "projection" gain. The standard Kalman filter recursive loop can be found in e.g., *Rocadenbosch et al.* [1998a].

The measurement matrix is formulated as

$$\mathbf{H}_k(R;\mathbf{x}) = \left[\frac{\delta h(R)}{\delta R_{bl}}\ \frac{\delta h(R)}{\delta a}\ \frac{\delta h(R)}{\delta A}\ \frac{\delta h(R)}{\delta c}\right]\Bigg|_{\mathbf{x}=\hat{\mathbf{x}}_\mathbf{k}^-} = \Big[\mathbf{H}_k^1\ \mathbf{H}_k^2\ \mathbf{H}_k^3\ \mathbf{H}_k^4\Big]_{N\times 4}, \tag{5.15}$$

where

$$\mathbf{H}_k^1(a,R_{bl}) = \frac{\delta h(R)}{\delta R_{bl}} = \frac{Aa}{\sqrt{2\pi}}\exp\Big[-\frac{a^2}{2}(R-R_{bl})^2\Big],\ R\in[R_1',R_2'], \tag{5.16}$$

$$\mathbf{H}_k^2(a,R_{bl}) = \frac{\delta h(R)}{\delta a} = -\frac{A}{\sqrt{2\pi}}(R-R_{bl})\exp\Big[-\frac{a^2}{2}(R-R_{bl})^2\Big],\ R\in[R_1',R_2'], \tag{5.17}$$

and

$$\mathbf{H}_k^3(A,c) = \frac{\delta h(R)}{\delta A} = \frac{1}{2} - \frac{1}{2}\mathrm{erf}\Big[\frac{a}{\sqrt{2}}(R-R_{bl})\Big],\ R\in[R_1,R_1')\cup(R_2',R_2], \tag{5.18}$$

$$\mathbf{H}_k^4(A,c) = 1,\ R\in[R_1,R_1')\cup(R_2',R_2]. \tag{5.19}$$

Range intervals $[R_1', R_2']$ and $[R_1, R_1') \cup (R_2', R_2]$ respectively define the measurement-model fitting ranges inside and outside the ABL transition (Fig. 1.2). Variables into brackets $[(a, R_{bl})$ in Eqs.(5.16-5.17) and (A, c) in Eqs.(5.18-5.19)] indicate the estimation variables in each range interval. $\mathbf{H}_k^i, i = 1...4$ are $N \times 1$ vectors with N being the number of measurement samples in the measurement vector, $\mathbf{z}_k$. R is in continuous form for better clarity though in practice it is discretized as $R_i = R_{min} + (i-1)\Delta R;\ i = 1\dots N$, with R_{min} the minimum sounding inversion range and ΔR the raw-data spatial resolution.

The observation noise is modeled by its covariance matrix, $\mathbf{R}_k$, assuming white Gaussian additive noise with range-dependent variance $\sigma_n^2(R)$. Because the observations $\mathbf{z}_k$ are the range-corrected lidar returns (Eq. 5.12), or equivalently, Eq. 5.1, the noise covariance matrix takes the form,

$$\mathbf{R}_k = \begin{bmatrix} \sigma_n^2(R_1)R_1^4 & 0 & \dots & 0 \\ 0 & \ddots & & \vdots \\ \vdots & & \sigma_n^2(R_{N-1})R_{N-1}^4 & 0 \\ 0 & \dots & 0 & \sigma_n^2(R_N)R_N^4 \end{bmatrix}_{N\times N} \tag{5.20}$$

with $\sigma_n^2(R)$ the range-dependent noise estimate from the normalized measurements $\mathbf{z_k}$. Noise variance estimation can be carried out using, for example, piece-wise or parametric signal-to-noise ratio estimators [*Reba et al.*, 2006, 2007]. The noise model variance follows the well-known model described in *Rocadenbosch et al.* [1998a].

State-vector model.- The Kalman filter state-vector model is described by means of the recursive

discrete equation

$$\mathbf{x}_{k+1} = \mathbf{\Phi}_k \mathbf{x}_k + \mathbf{w}_k \,, \tag{5.21}$$

where $\mathbf{\Phi}_k$ is the transition matrix (4×4) from time t_k to time t_{k+1}, and $\mathbf{w_k}$ is the state-noise vector with covariance matrix $\mathbf{Q}_k$, which models the statistics of the state vector $\mathbf{x}_k$. The vector $\mathbf{w_k}$ is a zero-mean white Gaussian noise sequence that can be seen as the "driving" noise animating the state-vector dynamics. The model is initialized with a user input, $\hat{\mathbf{x}}_0^-$, describing the approximate initial value of the atmospheric state-vector (to be estimated), $\mathbf{x}_k$, along with the initial "a priori" error-covariance matrix $\mathbf{P_0^-}$ determining the user uncertainty on the initial estimation with respect to the actual (unknown) atmospheric initial state vector, $\mathbf{x_0}$.

The ABL physical variables describing the four state vector components in Eq. 5.5 are slowly varying with time and nearly constant over relatively large time scales (e.g., minutes to hours). Following *Rocadenbosch et al.* [1998a] and *Rocadenbosch et al.* [1999], a simple model representing this situation is the random walk [*Brown and Hwang*, 1997], which is characterized by a 4×4 transition matrix $\mathbf{\Phi}_k = \mathbb{1}$ in Eq. 5.21 above. This enables $R_{bl,k}$, a_k, A_k, and c_k to evolve with time as random-walk independent processes. As a result, the state-vector covariance matrix $\mathbf{Q}_k$ takes the diagonal form,

$$\mathbf{Q}_k = \begin{bmatrix} \sigma^2_{R_{bl}} & 0 & 0 & 0 \\ 0 & \sigma^2_a & 0 & 0 \\ 0 & 0 & \sigma^2_A & 0 \\ 0 & 0 & 0 & \sigma^2_c \end{bmatrix}, \tag{5.22}$$

where principal-diagonal terms are the user-proposed variances for each state-vector component describing approximate 1σ fluctuations. Though these variances are related to underlying physical processes (see text following Eq. 5.4), the simulation experiments carried out in *Lange et al.* [2013] show that even roughly relatively adjusted values are enough to enable reasonably good filter convergence.

5.2.5 Non-linear least-squares approach

The erf-curve parametric fitting problem described in Section 5.2.2 can also be tackled from NLSQ estimation [*Moré*, 1978] in which $R_{bl,k}$, a_k, A_k, and c_k are the ABL parameters to be estimated given a set of lidar measurements, $\mathbf{z}_k$. The NLSQ solution is found by minimizing the quadratic norm of the error function between the actual measurement $\mathbf{z_k}$ and the ABL model function $h(\hat{\mathbf{x}}_k^{LSQ})$

$$\epsilon(\mathbf{x}_k^{LSQ}) = \mathbf{z}_k - h(\hat{\mathbf{x}}_k^{LSQ}), \tag{5.23}$$

with respect to the state-vector variables, $\mathbf{x_k}$. That is,

$$\min\{\| \epsilon(\mathbf{x}_k^{LSQ}) \|^2\}|_{\mathbf{x_k}=[\mathbf{R_{bl,k}},\mathbf{a_k},\mathbf{A_k},\mathbf{c_k}]}. \tag{5.24}$$

Because the NLSQ is applied to each lidar measurement profile independently, a new estimation is carried out at each successive lidar return (non-memory estimation).

In comparison with the EKF adaptive behavior discussed in Sect. 5.2.1, it can be shown that

for $SNR \to \infty$ (i.e., with ideal noiseless measurements, $\mathbf{R}_k = 0$) or under no "a priori" knowledge of the state-vector statistics (i.e., $\mathbf{P}_0^- \to \infty$) the Kalman gain reduces to just the inverse of the observation matrix ($\mathbf{K}_k = \mathbf{H}_k^{-1}$, the so-called pseudo-inverse matrix) and hence, the EKF solution converges to the NLSQ solution. Under these conditions the deterministic NLSQ and the EKF yield the same solution for $\mathbf{x_k}$, which only depends on the measurement observables, $\mathbf{z}_k$ [*Brown and Hwang*, 1997; *Rocadenbosch et al.*, 1998a]. Similarly to the NLSQ, the annealing iterative search algorithm is also reported in the literature [*Steyn et al.*, 1999].

5.3 Experimental Results

In this section, two different scenarios (high- and low-SNR) have been analyzed in order to cross-examine EKF and NLSQ estimators against three of the most common classes of methods used to trace the ABL height. Measurements took place in the RSLab lidar laboratory (Sect. 1.2.1) on Dec. 16, 2010. The RSLab lidar characteristics are explained in Sect. 1.2.1. The measurements presented next correspond to NIR and UV elastic channels at 1064-nm and 355-nm wavelengths, respectively. In spite of the higher spectral scattering towards the UV, the emission energy at 355 nm is much lower than in the NIR (35 mJ and 160 mJ, respectively) UV and NIR channels are representative of low- and high-SNR cases, respectively [*Kumar et al.*, 2012].

The measurement chosen is an night measurement, 12 min long and 2.5 s temporal resolution. The lidar sounding LOS has been set along a slant-path (θ=52 deg. elevation), hence allowing a starting range of full overlap at a lower height (500 m) than with a vertically pointing lidar system. In turn, this permits to have more measurement samples in the range interval $[R_1, R_1']$ (Fig. 1.2, Table 5.1) where the average ML height is to be estimated. The slant arrangement assumes that the ABL is horizontally invariant along the sounding height, typically, 3-4 km. The slant-path range resolution is 3.75 m, which corresponds to a vertical resolution of 2.3 m. The EKF retrieved local ABL parameters to be presented next are given by the evolution of the local ABL top as $h_{ABL}(t_k) = R_{bl,k} sin\theta + 115$ m (ASL) and the ABL local transition thickness as $2.77a_k^{-1}$ (R is along range, h stands for vertical height).

The NLSQ estimator operates in the range interval $R = [R_1, R_2]$ while the EKF operates in the inner interval $R = [R_1', R_2']$ and in the outer intervals $[R_1, R_1']$ and $[R_2, R_2']$ (Eqs. 5.16-5.19). The ratio between the lengths of the inner and full-range intervals is usually set between 0.6 and 0.8.

The classical methods studied are the THM, derivative method, and VCM (Sect. 2.5). A comparison between these methods (except THM), can be found in Fig. 2.8.

Range smoothing and time averaging are enough to ensure sufficient SNR ($\geq$10) in the applicability of the classical methods compared in Fig. 2.8 though, they often give biased results and a reduced resolution [*Sicard et al.*, 2006; *Martucci et al.*, 2003]. As a common trait, almost all methods lack in some degree the requirements to operate in an unattended, real-time basis to monitor the ABL. Whereas statistical methods like the VCM cannot follow the fast time scales of the lidar profiles, non-adaptive geometrical methods do not have the capability to assimilate past ABL estimates to enhance their ABL estimates with time.

Table 5.1: EKF and NLSQ parameters

Initial ABL state-vector parameters

Parameter	Symbol	High-SNR	Low-SNR
Boundary-layer height	R_{bl}	0.79 km	0.79 km
EZ scaling factor	a	5.0 km^{-1}	3.0 km^{-1}
Backscatter-coefficient transition amplitude	$A' = \frac{A}{\beta_{mol}}$	0.5	5.0
Molecular-backscatter background	$c' = \frac{c}{\beta_{mol}}$	0.1	1.5

Observation range parameters (both high- and low-SNR)

Parameter	Symbol	Value
Initial observation range	R_1	0.58 km
Final observation range	R_2	1.16 km
Initial erf-like transition	R'_1	0.64 km
Final erf-like transition	R'_2	1.10 km
Erf-transition width	$R'_2 - R'_1$	0.46 km

5.3.1 High-SNR case study

In Fig. 5.2 it can be seen that under high-SNR conditions (typically $SNR \geq 10$ at the maximum sounding range [*Kumar et al.*, 2012]), the classical methods described at the beginning of this section, NLSQ and EKF estimators yield almost the same results. This is because long-time averages and range-smoothing techniques are applied to the range-corrected lidar signal, as explained in Sect. 5.3 above.

In this specific study case, a moving-average smoothing window for the derivative and VCM (Table 5.2 for smoothing parameters) has been used to avoid excessive false detection. In the THM, the threshold has been set as the mean value of the averaged-low and averaged-high levels for each time profile in the range intervals $[R_1, R'_1]$ and $[R_2, R'_2]$, respectively.

The initial parameters used to track the boundary layer height with the EKF and NLSQ methods are summarized in Table 5.1. The initial amplitude of the ML and FT has been estimated from the range-corrected lidar signal as the mean aerosol- plus molecular- backscatter ($\beta_{aer} + \beta_{mol}$) in $[R'_1, R_1]$ and the mean molecular-backscatter (β_{mol}) in $[R'_2, R_2]$, respectively (Fig.1.2).

From Fig. 5.2 and considering only the classical methods, the most accurate method is the GM. This is because the GM seeks the absolute minimum of the first derivative. This minimum can easily be identified thanks to a strong transition in the range-corrected lidar signal ($V_{ML} - V_{FT} = 2.5$ V km^2, Table 5.2), and because noise and atmospheric variability is reduced by time averaging and range-smoothing.

The THM also yields accurate estimation of the ABL height. Several discontinuities and large gradients between neighbor profiles can be observed due to noise contamination. The IPM yields an accurate estimation because the SNR of the signal is high and the residual noise is minimized by means of time and range averaging. However, some discontinuities can be observed due to variability of the atmosphere or power drop-outs.

On the other hand, the LGM method (not shown in Fig. 5.2) gives the worst estimation because noise is amplified when computing the derivative of the logarithm. The VCM needs higher time

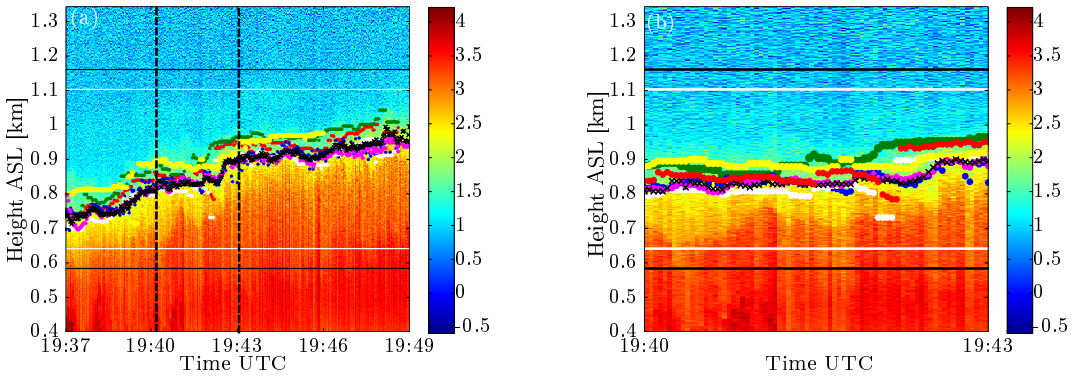

Figure 5.2: High-SNR case, ABL sunset (Barcelona UPC, Campus Nord, December 16, 2010). (*a*) Time-height plot of the range-corrected lidar signal for the 1064-nm channel. ABL height retrieval by the following methods: (red dots) GM, (green dots) LGM, (blue dots) THM, (white dots) IPM, (yellow dots) VCM, (black crosses) NLSQ estimator, and (magenta dots) EKF estimator. Lower and upper black lines represent R_1 and R_2 respectively, and lower and upper white lines represent R'_1 and R'_2. (*b*) Detail in the time interval 19:40 to 19:43.

Table 5.2: Classical-method parameters used for for high- and low-SNR case studies (units [V km^2] refer to the range corrected signal, $U(R)$)

Parameter	Symbol	High-SNR	Low-SNR
Initial observation range	R_1	0.58 km	0.58 km
Final observation range	R_2	1.16 km	1.06 km
1^{st} derivative temporal smoothing	$\Delta t_{1^{st}}$	25 s	50 s
2^{nd} derivative temporal smoothing	$\Delta t_{2^{nd}}$	25 s	50 s
VCM temporal smoothing	Δt_{VCM}	190 s	190 s
1^{st} derivative range smoothing	$\Delta R_{1^{st}}$	80 m	92 m
2^{nd} derivative range smoothing	$\Delta R_{2^{nd}}$	80 m	92 m
VCM range smoothing	ΔR_{VCM}	103 m	126 m
THM threshold level	THM	2.0 $V \cdot km^2$	1.6 $V \cdot km^2$
V_{ML} relative amplitude	ML	3.3 $V \cdot km^2$	1.9 $V \cdot km^2$
V_{FT} relative amplitude	FT	0.8 $V \cdot km^2$	1.4 $V \cdot km^2$

and range averages due to noise and shear-induced turbulence, its performance being comparable to the LGM (this effect can also be observed in Fig. 2.8).

It should be noted that because of the temporal window length required to compute the time averaging, all classical methods except the VCM can estimate the ABL height only up to the end of the time series minus $\Delta t_{1^{st}}$ or $\Delta t_{2^{st}}$, Δt_{VCM} in the case of VCM.

Regarding the NLSQ and the EKF, estimation runs until the end of the time series because no time or range smoothing is necessary. Both methods give nearly identical results. There is only a difference at the beginning of the time series because the ABL height parameter R_{bl} was initialized with a considerably higher value than the real height just to show the robustness of the method under wrong parameters.

5.3.2 Low-SNR case study

The low-SNR case illustrate the robustness ($SNR \backsimeq 1$ at the maximum sounding range [*Kumar et al.*, 2012]) of EKF as compared to all other methods presented so far (Fig. 5.3). Even using time averaging and range smoothing classic methods cannot estimate the ABL height in a proper way because time-averaging and range-smoothing techniques cannot sufficiently counteract noise.

In Fig. 5.3 the minimum of the first derivative of the signal (GM) or the logarithm of the signal (LGM), inflection point (IPM), or the local maximum of the variance profile (VCM) can hardly be obtained. Besides, the THM cannot follow the ABL height because there is not a single threshold level giving acceptable results that can be adjusted by trial and error. This is basically due to two factors: One is that first and second derivatives of the range-corrected lidar signal largely amplify the noise component. Another is that because of the higher molecular scattering in the UV, there is less aerosol content and hence, a much lower difference between the relative amplitudes of the ML and FT (Fig. 1.2).

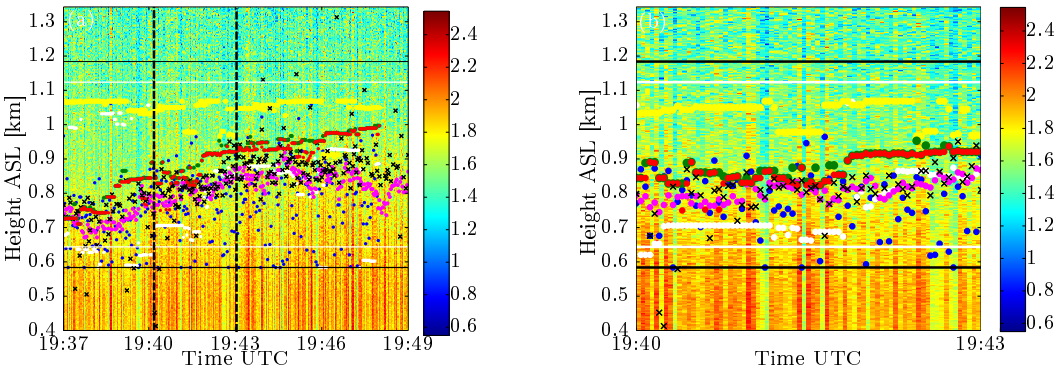

Figure 5.3: Low-SNR case ABL sunset case (Barcelona UPC, Campus Nord, December 16, 2010). (*a*) Time-height plot of the range-corrected lidar signal for the 355-nm channel. ABL height retrieval by the following methods: (red dots) GM, (green dots) LGM, (blue dots) THM, (white dots) IPM, (yellow dots) VCM, (black crosses) NLSQ estimator, and (magenta dots) EKF estimator. Lower and upper black lines represent R_1 and R_2 respectively, and lower and upper white lines represent R'_1 and R'_2. (*b*) Detail in the time interval 19:40 to 19:43.

Despite this fact, the GM and the LGM offer the best performance among all classical methods.

The IPM fails in its estimation because noise is highly amplified when computing the second derivative and, therefore the inflection point is mistaken jumping between peaks far from the ML top (e.g., 19:38:00 to 19:39:00 in Fig. 5.3). The VCM performs poorly almost all the time.

Comparing the NLSQ and the EKF, it can be seen that the NLSQ follows the ABL height but exhibiting a much lower performance than for the high-SNR case. The NLSQ rambles between time-adjacent profiles in such a way the ABL height estimates become time discontinuous. On the other hand, the EKF follows the ABL height fairly consistently in instances where all other methods evidence limitations. Thus, the EKF exhibits higher temporal and spatial resolution because in order to obtain consistent time-continuous estimates the GM and the LGM require temporal and spatial smoothing as evidenced by piece-wise discontinuous estimates in Fig.5.3 (e.g., time intervals, 19:37 to 19:38 in Fig.5.3a or 19:40 to 19:41 in Fig.5.3b). In addition, the GM and the LGM, when compared to the EKF, overestimate the ABL height with estimates starting to fall in the FT zone (Fig.5.3b).

5.4 Conclusions

It has been shown that in a scenario with a well-mixed layer, without stratifications, and under high-SNR conditions both classical and adaptive methods perform reasonably well without unambiguous results (Fig. 5.2). On the other hand, under low-SNR scenarios ambiguities arise among these methods (Fig. 5.3). EKF approach emerges as the most suitable method to track the temporal evolution of the ABL height. NLSQ yields time-discontinuous ABL estimates that do not take benefit from past estimates and that fail to perform a "true" time tracking of the ABL height.

Thus, in low-SNRs, derivative methods such as GM and LGM perform reasonably well only if the lidar signal is averaged in time and smoothed in range before these methods are applied. Even in these conditions, the IPM performs poorly because first and second derivatives of the range-corrected lidar signal largely amplify measurement noise. The TM, which shares with the derivative methods using a geometrical approach also performs poorly because it is very difficult to set a physically consistent threshold to estimate the ABL height in the erf-like zone, besides, there is not a unique solution. In all these methods, if the difference between ML and FT average levels is small (as is usually the case in the UV), or if the lidar signal is too noisy, false peaks lead to mis-estimation of the ABL height.

The VCM uses a statistical approach that requires a large number of profiles to compute a statistically significant variance (Sect. 2.5). In low-SNR conditions the VCM is often misled due to noise fluctuations or shear-induced turbulence.

The EKF approach presented is based on estimating four time-adaptive coefficients (Sect. 5.2) of an oversimplified erf-like curve model representing the ABL transition. Furthermore, the filter is able to combine previous estimates in order to improve the actual one, which permits to work with low-SNR atmospheric scenes without excessively losing the temporal resolution of the lidar instrument by a long pulse averaging. This issue clearly outperforms the NLSQ estimates. These capabilities allow the EKF to avoid sudden changes or drop-outs in the estimates of consecutive profiles, as it happens with the NLSQ.

EKF and NLSQ methods perform better than the classical methods so far presented specially under low-SNR conditions. Under high-SNR conditions both estimators reduce to the same solution, as it can be shown theoretically that the EKF converges to the NLSQ for SNR$\rightarrow \infty$ (Sect. 5.2.5).

Simulation tests in *Lange et al.* [2013] have shown that the ABLH, R_{bl}, and the transition amplitude, A, are the easiest parameters to estimate (higher sensitivity) while the EZ-scaling parameter, a, and the molecular-background parameter, c, are the least sensitive ones in Eq.5.4.

Chapter 6

ABLH estimation using a Kalman filter and a FMCW radar

An adaptive solution based on the EKF is proposed to estimate the ABLH from FMCW S-band clear-air radar returns. The EKF estimator departs from previous results in the lidar field presented in Chapter 5), in which the ML – FT transition interface is modeled by means of an erf-like parametric function and which is now applied to the radar case.
The method has successfully been implemented in clear-air, single-layer, convective boundary layer conditions. ABLH estimates from the proposed radar-EKF method have been cross-examined with those from a collocated lidar ceilometer yielding a correlation coefficient as high as $\rho = 0.93$ *(mean SNR=18, at the ABLH) and in relation to the classic threshold method.*

6.1 Introduction

In contrast to lidar remote sensing where aerosols give strong backscatter returns over the whole ML, clear-air radar reflectivity returns (refractive turbulence or Bragg's scattering) only shows strong returns on the ML-FT interface. Besides, they are corrupted by "insect" noise (impulsive noise associated to insects and birds Rayleigh's scattering), all of which requires a specific treatment of the problem and the measurement noise for the clear-air radar case. The proposed radar-ABLH estimation method uses: (*i*) a first pre-processing of the reflectivity returns based on median filtering and threshold-limited decision to come up with a clean reflectivity signal, (*ii*) a modified EKF with adaptive range intervals as time tracking estimator, and (*iii*) ad-hoc modeling of the observation noise covariance.

There are at least two differential elements worth mentioning as compared to Chapter 5 [*Lange et al.*, 2013], in which the EKF is applied to backscatter lidar returns:

First is the application of the EKF to the radar case itself. While in the lidar case, and under similar single-layer convective boundary layer conditions, the ML–FT transition interface was well modeled by means of an erf-like function, in the radar case, these atmospheric regions as well as the EZ in between are largely distorted by a huge number of noise peaks due to insect-and-birds echoes (Fig. 6.1a and Fig. 6.2) [*Contreras and Frasier*, 2008; *Vaughn*, 1985]. As a result, traditional ABLH derivative methods, for which noise peaks are largely amplified by the derivative operator, are insufficient to deal with raw radar returns. Second is the elimination of interfering Rayleigh noise component (birds and insects), which involves a specific pre-processing for the radar case and appropriate modeling of the residual noise as observation-noise to the filter.

This Chapter is organized as follows: Sect. 6.2 develops the pre-processing steps used to remove the contribution of "noisy" Rayleigh scatters (insects and birds). Sect. 6.3 expands the EKF adaptive ABLH detection method to the radar case departing from the RSLAB works in Chapter. 5 and *Lange et al.* [2013]. Sect. 6.4 establish the necessary observation noise treatment in the radar case. Sect. 6.5 illustrates a real-case 1.5-h tracking scene where the radar EKF estimates are cross-examined with those from a lidar ceilometer as ground truth. Finally, Sect. 6.6 gives concluding remarks.

6.2 Radar reflectivity pre-processing

The pre-processing steps explained next are aimed at outputting "clean" time-height profiles of the radar reflectivity (Eq. 2.40 and Eq. 2.43) as the key data product for ABLH estimation (Fig. 6.1). When looking at a profile of the measured reflectivity (Fig. 6.2) it can be though as the superposition of two components: (*i*) the signal component or noiseless atmospheric-reflectivity profile, which is due to Bragg scattering and whose shape is to permit to estimate the ABLH (Sect. 6.3), and (*ii*) the observation-noise component corrupting the measured reflectivity profile. In turn, there are two main types of noise contributing to the observation noise: the *instrumental noise* of the radar itself and *impulsive noise* due to insects. The first is of thermal origin and arises as a *Gaussian-equivalent noise component* superimposed to the reflectivity profile (low-intensity random noise in Fig. 6.2). The second is a Rayleigh scattering interferent component due to insects that appears as high-intensity impulsive noise (blue peaks) in Fig. 6.2 and Fig. 6.1a.

The aim of the pre-processing stage is to remove insect's interference in the radar reflectivity measurement, so that the ABLH can be estimated from an almost "clean" Bragg scattering atmosphere (Fig. 6.1f). Towards this aim, the pre-processing methodology outlined in *Contreras and Frasier* [2008] is analytically formulated and implemented in signal-processing block-diagram form next.

The pre-processing block diagram is shown in Fig. 6.3 and the successive pre-processing steps are shown in Fig. 6.1, each panel (a-f) corresponding to one step. In Fig. 6.1a, the time-height measured reflectivity image, $\eta_{raw,1}$, is a $M \times N$ matrix consisting of M time profiles of N range samples each. The spatial resolution, ΔR, is 5 m/sample and the temporal resolution, Δt, 16 s/sample. Further measurement details are given in Sect. 6.5.

Impulsive noise due to insects can be virtually removed by using a 7×7-sample median filter

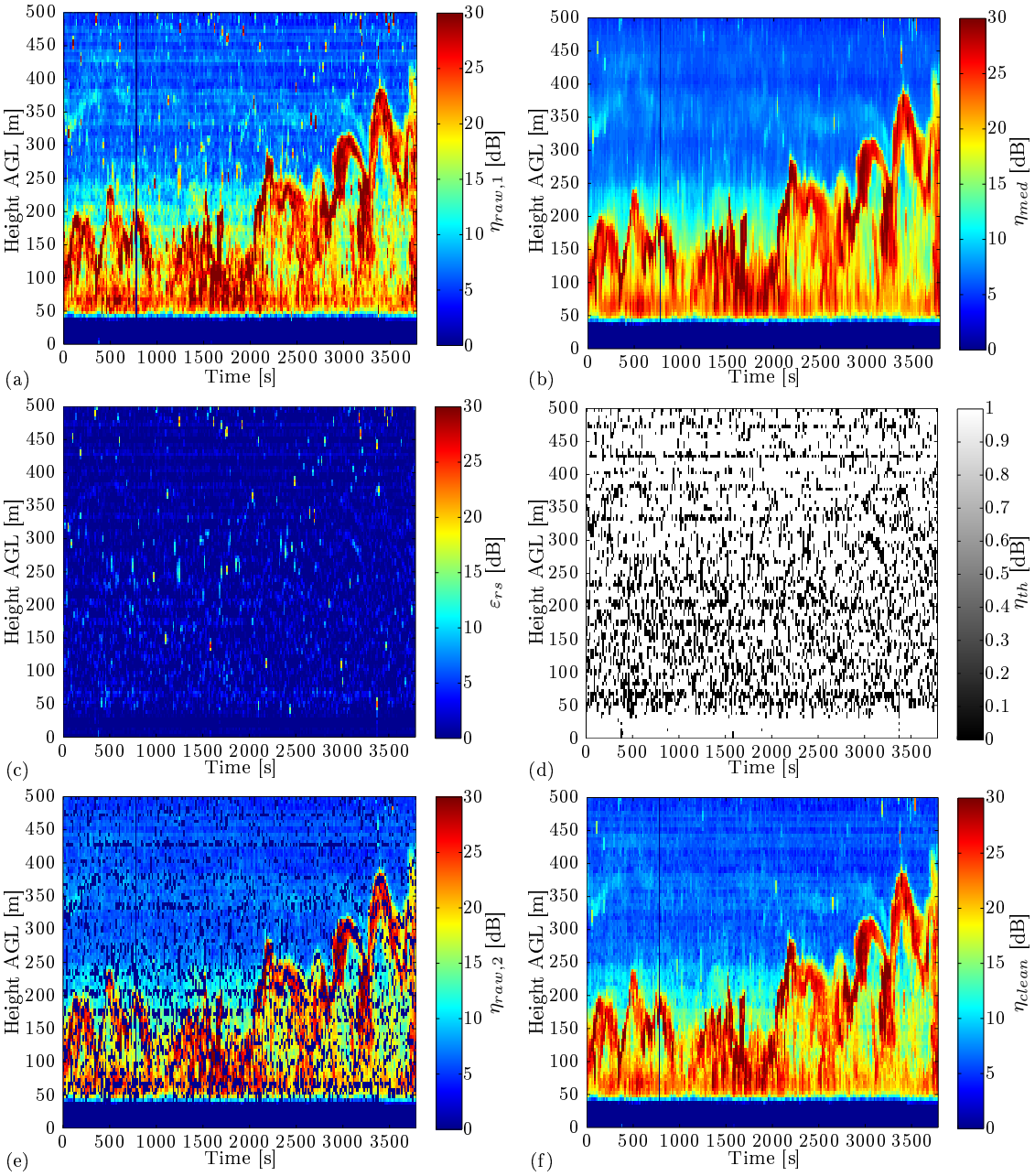

Figure 6.1: Radar reflectivity pre-processing case example (Boulder, CO., August 16, 2007, 14:41:36 UTC (08:41:36 LT) to 15:44:43 UTC, time records t_{100} to t_{335}). (*a*) Raw reflectivity image, $\eta_{raw,1}$. Isolated red dots visible from approximately 200–450 m in height correspond to "insect noise". Vertical line around 800 s is dead time where the radar is not measuring (data backup). (*b*) Median-filtered image, η_{med}, by using a 7×7-sample filter applied to (*a*). (*c*) Residual error, ε_{rs}, computed as image (*a*) minus image (*b*). (*d*) Black&white mask, η_{th}, referred to as "insect echo image", Eq. 6.2. The figure represents η_{th} in inverted black-and-white colour-map form, so that 1 ("insect") is coded as black and 0 ("no insect") is coded as white. (*e*) Bragg scattering image, $\eta_{raw,2}$, composed after masking (*a*) with mask (*d*), Eq. 6.3. Note that insects have been replaced by voids. (*f*) Clean reflectivity image, η_{clean}, composed by "filling" these voids in image (*e*) with the median-filtered values in (*b*).

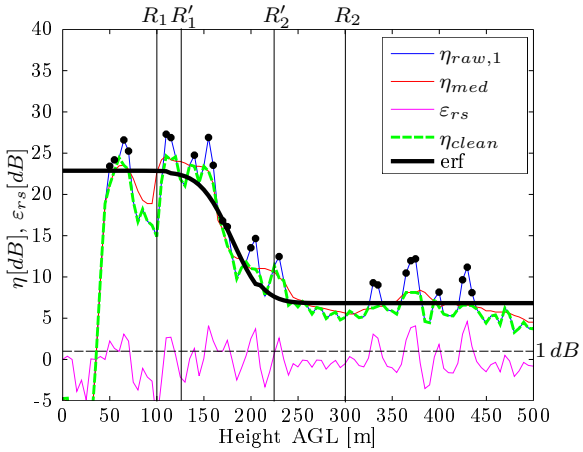

Figure 6.2: Radar reflectivity as a function of range (height AGL). Time profile, t_{120}=1917 s (14:46:58 UTC) in Fig. 6.1. (Blue) Raw reflectivity, $\eta^{120}_{raw,1}$ (compare with Fig. 6.1a). (Red) Median-filtered reflectivity, η^{120}_{med} (compare with Fig. 6.1b). (Magenta) Residual error, ε^{120}_{rs} (compare with Fig. 6.1c). (Horizontal dashed black line) 1-dB threshold level. Black dots superimposed to $\eta^{120}_{raw,1}$ indicate ranges where the residual error exceeds the 1-dB threshold of Eq. 6.2 and hence an "insect" or interfering Rayleigh scatterer is detected. (Dashed green) Clean reflectivity, η^{120}_{clean} (compare with Fig. 6.1f). (Thick black) Erf-like model profile fitted to the clean reflectivity, $\eta^{120}_{raw,1}$. R_1 and R_2 indicate initial and end data-processing ranges of the EKF, respectively, at time t_{120}. R'_1 and R'_2 indicate the approximate start and end ranges of the erf transition.

applied to the time-height radar reflectivity raw image, $\eta_{raw,1}$, of Fig. 6.1a (blue trace in Fig. 6.2). Though the optimum window size of the median filter depends on the density of insects, by experiment a 7×7-sample window yields the best trade-off between temporal/spatial resolution and impulse-noise cancellation [*Contreras and Frasier*, 2008]. The filter serves to remove isolated impulsive echoes that occupy less than half of window size. The resulting median-filtered image, η_{med} (Fig. 6.1b and red trace in Fig. 6.2), is subtracted from the original one to yield a *differential* image (Fig. 6.1c and magenta trace in Fig. 6.2),

$$\varepsilon_{rs} = \eta_{raw,1} - \eta_{med}. \tag{6.1}$$

According to *Contreras and Frasier* [2008], a 1-dB threshold level is applied to the differential image of Eq. 6.1 above. Pixels equal to or above this threshold are identified as "impulsive noise" (i.e., insect pixel) and hence they are reset to zero. Pixels below are assumed to be "signal component" (i.e., Bragg scattering) and are retained. Formally,

$$\eta_{th} = \begin{cases} 1 & \text{if } \varepsilon_{rs} \geq 1\,dB \\ 0 & \text{if } \varepsilon_{rs} < 1\,dB \end{cases} \tag{6.2}$$

The 1-dB threshold equals two standard deviations above the average echo power for an averaged profile of 100 samples and assumes a probability of false alarm (i.e., identifying a pixel as containing an insect when it does not) of less than 2.5% [*Contreras and Frasier*, 2008].

This filtered and thresholded image, η_{th}, is referred to as the "insect-echo" image. Because η_{th} is of Boolean type, it is represented as a black-and-white image in Fig. 6.1d (dots in Fig. 6.2). In Fig. 6.1d, η_{th} is represented by using an inverted black-and-white colour-map, that is, with 1 ("insect")

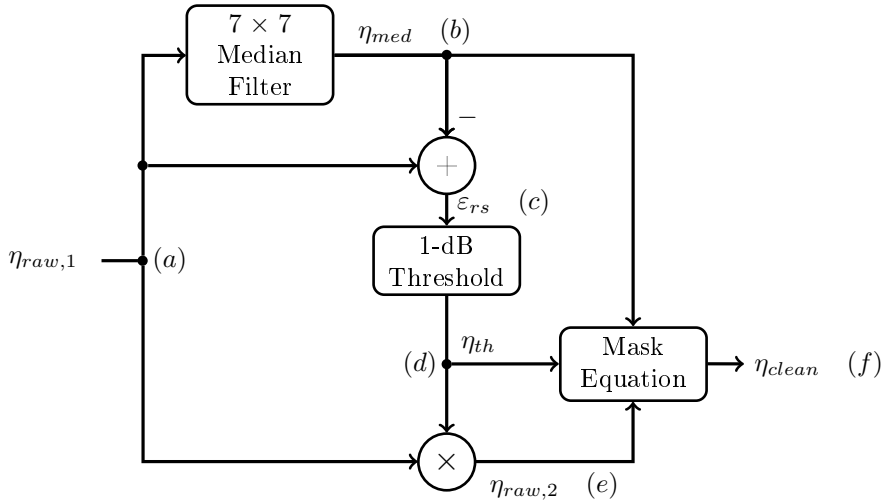

Figure 6.3: Radar reflectivity pre-processing block diagram. Letters in brackets refer to the different processing stages in Fig. 6.1 panel.

coded as black and 0 ("no insect") coded as white. By this means, this black-and-white figure can be better interpreted as a black-and-transparent mask that once visually superimposed to the raw reflectivity image, $\eta_{raw,1}$ of Fig. 6.1a, it enables to see the raw-reflectivity part of the image that is free from insects. Mathematically, when the mask η_{th} is applied to $\eta_{raw,1}$, the free-of-insects Bragg scattering image, $\eta_{raw,2}$, is obtained as

$$\eta_{raw,2} = \eta_{raw,1}\,\overline{\eta_{th}}. \tag{6.3}$$

The Bragg scattering image above is noted $\eta_{raw,2}$ because it is still a raw image with insects replaced by voids (zeroes). In Fig. 6.1e, these voids correspond to the above-1-dB-threshold pixels identified in Eq. 6.2.

The next step is to replace them with the median-filtered values of Fig. 6.1b, which are the interpolated values for the voids using the available data. Thus, the clean reflectivity signal (Fig. 6.1f) or equivalently, the green trace in Fig. 6.2, which is due only to Bragg scattering, is constructed as

$$\eta_{clean} = \eta_{raw,2} + \eta_{med}\,\eta_{th}. \tag{6.4}$$

If Eq. 6.3 is substituted into Eq. 6.4,

$$\eta_{clean} = \eta_{raw,1}\,\overline{\eta_{th}} + \eta_{med}\,\eta_{th}, \tag{6.5}$$

η_{th} can be seen as a binary digital selector (0/1) so that any pixel identified as "insect" ($\eta_{th} = 1$) is replaced by its corresponding median filtered one and any other pixel identified as "no-insect" ($\eta_{th} = 0$) retains the measured reflectivity, $\eta_{raw,1}$. The outcome of this pre-processing is that impulsive noise due to insects becomes smoothed out in the clean reflectivity image and without loss of the original spatial/temporal resolution of the measured data, $\eta_{raw,1}$, for those pixels not corrupted with insects (for corrupted pixels the image resolution is approximately degraded by a factor 7, the median-filter window size).

6.3 ABLH estimation using an EKF

After the pre-processing steps carried out in Sect. 6.2, the ABLH is now estimated from the clean reflectivity image, η_{clean} (Fig. 6.1f) using an Extended Kalman Filter. In what follows, η_{clean} will be noted η to simplify notation.

The formulation of the EKF is essentially the same as the one proposed in Chapter 5 [*Lange et al.*, 2013] for the lidar case with the exception that now backscatter lidar return measurements (the "observables" in Kalman Filter terminology) have been replaced by the radar reflectivity ones. Extension of the EKF to the FMCW-radar case is summarized next for completeness in the understanding of the present work. Noise modeling, as a key distinguishing feature of its application to the radar case, is discussed in Sect. 6.4.

The EKF is a recursive adaptive filter that uses a parameterization of the ABL – the so-called *state vector,* $\mathbf{x}_k$ – to estimate the ABLH and accessory ABL-related parameters at each succeeding discrete time, t_k. Besides, the filter uses two models: (i) the measurement model and (ii) the state-vector model.

Measurement model.- Following *Steyn et al.* [1999], the ML–FT interface is modeled by means of an erf-like function, which is parameterized as [*Lange et al.*, 2013]

$$h(R; R_{bl}, a, A, c) = \frac{A}{2}\left\{1 - erf\left[\frac{a}{\sqrt{2}}(R - R_{bl})\right]\right\} + c, \quad R \in [R_1, R_2]\,, \tag{6.6}$$

and where the state vector is defined by the column vector,

$$\mathbf{x}_k = [R_{bl,k}, a_k, A_k, c_k]^T\,, \tag{6.7}$$

with subscript k a reminder of discrete time t_k. In Eq. 6.7 above, R stands to the range (height), usually in the form of a N-sample discrete vector, $[R_1, R_2]$ is the inversion range, $R_{bl,k}$ stands for the ABLH at time t_k, a_k is a scaling factor related to the EZ-transition thickness $\left(2.77a^{-1}\right)$ at time t_k, A_k is the transition amplitude of the radar reflectivity profile (equivalently, the difference between ML and FT reflectivity values), and c_k is an offset term modeling the FT reflectivity level at the end of the inversion range. An example of this erf-like behavior is depicted in Fig. 6.2 (thick black trace).

Formally, the measurement model can be formulated as

$$\mathbf{z}_k = h(\mathbf{x}_k) + \mathbf{v}_k, \tag{6.8}$$

where $\mathbf{z}_k$ is the observation vector or noisy radar reflectivity, η_k (dB), h is the ABL transition model of Eq. 6.6, and $\mathbf{v}_k$ is the observation noise at time t_k. The latter merges into a single body both measurement noise and modeling errors by means of its associated noise covariance matrix $\mathbf{R}_k = E\left[\mathbf{v}_k\mathbf{v}_k^T\right]$ (see Sect. 6.4).

In the Kalman filter recursive cycle, the observation model of Eq. 6.8 is linearized around the "a priori" state-vector estimate, $\hat{\mathbf{x}}_k^-$ (i.e., prior to assimilate the present measurement at time t_k),

in the form of a $N \times 4$-Jacobian or "sensitivity" matrix [*Brown and Hwang*, 1997],

$$\mathbf{H}_k(R;\mathbf{x}) = \left[\frac{\delta h(R)}{\delta R_{bl}}, \frac{\delta h(R)}{\delta a}, \frac{\delta h(R)}{\delta A}, \frac{\delta h(R)}{\delta c}\right]\Bigg|_{\mathbf{x}=\hat{\mathbf{x}}_k^-}. \tag{6.9}$$

In Eq. 6.9 each column is the first-order derivative of Eq. 6.6 with respect to components 1-4 of the state vector, $\mathbf{x}_k$, and each row corresponds to a discrete range R_i, $i = 1..N$.

Because of the different slopes or sensitivities of the erf function in the range interval $[R_1, R_2]$, the first two derivatives ($\frac{\delta h(R)}{\delta R_{bl}}$ and $\frac{\delta h(R)}{\delta a}$) are computed in the inner range interval, $[R'_1, R'_2]$, where the idealized erf-transition structure occurs (see Fig. 6.2). The second two derivatives ($\frac{\delta h(R)}{\delta A}$ and $\frac{\delta h(R)}{\delta c}$) are computed in the outer range intervals, $[R_1, R'_1] \bigcup [R'_2, R_2]$, where the erf-model is nearly constant ("plateau" intervals). Selection of ranges R'_1 and R'_2 is not critical, the key requirement being that they must define inner and outer range intervals containing erf-transition and erf-plateau characteristics, respectively, as described above.

In the present implementation of the EKF, boundaries R'_1 and R'_2 are allowed to adaptively change with time. Though this is not a requirement, this is of computational advantage in instances where the ABLH, $R_{bl,k}$, may substantially change from its initialization value during the time frame under study or when the time frame to be tracked by the EKF is long (e.g., a 3–h time frame of the diurnal cycle). As example in the present implementation of the EKF, R'_1 and R'_2 (inner part of the erf-like model where the function is more abrupt), and R_1 and R_2 (outer part of the erf-like model, "plateau" ranges) change adaptively with the estimated ABLH, $R_{bl,k}$, but constrained to constant range interval widths, W_i, $i = 0..2$, which are preset from the user side (refer to Fig. 6.2),

$$R'_{2,k} - R'_{1,k} = W_0, \quad R'_{1,k} - R_{1,k} = W_1, \quad R_{2,k} - R'_{2,k} = W_2, \quad \forall k. \tag{6.10}$$

The recursive procedure to adaptively update the boundary ranges ensures that R'_1 and R'_2 are always centered around the estimated ABLH, $R_{bl,k}$, via the recursive step,

$$R'_{1,k+1} = R_{bl,k} - W_0/2, \quad R'_{2,k+1} = R_{bl,k} + W_0/2. \tag{6.11}$$

R_1 and R_2 are updated accordingly by using Eq. 6.10 above.

State-vector model.- This model formulates a random transition model for the state vector from time t_k to time t_{k+1} of the form,

$$\mathbf{x}_{k+1} = \mathbf{\Phi}_k \mathbf{x}_k + \mathbf{w}_k. \tag{6.12}$$

From Sect. 5.2.4, a Gauss-Markov random model with $\mathbf{\Phi}_k = I$, I the identity matrix, has been found a simple and convenient model. The state-vector model requires of three "a priori" information inputs to be provided by the user: (1) An initial guess of the state vector to be estimated, $\hat{\mathbf{x}}_0^-$, (2) an estimate of the atmospheric state-noise covariance matrix, $\mathbf{Q}_k = E\left[\mathbf{w}_k \mathbf{w}_k^T\right]$, and (3) an estimate of the initial "a priori" state-vector error covariance matrix, $\mathbf{P}_0^- = E\left[\mathbf{e}_0^- \mathbf{e}_0^{-T}\right]$, where $\mathbf{e}_0^- = \mathbf{x}_0 - \hat{\mathbf{x}}_0^-$ is the "a priori" error between the atmospheric state vector, $\mathbf{x}_0$ (unknown), and the initial guess, $\hat{\mathbf{x}}_0^-$. The state-noise covariance matrix is aimed at statistically modeling the atmospheric fluctuations or "nervousness" in the state-vector components, which formally should be formulated in terms of assumed variances and correlations among them [*Rocadenbosch et al.*, 1998b].

In the lidar case (Sect. 5.2.4), a diagonal matrix, $\mathbf{Q}_k = diag\left[\sigma^2_{R_{bl}}, \sigma^2_a, \sigma^2_A, \sigma^2_c\right]$, with standard deviations proportional to the state-vector initial guess $(\sigma_{R_{bl}}, \sigma_a, \sigma_A, \sigma_c) = \mu_Q\,(R_{bl,0}, a_0, A_0, c_0)$ via a factor μ_Q has been found to successfully express this concept in pretty simple form and, by experiment, to be a convenient extension of the lidar model to the radar case presented here. In short form,

$$\sigma_{\mathbf{Q}} = \mu_Q \hat{\mathbf{x}}_0^-, \quad \sigma_{\mathbf{Q}} = (\sigma_{R_{bl}}, \sigma_a, \sigma_A, \sigma_c)\,. \tag{6.13}$$

For example, if the ABLH at the filter start-up time, t_0, is initialized with $R_{bl,0} = 2000\ m$ and $\mu_{\mathbf{Q}} = 0.1$, this means, after Eq. 6.13, that 3-σ fluctuations in the ABLH are expected to be of roughly $\pm$600 m.

Also from Sect. 5.2.4 and by experiment in its extension to the radar case, the "a priori" state-vector error covariance matrix is also expressed in diagonal form, $\mathbf{P}_0^- = diag\left[\sigma^2_{e,R_{bl}}, \sigma^2_{e,a}, \sigma^2_{e,A}, \sigma^2_{e,c}\right]$, where $\sigma_{e,X}$ is the user's "a priori" error on the state-vector components, $X = R_{bl}, a, A, c$. Or, equivalently to Eq. 6.13, it can be formulated,

$$\sigma_{\mathbf{P}} = \mu_P \hat{\mathbf{x}}_0^-, \quad \sigma_{\mathbf{P}} = (\sigma_{e,R_{bl}}, \sigma_{e,a}, \sigma_{e,A}, \sigma_{e,c})\,, \tag{6.14}$$

where $\sigma_{\mathbf{P}}$ denotes $\sigma_{\mathbf{P_0^-}}$ and μ_P is the "a priori" state-vector covariance matrix factor.

At each successive iteration of the EKF, a new reflectivity measurement $\mathbf{z}_k$ is assimilated and (i) a new state vector $\hat{\mathbf{x}}_k$, (ii) a new "a posteriori" (i.e., after assimilating the current measurement from time t_k) error covariance matrix, $\mathbf{P}_k$, and (iii) a new Kalman gain, $\mathbf{K}_k$ (the "projection" gain) are estimated. With this information, the filter can correct its projection trajectory and enhance its current estimation of the state vector parameters, $\hat{\mathbf{x}}_k$ and, more specifically, of the ABLH.

6.4 Treatment of the observation noise

The noise covariance matrix $\mathbf{R}_k$ at a time t_k is defined as the covariance of the observation noise vector $\mathbf{v}_k$. This covariance matrix merges into a single body both measurement noise and modeling errors, and it is aimed at informing the filter on the quality of the measurement observables, $\mathbf{z}_k$, at each successive t_k. Formally,

$$\mathbf{R}_k = E[\mathbf{v}_k \mathbf{v}_k^T], \tag{6.15}$$

where $E[\ \ ]$ is the expectancy operator over the ensemble of noise realizations, and $\mathbf{v}_k$ is the N-component noise vector, i.e., associated to height ranges, R_i, $i = 1..N$.

Under the assumption of clean radar reflectivity measurements corrupted with white Gaussian additive noise, $\mathbf{R}_k$ takes the form of the diagonal matrix,
$R_k = diag[\sigma_n^2(R_1), \sigma_n^2(R_2), \ldots, \sigma_n^2(R_N)]\big|_{t=t_k}$, where each element along the diagonal is the noise variance, $\sigma_n^2(R_i)$, $i = 1..N$. A major difficulty impairing to estimate the noise covariance matrix at each successive time t_k is that only *one* single noise realization $\nu_k = [\nu\,(R_1)\,, \nu\,(R_2)\,, ..., \nu\,(R_N)]|_{t=t_k}$ is available at each measurement, not an ensemble of realizations from which to compute Eq. 6.15.

There is a way out if the ergodicity principle [*Barlow*, 1989] is assumed to compute the noise covariance statistics over uniformly spaced range intervals, which is equivalent to replacing the time

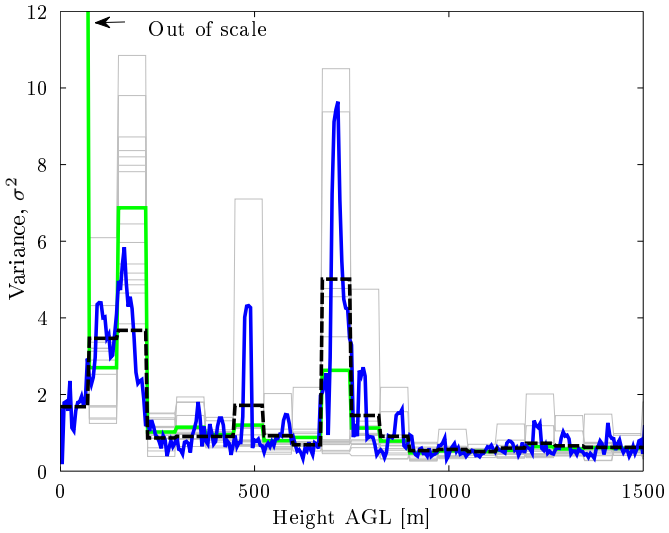

Figure 6.4: Spatial and temporal variances of the observation noise (case example of Fig. 6.1). N =300 range cells (spatial resolution, 5 m), P =20 range intervals, Δ =15 samples/interval. 15 measurement records, (time resolution, 16 s). (Grey lines) Instantaneous piece-wise *spatial noise variance*, $\sigma_n^2(I_p)|_{t=t_k}$, $p = 1..P$ computed along the 20 range intervals, I_p. There are 15 variance estimates (horizontal lines) per range interval. Each variance estimate is associated to a time realization, t_k, of the reflectivity, η_{clean}. (Green thick line) Time-averaged piece-wise spatial variance, $\overline{\sigma}_n^2(I_p)$. Computed as the time average of these 15 spatial variance estimates in each range interval, I_p.(Blue thick line) Range-dependent *temporal variance*, $\sigma_n^2(R_i) = E[v_k(R_i)\, v_k^T(R_i)]$, $i = 1..N$. Computed as the time ensemble of the 15 radar reflectivity realizations. (Black thick dashed line) *Piece-wise temporal variance*. Average of the blue thick line over each range interval, I_p, for visual comparison.

ensemble by the spatial ensemble. The method is based on subdividing the measurement range R_i, $i = 1..N$ into uniform-length intervals, $I_p, p = 1, \ldots, P$ (P=20 in Fig. 6.4), where the variance is to be estimated at time t_k. Therefore, the instantaneous noise covariance matrix estimate is computed as

$$\hat{\mathbf{R}}_k = diag[\sigma_n^2(I_1), \sigma_n^2(I_2), \ldots, \sigma_n^2(I_P)]\big|_{t=t_k}, \quad p = 1..P, \tag{6.16}$$

where $\sigma_n^2(I_i)$ is the piece-wise spatial noise variance computed over the range interval $I_p : [R_{(p-1)\Delta+1} ... R_{p\Delta}]$, $\Delta = \frac{N}{P}$; $p = 1..P$. Reba et al. *Reba et al.* [2006, 2007] from the RSLab have successfully applied piece-wise estimation methods to assess the signal-to-noise ratio from elastic backscatter lidar signals.

The ergodicity principle for stationary random processes assumes that the variance computed over random samples of a given realization of the process is equal to the variance computed over the ensemble of realizations. To test the validity of the ergodicity hypothesis applied to the radar case of Fig. 6.1, Fig. 6.4 compares the time-averaged piece-wise *spatial variance* of the noise, $\overline{\sigma}_n^2(I_p)$ (green thick line), with the range-dependent *temporal variance* (blue thick line), $\sigma_n^2(R_i) = E[\mathbf{v}_k(R_i)\, \mathbf{v}_k^T(R_i)]$, $i = 1..N$. While $\sigma_n^2(I_p)|_{t_k}$ is computed "on-line" by the EKF, $\sigma_n^2(R_i) = E[\mathbf{v}_k(R_i)\, \mathbf{v}_k^T(R_i)]$ must be computed "off-line" as it requires to have the whole set of measurements available.

The fact that both temporal and spatial variances are approximately coincident in Fig. 6.4 except for the first interval I_1 validates the ergodicity hypothesis previously assumed. The discrep-

ancy in interval I_1 is due to the emission-reception cross-over function of the radar antennas having full overlap above 50–100 m in height and to ground clutter effects blinding the radar. The reader will also notice that Fig. 6.4 displays a height range up to 1500 m (in contrast to the usual 500 m in Fig. 6.1) to show the strong returns from "insect" noise above 400 m, where the atmosphere is expected to be clear. Strong peaks appear around 500 and 700 m in height along with a large amount of scattered residual peaks from 400 m up.

6.5 Experimental results

The case example presented here and already introduced from Fig. 6.1 was taken on August 16^{th}, 2007, 14:15:01 UTC (08:15:01 LT) to 15:44:43 UTC when the University of Massachusetts deployed an S-band FMCW radar along with a Vaisala CL-31 lidar ceilometer (910-nm wavelength, 1.2 μJ energy, 100 ns pulse width, 10 kHz repetition rate) at NOAA's Boulder Atmospheric Observatory (BAO) in Erie, Colorado. Because inside the ML the aerosol mixture can be considered homogeneous, causing strong optical lidar backscatter returns, the ceilometer instrument was taken as reference ground truth. Table 6.1 shows the initialization parameters used for the EKF in both systems.

The ceilometer was co-located with the radar to monitor the ABL and cloud cover [*Frasier et al.*, 2008] with both instruments pointed vertically. The radar was configured to operate with ΔR^{raw}_{radar} =5 m spatial resolution (20 MHz sweep bandwidth over 6.4 ms and 75-Hz sweep rate. This configuration provided a Nyquist velocity interval of $\pm$ 3.75 m/s and height coverage up to 2.8 km. The temporal resolution was Δt^{radar}_{raw} =1 s. The ceilometer was operated with ΔR^{ceil}_{raw} =10 m spatial resolution and Δt^{ceil}_{raw} =16 s temporal resolution. Because of the different temporal resolutions between both instruments, radar measurements have been time averaged in blocks of 16 s (Fig. 6.1a) to yield the same data temporal resolution as that of the ceilometer (the so-called, "clean data" time resolution, $\Delta t = \Delta t^{radar}_{clean} = \Delta t^{ceil}_{clean} = 16 s$). A further advantage of this averaging has been to increase the SNR and hence to comparatively minimize the impact of synchronous interferences (weak horizontal lines in Fig. 6.1d) with the emission of radar pulses.

The pre-processing steps described in Sect. 6.2 do not virtually degrade the spatial/temporal resolutions above as evidenced by the fact that the masking procedure does not seriously blurs Fig. 6.1f when compared to Fig. 6.1a. This is because the 7×7 median filter is only applied to a comparatively small population of random pixels occupied by insects. As a result, clean spatial and temporal resolutions, ΔR_{radar} = 5 m and ΔR_{ceil} = 10 m, and Δt =16 s can respectively be assumed.

Fig. 6.5 shows radar and ceilometer *observables* (clean radar reflectivity and range-corrected attenuated backscatter lidar returns, respectively) in colour-plot form for the whole observation period. The ABLH estimated by the ceilometer EKF and the radar EKF is superimposed. Ceilometer EKF implementation is described in *Lange et al.* [2013] and filter initialization parameters are summarized in Tab. 1. The blue bands and the bottom of the radar and ceilometer plots of Fig. 6.5 are due to the different starting measurement ranges of these instruments.

Radar-EKF observation-range parameters, R_1, and R_2, and R'_1 and R'_2 have been initialized

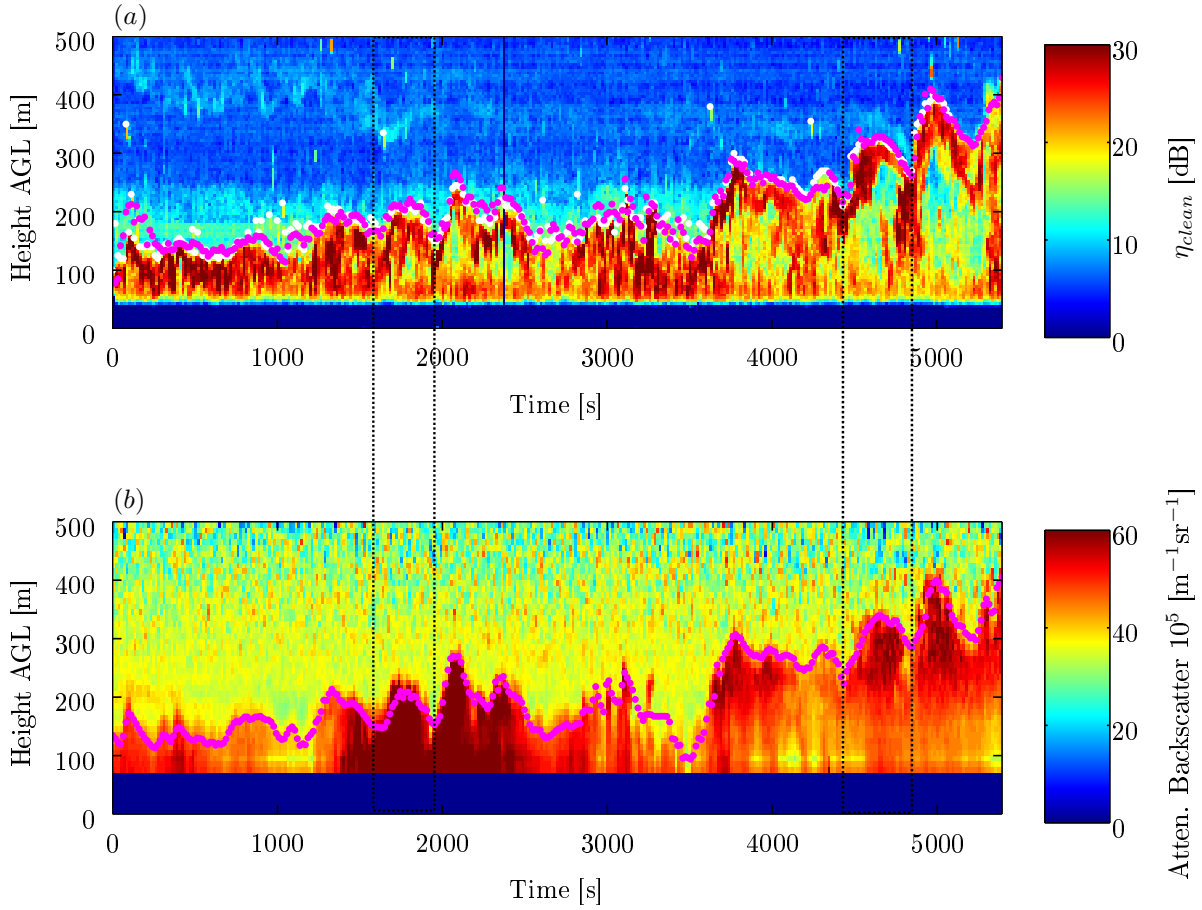

Figure 6.5: FMCW-radar and ceilometer observables to the EKF along with ABLH estimates. (Boulder, CO., August 16, 2007, 14:15:01 UTC (08:15:01 LT) to 15:44:43 UTC). *a*) (Magenta dots) ABLH estimated from radar reflectivity measurements and the radar EKF. (White dots) Comparison with the classic THM. *b*) Validation using Vaisala CL-31 lidar ceilometer. (Magenta dots) ABLH from the ceilometer EKF. Dotted lines in time intervals 1600 to 2000, and 4500 to 4900 s delimit "thermals" (see discussion).

Table 6.1: Initialization parameters for the radar and ceilometer EKFs.
(*) This parameter refers to the *reflectivity-profile transition amplitude* (radar case) and to the *backscatter-coefficient transition amplitude* (ceilometer case).

Parameter	Symbol	Value (radar)	Value (ceilometer)
Observation-range parameters			
Observation start range	R_1	100 m	76 m
Observation end range	R_2	300 m	316 m
Erf-transition start range	R'_1	125 m	116 m
Erf-transition end range	R'_2	225 m	216 m
State-vector parameters			
Initial ABLH	R_{bl}	130 m	136 m
EZ-scaling factor	a	2.77×10^4 km^{-1}	2.77×10^4 km^{-1}
Reflectivity profile / backscatter-coefficient transition amplitude*	A	20 dB	25 $km^{-1}sr^{-1}$
FT reflectivity / molecular-backscatter background	c	10 dB	15 $km^{-1}sr^{-1}$
Covariance matrix parameters			
State-vector covariance-matrix factor	μ_Q	0.1	0.1
A priori-error covariance-matrix factor	μ_P	0.3	0.1

from rough visual inspection of the first reflectivity profiles of Fig. 6.5, which are detailed in Fig. 6.6a-c, along with the guidelines of Sect. 6.3. Thus, R'_1 and R'_2 are a pair of ranges representative of the erf-falling transient (red trace in Fig. 6.6c and red-to-blue decay in Fig. 6.5a) resulting in an interval width, W_0 =100 m (Eq. 6.10). Once R'_1 and R'_2 are set, R_1 and R_2 define $[R_1, R'_1]$ and $[R'_2, R_2]$ "plateau" intervals of approximate widths, W_1 =25 m and W_2 =75 m, respectively (red trace in Fig. 6.6c; red and blue shades around the ML-FT transition in Fig. 6.5a). *State-vector parameters* have also been initialized from these first profiles.

In Fig. 6.6a, the mean reflectivity (black thick line) in the ML range $[R_1, R'_1]$ is approximately 30 dB and the mean reflectivity in the FT range $[R'_2, R_2]$ is 10 dB, which corresponds to a transition amplitude of 20 dB as initialization value for parameter A, and a 10-dB initialization figure for c. The ABLH is close to 130 m (initialization for R_{bl}), and the mean EZ thickness ($2.77a^{-1} \approx$100 m) is used to initialize the scaling parameter a.

Factors μ_Q and μ_P in Tab. 1 assume 1-σ fluctuations/a-priori uncertainties in the atmospheric state vector of 10% and 30%, respectively. For example, with the initialization $R_{bl,0}$=130 m and μ_P=0.3, the user expresses an "a priori" uncertainty at 1-σ of roughly $\pm$ 40 m. Similar reasoning can be applied to EKF-ceilometer parameters.

Performance.- Fig. 6.6b,e shows the instantaneous reflectivity profiles or "observables" estimated by the EKF. Notice that, in spite of the distorted shape of the reflectivity profile, the erf-like estimates fitted to the observables by the filter (thin lines) stick to Eq. 6.6 model with a cen-

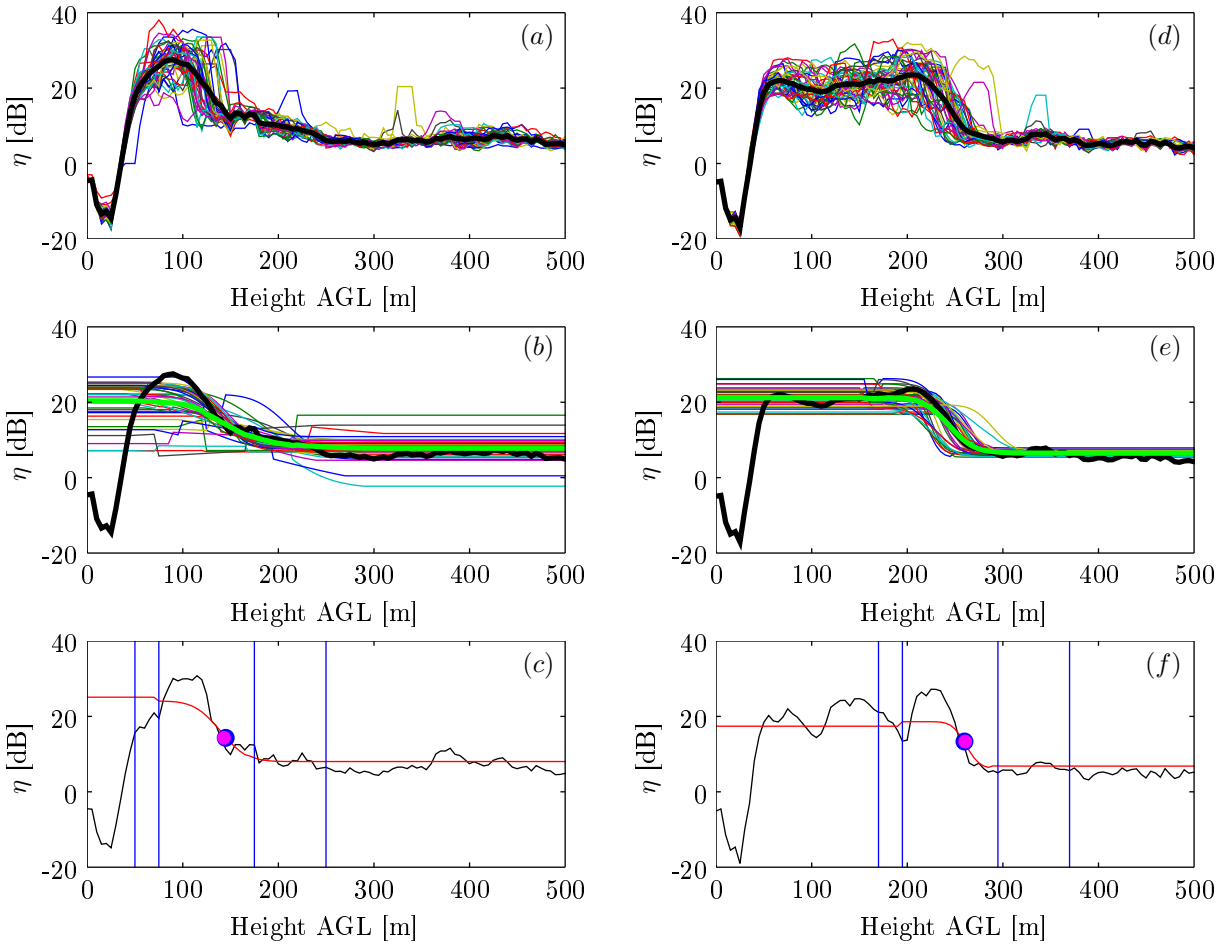

Figure 6.6: Comparison between measured and EKF-estimated reflectivity profiles in two different time intervals: Initialization (t_1 to t_{40}, 14.15:01 to 14:25:29 UTC, 1-628 s) and tracking-interval example (t_{240} to t_{280}, 15:19:12 to 15:29:56 UTC, 3851-4495 s in Fig. 6.1 and Fig. 6.5). (a) (Thin color lines) Profiles of the *measured clean reflectivity* as function of height or EKF "observables", $\eta^{(1-40)}$. (Black thick line) Mean clean reflectivity profile, $\overline{\eta}^{(1-40)}$. (b) (Thin color lines) Instantaneous *EKF-estimated reflectivity* profiles in response to (a). (Green thick line) Mean EKF-estimated reflectivity profile. (Black thick line) Mean clean reflectivity profile, same as (a). (c) Comparison with the classical THM (detail for time t_{28}): (Black line) Measured clean reflectivity profile, η^{28}. (Red line) EKF-estimated reflectivity. ABLH estimated with two different methods: (magenta dot) EKF, (blue dot) classic THM. Vertical blue vertical lines indicate, from left to right, adaptive ranges R_1, R_1', R_2' and R_2.(d) – (e) Same as (a) – (b) for time t_{240} to t_{280}. (f) Same as (c) for time t_{250}=4013 s (15:21:54 UTC).

ter point, R_{bl}, varying with time. The mean EKF-estimated reflectivity profile (green thick line) reencounters a smooth erf model.

In Fig. 6.6c,f the ABLH estimated from the radar EKF is compared with the well-known threshold method (THM) with excellent agreement. In the classic THM [*Melfi et al.*, 1985; *Boers and Eloranta*, 1986; *Batchvarova et al.*, 1999], the instantaneous ABLH is determined as the height associated to a user-defined threshold reflectivity of 15 dB, which is approximately the mean value between the peak-high (30 dB) and peak-low (0 dB) reflectivity levels in the ML interval and FT interval of the first measured profiles. As discussed in the literature, the main disadvantage of the classic THM is the difficulty to assess a consistent threshold because noise spikes would largely change it from one observable to the other.

Finally, Fig. 6.7 compares the time evolution of the ABLH retrieved by the radar and ceilometer EKFs, again with excellent agreement. To quantify it, Fig. 6.7b plots ABLH estimates in scatter-plot form. Radar and ceilometer ABLHs exhibit linear correlation with negligible bias and correlation coefficient as high as $\rho = 0.93$ (determination coefficient, $\rho^2 = 0.87$, *Barlow* [1989]). The narrow departure from the ideal linear correlation case ($\rho = 1$) is mainly attributed to the fact that both instruments measure different physical quantities as proxies of the ABLH, which results in a mismatch on the detection of the thermal boundaries, and, to a lesser extent, to their different temporal and spatial raw resolutions. Thus, following *Stull* [1988b], while the ceilometer measures aerosol backscatter lidar returns that typically show diameters of thermals decreasing with height, the Doppler sodar reflectivity (and by extension Doppler radar in this work) usually shows constant or increasing diameters [*Taconet and Weill*, 1983; *Coulter and Martin*, 1986]. This is evidenced by slightly narrower "inverted U-shaped peaks" in Fig. 6.5b (ceilometer) than in Fig. 6.5a (radar), see dotted time intervals [1600, 2000] s and [4500-4900] s.

As discussed in *Lange et al.* [2013], in time intervals where the SNR is low (typically, $SNR \approx 5$ at the ABLH or $SNR \approx 1$ at the maximum range) classic methods cease to correctly estimate the ABLH. This is the case of the THM in, for example, the time interval 800-1450 s of Fig. 6.5a. If ABLH-radar estimates for both the EKF and the THM are compared in this time interval by using similar scatter-plot methodology as in Fig. 6.7, a determination coefficient as low as ρ^2=0.35 and a regression slope of 0.68 are obtained. For comparison, the mean SNR over the whole time frame of Fig. 6.5 is $SNR = 18$, which can be considered a medium-high SNR scene.

6.6 Conclusions

An Extended Kalman filter has successfully been applied to adaptively estimate and time track the ABLH from FMCW S-band radar returns under single-layer, convective boundary layer conditions. Application of the adaptive EKF to the radar case relies on three important aspects: (*i*) an ad-hoc processing of the radar reflectivity signal, (*ii*) formulation of the Kalman filter itself, and (*iii*) a convenient treatment of noise.

Radar pre-processing of the reflectivity signal has been formulated in Eqs. 6.1 – 6.5 and Fig. 6.3 block diagram and it is aimed at removing impulsive noise, mainly due to insects. This pre-processing yields a "clean" Bragg's scattering atmosphere evidencing a well-defined ML-FT transi-

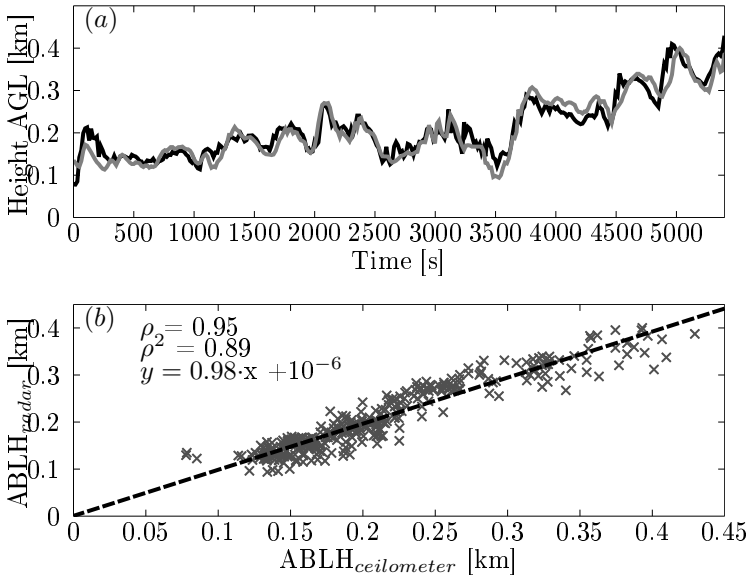

Figure 6.7: Comparison between radar and ceilometer ABLH estimates (see 6.5). *a*) ABLH estimates as a function of time: (Solid black) Radar EKF estimates. (Solid grey) Ceilometer EKF estimates. *b*) Scatter plot relating the ABLH estimated by the radar EKF (horizontal axis) with the ceilometer one ("ground truth", vertical axis). (Black dashed line) Regression line. Labels indicate regression-line and correlation coefficients.

tion.

Formulation of the Kalman filter relies on a parametric erf-like model used to describe the ML-FT interface (the so-called "observation" model) and on a simple Gauss-Markov transition model for the state vector (state-vector model). The formulation departs from a previous result shown in Chapter 5 [*Lange et al.*, 2013] on the application of the adaptive EKF (and in comparison with non-adaptive morphological classic methods) to the problem of ABLH estimation from aerosol backscatter lidar returns. Its extension to the radar case, for which the returns are physically due to refractive index turbulence and not to aerosols, continues to enable application of the erf-like model but, in contrast to the lidar case, radar returns in the ML and FT "plateau" intervals ($[R_1, R_1']$ and $[R_2', R_2]$, respectively) become severely distorted in shape (Fig. 6.2). This unwanted departure from the idealized erf-model, which is considered "modeling noise", requires careful modeling of the noise covariance matrix and that this matrix is updated at each successive discrete time, t_k. Because there is only one observable available at each successive discrete time, the noise covariance matrix cannot be estimated from the time ensemble of measurements but from the noise spatial statistics along the observation height, instead. This ergodicity assumption has also been validated by experiment (Fig. 6.4).

State-vector and a-priori error covariance matrices have been modeled as simple diagonal matrices with initial values proportional to the state vector (μ factor in Eqs. 6.13 – 6.14). The relatively large variability of the ABLH in the time frame under study has been solved by using adaptive ranges for the EKF observation model (range boundaries $[R_1, R_2]$ and $[R_1', R_2']$).

Radar-ABLH estimates have been validated from a collocated Vaisala CL-31 ceilometer in both cases using an EKF ("radar EKF" and "ceilometer EKF" prototype implementations) yielding a correlation coefficient, $\rho = 0.93$, and a regression-line slope of 0.97 with 0.01 bias for the case

example discussed. Because of the relatively high SNR at the ABLH (mean $SNR = 18$), ABLH height estimates from the classic THM also become in good agreement with those obtained from the EKF. However, in time intervals where the SNR is "low" ($SNR \approx 5$ or lower at the ABLH) the THM ceases to correctly estimate the ABLH, which underlines the advantage of the EKF not only for its time tracking capability but also for its ability to operate in low-SNR scenarios.

Chapter 7

RSLab lidar exploitation cases

This Chapter presents two application cases of the RSLab multi-spectral lidar system. Both cases corresponds to two eruptive events measured by RSLab lidar system, in synergy with EARLINET and other lidar networks.
First application case is an eruptive event from Nabro volcano in Eritrea. Eruption started on June 12th, 2011 generating a layer of sulfur aerosols that persisted in the stratosphere for several months. The event was monitored simultaneously with ground based lidar stations in the Northern Hemisphere, and satellite CALIPSO.
Second application case is the eruption of the Eyjafjallajökull volcano in Iceland in April–May 2010. The event was monitored by the available stations from EARLINET in 2010.
The application cases presented in this chapter are a short compilation of Sawamura et al. [2012] and Pappalardo et al. [2013] papers with relevant contributions from the author of this Ph.D.

7.1 Introduction

The injection of SO_2 due to volcanic eruptions is the biggest natural source of perturbations in the stratosphere. SO_2 converts to sulfuric acid which will quickly condense, forming fine sulfate aerosols in the stratosphere. These aerosols have longer residence times (1-3 years) compared to ash and tropospheric sulfate aerosols (typically days and weeks respectively), and have an impact on the climate ([*Robock*, 2000; *Solomon et al.*, 2011]). Sulfate and ash particles reflect solar radiation, act as cloud condensation and ice nuclei, and modify the radiative properties and lifetime of clouds, and therefore influence the precipitation cycle. These volcanic particles can also have an impact on environmental conditions and can be very dangerous for air traffic. Due to their extended

residence time once injected into the stratosphere, these particles can travel large distances. Global monitoring of the stratosphere is, therefore, of great importance.

Regardless of the source, the optical properties of stratospheric aerosols must be properly quantified. If neglected, the perturbations caused by these particles can represent an error source in lidar measurements of trace gases in the stratosphere and also in comparative studies of column-integrated versus ground-based measurements.

The impact of particularly violent volcanic eruptions on the stratospheric aerosol load has been studied with lidar remote sensing since the early 1970s [*Jäger*, 2005; *Deshler*, 2008]. The most important eruptions during this period were those of El Chichon (Mexico, 1982) and Mt. Pinatubo (Philippines, 1991). After 1996 there was a ten year period without appreciable volcanic activity, which ended by the end of 2006 when a series of several eruptions injected particles into the stratosphere that were recorded with lidar systems worldwide [*Mattis et al.*, 2010; *Sawamura et al.*, 2012; *Trickl et al.*, 2012]. Although many lidar observations are available for volcanic aerosol in the stratosphere, only a few are known for tropospheric events before 2010, such as those related to Etna volcanic eruptions in 2001 and 2002 [*Pappalardo et al.*, 2004a; *Villani et al.*, 2006; *Wang et al.*, 2008].

First application case is an eruptive event from Nabro volcano (13.37°N,41.70°E) in Eritrea (Fig. 7.1a-b). Eruption started on June 12th, 2011 generating a layer of sulfur aerosols that persisted in the stratosphere for several months. The event was monitored simultaneously with ground based lidar stations in the Northern Hemisphere, and satellite CALIPSO. Synergy between global lidar networks such as MPLNET, EARLINET and NDACC with independent lidar groups and satellite CALIPSO permitted to track the evolution of the stratospheric aerosol layer in various parts of the globe. The globally averaged *aerosol optical depth, (AOD)* due to the stratospheric volcanic aerosol layers was in the order of 0.018 ± 0.009 at 532 nm, ranging from 0.003 to 0.04. Compared to the total column AOD from the available collocated AERONET stations, the stratospheric contribution varied from 2% to 23% at 532 nm.

Second application case is the eruption of the Icelandic volcano Eyjafjallajökull in April–May 2010 (Fig. 7.1a-c). It represents a "natural experiment" to study the impact of volcanic emissions on a continental scale. For the first time, quantitative data about the presence, altitude, and layering of the volcanic cloud, in conjunction with optical information, are available for most parts of Europe derived from the observations by EARLINET.

The *four-dimensional (4-D)* distribution of the Eyjafjallajökull volcanic cloud in the troposphere over Europe as observed by EARLINET during the entire volcanic event (15 April–26 May 2010) is shown. During the first days after the eruption, volcanic particles were detected over Central Europe within a wide range of altitudes, from the upper troposphere down to the local ABL. After 19 April 2010, volcanic particles were detected over southern and south-eastern Europe. During the first half of May (5–15 May), material emitted by the Eyjafjallajökull volcano was detected over Spain and Portugal and then over the Mediterranean and the Balkans. The last observations of the event were recorded until 25 May in Central Europe and in the Eastern Mediterranean area.

Lidar techniques represent a powerful method for monitoring the dispersion of a volcanic cloud in the atmosphere because of their profiling capability. In particular, lidar techniques provide geomet-

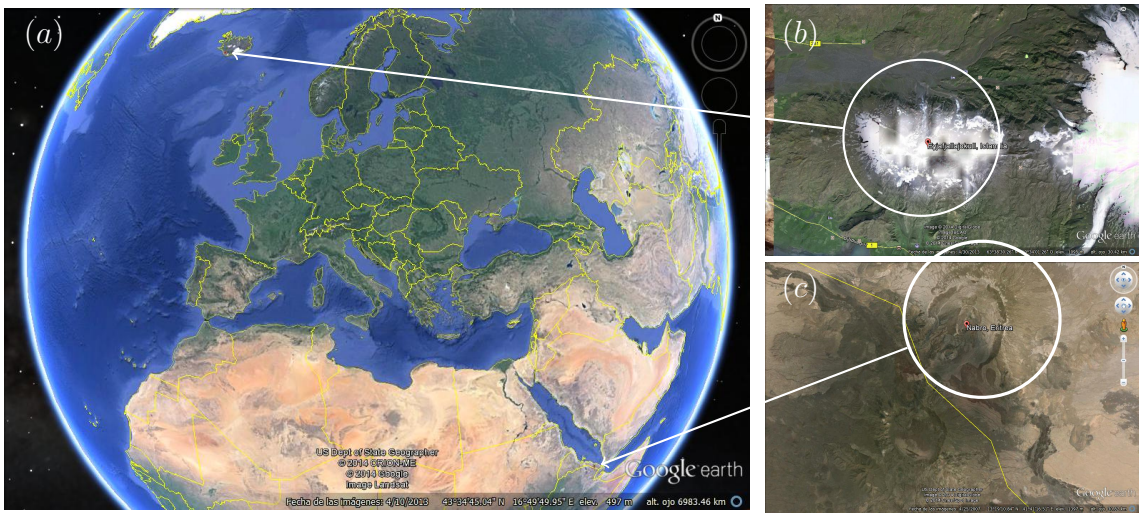

Figure 7.1: Location of the two applications cases studied. (a) World map showing the location of Nabro and Eyjafjallajökull (April, 30^{th}, 2013), LANDSAT image. (b) Nabro image, showing the volcano in the middle of the white circle (April, 10^{th}, 2013), CNES-SPOT image. (c) Eyjafjallajökull image, showing the volcano in the middle of the white circle (April, 25^{th}, 2007), CNES-SPOT image. Source: Google Earth for the three images, US Dept. of State Geographer, for the (a) and (c), and DigitalGlobe for (b) and (c).

rical properties (top, bottom, and thickness) for each volcanic layer, optical properties (extinction, backscatter, and optical depth), aerosol typing and in some cases also microphysical properties if advanced multi-wavelength Raman lidar systems are used.

In this chapter, synergistic measurements from a volcanic eruption are reported, taken from multiple lidar networks and satellite CALIPSO. The evolution of the stratospheric aerosols in the Northern Hemisphere is tracked, focusing in EARLINET stations.

It is already well recognized that lidar remote sensing, is an important tool to help assess the vertical distribution of aerosol in the atmosphere. Space-borne lidar, like the *Cloud-Aerosol LIdar with Orthogonal Polarization (CALIOP)* on-board CALIPSO [*Winker et al.*, 2003], has a narrow swath and therefore does not provide complete global coverage. To fill those gaps in terms of spatial coverage, networks of ground-based lidars such as EARLINET, MPLNET and NDACC are of extreme value.

The chapter is organized as follows: Sect. 7.2 introduces the first application case, Nabro volcano, Sect. 7.3 considers the second application case, Eyjafjallajökull volcano, and Sect. 7.4 summarizes the results and conclusions obtained in both cases.

7.2 Application Case (I): Nabro Volcano eruption, 2011

Nabro is a stratovolcano located in the Afar Triangle at the border between Northeastern Ethiopia and Southern Eritrea (Fig. 7.1c). It is a 2,218 m high volcano, the highest in the Afar Triangle, sitting at the triple junction between the Arabian, Somalian and Nubian tectonic plates along the East African Rift Zone [*Wiart and Oppenheimer*, 2005].

Nabro's first ever recorded eruption occurred on the night of June 12th, 2011 when it spewed

copious amounts of ash disrupting the air traffic in Eastern Africa. According to reports from the *Toulouse Volcanic Ash Advisory Center (VAAC)*, Nabro started erupting between 0000 to 0200 EAT (East Africa Time = UTC +3h) with visible plumes rising up to an altitude of 11 km, consisting mainly of water vapor and sulfur dioxide gas. Preliminary analysis suggests an SO_2 release of approximately 1.5 to 2 Tg in the first few days one of the largest volcanic SO_2 emissions measured since Nyamuragira volcano, Congo in 1994 [*Carn and Bluth*, 2003] and Mt. Pinatubo eruption in 1991 which injected about 20 Tg of SO_2 into the stratosphere. which increased the globally averaged temperature in the lower stratosphere by approximately 2-3 K, but lowered the globally averaged surface temperature by about 0.3 K in the following two years [*Stenchikov et al.*, 2002].

The observations described are from CALIPSO, MPLNET, EARLINET, NDACC and from the Key Laboratory of Atmospheric Composition and Optical Radiation in Hefei, China, spanning from June 14th until early September, 2011. Regarding the scope of this document, only EARLINET stations will be considered in depth including, for comparison purposes, limited information from the others, whenever necessary. Extensive details can be found in *Pappalardo et al.* [2013].

Lidar stations that observed stratospheric plumes are listed in Table 7.1 and Fig. 7.2 shows the temporal and zonal distribution of the observations. Santa Cruz de Tenerife, Kanpur, Trinidad Head, Sede Boker and *Goddard Space Flight Center (GSFC)* are all MPLNET stations. Universidad de Granada (Centro Andaluz de Medio Ambiente, CEAMA), Universitat Politècnica de Catalunya (UPC), Istituto di Metodologie per l' Analisi Ambientale (Consiglio Nazionale delle Ricerche, CNR-IMAA) are EARLINET stations. Mauna Loa Observatory (MLO) and Observatoire de Haute-Provence (OHP) are members of NDACC.

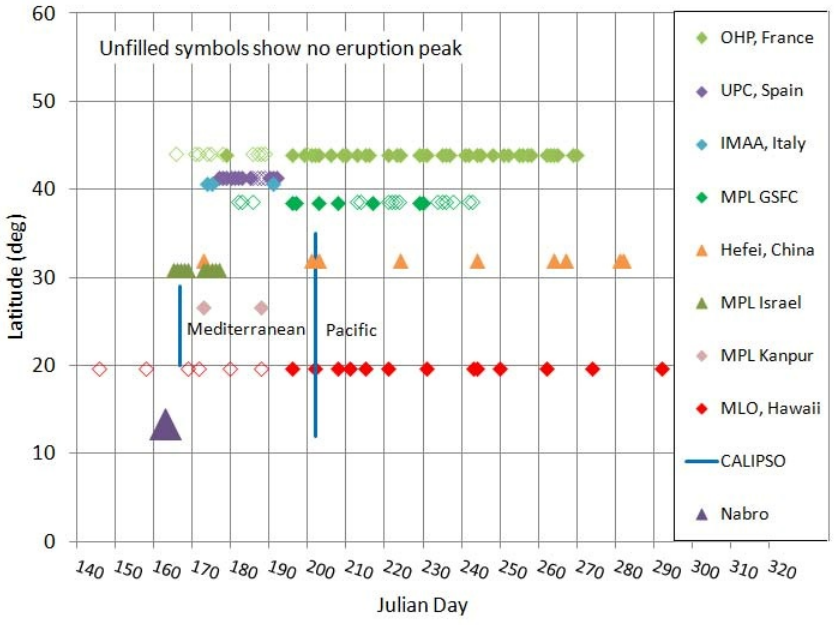

Figure 7.2: Zonal and temporal distribution of lidar observations from June to October, 2011. Nabro marker represents the location and eruption date. Unfilled symbols mean that measurements were available but no stratospheric signature was observed.

Table 7.1: Lidar systems description

Location	(Lat, Lon)	Elevation (a.s.l.)	System
Sede Boker, Israel	(30.85°N, 34.78°E)	480 m	MPL @ 523 nm
Sta. Cruz de Tenerife, Spain	(28.47°N, 16.25°W)	52 m	MPL @ 523 nm
GSFC, USA	(38.99°N, 76.84°W)	50 m	MPL @ 527 nm
Trinidad Head, USA	(41.05°N, 124.15°W)	107 m	MPL @ 527 nm
Kanpur, India	(26.52°N, 80.23°E)	150 m	MPL @ 532 nm
UPC, Spain	(41.39°N, 2.11°E)	115 m	Nd:YAG @ $3\lambda_0 + 2\lambda_{N_2}$
CEAMA, Spain	(37.16°N, 3.61°W)	680 m	Nd:YAG @ $3\lambda_0 + 2\lambda_{N_2}$
MLO, Hawaii	(19.54°N, 155.58°W)	3,397 m	Nd:YAG @ 1064 and 532 nm
IMAA, Italy	(40.60°N, 15.73°E)	760 m	ND:YAG @ $3\lambda_0 + 2\lambda_{N_2}$
Hefei, China	(31.9°N, 117.2°E)	30 m	Nd:YAG @ 532 nm
OHP, France	(43.93°N, 5.71°E)	650 m	DIAL @ 355 nm

$3\lambda_0$ are elastic channels at 1064, 532 and 355 nm, and $2\lambda_{N_2}$ are N_2 Raman channels at 387 and 607 nm.

7.2.1 Timeline of the observations

Back-trajectories were run for each lidar observation using the *Hybrid Single Particle Lagrangian Integrated Trajectory Model (HYSPLIT)* [*Draxler and Rolph*, 2003, 2012] to confirm whether or not the stratospheric layers observed were due to Nabro's eruption. Forward trajectories were also run from Nabro's location to assess the airmass transport during the days immediately following the eruption. All HYSPLIT trajectories were computed using *Global Data Assimilation System (GDAS)* meteorological data, vertical velocity model for vertical motion and maximum run time of 300 hours.

In Europe, the first layers were reported on June 23rd over Potenza, Italy (CNR-IMAA) at 16 km. A coincident CALIPSO overpass confirmed the layer presence at 16 km of altitude over Italy extending all the way to Southern Nigeria. CNR-IMAA continued to observe residual signature until late August. In Spain, a layer between 16-17 km was first observed over Granada (SE Spain) on June 26th and then in Barcelona (NE Spain) at 17 km. Weak signatures were observed over Granada until July 11th . Over southern France layers were observed from June 28th to July 2nd and then again, although with weaker signals, from July 15th until late August. Back-trajectories from the lidar stations in Europe and Asia are presented on Fig. 7.3.

7.2.2 Stratospheric AOD from lidar data

Many lidar stations participating in this study have Raman lidar capabilities but most of the AOD values here presented were obtained from elastic measurements. The Klett-Fernald method (Sect. 2.2.6) for the case of stratospheric aerosols is able to provide satisfactory results given an assumed value for S_{aer}. *Mattis et al.* [2010] reported S_{aer} values in the range of 30–60 sr at 355 nm and 30-45 sr at 532 nm in the stratosphere due to volcanic aerosols measured between 2008–2009 over central Europe with a multi-wavelength Raman lidar. In the case of RSLab, the AOD was computed using the methodology presented in *Reba* [2010] Ph.D, guided by F. Rocadenbosch.

The mean S_{aer} value of 50 sr at 532 nm was assumed by most groups in this study, including MLO, RSLab and also in the CALIOP retrievals, with exception to CEAMA group which assumed values of 45- and 38-sr for 355- and 532-nm, respectively. CNR-IMAA was the only group to

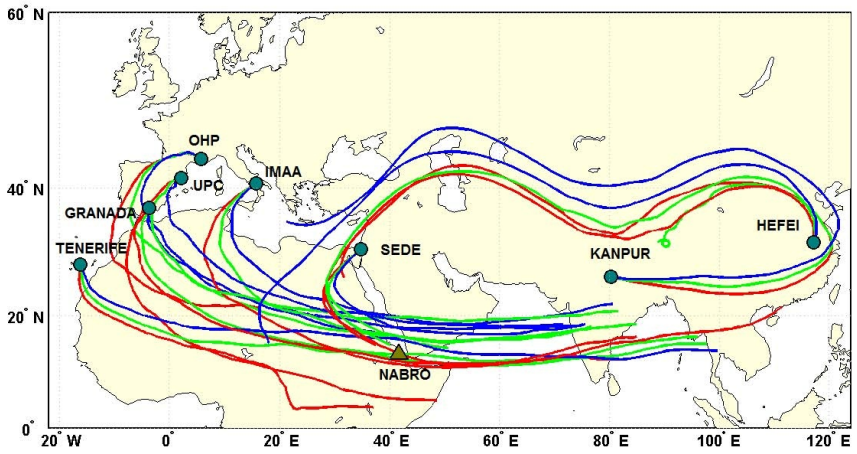

Figure 7.3: Back-trajectories for all sites included in the study with exception of the ones located in the United States. The start time and altitudes denoted by each set of red, blue and green lines varies according to the date/time and altitudes of the first stratospheric layers observed by the lidar groups participating in this study.

measure S_{aer} values utilizing the Raman technique. They measured S_{aer} values of 48- and 55-sr at 532- and 355-nm, respectively. The S_{aer} values assumed/measured (depending on the inversion algorithm they use) by each group and the respective AOD values obtained from each profile are summarized in Table 7.2.

Table 7.2: AOD values calculated from the profiles shown on Fig. 7.10 (layers) and AERONET colocated measurements of AOD (total column).

Location	$S_{aer_{355}}$ **sr**	AOD_{355}	$S_{aer_{532}}$ **sr**	AOD_{532}	AOD_{CAL}	AOD_{AERO}
Sede Boker	—-	—	50	06/14: 0.17	0.012	0.33
Tenerife	—	—	50	06/29: 0.019	—	0.30
GSFC	—	—	50	07/15: 0.003	0.007	0.18
	—	—		07/22: 0.008	—	0.44
Trinidad	—	—	50	07/17: 0.02	0.010	—
Kanpur	—	—	50	07/07: 0.015	0.018	—
UPC	—	—	50	06/27: 0.04	0.012	—
Granada	45	06/26: 0.05	38	06/26: 0.02	0.012	@500: 0.32
					—	@340: 0.42
MLO	—	—	50	07/15: 0.01	0.008	0.015
	—	—		07/21: 0.022	—	0.05
	—	—		08/31: 0.011	—	0.04
CNR-IMAA	55 ± 18	06/24: 0.04	48	06/24: 0.03	0.010	@500: 0.11
					—	@340: 0.19
Hefei	—	—	50	06/22: 0.023	—	—
	—	—		07/20: 0.011	—	—
	—	—		07/22: 0.023	—	—
	—	—		08/12: 0.010	—	—
OHP	$\overline{S(z)} = 53 \pm 6$	June 28: 0.04	—	—	0.012	0.24
		$\overline{AOD}_{Jul}$: 0.013 ± 0.007	—	—	—	0.20
		$\overline{AOD}_{Aug}$: 0.022 ± 0.005	—	—	—	0.20
		$\overline{AOD}_{Sep}$: 0.029 ± 0.006	—	—	—	0.28

CNR-IMAA used Raman technique, and OHP $\overline{S(z)}$ is the mean lidar ratio from 10 to 25 km.

Fig. 7.4 shows the scattering ratio profiles obtained from lidar measurements pertinent to this

study. The *scattering ratio (SR)* is defined as the ratio between the total backscatter, β_{tot} (due to molecular and aerosol contributions), and the molecular backscatter, β_{mol},

$$SR = \frac{\beta_{tot}}{\beta_{mol}}, \tag{7.1}$$

which can be calculated from radiosonde measurements of pressure and temperature, or from standard atmosphere models. In the absence of aerosols, SR = 1. The aerosol backscatter profiles for the MPLNET stations in this study were retrieved from the MPLNET level 1 *normalized relative backscatter (NRB)* product. One hour averages of NRB profiles from nighttime measurements were used to avoid SNR issues due to the solar background. The aerosol layer is isolated by assuming an aerosol-free atmosphere under and over the layer and the aerosol backscatter profiles is then obtained using an iterative method. The algorithm utilized for the retrievals of aerosol backscatter profiles from MPL data in this study was developed independently from the MPLNET retrieval algorithms. The AOD values obtained from MPLNET data are the product of the integrated backscatter coefficient in the aerosol layer with a range-independent $S_{aer} = 50$ sr.

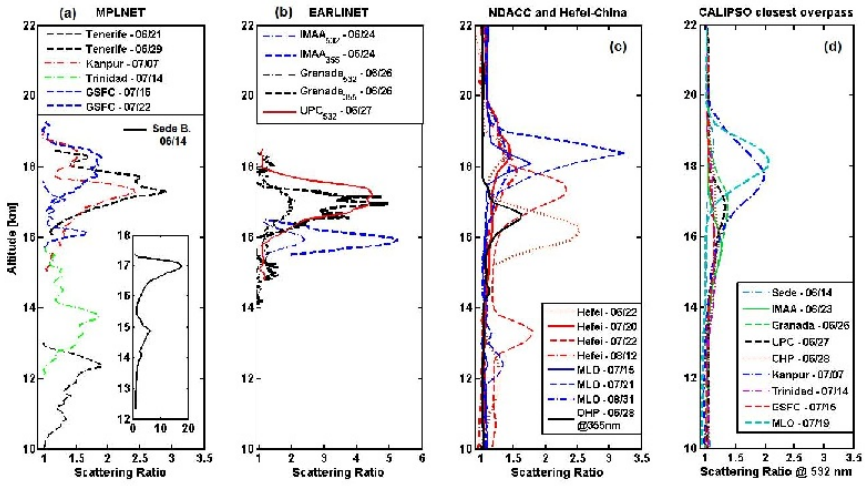

Figure 7.4: Scattering ratio profiles from MPLNET. *a*) EARLINET stations *b*) NDACC and Hefei *c*) and from CALIPSO's closest overpass to the lidar stations. Subplot on *c*) are the mean profiles of available observations from those stations. Number of averaged observations were 13, 11, 7 and 5, respectively. *d*) CALIOP SR profiles from closest overpasses with respect to the ground lidar stations. Please note that different scales are used in figures *a*), *b*) and in subplot of *c*).

Fig. 7.5 shows the mean AOD over the entire globe retrieved from CALIOP measurements at 532 nm from July 16th to July 31st . The AOD was retrieved only in the stratosphere between 12 and 20 km which gives an estimate of the contribution of Nabro's volcanic aerosols to the global AOD. Values approximately between 0.012 and 0.03 were observed over most of Southern Europe and all over Asia, branching out over the Pacific and towards the West Coast of the US. Although most of the sulfate aerosols due to Nabro's eruption were observed East of Nabro's location, Fig. 7.5 shows slightly elevated values of AOD crossing the Atlantic towards the East Coast of the US, which is consistent with the back-trajectories discussion from the previous section. It should be noted that CALIOP data was not available from the 7th to the 14th of June.

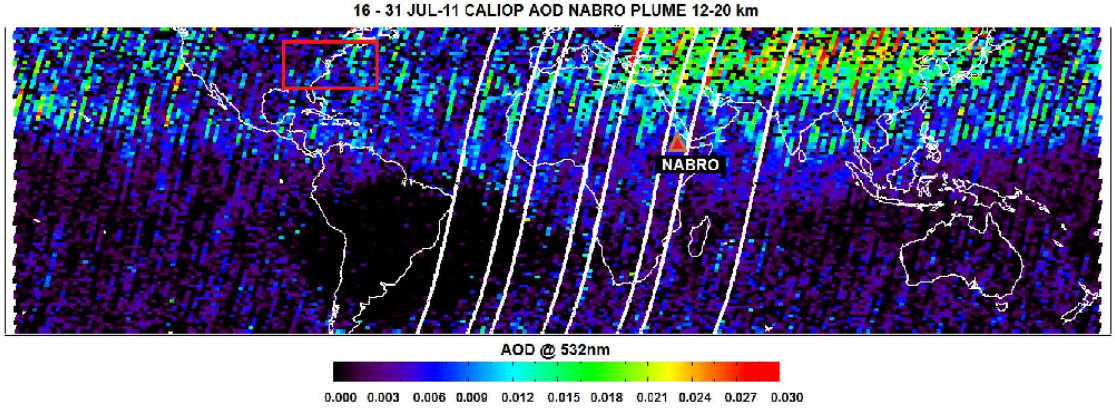

Figure 7.5: Global CALIOP AOD retrieval from July 16 to July 31.

7.2.3 Stratospheric contribution to total column AOD

AOD measurements from collocated AERONET stations were available for most lidar stations in this study. As mentioned in Sect. 2.2.6, retrievals of extinction and backscatter coefficients from elastic lidars require an assumption of range-independent lidar ratio. Collocated measurements of AOD can also be utilized as an additional a priori information for retrievals in the lower troposphere. When most of the aerosol load is confined to the lowest troposphere, which is often the case, the AOD can be used as a boundary condition to obtain the best estimate of lidar ratio, since AOD is, by definition, the integral of the extinction profile. However, in the presence of aerosol layers aloft AERONET AOD values will not only represent the tropospheric contribution but also that of the layer.

Most lidar data in this study were obtained at nighttime when no sun photometer measurements are available. Therefore, to estimate the stratospheric AOD contribution to the total AOD as measured at the collocated AERONET stations, a linear interpolation was considered between the last data points from the day before and the first data points from the day when the layers were observed. Only the last/first 3 to 5 data points of each day were considered in the interpolation and we utilized the AOD values at 340 nm and 500 nm to compare with the measurements at 355 nm and 532 nm, respectively. The interpolated values of AOD are presented in Table 7.2 as AOD_{AERO}. In Santa Cruz de Tenerife the contribution of the stratospheric AOD to the total AOD was about 6%, 2% at GSFC, 12% and 5% in Granada for 355 nm and 532 nm respectively, 22% and 23% at CNR-IMAA for 355 nm and 532 nm respectively. At OHP for the June 28th case the contribution was of 17% at 355 nm and for the monthly averages the contributions were of 6%, 11% and 10% for July, August and September, respectively. At MLO, due to the site's high elevation (around 3 km), the contributions were even larger: 65%, 48% and 26% for July 15th, July 21st and August 31st, respectively.

7.2.4 RSLAB measurements, June 27^{th}, 2011

Volcanic plumes in Barcelona were observed from June, 27^{th}, to July, 11^{th}, 2011 (purple diamonds en Fig. 7.2). During the whole period, two daily 1-h measurements were carried out, one in the

morning and another in the afternoon. The RSLab contributed to *Sawamura et al.* [2012] with all the available measurements monitoring the volcanic event.

Next, Fig. 7.6 shows two 1-h-long measurements corresponding to 27^{th}, 2011, which was the date a volcanic layer over Barcelona was first detected. Since the dust layer was present in the near range, and the volcanic plume in the far range, neither the analog nor the photon-counting signal coming from the PMTs can solely be used to characterize both layers without distortion. As mentioned in Chapter 4, to solve that, the dynamic of the elastic lidar reception channel is enlarged by gluing analog and PC raw-data records (See enhanced "gluing" algorithm in Sect. 4.2).

Fig. 7.6a corresponds to late-afternoon measurements (start time at 18:59 UTC), with sunset time at 19:30 UTC. Fig. 7.6b illustrate the measurement started just after, in the time-frame 20:05 UTC to 21:04 UTC.

Saharan dust intrusions are common during summer time in Barcelona [*Sicard et al.*, 2009c], and as it happens in some of the measurements show the volcanic layer above 17 km and dust layers below 4 km. No merging between both type of aerosols were detected. Also, it is possible to detect forest fire plume traces coming from North America. According to HYSPLIT back-trajectories (not shown), the thin layer at 3 km in height in Fig. 7.6a-b do comes from North America's middle-east zone, where forest fire zones were located around July, 17^{th} [*Forest Fire North America*, 2014].

Regarding to KFS inversion, the RSLab assumed a range-independent lidar ratio, S_{aer}, of 50 sr at 532 nm. The AOD was computed using the methodology presented in *Reba* [2010], and its value was 0.12.

Fig. 7.7 shows the extinction (α_{Mie} and α_{Ray}) and backscatter profiles (β_{Mie} and β_{Ray}) for the range-corrected glued signal shown in Fig. 7.6a.

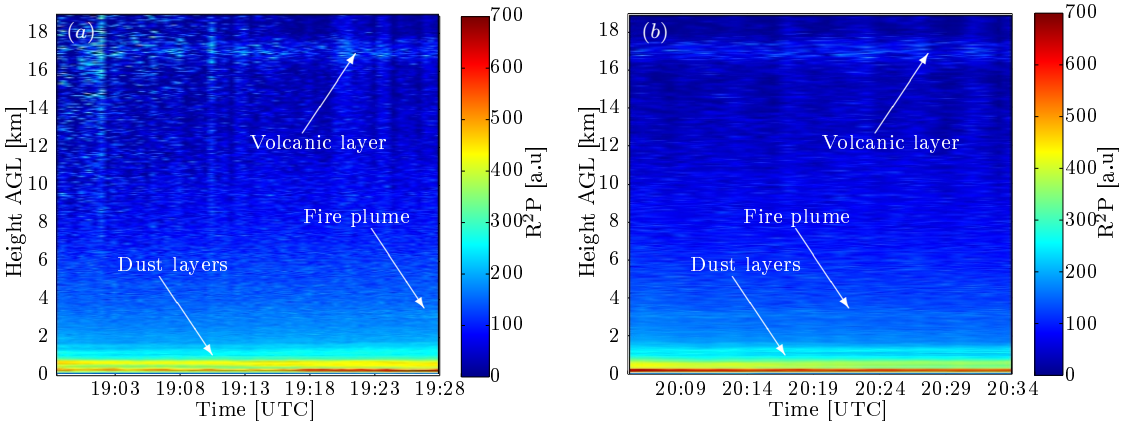

Figure 7.6: Time-height plot of the glued range-corrected lidar signal for the 532-nm channel from the Nabro's volcanic event (Barcelona UPC, Campus Nord, June, 27^{th}, 2011). (*a*) Time interval from 18:59 to 19:58 UTC. (*b*) Time interval from 20:05 to 21:04 UTC.

7.2.5 Discussion

The MPL profile over Sede Boker (June 14th) was the first available profile after Nabro's eruption. It showed the strongest peak in terms of backscatter compared to the other profiles, as displayed

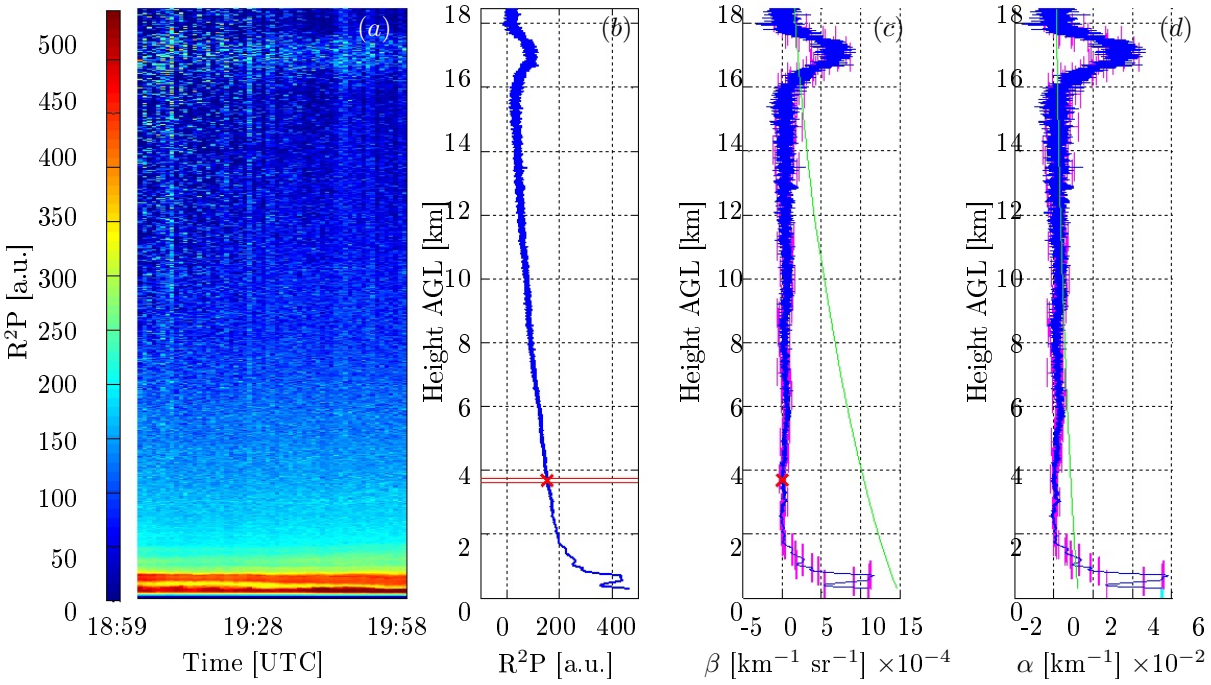

Figure 7.7: Optical-atmospheric parameters inversion example for Fig. 7.6a case, using RSLab lidar data Link-Detect GUI lidar inversion platform. KFS method was used [*Klett*, 1985]. (*a*) Time-height plot of the glued range-corrected lidar signal for the 532-nm channel. (*b*) Time-averaged range-corrected lidar signal. The calibration range is 3.7 km (red cross). The range interval (red lines) where the power calibration is smoothed is ± 100 m around he calibration range. (*c*) Aerosol (blue trace) and molecular (green trace) backscatter coefficients, β_{aer} and β_{mol}, respectively. Error bounds have been computed according to Sect. 3.4. (*d*) Aerosol (blue) and molecular (green) extinction coefficients, α_{aer} and α_{mol}, respectively. The S_{aer} is 50 sr, and the estimated AOT is 0.12 [*Reba et al.*, 2010].

in 7.4a and the highest AOD of 0.17, 51% contribution to the total AOD. Given the short time between Nabro's first explosive eruption and the first observation at this site, we believe that the layer could be composed of ash and sulfate aerosols. Due to their size compared to sulfate aerosols, ash particles are quickly removed from the stratosphere, which might explain the difference in scattering magnitude from this measurement and all the other measurements from June 2011, which were, most likely, measurements of sulfate aerosols only.

With respect to the source of the layers observed over Santa Cruz de Tenerife on June 21st between 10 and 13 km, back-trajectories (not shown here) suggested long range transport of smoke particles from fires that were occurring in North America in that period. However, given the date and location of observation, one cannot exclude the possibility of contributing ash/sulfate particles from smaller eruptions that followed the major one on June 12th. The AOD obtained for that layer was 0.022, a 5% contribution for the total AOD of that day (0.4 at 500 nm). Unfortunately there were no additional measurements, such as depolarization measurements that could help us determine whether or not ash particles were present in this case. The back-trajectories for June 29th case as shown in Fig. 7.3 confirmed Nabro as the source of the layer observed. It should be noted that the presence of another volcano in that same island (Hierro volcano) was irrelevant in this case, as it was not displaying activity in that period.

In terms of S_{aer} values, most groups assumed a value of 50 sr at 532 nm. In Sede Boker's case (June 14th) this assumption may not be truly representative if a mix of ash/sulfate was indeed present in the stratosphere. Unfortunately there aren't many reports on S_{aer} values measured from ash particles in the stratosphere due to their relatively short residence time. *Pappalardo et al.* [2004a] reported a S_{aer} value of 55 sr at 355 nm in the lower troposphere and *Ansmann et al.* [2001] reported S_{aer} values of 50 sr for ash and 40-80 sr for non-ash (fine mode) at 532 nm also in the lower troposphere. One cannot assume however, that those same S_{aer} values would apply in the stratospheric case since both layers are characterized by completely different dynamics and water vapor content which could greatly influence the S_{aer} values in cases when hygroscopic aerosols, e.g. sulfates, can be found in the mixture.

7.3 Application case (II): Eyjafjallajökull volcano, 2010

7.3.1 Eyjafjallajökull Volcano

Eyjafjallajökull is a stratovolcano completely covered by an ice cap, and is located in Iceland, north of Skógar and to the west of Mýrdalsjökull (Fig. 7.1b). it has a summit elevation of 1,651 m and has a crater of 3 to 4 km in diameter. The volcano has erupted relatively frequently since the last glacial period, most recently in 2010 [*Thordarson and Larsen*, 2007].

After seismic activity recorded during December 2009, a first eruption started on 20 March 2010. After a brief stop, a new phase started on 14 April, when meltwater penetrated to the central crater beneath the glacier. After a short hiatus in eruptive activity, a new set of craters opened up in the early morning of 14 April under the volcano's ice-covered central summit caldera. Meltwater started to emanate from the ice cap around 07:00 UTC on 14 April, and an eruption plume was

observed in the early morning. The Eyjafjallajökull explosive eruptive phase started on 14 April 2010 and lasted until 21 May 2010 [*Langmann et al.*, 2012].

The ash-loaded eruption plume rose to more than 10 km height, deflected to the east by westerly winds. The height of the emitted plume was around 8 km until 16 April and decreased to a typical maximum height of 3–4 km in the following days [*Arason et al.*, 2011]. The plume rose up again to an altitude of 5–6 km in the period of 4–20 May [*Langmann et al.*, 2012].

Depending on the wind direction, the eruption plume was transported toward different regions of continental Europe and toward the Atlantic Ocean at different altitudes. Even though this eruption was only moderate in intensity, it had a strong impact on air traffic. In order to prevent possible damages to aircraft engines, the airspace over large parts of Northern Europe was closed on 15 April when the first parts of the eruption plume reached continental Europe. Air traffic restrictions and partial closure of European airspace were not uniform during the eruption period and differed from region to region depending on the volcanic ash transport pattern and the (sparse) information on height and density of volcanic aerosol at the time.

A study presenting profiling observations for the whole volcanic event on a continental scale has not been published yet. The *main objectives* of this work is to summarize the spatial and temporal evolution of the volcanic cloud during the entire volcanic event (April, 15^{th} to May, 26^{th}), as observed by EARLINET coordinated ground-based lidar network.

7.3.2 Timeline of the observations

Volcanic particle layers have been identified for all the EARLINET stations using a specific back-trajectory-models lidar observations integrated methodology for a volcanic aerosol masking *Mona et al.* [2012].

For the occurrence of special atmospheric events an alerting system has been implemented in EARLINET. In the case of the volcanic eruption of Eyjafjallajökull, an alert was sent to the whole network on 15 April 2010.

The first characterization of the volcanic ash cloud was provided by *Ansmann et al.* [2010] relying on EARLINET lidar observations at Leipzig and Munich, Germany. EARLINET performed almost continuous measurements from 15 April 2010 in order to follow the evolution of the volcanic cloud over Europe. During the event (15 April–26 May 2010), the volcanic cloud was transported to different regions of Europe at different altitudes and times and with a large variety in load. Volcanic particles were first observed in the UK, Ireland, the Netherlands, Germany, and France from very low altitudes up to the upper troposphere [*Ansmann et al.*, 2011; *Pappalardo et al.*, 2010a; *Schumann et al.*, 2011; *Hervo et al.*, 2012; *Matthias et al.*, 2012]. The volcanic cloud was then observed over Switzerland, Poland, and Norway [*Pietruczuk et al.*, 2010; *Schumann et al.*, 2011]. The cloud reached Italy and Greece after 19 April [*Mona et al.*, 2012; *Papayannis et al.*, 2012]. In May 2010, the volcanic cloud was transported over the Iberian Peninsula ([*Sicard et al.*, 2012; *Navas-Guzmán et al.*, 2013] and then moved towards the East, reaching Italy, Greece, and Turkey [*Mona et al.*, 2012; *Perrone et al.*, 2012; *Papayannis et al.*, 2012]. A series of publications covered the in-depth characterization of the ash cloud over different parts of Europe, combining

measurements of lidars, sun photometers, and in situ probes. *Schumann et al.* [2011] reported on measurements on board the German research aircraft Falcon that covered several flights over Central Europe, Iceland, and the North Sea. *Groß et al.* [2012] demonstrated the potential of lidar-derived intensive aerosol properties to distinguish volcanic aerosol from other types.

On 15 April the eruption plume reached continental Europe, causing closure of the airspace over large parts of Northern Europe. Almost all EARLINET stations promptly started continuous measurements, whenever weather conditions allowed it.

Despite the fact that EARLINET stations are not truly operational, the lidar systems were run almost continuously, weather permitting, coordinated by daily alerts. More than 5000 h of measurements were performed day and night during the period 15 April–26 May 2010. A page with the time plots of the lidar range-corrected signals was made available on the EARLINET website in order to provide near-real-time qualitative information about the presence and altitudes of the volcanic cloud over Europe.

A first volcanic layer was observed at an altitude from 3 to 6 km over Hamburg in the early morning of 16 April. On the morning of 16 April, the major ash plume reached Central Europe (Germany and France) at 5–6 km a.s.l. and Belarus at ca. 4 km a.s.l. The volcanic cloud crossed Central and Eastern Europe on 16 and 17 April. Most EARLINET stations discovered a distinct feature at that time. The layer appeared first at 5–8 km a.s.l. and then decreased with time. Finally, volcanic aerosol was mixed into the ABL. After 17 April the volcanic plume was dispersed towards Western and Eastern Europe.

The transport to the south was almost completely blocked by the Alps until 19 April when a redistribution of aged volcanic aerosol from west to east and from north to south occurred. On 20 April Italian EARLINET stations observed a clear signature of the plume for the first time. Afterwards, the plume was further dispersed across Europe and reached Greece on 21 April.

The volcanic plume persisted over Central Europe for the whole period of 15–26 April, even though with different aerosol load. Only small amounts of material were emitted by Eyjafjallajökull between 19 April and 3 May. However, new significant eruptions occurred from 4–9 May and 14–19 May. The first of these phases mainly influenced Western Europe, from Great Britain to the Iberian Peninsula. EARLINET stations in Spain and Portugal reported the arrival of the first volcanic layers on 5 May [*Sicard et al.*, 2012; *Navas-Guzmán et al.*, 2013]. On 16 May, a distinct ash plume traveled over Great Britain toward Central Europe again and reached the Central European EARLINET stations in the Netherlands and Germany in the night of 16–17 May [*Schumann et al.*, 2011]. Volcanic layers were observed in Central Europe and in the Central and Eastern Mediterranean area on 18–22 May. Last observations of the event were recorded over Central Europe by 25 May.

7.3.3 Volcanic aerosol mask

A volcanic aerosol mask has been generated based on all EARLINET observations, using only aerosol backscatter coefficients at one wavelength, so that daytime measurements could be included in the study and potential observational limitations of some stations were eliminated. For each

station, the aerosol backscatter coefficient at the longest available wavelength (355, 532 or 1064 nm) range was used for the layering, thereby taking advantage of the better sensitivity to the aerosol structure at longer wavelengths. For *aerosol typing*, backtrajectory analyses together with the multi-wavelength Raman lidar measurements performed within the network during this event.

The mask was generated with a temporal resolution of 1 h. The volcanic mask is provided with the best possible effective vertical resolution, as determined individually by each group within EARLINET, typically between 60 and 180 m. Only backscatter data with a relative statistical error lower than 50% are considered in order to gain a reliable aerosol mask. The aerosol mask methodology is described in detail by *Mona et al.* [2012]. The most relevant points are therefore only summarized here in brief.

The first step is the *layer identification* through the first derivative of the particle backscatter profiles. Tests performed on several EARLINET station data identified 30% as a reasonable statistical error limit for the application of the derivative method. At altitudes where the derivative method is not applicable, because the SNR is too low, layers are identified as those regions where the scattering ratio (i.e. the total-to-molecular backscatter ratio) is higher than a pre-defined threshold chosen as the value for typical aerosol background conditions plus 15%.

The second step in the procedure is to perform a *rigorous cloud screening* on the data and to assign an *aerosol type* to each identified layer. Cloud screening is performed manually by each station (low clouds) and in a centralized way (cirrus clouds). In particular, cirrus clouds are identified on the basis of cirrus high particle depolarization ratio, neutral wavelength dependence and temporal evolution. Backward trajectory analyses and model outputs are used to investigate the origin and nature of the identified aerosol layers. In particular, ten-day HYSPLIT backtrajectory analysis is used, because the arrival altitudes and times could be chosen in a flexible way, which makes it very useful for a study on aerosol typing based on lidar data with high vertical and temporal resolution.

Once the particle path is identified through backtrajectory analysis, the type of the aerosol is investigated using model output and the support of the multi-wavelength Raman lidar measurements performed within the network. The Eyjafjallajökull volcanic activity and emission heights are also taken into account by using the reports provided by the Iceland Meteorological Office, VAAC, and dedicated studies *Langmann et al.* [2012].

Within EARLINET, it has been shown that a careful analysis based on lidar observations, airmass backtrajectories and modeling tools allows for a detailed classification of the observed aerosols [*Mona et al.*, 2006; *Pappalardo et al.*, 2010b]. The methodology described above has been manually applied to all the layers identified. In most of the cases reported in this paper, the origin and type of the observed particles are clearly defined through the backtrajectories-models combined approach. Particular attention was needed in cases of transition between different atmospheric conditions because of the high instability of the backtrajectory analysis in the transient regimes. For these cases, advanced lidar observational capability and climatological analysis available at the observational site could permit the aerosol typing. An example of the aerosol typing for this condition is reported in detail in *Mona et al.* [2012]. Situations not clearly identified with this kind of approach still remain and are reported as "unknown" aerosol in the masking.

Many types of aerosol may have been present over Europe during the whole eruptive period.

Specific models and satellite observations are used in order to check the occurrences of other specific aerosol-related events along the identified aerosol paths. The potential presence of Saharan dust for instance is checked using the *Dust REgional Atmospheric Model (DREAM)* forecasts in terms of maps of the dust loading and dust concentration profiles at each EARLINET site, both available every six hours [*BSC-DREAM*, 2014]. The results of the *ATSRWorld Fire Atlas (Advanced Along Track Scanning Radiometer)* [*ATSRWorld*, 2014] are used for identifying the presence of forest fire episodes. Cases with backtrajectories that are locally confined and without the presence of any specific source resulted in aerosol being classified as continental. For all the other cases with uncertain situations, aerosol is classified as "unknown". All possible mixes among these types of aerosol are also taken into account.

As far as volcanic aerosol is concerned, it should be noted that aerosol layers identified through this approach could consist of different *ash and sulfate mixing ratios* for different sites. Moreover, the observed particles of volcanic origin may be affected by modification processes and mixing with other air masses during transport. Aerosol layers, for which other aerosol sources besides the Eyjafjallajökull volcano can be identified, are classified as mixed aerosols.

The particle layer identification and typing is performed for each station on individual backscatter profiles. A consistency check is carried out on the temporal evolution of the resulting layering for each station. A further check is performed by taking advantage of the geographical distribution of EARLINET stations. In particular, stations located at relatively short distances (below 500 km) from each other can be considered representative for a specific region, giving us the opportunity to also study local phenomena. When a doubtful atmospheric scenario is observed in a specific region, multi-spectral Raman lidar data from at least one close station, including lidar ratio, *Ångström exponent*, and *particle linear depolarization ratio*, are used as additional information supporting aerosol typing.

In this Section, two of the four examples in *Pappalardo et al.* [2013] will be shown. The first one corresponds to the co-presence of dust and volcanic aerosol over France and other Mediterranean countries during the first phase of the eruption; and the second case example corresponds to the almost direct transport over the Iberian Peninsula at the beginning of May. The other two case examples [*Pappalardo et al.*, 2013] show the transport towards Central Europe at the end of May and the almost direct transport towards Central Europe during the first phase of the eruption.

For each example, the *aerosol mask* is reported providing in particular the following information (Fig. 7.8):

- *Minimum* and *maximum altitudes* covered in measurements. These can vary for each site depending on the corresponding lidar instrument performances and atmospheric conditions.
- *ABL height*, as derived directly by the lidar signals [*Steyn et al.*, 1999].
- *Volcanic aerosol layers* are reported in shades of grey. Different shades of grey refer to different aerosol backscatter values (β_λ), in $m^{-1}sr^{-1}$. Black: $\left(\beta_{532} > 1 \times 10^{-6}\right)$; grey: $\left(1 \times 10^{-7} < \beta_{532} < 1 \times 10^{-6}\right)$; light grey: $\left(\beta_{532} < 1 \times 10^{-7}\right)$. Black: $\left(\beta_{1064} > 5 \times 10^{-7}\right)$; grey: $\left(5 \times 10^{-8} < \beta_{1064} < 1 \times 10^{-7}\right)$; light grey: $\left(\beta_{1064} < 1 \times 10^{-8}\right)$. No distinction between ash particles and smaller non-ash particles (mainly sulfate aerosol) of volcanic origin is made.

The grey layers contain both of these components of aerosol, originating from the volcanic eruption and then eventually being subject to modifications that occur during the transport across the European continent.

- *Aerosol types:* aerosol in the ABL (mainly local) is reported in yellow; continental aerosol in dark yellow, forest fires in light green; desert dust in orange; cloud/cirrus in cyan; volcanic mixing cases are shown in magenta. If the identification of the origin of particles in a layer was not possible, the corresponding aerosol was classified as unknown (purple).

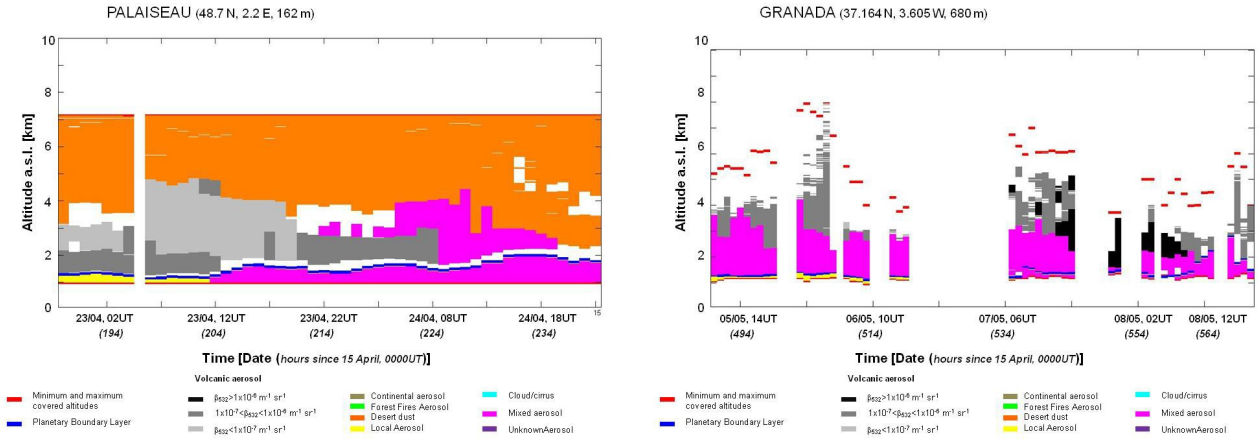

Figure 7.8: Aerosol mask for the Palaiseau and Granada sites. (*a*) Palaiseau, April, 23–24th, 2010. (*b*) Granada, May, 5–7th, 2010.

7.3.3.1 France and other Mediterranean countries

Fig. 7.8a shows the aerosol mask for Palaiseau, France, for the period 23–24 April 2010. This is a very interesting period of the eruption event, where Saharan dust above 4 km and a layer of volcanic particles beneath it was observed. Aerosol typing in situations with different long-range transported aerosols is really challenging. In such cases advanced lidar observational capability and climatological analysis available at EARLINET sites could permit the aerosol typing. In particular, intensive properties and their temporal evolution are used here for discriminating different aerosol types such as dust and volcanic particles. A detailed example of aerosol typing for mixing situations is described in *Mona et al.* [2012].

Intrusion into the ABL was observed on 23 April starting at 11:00 UTC when the top altitude of the ABL rose while volcanic particles entered into the ABL. A mixed aerosol layer consisting of volcanic particles and Saharan dust was then observed on the evening of 23 April when the Saharan dust layer started to decrease in altitude, merging with the volcanic aerosol layer.

7.3.3.2 Iberian peninsula

During most of the volcanic eruption period, the Iberian Peninsula was not affected by the presence of the volcanic cloud. The only exception was a ten-day period in May during which the wind

transported volcanic particles directly toward Spain and Portugal. Fig. 7.8b shows the volcanic aerosol mask over Granada, Spain, for the period 5–7 May 2010. This example shows a situation where volcanic particles were observed almost over the entire altitude range covered by the lidar instrument and intrusion into the ABL was also observed. Mixing of volcanic particles with local and dust particles was observed for the whole period up to an altitude of ca. 3 km. Above 3 km, the particle linear depolarization ratio was measured to be around 7%. The values of 4–5 % for the lower layer suggest the mixing of volcanic particles with other particles [*Sicard et al.*, 2012; *Navas-Guzmán et al.*, 2013].

7.3.4 Distribution of volcanic aerosol over Europe

The methodology described in Sect. 7.3.3 was applied to all EARLINET data provided individually by each station with the required 1 h temporal averaging. In this way, information about the aerosol layering and types within the whole network was gathered. Geometrical properties of the volcanic cloud over Europe are presented with high resolution (typically 60–180 m) in terms of the base and top of the volcanic layer. Once the top and the base of a layer are identified, the center of mass of the aerosol layer can be also estimated from lidar profiles. The *center of mass* gives us information about the altitude where the most relevant part of the aerosol load is located. In absence of wind, the temporal evolution of the center of mass of the aerosol layer could give insight about the dynamics of the whole layer.

Assuming the micro-physical properties to be homogeneous within an aerosol layer, the *center of mass can be estimated as the mean altitude of the identified layer weighted by the altitude-dependent aerosol backscatter coefficient* [*Mona et al.*, 2006]. Due to the large number of performed measurements the arrival of volcanic cloud over Europe could be timed very accurately. Information about cases of mixing with other aerosol types and intrusions into the local ABL was gathered.

Results are grouped into clusters representing *five geographical regions*: Central Europe – CE (Fig. 7.9), Central Mediterranean – CM (Fig. 7.10a), Western Mediterranean – WM (Fig. 7.10b), Eastern Mediterranean – EM, and Eastern Europe – EE. Following, Central Europe, Central Mediterranean and Western Mediterranean clusters will be explained. Detailed information can be found in *Pappalardo et al.* [2013]. For each cluster, the temporal evolution of the volcanic layer is reported for each station for which a long record of data is available. Stations are listed in order of decreasing latitude, i.e. from North (top) to South (bottom) for each cluster. Further data from other stations (Andoya, Cork, Garmisch-Partenkirchen, Neuchatel, Payerne, Sofia, Barcelona, and Madrid) are not shown in the figures.

Starting from 15 April, 00:00 UTC, the *following quantities are provided hourly*:

- *Center of mass* of the identified volcanic layer (multiple layers are regarded as a unique extended layer).
- *Base and top* of the identified volcanic layer. These quantities are shown as black dots, blue lines, and cyan lines, respectively.
- *Scenarios* where a layer with volcanic aerosol mixed with another kind of aerosol are noted

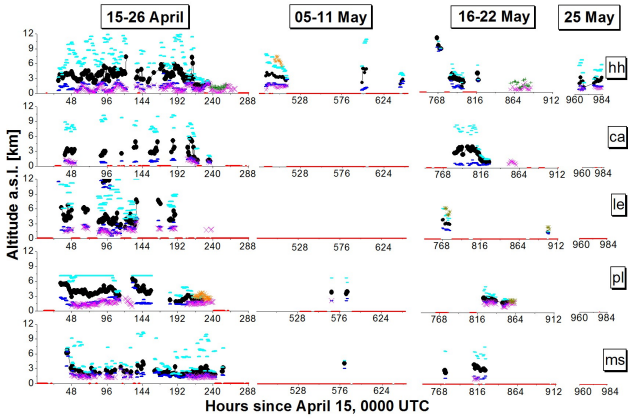

Figure 7.9: Results for Central Europe cluster: Hamburg (hh), Cabauw (ca), Leipzig (le), Palaiseau (pl) and Maisach (ms). The following quantities are reported hourly: center of mass of the identified volcanic layer (black dots), base and top of the identified volcanic layer (blue and cyan lines, respectively). Mixing with dust and continental aerosol is highlighted by orange and dark yellow symbols, respectively. Mixing with local aerosol above the ABL is reported in green. The intrusion in the ABL and, therefore, the mixing with local aerosol is indicated by a magenta cross located at the top of the ABL as obtained from lidar observations. Red line on the abscissa axes indicates no measurements.

as well. For these cases the center of mass of the mixed layer is indicated.

- *Mixes with dust and continental aerosol* are highlighted by orange and dark yellow symbols, respectively.
- *Mixing with local aerosol* above the ABL is reported in green.
- The *intrusion into the ABL* and the subsequent mixing with local aerosol is indicated by magenta crosses located at the top of the ABL.

All cirrus clouds have been removed following the methodology described above, even though the presence of volcanic particles within the cirrus clouds cannot be ruled out and probably occurred regularly in the time period concerned. However, this aspect is outside the scope of the current publication and a devoted study related to cloud properties during the volcanic event would be required to address this issue.

Finally, a red line is shown on the abscissa axes of the figures for hours when no measurements were performed. This situation typically arose during adverse weather conditions, but sometimes also because of technical problems. It should be noted that the network is not designed to be fully operational around the clock and that intensive measurement series lasting for more than one month imply a considerable effort for most of the stations.

Geometrical and optical properties of the volcanic layers are reported for each cluster in Table 7.3. Specifically, median values and minimum/maximum range values of base, top, center of mass, aerosol backscatter coefficient, and *integrated backscatter*, $IB = \int_{Z_l}^{Z_u} \beta_{aer}(u)dr$ (where Z_l and Z_u are the lower and upper limits of the observed layer, respectively) at 532 nm are provided together with the maximum aerosol backscatter coefficient value (peak value) with corresponding altitude, location, and time. The aerosol backscatter coefficient at 532 nm has been chosen because it is available in each cluster.

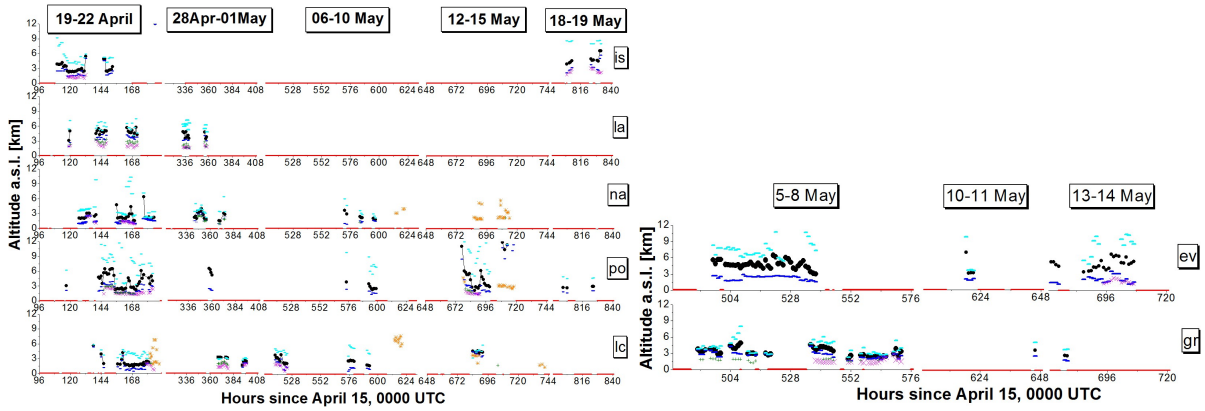

Figure 7.10: Results for Central and Western Mediterranean clusters. (*a*) Same as Fig. 7.9 for Central Mediterranean cluster: Ispra (is), L'Aquila (la), Naples (na), Potenza (po) and Lecce (lc). (*b*) Same as Fig. 7.9 for Western Mediterranean cluster: Evora (ev) and Granada (gr).

Cluster	Base [km]	Top [km]	CoM [km]	IB[$10^{-3} sr^{-1}$]	β	PA	Maxβ	Max T [UTC]
Central Europe	1.7	6.5	3.3	1.0315	3.6 ± 2.6	2.8	26.6×10-6	16 April 2010 –
	0.2–11.7	1.6–14.5	1.0–13.0	0.016–26	0.8–99.9			05:00 (hh)
Central	2.0	5.2	3.1	1.18	5.8 ± 3.9	3.1	6.7 × 10-6	20 April 2010 –
Mediterranean	0.5–13.8	2.1–16.2	1.4–14.5	0.009–9.2	0.4–19.2			08:00 (is)
Western	2.5	6.2	4.1	0.6865	2.1 ± 1.2	3	17.9×10-6	13 May 2010 –
Mediterranean	1.1–7.4	1.7–18.1	1.5–7.9	0.003–6	0.2–42.2			06:00 (gr)
Eastern	1.8	5.0	2.7	1.988	7.1 ± 5.3	1.3	5.02×10-6	22 April 2010 –
Mediterranean	1.0–6.4	1.7–12.2	1.5–7.7	0.02–10	0.6–23.4			17:00 (th)
Eastern Europe	3.5	5.7	4.5	0.48	1.8 ± 0.5	2.3	1.35×10-6	17 April 2010 –
	1.2–8.2	2.9–13.4	2.8–8.2	0.3–2	0.8–3.4			14:00 (mi)

Table 7.3: Geometrical and optical properties of the volcanic layers for each of the clusters: median value and minimum-maximum range value of base, top, center of mass (CoM), IB [10^{-3}sr^{-1}] and β [10^{-7}m$^{-1}sr^{-1}$] at 532 nm are reported together with the maximum backscatter value (peak value [m$^{-1}sr^{-1}$]) with corresponding altitude (PA) [km], location, and time.

Central Europe cluster.- During the first period (15–26 April) all stations within the CE (Hamburg, Cabauw, Leipzig, Palaiseau, and Maisach) observed volcanic particles (Fig. 7.9). Clouds were also very frequently observed. Low clouds over Cabauw often did not permit lidar data inversion. In the successive periods substantial cloud cover and rain limited the possibility to perform measurements, hence data had to be taken more sporadically. The center of mass of the volcanic layer was typically around 3–3.5 km for all stations apart from Maisach where it remained at about 2.5 km. Intrusion into the ABL was a common feature for almost all observations. In the case of Maisach the volcanic layer came into contact with the boundary layer during the afternoon of 17 April. The process of mixing of the ash with locally produced aerosol was investigated with a very high temporal resolution of one hour [*Groß et al.*, 2011].

Typical volcanic layers were observed between 1.7 and 6.5 km height. Measured aerosol backscatter coefficients at 532 nm ranged from the minimum of 0.8×10^{-7} m^{--1}sr^{-1} to the maximum values of 26.6×10^{-6} m^{-1}sr^{-1} observed at an altitude of 2.8 km over Hamburg at 05:00 UTC on 16 April. The latter value represented the largest aerosol backscatter coefficient measured by EARLINET over Europe for the whole event. Extensive and intensive optical properties observed by the multispectral Raman lidar systems available in this region, together with sun photometer observations, allowed for the discrimination between sulfate particles and ash in the most intense volcanic layers [*Ansmann et al.*, 2011].

Central Mediterranean cluster.- Ispra, L'Aquila, Naples, Potenza, and Lecce (see Fig. 7.10a) observed the volcanic cloud later in comparison to the Central Europe cluster. All the Italian stations observed the volcanic cloud in the period 19–22 April 2010 with the center of mass of the volcanic layer at lower altitudes (at about 2.8 km) compared to the Central Europe cluster. During 6–10 May and 12–15 May, when there was air mass transport from the west, the volcanic cloud was observed only over the southern stations (Naples, Potenza, and Lecce). In the period 18–19 May, the volcanic cloud was observed also in Northern Italy, over Ispra, in agreement with observations in the Central Europe cluster and over Maisach in particular.

An apparent descending layer between 10 and 5 km a.s.l. was observed over Potenza from 21 April, 02:00 UTC to 11:00 UTC (146 to 155 h since 15 April, 00:00 UTC). In the Central Mediterranean cluster, intrusion into the ABL was also observed very often. Mixing with Saharan dust also occurred during May for all southern stations.

The values of the aerosol backscatter coefficient were much lower compared to those measured over Central Europe. Here typical backscatter coefficient values at 532 nm were around 5.8×10^{-7} m^{-1}sr^{-1} with a maximum of 6.7×10^{-6} m^{-1}sr^{-1} observed over Ispra on 20 April, 08:00 UTC. Extensive and intensive optical properties measured in this cluster revealed the presence of mainly sulfate aerosols with the presence in few cases of some aged diluted ash [*Mona et al.*, 2012; *Perrone et al.*, 2012].

Iberian Peninsula.- Was affected by the volcanic cloud only for few days in May when the wind transported the plume from Iceland towards the southwest. The weather was quite unstable, characterized by the presence of clouds and rain over the peninsula. Only few sporadic measurements were possible over Barcelona and Madrid and are therefore not reported here. More measurements were possible for more western stations: Evora and Granada. The results are shown in Fig. 7.10b.

First observations of the volcanic cloud were made on 5 May, 10:00 UTC (490 h since 15 April, 00:00 UTC) over Granada. The typical altitude for the center of mass of the volcanic layer was about 4.1 km. Similar patterns in the center of mass behavior were observed at both stations on 6 May. There was, however, a time delay of about 8 h between Granada (535 to 544 h since 15 April, 00:00 UTC) and Evora (527 to 537 h since 15 April, 00:00 UTC). Data from Evora furthermore showed the center of mass to be approximately 300 m higher than over Granada.

Typical aerosol backscatter coefficient values at 532 nm were found to be for this cluster around 2.1×10^{-7} $m^{-1}sr^{-1}$ with the maximum of 19.7×10^{-6} $m^{-1}sr^{-1}$ observed over Granada at 06:00 UTC on 13 May. Multi-wavelength Raman lidar data from Granada were also used to retrieve microphysical properties during the night from 7 to 8 May. Particle effective radius ranged from 0.30 ± 0.11 to 0.55 ± 0.13 μm in the volcanic plume along this night. This study indicated that the volcanic plume over this station was mainly composed by sulfate and sulphuric acid droplets [*Navas-Guzmán et al.*, 2013].

Fig. 7.11 provides an overview of the volcanic aerosol content as observed by EARLINET. IB at 532 nm is reported because the dataset of this optical property is the most abundant. For each cluster the mean IB evaluated inside the volcanic aerosol layer identified and discussed above and averaged inside the cluster is reported for each hour of observation. As a reference, the IB as measured at a representative site inside each cluster is reported too. Three main periods (15–26 April, 5–13 May and 17–20 May) are observed by the network and are characterized by: different vertical distributions (discussed above), different amounts of volcanic particles, specific horizontal path, and different modification and dispersion processes over Europe. During the first phase (15–26 April), the volcanic cloud moved from the CE cluster down to the CM and then to EM. An almost constant IB at 532 nm over the clusters (around 0.007 sr^{-1}) was observed in the first hours of the volcanic cloud observation. A sudden decrease in the IB values was found for all the 3 interested clusters down to 0.002 sr^{-1} for CE and 0.001 sr^{-1} for CM and EM. For the sake of completeness, it is important to remember here that just a few hourly data of high IB at 532 nm are measured over Hamburg in the early 16 April (see Table 7.3) which are out of the Fig. 7.11 scale. On the contrary, small IB values are observed over EE and there are no observations of the volcanic cloud over the WM.

During the second period, the volcanic aerosol content was instead around 0.005 sr^{-1} over the WM and was considerably reduced in intensity during the transport over Europe toward CE, CM, EM and EE. The third interesting phase (17–20 May) was characterized by moderately high IB values (around 0.003 sr^{-1}) on CE, CM and EM clusters. In this case, the IB over southern regions was occasionally higher than CE ones, probably because of aging processes of the particles.

All these results are in fair agreement with the volcanic cloud dispersion as forecast by *EURAD (EURopean Air Pollution Dispersion)* [*EURAD*, 2014] model: a complex dispersion of the volcanic cloud over a large part of Europe for the first days after 15 April (Fig. 7.12a), the transport from Iceland to the Iberian peninsula and afterwards in the west-east direction for the first days of May (Fig. 7.12b) and finally a well-defined transport along the north-west to south-east for the last part of the event (Fig. 7.13). Overlaying the EURAD forecast with maximum in IB as observed by EARLINET stations (Figs. 7.12 – 7.13) allows for a better appreciation of the fair agreement

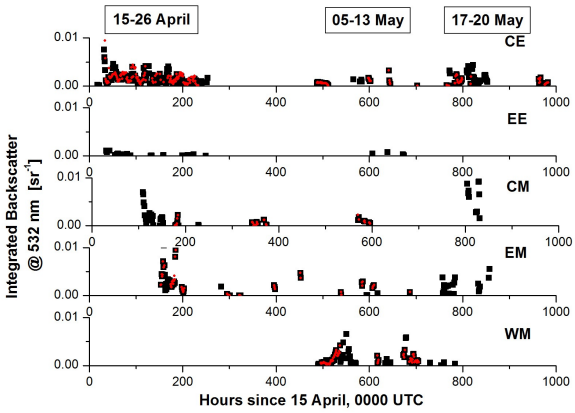

Figure 7.11: IB at 532 nm measured by EARLINET in the volcanic layers over the 5 clusters: Central Europe (CE), Eastern Europe (EE), Central Mediterranean (CM), Eastern Mediterranean (EM), and Western Mediterranean (WM). Mean values observed over the cluster are reported as black squares. Values measured at representative site for each cluster are reported as red dots: Hamburg, Belsk, Naples, Thessaloniki and Evora stations were selected as representative because of their large number of backscatter measurements at 532 nm.

between model and observations. The illustration is based on the EURAD forecast provided on the website daily during the event.

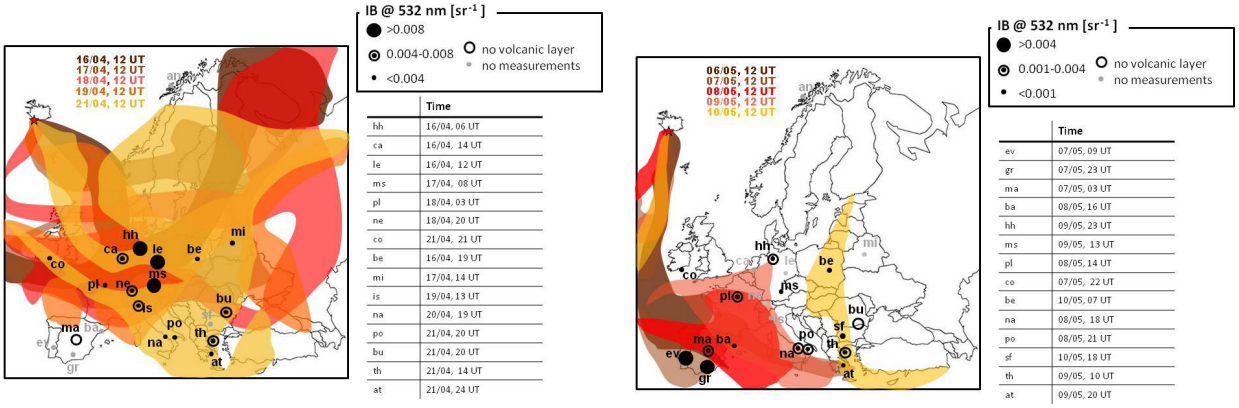

Figure 7.12: Dispersion of the Eyjafjallajökull (red star) volcanic aerosol plume (the approximate location of the plume). (*a*) 3–5 km height range for 12:00 UT on 16 April (dark brown), 17 April (light brown), 18 April (red), 19 April (orange), and 21 April 2010 (yellow). (*b*) 3–5 km height range for 12:00 UT on 6 May (dark brown), 7 May (light brown), 8 May (dark red), 9 May (light red), and 10 May 2010 (yellow). The maximum IB at 532 nm measured by each station is reported in black. The exact time location of the maximum IB is reported in the legend.

7.3.5 RSLab measurement, May 8^{th}, 2010

The RSLab conducted measurements during the volcanic alert whenever the atmospheric conditions allowed to do (no low clouds, no rain). The atmospheric conditions in the Iberian peninsula were much better for EARLINET Granada's lidar station, which caused that not enough Barcelona records were included in *Pappalardo et al.* [2013].

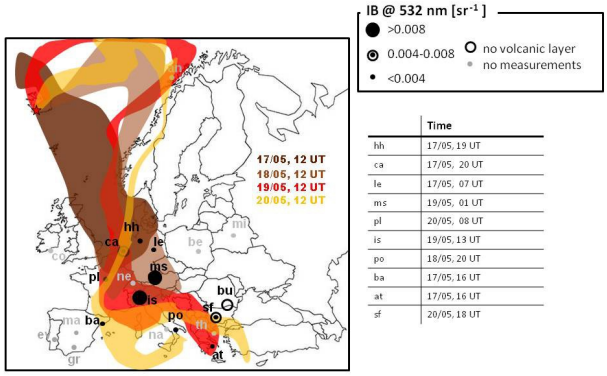

Figure 7.13: Map of Europe showing the dispersion of the Eyjafjallajökull (red star) volcanic aerosol plume during the 17–20 May 2010 period. The approximate location of the plume in the 3–5 km height range is given for 12:00 UT on 17 May (dark brown), 18 May (light brown), 19 May (red), and 20 May 2010 (yellow). The maximum IB at 532 nm measured by each station is reported in black. The exact time location of the maximum IB is reported in the legend.

It must be noted that the measurements were taken using the RSLab 2+1 lidar system [*Sicard et al.*, 2010], because the actual 3+3 multi-spectral lidar system had just been deployed. However, from the KFS inversion algorithm point of view, there is no difference between the range-corrected lidar signals from either lidar system. Unlike Nabro's case, only the analog signal was needed since the volcanic layer fell in the near range.

Fig. 7.14 is a 1-h measurement example showing the volcanic layer intrusion into the ABL for the 8^{th} of May, 2010, starting at 15:32 UTC.

According to HYSPLIT back-trajectories (not shown), layer between 2 to 3 km corresponds to the volcanic plume coming from Eyjafjallajökull volcano. Regarding to KFS inversion, the RSLab assumed a range-independent lidar ratio, S_{aer}, of 50 sr at 532-nm channel. The AOD value was 0.10 and it was computed using the methodology presented in *Reba* [2010].

7.3.6 Discussion

First of all we can conclude that the EARLINET network, even if not operative, covered the volcanic cloud dispersion in each identified phase, providing a detailed 4-D analysis of the event. In general there is good agreement in terms of timing of peak observations and in terms of aerosol amount: larger IB values are observed at stations interested for the first by the plume transport, afterwards a decrease in IB is observed moving far from the source. Differences are found in some cases in particular for stations located at the boundary of the dispersion plume. More details about the Eyjafjallajökull 2010 EARLINET relational database can be found in the data user manual available on the EARLINET website.

Quantitative optical data, specifically aerosol backscatter and extinction coefficient profiles and particle linear depolarization ratio at different wavelengths, are also available in the EARLINET database, in the volcanic category. From these data, it is possible to derive lidar ratio and Ångström exponent data.

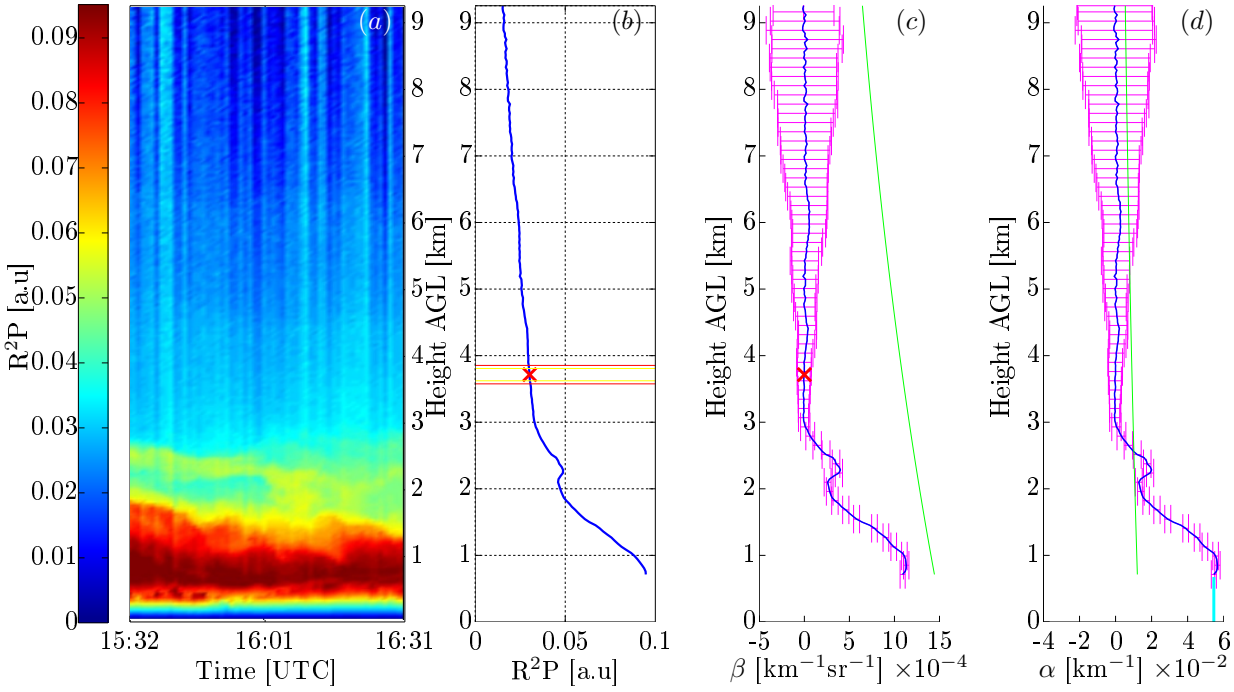

Figure 7.14: Optical-atmospheric parameters inversion example for Eyjafjallajökull volcanic event (Barcelona UPC, Campus Nord, May, 8^{th}, 2010) by using RSLab Link-Detect GUI lidar inversion platform. KFS method was used [*Klett*, 1985]. (*a*) Time-height plot of the analog range-corrected lidar signal for the 532-nm channel. (*b*) Time-averaged range-corrected lidar signal. The calibration range is 3.7 km (red cross).The range interval (red lines) where the power calibrations is smoothed is ± 100 m. (*c*) Aerosol (blue trace) and molecular (green trace) backscatter coefficients, β_{aer} and β_{mol}, respectively. Error bounds have been computed according to Sect. 3.4. (*d*) Aerosol (blue) and molecular (green) extinction coefficients, α_{aer} and α_{mol}, respectively. The S_{aer} is 50 sr, and the estimated AOT is 0.10 [*Reba et al.*, 2010].

Table 7.4 summarizes the values for geometrical and optical properties (aerosol optical depth, lidar ratio, linear particle depolarization ratio, and Ångström exponent) observed from specific EARLINET multi-wavelength Raman lidar stations in specific periods of the event.

Date and hour UTC	Location	Height $[km]$	AOD_{532}	$S_{355}[sr]$	$S_{532}[sr]$	δ_{355}	δ_{532}	355/532
16-04-10, 14:15–15:30	Leipzig	2.6–4.3	0.35	60 ± 5	60 ± 5		0.33 ± 0.03	0.03 ± 0.40
17-04-10, 01:40–02:30	Munich	2.6–3.5		50–60	55 ± 5	0.35 ± 0.02	0.37 ± 0.02	-0.11 ± 0.18
20-04-10, 21:00–23:05	Potenza	2.0–3.0		42 ± 2	50 ± 3		0.15 ± 0.03	1.4 ± 0.2
07-05-10, 00:30–01:30	Evora	2.7–3.7	0.07	39 ± 10	32 ± 4			0.68 ± 0.63
08-05-10, 03:30–04:30	Granada	2.6–2.9		47 ± 7	48 ± 16		0.066 ± 0.005	0.79 ± 0.54
13-05-10, 20:16–21:01	Potenza	1.5–2.3		60 ± 11	78 ± 12		0.16 ± 0.07	1.1 ± 0.4
17-05-10, 20:15–20:45	Cabauw	2.7–6	0.53	42 ± 1	44 ± 24		0.30 ± 0.03	0.1 ± 1.1
19-05-10, 20:30–21:30	Athens	3.0–4.8	0.05	67 ± 13	89 ± 3			0.57 ± 0.26

Table 7.4: Values for geometrical properties and optical properties (aerosol optical depth (AOD), lidar ratio (S), linear particle depolarization ratio (δ), and Ångström exponent) observed from specific EARLINET multi-wavelength Raman lidar stations in specific periods of the Eyjafjallajökull eruption (April–May 2010). The table reports also the retrieved volcanic aerosol type.

7.4 Conclusion

Ground-based lidar networks are specially valuable during large scale events like long range transport of dust and smoke or major volcanic eruptions, e.g. volcano Eyjafjallajökull, Iceland in 2010 [*Pappalardo et al.*, 2013; *Sicard et al.*, 2012] for they can reliably vertically resolve the aerosol layers within the atmosphere. Multi-wavelength Raman lidar retrievals for example, can help track the evolution of the aerosol properties as they age while transported [*Mattis et al.*, 2010; *Noh et al.*, 2011; *Alados-Arboledas et al.*, 2011]. And in volcanic events, lidars have also demonstrated to be a good validation and/or input tool for transport models and retrievals of SO_2 again thanks to lidars' vertical resolving capabilities [*Carn et al.*, 2007]. In an effort to facilitate knowledge and data exchange between lidar groups, the GALION was formed envisioning the cooperation among existing lidar networks and also independent research institutes that carry lidar measurements across the globe.

First application case.- In this study, although not formally in the framework of GALION, it was shown how the synergy proposed by it would aid the scientific community to rapidly assess the outcome of future (and possibly more explosive) volcanic eruptions.

The AOD values obtained from lidar data at 532 nm in this study (excluding Sede Boker) ranged from 0.003 to 0.04, with an average of 0.018 ± 0.009 with S_{aer} ranging from 38 to 50 sr. At 355 nm (CNR-IMAA, OHP and Granada) AOD ranged from 0.04 to 0.05. CALIOP global retrieval obtained a maximum AOD of 0.03 at 532 nm mostly over Eastern Europe and Asia. As previously mentioned, the AOD calculation from most of our lidar data (with exception of CNR–IMAA group) relies on a reasonable estimation for the S_{aer} value. 50 sr is likely to be close to the upper limit of acceptable values of S_{aer} for sulfate aerosols in the stratosphere, which would then result in even lower AOD values. In either case, it is unlikely that the aerosol generated after Nabro's eruption would have a significant long-term effect on the radiative balance of the atmosphere like Pinatubo did.

Second application case.- EARLINET made a very substantial effort to monitor the Eyjafjallajökull eruption event in April–May 2010 by performing almost continuous lidar measurements

during the entire period. The coordinated observations by EARLINET and a methodology that was specifically designed ad hoc for this event provided a detailed description of the 4–D distribution of the volcanic cloud over Europe for the whole event. Geometrical properties of the volcanic cloud over Europe were provided with high vertical resolution (typically 60–180 m) in terms of base, top, and center of mass of the volcanic layer.

Mixing of volcanic particles with other kind of aerosol (dust, continental and local) was identified. Mixing with Saharan dust was observed mainly during May for all southern stations.

The results about the 4–D distribution of the volcanic cloud are reported in a specific relational database available on request through the EARLINET website.

Quantitative optical data, specifically aerosol backscatter and extinction coefficient profiles, linear depolarization ratio at different wavelengths, and derived lidar ratio and Ångström exponent profiles, are available through the EARLINET database in the volcanic category.

Chapter 8

Conclusions

This Chapter gives concluding remarks and future research lines mainly derived from Chaps. 2–7 of this Ph.D thesis.

8.1 Conclusions

On backscatter-coefficient inversion error bounds.- Considering the two-component KFS lidar inversion algorithm for elastic lidar signals (i.e., without wavelength shift in reception) two different types of error bounds have been formulated in Chapter 3: first-order error bounds (Sect. 3.3) and total-increment error bounds (Sect. 3.4). Major achievements are that (*i*) their mathematical formulation is in explicit analytical form (Tabs. 3.3-3.4) and (*ii*) error sources 1-4, namely, the systematic error due to the backscatter-coefficient calibration (error source 1), the systematic error due to the range-dependent lidar ratio (error source 2), and random errors due to the measurement noise at the calibration cell (error source 4) and at all-other range cells (error source 3) are considered.

First-order error bounds have been obtained by using classic error-propagation techniques and hence, they yield symmetric approximate bounds around the true backscatter-coefficient profile. Error bound amplitudes encompass most of Monte-Carlo's (MC) inverted population of backscatter profiles in many practical situations (SNR$\geq$5, lidar-ratio relative error strength, p$<$30% , Sect. 3.5).

Total-increment error bounds (exact) at 3-σ yield exact results coincident with MC envelopes for error sources 1, 2, and 4. Exact error bounds have not been found for error source 3 because of the multi-dimensionality of the problem.

Though conceptually different, error sources 1 and 4 cause similar effects on the inversion of the backscatter coefficient via Eq. 3.10, and thus, error sources 2 and 4 are the ones of most concern. This Ph.D. contribution assimilates a long-time effort encompassing works from two others Ph.D.s, *Reba* [2010]; *Kumar* [2012] in *Rocadenbosch et al.* [2012].

On ABLH retrieval using an Extended Kalman Filter (EKF).- Two different remote sensing applications of the EKF retrieval of the ABLH have been presented in Chap. 5 (lidar case, *Lange et al.* [2013]) and Chap. 6 (clear-air S-band radar case, peer-review journal publication in preparation).

In the EKF application to ABLH estimation from *backscattered lidar returns*, it has been shown that in atmospheric scenes with a well-mixed mixing layer, with no stratifications (single layer), and under high-SNR conditions (typically, SNR$\geq$10 at the end of the ML) both classic ABLH-detection methods (GM, LGM, IPM, THM, VCM) perform acceptably well yielding unambiguous results (Fig. 5.2). The key advantage of the EKF arises under low-SNR conditions where the filter clearly outperforms classic ABLH-estimation methods. This is due to its capability to yield time-continuous ABLH estimates, with no outliers or drop-outs in its estimates and without degrading the temporal and spatial resolution of the lidar instrument. Besides, this time-continuous feature of the filter is a consequence of the way it combines past estimates with present ones in order to match the lidar observables with the projected ones under a mean-square-error criterion over time, and the way the filter assimilates "a priori" error-uncertainty, model, and noise information via covariance matrices. In this present implementation of the filter an erf-like function has been used to model the single-layer ML-FT transition departing from the work of *Tomás* [2011]. Therefore, this predictive behavior is optimal to follow the convective boundary layer and residual layer along the atmospheric diurnal cycle.

When the EKF is compared with classical ABLH-estimation methods, derivative methods (GM, LGM) perform well only if the lidar-signal raw data is time averaged and range smoothed long enough to sufficiently boost the SNR prior to application of these derivative methods. Nevertheless, this is in exchange of deteriorating the time and spatial resolution of the ABLH estimates. Under these circumstances, the IPM performs poorly than the GM and the LGM because taking first- and second-order derivatives on the range-corrected lidar signal observable largely amplifies measurement noise. On the other hand, the THM (non-derivative method) is hampered by the difficulty to set a constant (i.e., non-adaptive) and physically consistent threshold to estimate the ABLH over time.

The results above have been derived from practical measurements carried out with the RSLab lidar (see discussion case in Sect. 5.3 5.3).

In the EKF application to ABLH estimation from *clear-air S-band radar returns* in CBL conditions, its formulation departs from that of the lidar case but warrants some comments: *First*, because the atmospheric returns of interest are due to refractive-index turbulence (Bragg's scattering) and not to atmospheric aerosols and molecules as in the lidar case, Rayleigh's scattering from insects and birds becomes a major interferent noise source in this band of frequencies. *Second*, the fast ML-FT transition characteristic of the EZ continues to enable application of the erf-like model but, in contrast to the lidar case, radar returns in the ML and FT "plateau" intervals ($[R_1, R_1']$ and $[R_2', R_2]$, respectively) become severely distorted in shape (Fig. 6.2), which is the most prominent modeling error. *Third*, there was a much faster variability of the ABLH in the atmospheric scenes studied, which imposes a further tracking difficulty to the filter.

The present radar-EKF implementation has solved these difficulties as follows: (*i*) "Insect" noise has virtually been canceled out by pre-processing the raw-radar reflectivity signal following Fig. 6.3 block diagram (see example in Fig. 6.1). (*ii*) The unwanted departure from the idealized erf-like mode has been solved by treating it as "modeling" noise and by assimilating it in the Kalman filter loop via the noise-covariance matrix, which has been estimated at each successive time t_k. (*iii*)

Adaptive range boundaries, $[R_1, R_2]$ and $[R'_1, R'_2]$, have been used to better inform the filter about the ML and FT intervals.

Radar-ABLH estimates have been validated against a Vaisala CL-31 lidar ceilometer (910-nm wavelength) at NOAA's Boulder Atmospheric Observatory (BAO), Erie, Colorado as part of the 3-month stay of the candidate at the Dept. of Electrical and Computer Engineering of the University of Massachusetts (UMass) during this Ph.D. The correlation coefficient obtained between both instruments is ρ=0.93.

On RSLab lidar exploitation (elastic-wavelength channels).- A new "gluing" algorithm has been presented in Chap. 4 to enhance the dynamic range elastic-wavelength channels (mainly, 355- and 532-nm wavelengths) providing simultaneous photon-counting (PC) and analog acquisition of the lidar returns. In simple words, the gluing algorithm fits the analog record to the dead-time-corrected PC record in a range interval where both acquisition channels operate linearly. While in Licel's gluing algorithm the range interval depends on which kind of photo-detector is being used, the enhanced data-gluing algorithm presented in this Ph.D. automatically determines the spatial range where both analog and photon-counting signals are more similar to glue them by using a combined fitting-error-norm and SNR criterion. Besides, formulation of both Licel's (classic algorithm) and "new" gluing algorithm has been presented in least-squares (LSQ) signal-processing form (Fig. 4.1).

Concerning *exploitation of the RSLab lidar for atmospheric observation*, two application cases have been discussed in Chap. 7:

As mentioned, it has been shown how ground-based lidar networks become specially valuable during large-scale events of dust and smoke transport as in the eruptions of Eyjafjallajökull volcano (Iceland 2010) [*Pappalardo et al.*, 2013] and Nabro volcano (Ethiopia, 2011) [*Sawamura et al.*, 2012] in order to identify the aerosol layers within the troposphere, track the evolution of aerosol properties and as inputs for transport models and retrievals of SO_2.

In the *first application case* (Sect. 7.2), the AOD values obtained from lidar data at 532 nm (excluding Sede Boker) ranged from 0.003 to 0.04, with an average of 0.018 $\pm$ 0.009 with S_{aer} ranging from 38 to 50 sr. Because in the AOD calculation all involved research groups (except CNR-IMAA) used an estimated lidar ratio value of 50 sr (likely to be close to the upper limit of acceptable values for sulfate aerosols in the stratosphere) the AOD values given may even be slightly overestimated.

In the *second application case* (Sect. 7.3) EARLINET lidar network has been shown an example of coordinated continuous measurements to continuously monitor Eyjafjallajökull eruption event (April-May 2010). The results of the 4-D (space-time) distribution of the volcanic cloud (geometrical properties o the volcanic cloud cover, mixture composition of the volcanic particles with other kinds of aerosols, quantitative optical extinction and backscatter coefficients, depolarization ratio, lidar ratio, spectral dependency) are reported in a specific relational database available on request through the EARLINET website, *EARLINET* [2013].

All in all, atmospheric remote sensing by means of lidar, clear-air radar, and cooperative sensors (e.g., radiometers, sun-photometers, and in-situ sensors), specially when operated in network multi-spectral fashion and in combination with appropriate signal processing tools and transport

models holds promise of successful monitoring of our planet. GALION (Global Atmospheric Watch Aerosol Lidar Observation Network)-GEOSS (Global Earth Observation System of Systems) are key initiatives towards this aim.

8.2 Future lines

(1) It has been shown that the EKF can be applied to different types of active remote sensing systems (lidar/ceilometer, clear-air S-band radar) with excellent results. Thus, both the lidar-EKF and the radar-EKF estimate the ABLH in good agreement with well-known classic methods, and clearly outperform them when the SNR is low or when interferent noise ("insect" noise in the radar case) is present. This is done without virtually degrading the temporal or spatial resolution. Within this framework, three future research lines arise:

- Improve the present realization of the EKF towards the identification of multiple layers in the ABL (e.g., dust layers, fire plumes), intruding clouds, and towards the identification of the stable, convective, and residual boundary layers.
- Regarding the radar reflectivity and, as proposed by one of the reviewers of this PhD, it is recommended to also test a different model for the ABL radar-reflectivity profile (instead of the erf-like profile used in Chap. 6, which might yield even better results. Specifically, removing the assumption that the radar reflectivity is uniform throughout the mixing layer. Hints to such a profile shape are given in *Fairall* [1987].
- Concerning the lidar (and the collocated EU-project NEPTUNE within the RSLab), it is recommended to extent the application of the EKF-ABLH estimation to the Doppler lidar case, from which wind velocity and direction in the ABL can be used as measurement observables to the filter.
- Test the ABLH-EKF estimation approach in atmospheric instruments other than lidars and radars.

(2) The fact that analytical error bounds in explicit mathematical form (joint research work) have been derived for the optical atmospheric backscatter coefficient warrants a similar effort to be developed for the extinction error bounds.

(3) Last but not least, it is recommended to better exploit the synergy between remote sensing instruments (e.g., lidar-radar, lidar-radiometer, radar-radiometer) in the same way that lidar, sun-photometer, and radiosonde data is systematically analyzed in nearly all EARLINET stations.

Appendix A

List of Publications

A.1 Journals

1. Wang, Y., K. N. Sartelet, M. Bocquet, P. Chazette, M. Sicard, G. D'Amico, J. F. Léon, L. Alados-Arboledas, A. Amodeo, P. Augustin, J. Bach, L. Belegante, I. Binietoglou, X. Bush, A. Comerón, H. Delbarre, D. García-Vízcaino, J. L. Guerrero-Rascado, M. Hervo, M. Iarlori, P. Kokkalis, D. Lange, F. Molero, N. Montoux, A. Muñoz, C. Muñoz, D. Nicolae, A. Papayannis, G. Pappalardo, J. Preißler, F. Rocadenbosch, K. Sellegri, F. Wagner, and F. Dulac, Assimilation of lidar signals: application to aerosol forecasting in the Mediterranean basin, *Atmospheric Chemistry and Physics Discussions*, 14 (9), 13,059-13,107, doi: 10.5194/acpd-14-13059-2014, 2014.

2. Lange, D., J. Tiana-Alsina, U. Saeed, S. Tomás, and F. Rocadenbosch, Atmospheric boundary layer height monitoring using a Kalman Filter and backscatter lidar returns, *Geoscience and Remote Sensing, IEEE Transactions on*, PP(99), 1-12, doi: 10.1109/TGRS.2013.2284110, in press (accepted on October 24, 2013), 2013.

3. Pappalardo, G., L. Mona, G. D'Amico, U. Wandinger, M. Adam, A. Amodeo, A. Ansmann, A. Apituley, L. Alados Arboledas, D. Balis, A. Boselli, J. A. Bravo-Aranda, A. Chaikovsky, A. Comeron, J. Cuesta, F. De Tomasi, V. Freudenthaler, M. Gausa, E. Giannakaki, H. Giehl, A. Giunta, I. Grigorov, S. Groß, M. Haeffelin, A. Hiebsch, M. Iarlori, D. Lange, H. Linné, F. Madonna, I. Mattis, R.-E. Mamouri, M. A. P. McAuliffe, V. Mitev, F. Molero, F. Navas-Guzman, D. Nicolae, A. Papayannis, M. R. Perrone, C. Pietras, A. Pietruczuk, G. Pisani, J. Preißler, M. Pujadas, V. Rizi, A. A. Ruth, J. Schmidt, F. Schnell, P. Seifert, I. Serikov, M. Sicard, V. Simeonov, N. Spinelli, K. Stebel, M. Tesche, T. Trickl, X. Wang, F. Wagner, M. Wiegner, and K. M. Wilson, Four-dimensional distribution of the 2010 Eyjafjallajökull volcanic cloud over Europe observed by EARLINET, *Atmospheric Chemistry and Physics*, 13 (8), 4429-4450, doi: 10.5194/acp-13-4429-2013, 2013.

4. Rocadenbosch, F., S. Frasier, D. Kumar, D. Lange, E. Gregorio, and M. Sicard, Backscatter Error Bounds for the Elastic Lidar Two-Component Inversion Algorithm, *Geoscience and Re-*

mote Sensing, IEEE Transactions on, 50 (11), 4791-4803, doi: 10.1109/TGRS.2012.2194501, 2012.

5. Sawamura, P., J. Vernier, J. Barnes, T. Berkoff, E. Welton, L. Alados-Arboledas, F. Navas-Guzmán, G. Pappalardo,L. Mona, F. Madonna, D. Lange, M. Sicard, S. Godin-Beekmann, G. Payen, Z. Wang, S. Hu, S. Tripathi, C. Córdoba-Jabonero, and R. Hoff, Stratospheric AOD after the 2011 eruption of Nabro volcano measured by lidars over the Northern Hemisphere, *Environmental Research Letters*, 7 (3), 034,013, doi:10.1088/1748-9326/7/3/034013, 2012.

- Lange, D., S. Frasier, J. Tiana-Alsina, and F. Rocadenbosch, Atmospheric Boundary Layer Height estimation using a Kalman Filter and a FMCW radar, *Geoscience and Remote Sensing, IEEE Transactions on*, in preparation.

A.2 International Conferences

1. Totems, J., M. Sicard, S. Bertolin, M. Boytard, P. Chazette, A. Comerón, F. Dulac, S. Hassanzadeh, D. Lange, F. Marnas, C. Muñoz, and S. Xi, In-situ, sunphotometer and Raman lidar observations of aerosol transport events in the western Mediterranean during the June 2013 ChArMEx campaign, in *EGU General Assembly Conference Abstracts*, vol. 16, Vienna, Austria, accepted, 2014.

2. Papagiannopoulos, N., G. D'amico, A. Giunta, G. Pappalardo, L. Alados-Arboledas, A. Amodeo, L. Belegante, M. Iarlori, D. Lange, R. E. Mamouri, M. A. Mcauliffe, D. Nicolae, P. Kokkalis, J. Preißler, J. Putaud, J. L. Guerrero-Rascado, V. Rizi, A. A. Ruth, M. Sicard, F. Wagner, and L. Mona, EARLINET intensive observation period during summer 2012, *International Conference on Atmospheric Dust*, Castellaneta Marina, Italy, accepted, 2014.

3. Basart, S., M. Sicard, J. M. Baldasano, D. Lange, and A. Comerón, Optical characteristics of biomass burning and desert dust over the Western Mediterranean during summer: a case study, *EGU General Assembly*, Vienna (Austria), 2013.

4. Lange, D., D. Kumar, and F. Rocadenbosch, Backscattered signal level and SNR validation methodology for tropospheric elastic lidars, *IEEE International Geoscience and Remote Sensing Symposium*, Munich (Germany), 2012.

5. Kumar, D., D. Lange, F. Rocadenbosch, S. Tomás, M. Sicard, C. Muñoz, and A. Comerón, Power budget and performance assessment for the RSLAB multispectral elastic/Raman lidar system, *IEEE International Geoscience and Remote Sensing Symposium*, Munich (Germany), 2012.

6. Sawamura, P., J. Vernier, J. Barnes, T. Berkoff, E. Welton, L. Alados-Arboledas, F. Navas-Guzmán, G. Pappalardo,L. Mona, D. Lange, M. Sicard, S. Godin-Beekmann, G. Payen, Z. Wang, S. Tripathi, and R. Hoff, Lidar observations of stratospheric aerosol over the Northern Hemisphere from Nabro volcano: MPLNET, EARLINET, CALIPSO, NDACC synergy, *European Aerosol Conference (EAC)*, Granada (Spain), 2012.

7. Kumar, D., F. Rocadenbosch, M. Sicard, A. Comerón, C. Muñoz, D. Lange, S. Tomás, and E. Gregorio, Six channel polychromator design and implementation for the U.P.C. elastic/Raman LIDAR, 8182, pp. 81,820W/1-81,820W/10, *Proc. SPIE*, Prague, (Czech Republic), 2011.

8. Comerón, A., M. Sicard, D. Kumar, F. Rocadenbosch, and D. Lange, Utilization of a field lens to improve the overlap function in lidar systems using optical fibers, *Proc. 20th ILRC*, Porto Heli (Greece), 2012.

9. Lange, D., D. Kumar, F. Rocadenbosch, M. Sicard, and A. Comerón, Optimized data-gluing method for mixed analog/photon-counting lidar signals, *6th Workshop on Lidar Measurements in Latin America (WLMLA 6)*, La Paz (Bolivia) 2011.

10. M. Sicard, J. L. Guerrero, F. Navas, J. Preißler, F. Molero, L. Alados-Arboledas, A. Comerón, F. Wagner, S. Tomás, J. M. Bolarín, F. Rocadenbosch, D. Kumar, D. Lange, J. Bravo, J. Bolarin, M. Pujadas, and A. Requena, Coordinated measurements of the eruption of the Eyjafjalla Volcano by five SPALINET Lidar stations, *6th Workshop on Lidar Measurements in Latin America (WLMLA 6)*, La Paz (Bolivia) 2011.

11. M. Molero, F., A. J. Fernandez, M. Pujadas, M. Sicard, S. Tomás, A. Comerón, D. Lange, D. Kumar, J. Giner, C. Muñoz, F. Rocadenbosch, F. Navas-Guzmán, M. J. Granados, L. Alados-Arboledas, J. A. Bravo, J. Preißler, F. Wagner, and J. L. Guerrero-Rascado, Study on aerosol properties over Madrid (Spain) by multiple instrumentation during EARLINET lidar intercomparison campaign: SPALI10, *6th Workshop on Lidar Measurements in Latin America (WLMLA 6)*, La Paz (Bolivia) 2011.

12. Molero, F., F. J. Andrey, J. Preißler, F. Navas-Guzmán, A. Giunta, M. Sicard, A. J. Fernandez, M. C. Parrondo, F. Wagner, M. J. Granados, G. D'Amico, S. Tomás, M. Pujadas, C. Córdoba-Jabonero, J. L. Guerrero-Rascado, L. Alados-Arboledas, A. Amodeo, A. Comerón, J. A. Bravo, G. Pappalardo, D. Kumar, I. Mattis, V. Freudenthaler, D. Lange, J. Giner, C. Muñoz, and F. Rocadenbosch, Aerosol size distribution study by airborne and ground-level in-situ measurements and remote sensing during EARLINET lidar intercomparison campaign: SPALI10, *European Aerosol Conference (EAC2011)*, Manchester (United Kingdom), 2011.

A.3 National Conferences

1. Molero, F., A. Amodeo, M. Sicard, J. Preißler, F. Navas-Guzmán, V. Freudenthaler, A. J. Fernandez, A. Giunta, S. Tomás, F. Wagner, M. Granados, I. Mattis, M. Pujadas, G. D'Amico, A. Comerón, J. Guerrero-Rascado, L. Alados-Arboledas, D. Lange, J. Bravo, D. Kumar, G. Pappalardo, J. Giner, C. Muñoz, and F. Rocadenbosch, Study on aerosol properties over Madrid (Spain) by multiple instrumentation during SPALI10 lidar campaign, *V Reunión Española de Ciencia y Tecnología de Aerosoles (RECTA)*, pp. B4/1-B4/6, 2011.

References

Achtemeier, G. L., The Use of Insects as Tracers for "Clear-Air" Boundary-Layer Studies by Doppler Radar, *Journal of Atmospheric and Oceanic Technology*, *8*(6), 746–765, doi: 10.1175/1520-0426(1991)008<0746:TUOIAT>2.0.CO;2, 1991. 35

Ahmed, R., P. Siqueira, and S. Hensley, Analyzing the Uncertainty of Biomass Estimates From L-Band Radar Backscatter Over the Harvard and Howland Forests, *Geoscience and Remote Sensing, IEEE Transactions on*, *PP*(99), 1–19, doi: 10.1109/TGRS.2013.2273738, 2013. 7

Aixendri, S. C., Algoritmos de inversión Raman para un sistema Lidar (radar laser), Master's thesis, Escola Tècnica Superior d'Enginyeria de Telecomunicació de Barcelona (ETSETB), Dept. of TSC, Universitat Politècnica de Catalunya (UPC), Advisor: Dr. F. Rocadenbosch, 1998. 11

Alados-Arboledas, L., D. Müller, J. L. Guerrero-Rascado, F. Navas-Guzmán, D. Pérez-Ramírez, and F. J. Olmo, Optical and microphysical properties of fresh biomass burning aerosol retrieved by raman lidar, and star-and sun-photometry, *Geophysical Research Letters*, *38*(1), n/a–n/a, doi: 10.1029/2010GL045999, 2011. 127

Anderson, K., S. Doss-Hammel, D. Tsintikidis, B. Brooks, M. Smith, P. Caffrey, A. Clarke, L. Cohen, A. D. Jong, G. D. Leeuw, M. Moerman, K. Crahan, K. Davidson, P. Frederickson, D. Dion, C. Friehe, D. Khelif, T. Hristov, J. Reid, S. Reising, and E. Terrill, The red experiment: An assessment of boundary layer effects in a trade winds regime on microwave and infrared propagation over the sea, *Bull. Amer. Meteor. Soc.*, *85*, 1355–1365, doi: 10.1175/BAMS-85-9-1355, 2004. 8

Andrews, L., *Field guide to Atmospheric Optics*, SPIE Press, Bellingham, Washington USA, 2004. 22, 24

Angevine, W., A. White, and S. Avery, Boundary-layer depth and entrainment zone characterization with a boundary-layer profiler, *Boundary-Layer Meteorology*, *68*(4), 375–385, doi: 10.1007/BF00706797, 1994. 42

Angevine, W. M., Errors in Mean Vertical Velocities Measured by Boundary Layer Wind Profilers, *Journal of Atmospheric and Oceanic Technology*, *14*(3), 565–569, doi: 10.1175/1520-0426(1997)014<0565:EIMVVM>2.0.CO;2, 1997. 32, 35

Angevine, W. M., S. K. Avery, and G. L. Kok, Virtual Heat Flux Measurements from a Boundary-Layer Profiler-RASS Compared to Aircraft Measurements, *Journal of Applied Meteorology*, *32*(12), 1901–1907, doi: 10.1175/1520-0450(1993)032<1901:VHFMFA>2.0.CO;2, 1993. 32

Ansmann, A., Ground-truth aerosol lidar observations: Can the Klett solutions obtained from ground and space be equal for the same aerosol scenario?, *Appl. Opt.*, *45*, 3367–3371, 2006. 10, 44

Ansmann, A., U. Wandinger, M. Riebesell, C. Weitkamp, and W. Michaelis, Independent measurement of extinction and backscatter profiles in cirrus clouds by using a combined Raman elastic-backscatter lidar, *Appl. Opt.*, *31*(33), 7113–7131, 1992. 9, 10, 18, 28, 29, 52

Ansmann, A., F. Wagner, D. Althausen, D. Müller, A. Herber, and U. Wandinger, European pollution outbreaks during ACE 2: Lofted aerosol plumes observed with Raman lidar at the Portuguese coast, *Journal of Geophysical Research: Atmospheres*, *106*(D18), 20,725–20,733, doi: 10.1029/2000JD000091, 2001. 113

Ansmann, A., J. Bösenberg, A. P. Chaikovsky, A. Comerón, R. Eixmann, V. Freudenthaler, P. Ginoux, L. Konguem, H. Linné, M. Á. L. Márquez, S. Manoj, V. Matthias, I. Mattis, V. Mitev, D. Müller, S. Nickovic, J. Pelon, L. Sauvage, P. Sobolewsky, A. Stohl, O. Torres, G. Vaughan, U. Wandinger, and M. Wiegner, Long-range transport of Saharan dust to northern Europe: The 11-16 October 2001 outbreak with EARLINET, *Journal of Geophysical Research*, *108*(D24), 4783, doi:10.1029/2003JD00375, 2003. 4

Ansmann, A., M. Tesche, S. GroSS, V. Freudenthaler, P. Seifert, A. Hiebsch, J. Schmidt, U. Wandinger, I. Mattis, D. Müller, and M. Wiegner, The 16 April 2010 major volcanic ash plume over central Europe: EARLINET lidar and AERONET photometer observations at Leipzig and Munich, Germany, *Geophysical Research Letters*, *37*(13), n/a–n/a, doi: 10.1029/2010GL043809, 2010. 114

Ansmann, A., M. Tesche, P. Seifert, S. GroSS, V. Freudenthaler, A. Apituley, K. M. Wilson, I. Serikov, H. Linné, B. Heinold, A. Hiebsch, F. Schnell, J. Schmidt, I. Mattis, U. Wandinger, and M. Wiegner, Ash and fine-mode particle mass profiles from EARLINET-AERONET observations over central Europe after the eruptions of the Eyjafjallajökull volcano in 2010, *Journal of Geophysical Research: Atmospheres*, *116*(D20), n/a–n/a, doi: 10.1029/2010JD015567, 2011. 114, 122

Arason, P., G. N. Petersen, and H. Bjornsson, Observations of the altitude of the volcanic plume during the eruption of Eyjafjallajökull, April-May 2010, *Earth System Science Data*, *3*(1), 9–17, doi: 10.5194/essd-3-9-2011, 2011. 114

ATSRWorld, ATSRWorld Fire Atlas, `http://due.esrin.esa.int/wfa/`, European Space Agency, 2014. 117

Balanis, C. A., *Wiley: Antenna Theory: Analysis and Design, 3rd Edition - Constantine A. Balanis*, 3 ed., 1136 pp., Wiley-Interscience, New York, 2005. 33

Barlow, R., Estimation, in *Statistics: A Guide To The Use of Statistical Methods In The Physical Sciences*, edited by F. Mandl, R. Ellison, and D. Sandiford, chap. 5, pp. 68–96, Wiley, Chichester, England, 1989. 94, 100

Batchvarova, E., X. Cai, S.-E. Gryning, and D. Steyn, Modelling internal boundary-layer development in a region with a complex coastline, *Boundary-Layer Meteorology*, *90*(1), 1–20, doi: 10.1023/A:1001751219627, 1999. 39, 40, 100

Beer, A., Determination of the absorption of red light in colored liquids, *Ann. Phys*, *86*, 78–88, 1852. 22

Bioucas-Dias, J., A. Plaza, N. Dobigeon, M. Parente, Q. Du, P. Gader, and J. Chanussot, Hyperspectral unmixing overview: Geometrical, statistical, and sparse regression-based approaches, *Selected Topics in Applied Earth Observations and Remote Sensing, IEEE Journal of*, *5*(2), 354–379, doi: 10.1109/JSTARS.2012.2194696, 2012. 7

Bioucas-Dias, J. M., J. M. N. Leitão, and E. S. R. Fonseca, Reconstruction of backscatter and extinction coefficients in lidar: a stochastic filtering approach., *IEEE T. Geoscience and Remote Sensing*, *42*(2), 443–456, 2004. 13

Bissonnette, L. R., Sensitivity Analysis of Lidar Inversion Algorithms, *Appl. Opt.*, *25*(13), 2122–2125, 1986. 44

Blaunstein, N., S. Arnon, A. Zilberman, and N. Kopeika, *Applied aspects of optical communication and lidar*, Auerbach Publications, Boca Raton, FL, CRC press, 2010. 39

Böckmann, C., Hybrid regularization method for the ill-posed inversion of multiwavelength lidar data in the retrieval of aerosol size distributions, *Appl. Opt.*, *40*(9), 1329–1342, 2001. 10

Böckmann, C., U. Wandinger, A. Ansmann, J. Bösenberg, V. Amiridis, A. Boselli, A. Delaval, F. D. Tomasi, M. Frioud, A. Hågård, M. Horvat, M. Iarlori, L. Komguem, S. Kreipl, G. Larchevêque, V. Matthias, A. Papayannis, G. Pappalardo, F. Rocadenbosch, J. A. Rodriguez, J. Schneider, V. Shcherbakov, and M. Wiegner, Aerosol lidar intercomparison in the framework of EARLINET. 2. Aerosol backscatter algorithms, *Appl. Opt.*, *43*(4), 977–989, 2004. 4

Böckmann, C., D. Müller, L. Osterloh, P. Pornsawad, and A. Papayannis, From EARLINET-ASOS Raman-Lidar signals to microphysical aerosol properties via advances regularizing software, pp. (II–422)–(II–425), *IEEE International Geoscience and Remote Sensing Symposium*, 2008. 18, 44

Bodhaine, B. A., N. B. Wood, E. G. Dutton, and J. R. Slusser, On Rayleigh Optical Depth Calculations, *Atmos. and Ocean. Technol.*, *16*(11), 1854–1861, 1999. 29, 31, 55, 74

Boers, R., and E. Eloranta, Lidar measurements of the atmospheric entrainment zone and the potential temperature jump across the top of the mixed layer, *Boundary-Layer Meteorology*, *34*(4), 357–375, doi: 10.1007/BF00120988, 1986. 39, 100

Bösenberg, J., and R. Hoff, Plan for the implementation of the GAW Aerosol Lidar Observation Network (GALION), *Tech. rep.*, World Meteorological Organization, Hamburg, Germany, GAW Report no. 178, WMO/TD-No. 1443, 2007. 1, 4, 5, 9, 10, 29, 44, 78

Bösenberg, J., and V. Matthias, EARLINET: A European Aerosol Research Lidar Network to Establish an Aerosol Climatology, *Final report (2000-2003) 191*, Max-Planck Institut für Meteorologie, Hamburg (Germany), 2003. 3

Brown, R., and P. Hwang, *Introduction to Random Signals and Applied Kalman Filtering*, Wiley, New York, 1997. 13, 75, 77, 80, 81, 93

BSC-DREAM, BSC-DREAM8b v2.0 Atmospheric Dust Forecast System, `http://www.bsc.es/projects/earthscience/BSC-DREAM`, Earth Sciences Division of the Barcelona Supercomputing Center-Centro Nacional de Supercomputación (BSC-CNS), 2014. 117

CALIPSO, The Cloud-Aerosol Lidar and Infrared Pathfinder Satellite Observation (CALIPSO), `http://www-calipso.larc.nasa.gov/`, Last acceded: April, 2014, 2014. 5

Carn, S. A., and G. J. S. Bluth, Prodigious sulfur dioxide emissions from Nyamuragira volcano, D.R. Congo, *Geophysical Research Letters*, *30*(23), n/a–n/a, doi: 10.1029/2003GL018465, 2003. 106

Carn, S. A., N. A. Krotkov, K. Yang, R. M. Hoff, A. J. Prata, A. J. Krueger, S. C. Loughlin, and P. F. Levelt, Extended observations of volcanic SO_2 and sulfate aerosol in the stratosphere, *Atmospheric Chemistry and Physics Discussions*, *7*(1), 2857–2871, doi: 10.5194/acpd-7-2857-2007, 2007. 127

Cohn, S. A., and W. M. Angevine, Boundary Layer Height and Entrainment Zone Thickness Measured by Lidars and Wind-Profiling Radars, *Journal of Applied Meteorology*, *39*(8), 1233–1247, doi: 10.1175/1520-0450(2000)039<1233:BLHAEZ>2.0.CO;2, 2000. 40, 42

Collis, R., and P. Russell, Lidar measurements of Particles and Gases by Elastic Backscattering and Differential Absorption, in *Laser Monitoring of the atmosphere*, edited by E. Hinkley, chap. 4, pp. 71–102, Springer-Verlag, New York, 1976. 3, 9, 21, 22, 23, 24, 69

Comerón, A., F. Rocadenbosch, M. A. López, A. Rodríguez, C. Muñoz, D. García-Vizcaíno, and M. Sicard, Effects of noise on lidar data inversion with the backward algorithm, *Appl. Opt.*, *43*(12), 2572–2577, 2004. 9, 44, 49, 57

Comerón, A., F. Rocadenbosch, A. Rodriguez, M. A. Lopez, C. Munoz, D. Garcia Vizcaino, and M. Sicard, Lidar techniques for remote sensing of the atmosphere (invited paper), pp. 296–306, doi: 10.1117/12.618854, 2005. 20, 27

Contreras, R. F., and S. Frasier, High-Resolution Observations of Insects in the Atmospheric Boundary Layer, *J. Atmos. Oceanic Technol.*, *25*, 2176–2187, doi: doi:10.1175/2008JTECHA1059.1, 2008. 6, 32, 35, 36, 88, 90

Coulter, R., and T. Martin, Results from a high-power, high-frequency sodar, *Atmospheric Research*, *20*(2-4), 257–269, doi: 10.1016/0169-8095(86)90028-1, 1986. 100

Deirmendjian, D., Scattering and Polarization Properties of Water Clouds and Hazes in the Visible and Infrared, *Appl. Opt.*, *3*(2), 187–196, doi: 10.1364/AO.3.000187, 1964. 24

Deirmendjian, D., *Electromagnetic Scattering on Spherical Polydispersions*, RAND Corporation, 1969. 24

Deshler, T., A review of global stratospheric aerosol: Measurements, importance, life cycle, and local stratospheric aerosol, *Atmospheric Research*, *90*(2-4), 223 – 232, doi: http://dx.doi.org/10.1016/j.atmosres.2008.03.016, 17th International Conference on Nucleation and Atmospheric Aerosols {ICNAA07} O'Dowd {SI}, 2008. 104

Donovan, D. P., J. A. Whiteway, and A. I. Carswell, Correction for nonlinear photon-counting effects in lidar systems, *Appl. Opt.*, *32*, 6742–6753, 1993. 65

Draxler, R. R., and G. D. Rolph, NOAA Air Resources Laboratory, `http://www.arl.noaa.gov/ready/hysplit4.html`, Silver Spring, MD, 2003. 107

Draxler, R. R., and G. D. Rolph, HYSPLIT (HYbrid Single-Particle Lagrangian Integrated Trajectory) Model, `http://ready.arl.noaa.gov/HYSPLIT.php`, NOAA Air Resources Laboratory, Silver Spring, MD, 2012. 107

EARLINET, A European Aerosol Research Lidar Network to Establish an Aerosol Climatology: EARLINET, `http://www.earlinet.org/`, Last acceded: January, 2014, 2013. 5, 131

Eaton, F. D., S. A. McLaughlin, and J. R. Hines, A new frequency-modulated continuous wave radar for studying planetary boundary layer morphology, *Radio Science*, *30*(1), 75–88, doi: 10.1029/94RS01937, 1995. 18, 36

Emeis, S., K. Schäfer, and C. Münkel, Surface-based remote sensing of the mixing-layer height; a review, *Meteorologische Zeitschrift*, *17*(5), 621–630, doi: doi:10.1127/0941-2948/2008/0312, 2008. 9, 17

Emeis, S., K. Schäfer, and C. Münkel, Observation of the structure of the urban boundary layer with different ceilometers and validation by RASS data, *Meteorologische Zeitschrift*, *18*(2), 149–154, doi: doi:10.1127/0941-2948/2009/0365, 2009. 17

Endlich, R., F. Ludwig, and E. Uthe, An automatic method for determining the mixing depth from lidar observations, *Atmospheric Environment (1967)*, *13*(7), 1051 – 1056, doi: http://dx.doi.org/10.1016/0004-6981(79)90015-5, 1979. 17, 39

EURAD, EURopean Air Pollution Dispersion (EURAD) model system, `http://www.eurad.uni-koeln.de/index_e.html`, Rhenish Institute for Environmental Research at the University of Cologne, 2014. 123

Fairall, C. W., A Top-Down and Bottom-Up Diffusion Model of C T 2 and C Q 2 in the Entraining Convective Boundary Layer, *Journal of the Atmospheric Sciences*, *44*(6), 1009–1017, doi: 10.1175/1520-0469(1987)044<1009:ATDABU>2.0.CO;2, 1987. 132

Fernald, F. G., Analysis of Atmospheric Lidar Observations: Some Comments, *Appl. Opt.*, *23*(5), 652–653, 1984. 29

Fiocco, G., and L. D. Smullin, Detection of Scattering Layers in the Upper Atmosphere (60-140 km) by Optical Radar, *Nature*, *199*(4900), 1275–1276, doi: 10.1038/1991275a0, 1963. 2, 18

Flamant, C., J. Pelon, P. Flamant, and P. Durand, Lidar determination of the entrainment zone thickness at the top of the unstable marine atmospheric boundary layer, *Boundary-Layer Meteorology*, *83*(2), 247–284, doi: 10.1023/A:1000258318944, 1997. 76

Forest Fire North America, North America forest fire incident display system, http://fires.globalincidentmap.com/home.php, 2014. 111

Frasier, S., A. Muschinski, P.-S. Tsai, and M. Behn, Vertical Velocity Turbulence Observed with FMCW Radar, in *Geoscience and Remote Sensing Symposium, 2008. IGARSS 2008. IEEE International*, vol. 3, pp. III – 911–III – 914, doi: 10.1109/IGARSS.2008.4779498, 2008. 6, 8, 96

Freudenthaler, V., S. Gross, R. Engelmann, I. Mattis, U. Wandinger, G. Pappalardo, A. Amodeo, A. Giunta, G. D'Amico, A. Chaikovsky, F. Osipenko, A. Slesar, D. Nicolae, L. Belegante, C. Talianu, I. Serikov, H. Linne, F. Jansen, K. Wilson, M. de Graaf, A. Apituley, T. Trickl, H. Giehl, and M. Adam, Direct intercomparison of eleven EARLINET lidar systems, pp. 891–894, *Proc. 25nd International Laser Radar Conference* , 2010. 4, 5

Gilabert, J. B., Algoritmos de inversión 3D y campañas de medida, Master's thesis, Escola Tècnica Superior d'Enginyeria de Telecomunicació de Barcelona (ETSETB), Dept. of TSC, Universitat Politècnica de Catalunya (UPC), Advisor: Dr. F. Rocadenbosch, 1998. 11

Gossard, E. E., Radar research on the atmospheric boundary layer, in *Radar in Meteorology*, edited by L. J. Battan, D. Atlas, and A. M. Society, chap. 5, pp. 477–527, American Meteorological Society, 1990. 18, 36

Groß, S., M. Wiegner, V. Freudenthaler, and C. Toledano, Lidar ratio of Saharan dust over Cape Verde Island: Assessment and error calculation, *Journal of Geophysical Research*, *116*, D15,203, doi:10.1029/2010JD015435, 2011. 45, 122

Groß, S., V. Freudenthaler, M. Wiegner, J. Gasteiger, A. Geiß, and F. Schnell, Dual-wavelength linear depolarization ratio of volcanic aerosols: Lidar measurements of the Eyjafjallajökull plume over Maisach, Germany, *Atmospheric Environment*, *48*, 85–96, doi: 10.1016/j.atmosenv.2011.06.017, 2012. 115

Guerrero-Rascado, J. L., M. Sicard, F. Molero, F. Navas-Guzmán, J. Preißler, D. Kumar, J. A. Bravo-Aranda, S. Tomás, M. N. M. Reba, L. Alados-Arboledas, A. Comerón, M. Pujadas, F. Rocadenbosch, F. Wagner, and A. M. Silva, Monitoring of the Eyjafjalla Volcanic Plume at Four Lidar Stations over the Iberian Peninsula: 6 to 8 May 2010, *IV Reunión Española de Ciencia y Tecnología del aerosol (RECTA)*, pp. C15/1–C15/6, 2010. 67

Haeffelin, M., F. Angelini, Y. Morille, G. Martucci, S. Frey, G. Gobbi, S. Lolli, C. O'Dowd, L. Sauvage, I. Xueref-Rémy, B. Wastine, and D. Feist, Evaluation of Mixing-Height Retrievals from Automatic Profiling Lidars and Ceilometers in View of Future Integrated Networks in Europe, *Boundary-Layer Meteorology*, *143*(1), 49–75, doi: 10.1007/s10546-011-9643-z, 2012. 39

Hägeli, P., D. Steyn, and K. Strawbridge, Spatial And Temporal Variability Of Mixed-Layer Depth And Entrainment Zone Thickness, *Boundary-Layer Meteorology*, *97*(1), 47–71, doi: 10.1023/A:1002790424133, 2000. 39, 75, 76

Hamamatsu, P., *Photon Counting Using Photomultiplier Tubes*, 1998. 72

Hervo, M., B. Quennehen, N. I. Kristiansen, J. Boulon, A. Stohl, P. Fréville, J.-M. Pichon, D. Picard, P. Labazuy, M. Gouhier, J.-C. Roger, A. Colomb, A. Schwarzenboeck, and K. Sellegri, Physical and optical properties of 2010 Eyjafjallajökull volcanic eruption aerosol: ground-based, Lidar and airborne measurements in France, *Atmospheric Chemistry and Physics*, *12*(4), 1721–1736, doi: 10.5194/acp-12-1721-2012, 2012. 114

Hoff, R. M., J. Bösenberg, and G. Pappalardo, The GAW Aerosol Lidar Observation Network (GALION), *IEEE International Geoscience and Remote Sensing Symposium*, Boston MA, USA, 2008. 4

Holben, B. N., T. F. Eck, I. Slutsker, D. Tanre, J. P. Buis, A. Setzer, E. Vermote, J. A. Reagan, Y. J. Kaufman, T. Nakajima, F. Lavenu, I. Jankowiak, and A. Smirnov, AERONET: A federated instrument network and data archive for aerosol characterization, *Remote Sens. Environ.*, *66*, 1–16, 1998. 5

Hooper, W. P., and E. W. Eloranta, Lidar Measurements of Wind in the Planetary Boundary Layer: The Method, Accuracy and Results from Joint Measurements with Radiosonde and Kytoon, *J. Climate Appl. Meteor.*, *25*, 990–1001, doi: 10.1175/1520-0450(1986)025<0990:LMOWIT>2.0.CO;2, 1986. 42

Huneeus, N., and O. Boucher, One dimensional variational retrieval of aerosol extinction coefficient from synthetic LIDAR and radiometric measurements, *J. Geophys. Rsch.*, *112*(D14303), doi: 10.1029/2006JD007625, 2007. 44

Inaba, H., Detection of Atoms and Molecules by Raman Scattering and Fluorescence, in *Laser Monitoring of the Atmosphere*, edited by E. D. Hinkley, chap. 5, pp. 143–206, Springer-Verlag, New York, 1976. 28

İnce, T., S. J. Frasier, A. Muschinski, and A. L. Pazmany, An S-band frequency-modulated continuous-wave boundary layer profiler: Description and initial results, *Radio Science*, *38*(4), n/a–n/a, doi: 10.1029/2002RS002753, 2003. 6, 7, 8, 18, 36

Jäger, H., Long-term record of lidar observations of the stratospheric aerosol layer at Garmisch-Partenkirchen, *Journal of Geophysical Research: Atmospheres*, *110*(D8), n/a–n/a, doi: 10.1029/2004JD005506, 2005. 104

Kalman, R. E., A New Approach to Linear Filtering and Prediction Problems, *Transactions of the ASME Journal of Basic Engineering, (Series D)*(82), 35–45, 1960. 13

Klett, J. D., Stable Analytical Inversion Solution for Processing Lidar Returns, *Appl. Opt.*, *20*(2), 211–220, 1981. 9, 29, 30

Klett, J. D., Lidar Calibration and Extinction Coefficients, *Appl. Opt.*, *20*, 514–515, 1983. 43

Klett, J. D., Lidar Inversion with Variable Backscatter/Extinction Ratios, *Appl. Opt.*, *24*, 1638–1643, 1985. 11, 14, 29, 30, 31, 112, 126

Klett, J. D., Extinction boundary value algorithms for lidar inversion, *Appl. Opt.*, *25*(15), 2462–2464, 1986. 43

Knauss, D., Significance of the boundary value term in the Klett lidar inversion formula, *Appl. Opt.*, *21*(23), 4194, 1982. 49

Koshmieder, H., Theorie der horizontalen sichtweite, *Beitr. Phys. Freien Atmos.*, *12*, 33–53, 1924. 23

Kovalev, V. A., Lidar measurement of the vertical aerosol extinction profiles with rangedependent backscatter-to-extinction ratios, *Appl. Opt.*, *32*(30), 6053–6065, 1993. 10, 44

Kovalev, V. A., Stable near-end solution of the lidar equation for clear atmospheres, *Appl. Opt.*, *42*(3), 585–591, 2003. 10, 44

Kovalev, V. A., Fundamentals of the Lidar Technique, in *Elastic Lidar: Theory, Practice, and Analysis Methods*, edited by V. A. Kovalev and W. E. Eichinger, chap. 3, pp. 53–104, John Wiley & Sons, Inc., USA, 2004. 26, 73

Kruse, P. W., L. D. McGlauchlin, and R. B. McQuistan, *Elements of Infrared Technology*, Wiley, New York, 1963. 23

Kumar, D., Concept design, analysis, and Integration of the new U.P.C. multispectral lidar system, Ph.D. thesis, Universitat Politècnica de Catalunya (UPC), Barcelona (Spain), Thesis advisor: Dr. F. Rocadenbosch, 2012. 14, 129

Kumar, D., M. Sicard, S. Tomás, C. Muñoz, F. Rocadenbosch, and A. Comerón, Engineering of a water vapour, Raman, elastic-backscatter Lidar at the Technical University of Catalonia (Spain), 6367, pp. 63,670U/1–63,670U/12, *Proc. SPIE*, doi:10.1117/12.690701, 2006. 6

Kumar, D., F. Rocadenbosch, M. Sicard, A. Comerón, C. Muñoz, D. Lange, S. Tomás, and E. Gregorio, Six channel polychromator design and implementation for the U.P.C. elastic/Raman LIDAR, 8182, pp. 81,820W/1–81,820W/10, *Proc. SPIE*, doi: 10.1117/12.896305, 2011. 5

Kumar, D., D. Lange, F. Rocadenbosch, S. Tomás, M. Sicard, C. Muñoz, and A. Comerón, Power budget and performance assessment for the RSLAB multispectral elastic/Raman lidar system, *IEEE International Geoscience and Remote Sensing Symposium*, Munich (Germany), 2012. 6, 28, 69, 81, 82, 84

Kunkel, K. E., E. W. Eloranta, and S. T. Shipley, Lidar Observations of the Convective Boundary Layer, *J. Appl. Meteor.*, *16*, 1306–1311, 1977. 17

Kunz, G. J., Transmission as an input boundary value for an analytical solution of a singlescatter lidar equation, *Appl. Opt.*, *35*(18), 3255–3260, 1996. 10, 44

Kunz, G. J., and G. de Leeuw, Inversion of lidar signals with the slope method, *Appl. Opt.*, *32*(18), 3249–3256, 1993. 70

Kusunoki, K., A Preliminary Survey of Clear-Air Echo Appearances over the Kanto Plain in Japan from July to December 1997, *Journal of Atmospheric and Oceanic Technology*, *19*(7), 1063–1072, doi: 10.1175/1520-0426(2002)019<1063:APSOCA>2.0.CO;2, 2002. 35

Lammert, A., and J. Bösenberg, Determination of the convective boundary-layer height with laser remote sensing, *Boundary-Layer Meteorology*, *119*(1), 159–170, doi: 10.1007/s10546-005-9020-x, 2006. 17, 42

Lange, D., S. Frasier, J. Tiana-Alsina, and F. Rocadenbosch, Atmospheric Boundary Layer Height estimation using a Kalman filter and a FMCW radar, in preparation. 39, 87

Lange, D., D. Kumar, and F. Rocadenbosch, Backscattered signal level and SNR validation methodology for tropospheric elastic lidars, *IEEE International Geoscience and Remote Sensing Symposium*, Munich (Germany), 2012a. 6, 63, 64, 78

Lange, D., D. Kumar, F. Rocadenbosch, M. Sicard, and A. Comerón, Optimized data-gluing method for mixed analog/photon-counting lidar signals, *Óptica Pura y Aplicada*, 2012b. 63

Lange, D., J. Tiana-Alsina, U. Saeed, S. Tomás, and F. Rocadenbosch, Atmospheric boundary layer height monitoring using a kalman filter and backscatter lidar returns, *Geoscience and Remote Sensing, IEEE Transactions on*, *PP*(99), 1–12, doi: 10.1109/TGRS.2013.2284110, in press (accepted on October 24, 2013), 2013. 2, 41, 73, 80, 86, 87, 88, 92, 96, 100, 101, 129

Langmann, B., A. Folch, M. Hensch, and V. Matthias, Volcanic ash over Europe during the eruption of Eyjafjallajökull on Iceland, April-May 2010, *Atmospheric Environment*, *48*, 1–8, doi: 10.1016/j.atmosenv.2011.03.054, 2012. 114, 116

Lenoble, J., M. I. Mishchenko, and M. Herman, Absorption and scattering by molecules and particles, in *Aerosol Remote Sensing*, edited by J. Lenoble, L. Remer, and D. Tanré, chap. 2, pp. 13–51, Springer-Verlag Berlin Heidelberg, 2013. 21, 22, 24

Licel, Analysis example: Gluing analog and photon counting data, in *Licel Ethernet Controller-Installation and Reference Manual*, chap. 9.4, Licel, Germany, 2007a. 63, 64, 72

Licel, *Licel Ethernet Controller-Installation and Reference Manual*, Licel Gmbh, Germany, 2007b. 13, 69

Mahafza, B. R., and A. Z. Elsherbeni, Introduction to radar basics, in *Matlab Simulations for Radar Systems Design*, edited by CRC-Press, chap. 1, pp. 1–71, CRC Press, Boca Raton, FL, USA, 2004. xix, 8, 32, 33

Marchant, C. C., T. K. Moon, and J. H. Gunther, An Iterative Least Square Approach to Elastic-Lidar Retrievals for Well-Characterized Aerosols, *IEEE Trans. Geosci. Remote Sens.*, *48*(5), 2430–2444, 2010. 9, 13, 44

Martucci, G., V. Mitev, R. Matthey, and M. Srivastava, Remote-controlled automatic backscatter lidar for PBL and troposphere measurements: description and first results, 5235, pp. 661–672, SPIE, *Proc. of SPIE*, Bellingham, WA, 2003. 40, 41, 81

Matsumoto, M., and N. Takeuchi, Effects of misestimated far-end boundary values on two common lidar inversion solutions, *Appl. Opt.*, *33*(27), 6451–6456, 1994. 44

Matthias, V., D. Balis, J. Bösenberg, R. Eixmann, M. Iarlori, L. Komguem, I. Mattis, A. Papayannis, G. Pappalardo, M. R. Perrone, and X. Wang, Vertical aerosol distribution over Europe: Statistical analysis of Raman lidar data from 10 European Aerosol Research Lidar Network (EARLINET) stations, *J. Geophys. Res.*, *109*(D18201), doi:10.1029/2004JD004638, 2004a. 4

Matthias, V., V. Freudenthaler, A. Amodeo, I. Balin, D. Balis, J. Bosenberg, A. Chaykovski, G. Chourdakis, A. Comeron, A. Delaval, F. D. Tomasi, R. Eixmann, A. Hagard, L. Komguem, S. Kriepl, R. Matthey, V. Rizi, J. A. Rodrigues, U. Wandinger, and X. Wang, Aerosol lidar intercomparison in the framework of the EARLINET project. 1. Instruments, *Appl. Opt.*, *43*(4), 961–976, 2004b. 4

Matthias, V., A. Aulinger, J. Bieser, J. Cuesta, B. Geyer, B. Langmann, I. Serikov, I. Mattis, A. Minikin, L. Mona, M. Quante, U. Schumann, and B. Weinzierl, The ash dispersion over Europe during the Eyjafjallajökull eruption - Comparison of CMAQ simulations to remote sensing and air-borne in-situ observations, *Atmospheric Environment*, *48*(0), 184 – 194, doi: http://dx.doi.org/10.1016/j.atmosenv.2011.06.077, <ce:title>Volcanic ash over Europe during the eruption of Eyjafjallajöekull on Iceland, April-May 2010</ce:title>, 2012. 114

Mattis, I., A. Ansmann, D. Müller, U. Wandinger, and D. Althausen, Multiyear aerosol observations with dualwavelength Raman lidar in the framework of EARLINET, *J. Geophys. Res.*, *109*(D13203), doi:10.1029/2004JD004600, 2004. 31

Mattis, I., P. Siefert, D. Müller, M. Tesche, A. Hiebsch, T. Kanitz, J. Schmidt, F. Finger, U. Wandinger, and A. Ansmann, Volcanic aerosol layers observed with multiwavelength Raman lidar over central Europe in 2008-2009, *Journal of Geophysical Research: Atmospheres*, *115*(D2), n/a–n/a, doi: 10.1029/2009JD013472, 2010. 4, 104, 107, 127

McCormick, M. P., and K. R. Leavor, Active lidar remote sensing, in *Aerosol Remote Sensing*, edited by J. Lenoble, L. Remer, and D. Tanré, chap. 10, pp. 283–313, Springer-Verlag Berlin Heidelberg, 2013. 19, 24, 25, 26, 31

Measures, R. M., Interaction and Propagation of Radiation, in *Laser Remote Sensing: Fundamentals and Applications*, chap. 4, pp. 138–145, Krieger, Malabar, Fla., 1992a. 27

Measures, R. M., Laser Systems as Remote Sensors, in *Laser Remote Sensing: Fundamentals and Applications*, chap. 6, pp. 226–233, Krieger, Malabar, Fla., 1992b. 20, 27

Measures, R. M., Laser-Remote Sensor Equations, in *Laser Remote Sensing: Fundamentals and Applications*, chap. 7, pp. 237–280, Krieger, Malabar, FL USA, 1992c. 25, 26

Melfi, S. H., J. D. Spinhirne, S. H. Chou, and S. P. Palm, Lidar observation of vertically organized convection in the planetary boundary layer over the ocean, *J. Climate Appl. Meteor.*, *24*(8), 806–821, 1985. 17, 39, 40, 100

Menut, L., C. Flamant, J. Pelon, and P. H. Flamant, Urban Boundary-Layer Height Determination from Lidar Measurements Over the Paris Area, *Appl. Opt.*, *38*(6), 945–954, doi: 10.1364/AO.38.000945, 1999. 41, 42

Merritt, D. A., A Statistical Averaging Method for Wind Profiler Doppler Spectra, *Journal of Atmospheric and Oceanic Technology*, *12*(5), 985–995, doi: 10.1175/1520-0426(1995)012<0985:ASAMFW>2.0.CO;2, 1995. 32

MIRSL, The Microwave Remote Sensing Laboratory (MIRSL) at Department of Electrical and Computer Engineering at the University of Massachusetts Amherst, `http://mirsl.ecs.umass.edu/`, Last acceded: April, 2014. 8

Mok, T., and C. Rudowicz, A lidar study of the atmospheric entrainment zone and mixed layer over Hong Kong, *Atmospheric Research*, *69*(3-4), 147 – 163, doi: http://dx.doi.org/10.1016/j.atmosres.2003.09.004, 2004. 75

Molero, F., A. Amodeo, M. Sicard, J. Preißler, F. Navas-Guzmán, V. Freudenthaler, A. J. Fernandez, A. Giunta, S. Tomás, F. Wagner, M. Granados, I. Mattis, M. Pujadas, G. D'Amico, A. Comerón, J. Guerrero-Rascado, L. Alados-Arboledas, D. Lange, J. Bravo, D. Kumar, G. Pappalardo, J. Giner, C. Muñoz, and F. Rocadenbosch, Study on aerosol properties over Madrid (Spain) by multiple instrumentation during SPALI10 lidar campaign, *V Reunión Española de Ciencia y Tecnología de Aerosoles (RECTA)*, pp. B4/1–B4/6, 2011. 4, 12

Molero, F., A. J. Fernandez, M. Pujadas, M. Sicard, S. Tomás, A. Comerón, D. Lange, D. Kumar, J. Giner, C. Muñoz, F. Rocadenbosch, F. Navas-Guzmán, M. J. Granados, L. Alados-Arboledas, J. A. Bravo, J. Preißler, F. Wagner, and J. L. Guerrero-Rascado, Study on aerosol properties over Madrid (Spain) by multiple instrumentation during EARLINET lidar intercomparison campaign: SPALI10, *Óptica Pura y Aplicada*, 2012. 12

Molina, C. M., Creación de un entorno software para el acceso, segmentación y procesado de medidas lidar, Master's thesis, Escola Tècnica Superior d'Enginyeria de Telecomunicació de Barcelona (ETSETB), Dept. of TSC, Universitat Politècnica de Catalunya (UPC), Advisor: Dr. F. Rocadenbosch, 1998. 11

Mona, L., A. Amodeo, M. Pandolfi, and G. Pappalardo, Saharan dust intrusions in the Mediterranean area: Three years of Raman lidar measurements, *J. Geophys. Res.*, *111*(D16203), doi:10.1029/2005JD006569, 2006. 4, 116, 119

Mona, L., A. Amodeo, G. D'Amico, A. Giunta, F. Madonna, and G. Pappalardo, Multi-wavelength Raman lidar observations of the Eyjafjallajökull volcanic cloud over Potenza, southern Italy, *Atmospheric Chemistry and Physics*, *12*(4), 2229–2244, doi: 10.5194/acp-12-2229-2012, 2012. 114, 116, 118, 122

Moré, J., The Levenberg-Marquardt algorithm: Implementation and theory, in *Numerical Analysis*, *Lecture Notes in Mathematics*, vol. 630, edited by G. Watson, pp. 105–116, Springer Berlin Heidelberg, doi: 10.1007/BFb0067700, 1978. 80

Mukherjee, A., P. P. Adhikari, P. Nandi, P. Pal, and J. Das, Estimation of atmospheric boundary layer using Kalman filter technique, *Signal Processing*, *82*(11), 1763 – 1771, doi: http://dx.doi.org/10.1016/S0165-1684(02)00338-9, 2002. 75

Müller, D., A. Ansmann, I. Mattis, M. Tesche, U. Wandinger, D. Althausen, and G. Pisani, Aerosol type-dependent lidar ratio observed with Raman lidar, *Journal of Geophysical Research*, *112*, D16,202, doi:10.1029/2006JD008292, 2007. 4

Navas-Guzmán, F., D. Müller, J. A. Bravo-Aranda, J. L. Guerrero-Rascado, M. J. Granados-Muñoz, D. Pérez-Ramírez, F. J. Olmo, and L. Alados-Arboledas, Eruption of the Eyjafjallajökull Volcano in spring 2010: Multiwavelength Raman lidar measurements of sulphate particles in the lower troposphere, *Journal of Geophysical Research: Atmospheres*, *118*(4), 1804–1813, doi: 10.1002/jgrd.50116, 2013. 114, 115, 119, 123

Nishizawa, T., N. Sugimoto, I. Matsui, A. Shimizu, B. Tatarov, and H. Okamoto, Algorithm to retrieve Aerosol Optical Properties From High-Spectral-Resolution Lidar and Polarization Mie-Scattering Lidar Measurements, *IEEE Trans. Geosci. Remote Sens.*, *46*(12), 4094–4103, 2008. 10, 29

Noh, Y. M., D. Müller, I. Mattis, H. Lee, and Y. J. Kim, Vertically resolved light-absorption characteristics and the influence of relative humidity on particle properties: Multiwavelength Raman lidar observations of East Asian aerosol types over Korea, *Journal of Geophysical Research: Atmospheres*, *116*(D6), n/a–n/a, doi: 10.1029/2010JD014873, 2011. 127

Ottersten, H., Atmospheric Structure and Radar Backscattering in Clear Air, *Radio Science*, *4*(12), 1179–1193, doi: 10.1029/RS004i012p01179, 1969. 31

Pal, S., A. Behrendt, and V. Wulfmeyer, Elastic-backscatter-lidar-based characterization of the convective boundary layer and investigation of related statistics, *Annales Geophysicae*, *28*(3), 825–847, doi: 10.5194/angeo-28-825-2010, 2010. 39

Papayannis, A., V. Amiridis, L. Mona, G. Tsaknakis, D. Balis, J. Bösenberg, A. Chaikovski, F. D. Tomasi, I. Grigorov, I. Mattis, V. Mitev, D. Müller, S. Nickovic, C. Pérez, A. Pietruczuk, G. Pisani, F. Ravetta, V. Rizi, M. Sicard, T. Trickl, M. Wiegner, M. Gerding, R. Mamoury, G. D. Amico, and G. Pappalardo, Systematic lidar observations of Saharan dust over Europe in the frame of EARLINET (2000-2002), *J. Geophys. Res.*, *113*(D10204), doi:10.1029/2007JD009028, 2008. 4

Papayannis, A., R. E. Mamouri, V. Amiridis, E. Giannakaki, I. Veselovskii, P. Kokkalis, G. Tsaknakis, D. Balis, N. I. Kristiansen, A. Stohl, M. Korenskiy, K. Allakhverdiev, M. F. Huseyinoglu, and T. Baykara, Optical properties and vertical extension of aged ash layers over the Eastern Mediterranean as observed by Raman lidars during the Eyjafjallajökull eruption in May 2010, *Atmospheric Environment*, *48*, 56–65, doi: 10.1016/j.atmosenv.2011.08.037, 2012. 114

Pappalardo, G., A. Amodeo, A. Apituley, A. Comerón, V. Freudenthaler, H. Linné, A. Ansmann, J. Bösenberg, G. D'Amico, I. Mattis, L. Mona, U. Wandinger, V. Amiridis, L. Alados-Arboledas, D. Nicolae, and M. Wiegner, EARLINET: Towards an advanced sustainable European aerosol lidar network, in preparation. 6

Pappalardo, G., A. Amodeo, L. Mona, M. Pandolfi, N. Pergola, and V. Cuomo, Raman lidar observations of aerosol emitted during the 2002 Etna eruption, *Geophys. Res. Lett.*, *31*, 2004a. 4, 104, 113

Pappalardo, G., A. Amodeo, M. Pandolfi, U. Wandinger, A. Ansmann, J. Bosenberg, V. Matthias, V. Amiridis, F. D. Tomasi, M. Frioud, M. Iarlori, L. Komguem, A. Papayannis, F. Rocadenbosch, and X. Wang, Aerosol lidar intercomparison in the framework of the EARLINET project. 3 - Raman lidar algorithm for aerosol extinction, backscatter and lidar ratio, *Appl. Opt.*, *43*(28), 5370–5385, 2004b. 4

Pappalardo, G., J. Bösenberg, A. Amodeo, A. Ansmann, A. Apituley, L. Alados-Arboledas, D. Balis, C. Böckmann, A. Chaikovsky, A. Comerón, V. Freudenthaler, G. Hansen, V. Mitev, D. Nicolae, A. Papayannis, M. R. Perrone, A. Pietruczuk, M. Pujadas, J. P. Putaud, F. Ravetta, V. Rizi, V. Simeonov, N. Spinelli, D. Stoyanov, T. Trickl, and M. Wiegner, EARLINET-ASOS: European Aerosol Research Lidar Network-Advanced Sustainable Observation System, `www.earlinet.org`, American Meteorological Society Annual Meeting, San Antonio, Texas, USA, 2007. 5

Pappalardo, G., A. Amodeo, A. Ansmann, A. Apituley, L. Alados Arboledas, D. Balis, C. Boeckmann, A. Chaikovsky, A. Comeron, G. D'Amico, F. De Tomasi, V. Freudenthaler, E. Giannakaki, A. Giunta, I. Grigorov, O. Gustafsson, S. Gross, M. Haeffelin, M. Iarlori, S. Kinne, H. Linne, F. Madonna, R. Mamouri, I. Mattis, M. McAuliffe, F. Molero, L. Mona, D. Mueller, V. Mitev, D. Nicolae, A. Papayannis, M. Perrone, A. Pietruczuk, M. Pujadas, J.-P. Putaud, F. Ravetta, V. Rizi, I. Serikov, M. Sicard, V. Simeonov, N. Spinelli, K. Stebel, T. Trickl, U. Wandinger, X. Wang, F. Wagner, and M. Wiegner, EARLINET observations of the Eyjafjallajökull ash plume over Europe, in *Lidar technologies, techniques and measurements for atmospheric Remote Sensing VI*, edited by U. Singh and G. Pappalardo, Proceedings of SPIE-The International Society for Optical Engineering, SPIE-Int Soc OPtical Engeneering, 2010a. 114

Pappalardo, G., U. Wandinger, L. Mona, A. Hiebsch, I. Mattis, A. Amodeo, A. Ansmann, P. Seifert, H. Linné, A. Apituley, L. A. Arboledas, D. Balis, A. Chaikovsky, G. D'Amico, F. D. Tomasi, V. Freudenthaler, E. Giannakaki, A. Giunta, I. Grigorov, M. Iarlori, F. Madonna, R. E. Mamouri, L. Nasti, A. Papayannis, A. Pietruczuk, M. Pujadas, V. Rizi, F. Rocadenbosch, F. Russo, F. Schnell, N. Spinelli, X. Wang, and M. Wiegner, EARLINET correlative measurements for CALIPSO: First intercomparison results, *J. Geophys. Res.*, *115*(D00H19), doi:10.1029/2009JD012147, 2010b. 116

Pappalardo, G., L. Mona, G. D'Amico, U. Wandinger, M. Adam, A. Amodeo, A. Ansmann, A. Apituley, L. Alados Arboledas, D. Balis, A. Boselli, J. A. Bravo-Aranda, A. Chaikovsky, A. Comeron, J. Cuesta, F. De Tomasi, V. Freudenthaler, M. Gausa, E. Giannakaki, H. Giehl, A. Giunta, I. Grigorov, S. Groß, M. Haeffelin, A. Hiebsch, M. Iarlori, D. Lange, H. Linné, F. Madonna, I. Mattis, R.-E. Mamouri, M. A. P. McAuliffe, V. Mitev, F. Molero, F. Navas-Guzman, D. Nicolae, A. Papayannis, M. R. Perrone, C. Pietras, A. Pietruczuk, G. Pisani, J. Preißler, M. Pujadas, V. Rizi, A. A. Ruth, J. Schmidt, F. Schnell, P. Seifert, I. Serikov, M. Sicard, V. Simeonov, N. Spinelli, K. Stebel, M. Tesche, T. Trickl, X. Wang, F. Wagner, M. Wiegner, and K. M. Wilson, Four-dimensional distribution of the 2010 Eyjafjallajökull volcanic cloud over Europe observed by EARLINET, *Atmospheric Chemistry and Physics*, *13*(8), 4429–4450, doi: 10.5194/acp-13-4429-2013, 2013. 4, 67, 103, 106, 117, 119, 124, 127, 131

Pedros, R., V. Estelles, M. Sicard, J. Gomez-Amo, M. Utrillas, J. Martinez-Lozano, F. Rocadenbosch, C. Perez, and J. Recio, Climatology of the Aerosol Extinction-to-Backscatter Ratio from Sun-Photometric Measurements, *Geoscience and Remote Sensing, IEEE Transactions on*, *48*(1), 237–249, doi: 10.1109/TGRS.2009.2027699, 2010. 24, 31

Pérez, C., S. Nickovic, J. M. Baldasano, M. Sicard, F. Rocadenbosch, and V. E. Cachorro, A long Saharan dust event over the western Mediterranean: Lidar, Sun photometer observations, and regional dust modeling, *Journal of Geophysical Research*, *111*(D15214), 1–16, doi:10.1029/2005JD006579, 2006. 67, 74

Perrone, M. R., F. De Tomasi, A. Stohl, and N. I. Kristiansen, Integration of measurements and model simulations to characterize Eyjafjallajökull volcanic aerosols over south-eastern Italy, *Atmospheric Chemistry and Physics*, *12*(20), 10,001–10,013, doi: 10.5194/acp-12-10001-2012, 2012. 114, 122

Pietruczuk, A., J. W. Krzyścin, J. Jarosławski, J. Podgórski, P. Sobolewski, and J. Wink, Eyjafjallajökull volcano ash observed over Belsk (52°N, 21°E), Poland, in April 2010, *International Journal of Remote Sensing*, *31*(15), 3981–3986, doi: 10.1080/01431161.2010.498030, 2010. 114

Piironen, A. K., and E. W. Eloranta, Convective boundary layer mean depths and cloud geometrical properties obtained from volume imaging lidar data, *Journal of Geophysical Research: Atmospheres*, *100*(D12), 25,569–25,576, doi: 10.1029/94JD02604, 1995. 17

Pollard, B. D., S. Khanna, S. J. Frasier, J. C. Wyngaard, D. W. Thomson, and R. E. McIntosh, Local structure of the convective boundary layer from a volume-imaging radar, *J. Atmos. Sci.*, *57*, 2281–2296, doi: 10.1175/1520-0469(2000)057<2281:LSOTCB>2.0.CO;2, 2000. 6, 7

Qiu, J., Sensitivity of lidar equation solution to boundary values and determination of the values, *Adv. Atmos. Sci.*, *5*(2), 229–241, 1988. 44

Reagan, J. A., X. Wang, and M. T. Osborn, Spaceborn lidar calibration from cirrus and molecular backscatter returns, *IEEE Trans. Geosci. Remote Sens.*, *40*(10), 2285–2290, 2002. 9

Reba, M. N. M., Data processing and inversion interfacing the UPC elastic-Raman lidar system, Ph.D. thesis, Universitat Politècnica de Catalunya (UPC), Barcelona (Spain), Thesis advisor: Dr. F. Rocadenbosch, 2010. 11, 30, 107, 111, 125, 129

Reba, M. N. M., F. Rocadenbosch, and M. Sicard, A straightforward signal to-noise ratio estimator for elastic/Raman lidar signals, 6362, pp. 626,223/1–626,223/12, *Proc. SPIE*, 2006. 79, 95

Reba, M. N. M., F. Rocadenbosch, M. Sicard, C. Muñoz, and S. Tomás, Piece-wise variance method for signal-to-noise ratio estimation in elastic/Raman lidar signals, pp. 3158–3161, *Proc. IGARSS*, Barcelona(Spain), 2007. 79, 95

Reba, M. N. M., F. Rocadenbosch, M. Sicard, D. Kumar, and S. Tomás, On the lidar ratio estimation from the synergy between aeronet sun-photometer data and elastic lidar inversion, pp. 883–886, *Proc. 25th International Laser Radar Conference*, St. Petersburg (Russia), ISBN: 978-5-94458-109-9, 2010. 10, 11, 18, 44, 112, 126

Richter, J. H., High resolution tropospheric radar sounding, *Radio Science*, *4*(12), 1261–1268, doi: 10.1029/RS004i012p01261, 1969. 18, 36

Riley, J., Radar cross section of insects, *Proceedings of the IEEE*, *73*(2), 228–232, doi: 10.1109/PROC.1985.13135, 1985. 36

Robock, A., Volcanic eruptions and climate, *Reviews of Geophysics*, *38*(2), 191–219, doi: 10.1029/1998RG000054, 2000. 103

Rocadenbosch, F., Lidar-Wind, Raman and Other Sensing, in *Encyclopedia of Optical Engineering*, edited by D. D. Driggers, pp. 1114–1127, Marcel Dekker, New York, ISSN 0.8247-0939-X (print format), ISSN 0-8247-0940-3 (electronic format), 2003a. 28

Rocadenbosch, F., Lidar - Aerosol Sensing, in *Encyclopaedia of Optical Engineering*, edited by R. G. Driggers, pp. 1090–1102, Marcel Dekker, USA, 2003b. 3, 23, 24

Rocadenbosch, F., Lidar-Wind, Raman, and Other Sensing, in *Encyclopaedia of Optical Engineering*, edited by R. G. Driggers, pp. 1114–1127, Marcel Dekker, USA, 2003c. 3

Rocadenbosch, F., and A. Comerón, Error Analysis For The Lidar Backward Inversion Algorithm, *Appl. Opt.*, *38*(21), 4461–4474, 1999. 9, 13, 44

Rocadenbosch, F., A. Comerón, and D. Pineda, Assessment of lidar inversion errors for homogeneous atmospheres, *Appl. Opt.*, *37*(12), 2199–2206, 1998a. 13, 75, 79, 80, 81

Rocadenbosch, F., G. Vázquez, and A. Comerón, Adaptive Filter Solution for Processing Lidar Returns: Optical Parameter Estimation, *Appl. Opt.*, *37*(30), 7019–7034, doi: 10.1364/AO.37.007019, 1998b. 93

Rocadenbosch, F., C. Soriano, A. Comerón, and J. M. Baldasano, Lidar inversion of atmospheric backscatter and extinction-to-backscatter ratios by use of a Kalman filter, *Appl. Opt.*, *38*(15), 3175–3189, 1999. 9, 44, 75, 80

Rocadenbosch, F., M. N. M. Reba, M. Sicard, and A. Comerón, Practical analytical backscatter error bars for elastic one-component lidar inversion algorithm, *Appl. Opt.*, *49*(17), 3380–3393, 2010a. 9, 18, 44, 45, 46, 47, 49

Rocadenbosch, F., M. N. M. Reba, M. Sicard, S. Tomás, and D. Kumar, Lidar ratio estimation using a two-point calibration in an turbid layer aloft, pp. 59–62, *Proc. 25th International Laser Radar Conference*, ISBN: 978-5-94458-109-9, 2010b. 52

Rocadenbosch, F., S. Frasier, D. Kumar, D. Lange, E. Gregorio, and M. Sicard, Backscatter Error Bounds for the Elastic Lidar Two-Component Inversion Algorithm, *Geoscience and Remote Sensing, IEEE Transactions on*, *50*(11), 4791–4803, doi: 10.1109/TGRS.2012.2194501, 2012. 9, 10, 18, 129

Sasano, Y., and H. Nakane, Significance of the Extinction/Backscatter Ratio and the Boundary Value Term in the Solution for the Two-Component Lidar Equation, *Appl. Opt.*, *23*(1), 11–13, 1984. 44

Sasano, Y., and H. Nakane, Quantitative Analysis of RHI Lidar Data by an Iterative Adjustment of the Boundary Condition Term in the Lidar Solution, *Appl. Opt.*, *26*(4), 615–616, 1987. 43

Sasano, Y., E. V. Browell, and S. Ismail, Error Caused by Using a Constant Extinction/Backscattering Ratio in the Lidar Solution, *Appl. Opt.*, *24*(22), 3929–3932, 1985. 29, 44

Sauvageot, H., *Radar meteorology*, 374 pp., Artech House, 1992a. 2, 34, 35, 36, 39

Sauvageot, H., Basic concepts of radar, in *Radar meteorology*, chap. 1, pp. 1–68, Artech House, Norwood, MA, USA, 1992b. 32, 36, 39

Sawamura, P., J. Vernier, J. Barnes, T. Berkoff, E. Welton, L. Alados-Arboledas, F. Navas-Guzmán, G. Pappalardo, L. Mona, F. Madonna, D. Lange, M. Sicard, S. Godin-Beekmann, G. Payen, Z. Wang, S. Hu, S. Tripathi, C. Córdoba-Jabonero, and R. Hoff, Stratospheric AOD after the 2011 eruption of Nabro volcano measured by lidars over the Northern Hemisphere, *Environmental Research Letters*, *7*(3), 034,013, 2012. 4, 67, 103, 104, 111, 131

Scheve, T., and C. Swift, Profiling atmospheric water vapor with a K-band spectral radiometer, *Geoscience and Remote Sensing, IEEE Transactions on*, *37*(3), 1719–1729, doi: 10.1109/36.763294, 1999. 8

Schumann, U., B. Weinzierl, O. Reitebuch, H. Schlager, A. Minikin, C. Forster, R. Baumann, T. Sailer, K. Graf, H. Mannstein, C. Voigt, S. Rahm, R. Simmet, M. Scheibe, M. Lichtenstern, P. Stock, H. Rüba, D. Schäuble, A. Tafferner, M. Rautenhaus, T. Gerz, H. Ziereis, M. Krautstrunk, C. Mallaun, J.-F. Gayet, K. Lieke, K. Kandler, M. Ebert, S. Weinbruch, A. Stohl, J. Gasteiger, S. Groß, V. Freudenthaler, M. Wiegner, A. Ansmann, M. Tesche, H. Olafsson, and K. Sturm, Airborne observations of the Eyjafjalla volcano ash cloud over Europe during air space closure in April and May 2010, *Atmospheric Chemistry and Physics*, *11*(5), 2245–2279, doi: 10.5194/acp-11-2245-2011, 2011. 114, 115

Seibert, P., F. Beyrich, S.-E. Gryning, S. Joffre, A. Rasmussen, and P. Tercier, Review and intercomparison of operational methods for the determination of the mixing height, *Atmospheric Environment*, *34*(7), 1001 – 1027, doi: http://dx.doi.org/10.1016/S1352-2310(99)00349-0, 2000. 9, 17

Sekelsky, S. M., and E. E. Clothiaux, Parallax Errors and Corrections for Dual-Antenna Millimeter-Wave Cloud Radars, *J. Atmos. Oceanic Technol.*, *19*, 478–485, doi: doi:10.1175/1520-0426(2002)019<0478:PEACFD>2.0.CO;2, 2002. 8

Sicard, M., P. Chazette, J. Pelon, J. Gwang-Won, and S. C. Yoon, Variational method for the retrieval of the optical thickness and the backscatter coefficient from multiangle lidar profiles, *Appl. Opt.*, *41*(3), 493–502, 2002. 9, 10, 29

Sicard, M., C. Pérez, F. Rocadenbosch, J. M. Baldasano, and D. García-Vizcaino, Mixed-layer depth determination in the Barcelona coastal area from regular lidar measurements: methods, results and limitations, *Bound. Lay. Meteorol.*, *119*, 135–157, 2006. 39, 41, 42, 81

Sicard, M., A. Comerón, F. Rocadenbosch, A. Rodríguez, and C. Muñoz, Quasi-analytical determination of noise-induced error limits in lidar retrieval of aerosol backscatter coefficient by the Klett-Fernald-Sasano algorithm, *Appl. Opt.*, *48*(2), 176–182, 2009a. 9, 44, 46, 52, 54

Sicard, M., F. Molero, J. L. Guerrero-Rascado, R. Pedrós, F. J. Expósito, C. Córdoba-Jabonero, J. M. Bolarín, A. Comerón, F. Rocadenbosch, M. Pujadas, L. Alados-Arboledas, J. A. Martinez-Lozano, J. P. Díaz, M. Gil, A. Requena, F. Navas-Guzmán, and J. M. Moreno, Aerosol lidar intercomparison in the framework of SPALINET the SPAnish LIdar NETwork: methodology and results, *IEEE Trans. Geosci. Remote Sens.*, *47*, 3547Ű3559, 2009b. 4

Sicard, M., S. Tomás, M. N. M. Reba, A. Comerón, O. Batet, C. Muñoz, A. Rodríguez, F. Rocadenbosch, C. Muñoz-Tuñón, and J. Fuensalida, Aerosol stratification characterization of an astronomical site by means of a backscatter lidar at the Roque de los Muchachos Observatory, pp. 74,750P–1–74,750P–10, *Proc. SPIE*, 2009c. 111

Sicard, M., M. N. M. Reba, S. Tomás, A. Comerón, O. Batet, C. Muñoz, A. Rodríguez, F. Rocadenbosch, and J. J. Fuensalida, Site-testing results by means of an aerosol backscatter lidar at the Roque de los Muchachos Observatory, *Monthly Notices of the Royal Astronomical Society*, *405*, 129–142, dOI: 10.1111/j.1365-2966.2010.16468.x, 2010. 125

Sicard, M., J. L. Guerrero-Rascado, F. Navas-Guzmán, J. Preißler, F. Molero, S. Tomás, J. A. Bravo-Aranda, A. Comerón, F. Rocadenbosch, F. Wagner, M. Pujadas, and L. Alados-Arboledas, Monitoring of the Eyjafjallajökull volcanic aerosol plume over the Iberian Peninsula by means of four EARLINET lidar stations, *Atmospheric Chemistry and Physics*, *12*(6), 3115–3130, doi: 10.5194/acp-12-3115-2012, 2012. 4, 114, 115, 119, 127

Skolnik, M. I., *Introduction to Radar systems*, McGraw Hill, New York, 2001. 2, 25

Solomon, S., J. S. Daniel, R. R. Neely, J.-P. Vernier, E. G. Dutton, and L. W. Thomason, The Persistently Variable "Background" Stratospheric Aerosol Layer and Global Climate Change, *Science*, *333*(6044), 866–870, doi: 10.1126/science.1206027, 2011. 103

SPALINET, `http://www.lidar.es/spalinet/`, (accessed, January 2012), 2007. 4

Stenchikov, G., A. Robock, V. Ramaswamy, M. D. Schwarzkopf, K. Hamilton, and S. Ramachandran, Arctic Oscillation response to the 1991 Mount Pinatubo eruption: Effects of volcanic aerosols and ozone depletion, *Journal of Geophysical Research: Atmospheres*, *107*(D24), ACL 28–1–ACL 28–16, doi: 10.1029/2002JD002090, 2002. 106

Stephens, G. L., and R. J. Engelen, Toward retrieving properties of the tenuous atmosphere using space-based lidar measurements, *J. Geophys. Rsch.*, *106*(D22), 28.143–28.157, 2001. 9, 44

Steyn, D. G., M. Baldi, and R. M. Hoff, The detection of mixed layer depth and entrainment zone thickness from lidar backscatter profiles, *J. Atmos. Oceanic Technol.*, *16*, 953–959, doi: 10.1175/1520-0426(1999)016<0953:TDOMLD>2.0.CO;2, 1999. 75, 76, 81, 92, 117

Strauch, R. G., W. C. Campbell, R. B. Chadwick, and K. P. Moran, Microwave FM-CW Doppler radar for boundary layer probing, *Geophysical Research Letters*, *3*(3), 193–196, doi: 10.1029/GL003i003p00193, 1976. 36

Stull, R. B., Mean Boundary layer characteristics, in *An Introduction to Boundary Layer Meteorology*, chap. 1, pp. 1–28, Kluwer Academic Publishers, 1988a. 1, 2, 32, 38, 39

Stull, R. B., Measurements and simulation techniques, in *An Introduction to Boundary Layer Meteorology*, chap. 10, pp. 405–440, Kluwer Academic Publishers, 1988b. 2, 9, 100

Sugiyama, G. and Nasstrom, J. S., Methods for Determining the Height of the Atmospheric Boundary Layer, *Tech. Rep. UCRL-ID.133200*, Lawrence Livermore National Laboratory, 1999. 17

Taconet, O., and A. Weill, Convective plumes in the atmospheric boundary layer as observed with an acoustic Doppler sodar, *Boundary-Layer Meteorology*, *25*(2), 143–158, doi: 10.1007/BF00123971, 1983. 100

Tatarski'i, V., *Wave Propagation in a Turbulent Medium*, McGraw-Hill, 1961. 31, 36

Thordarson, T., and G. Larsen, Volcanism in Iceland in historical time: Volcano types, eruption styles and eruptive history, *Journal of Geodynamics*, *43*(1), 118 – 152, doi: http://dx.doi.org/10.1016/j.jog.2006.09.005, <ce:title>Hotspot Iceland</ce:title>, 2007. 113

Tomás, S., Contribution of Elastic-Backscatter Lidars to Wind Field Retrieval and Atmospheric Boundary Layer Monitoring, Ph.D. thesis, Universitat Politècnica de Catalunya (UPC), Barcelona (Spain), Thesis advisor: Dr. F. Rocadenbosch, 2011. 13, 130

Tomás, S., F. Rocadenbosch, and M. Sicard, Atmospheric boundary-layer height estimation by adaptive Kalman filtering of lidar data, pp. 782,704–782,704–10, doi: 10.1117/12.866477, 2010. 74

Trabal, J., J. Colom-Ustariz, S. Cruz-Pol, G. Pablos-Vega, and D. McLaughlin, Remote Sensing of Weather Hazards Using a Low-Cost and Minimal Infrastructure Off-the-Grid Weather Radar Network, *Geoscience and Remote Sensing, IEEE Transactions on*, *51*(5), 2541–2555, doi: 10.1109/TGRS.2012.2214227, 2013. 7

Trickl, T., H. Giehl, H. Jäger, and H. Vogelmann, 35 years of stratospheric aerosol measurements at Garmisch-Partenkirchen: from Fuego to Eyjafjallajökull, and beyond, *Atmospheric Chemistry and Physics Discussions*, *12*(9), 23,135–23,193, doi: 10.5194/acpd-12-23135-2012, 2012. 104

Vaisala, Vaisala Ceilometer CL-31, `http://www.vaisala.com/en/products/ceilometers/Pages/CL31.aspx`, Last accesed in February, 2014., 2014. 8

Vaughn, C., Birds and insects as radar targets: A review, *Proceedings of the IEEE*, *73*(2), 205–227, doi: 10.1109/PROC.1985.13134, 1985. 36, 88

Villani, M. G., L. Mona, A. Maurizi, G. Pappalardo, A. Tiesi, M. Pandolfi, M. D'Isidoro, V. Cuomo, and F. Tampieri, Transport of volcanic aerosol in the troposphere: the case study of the 2002 Etna plume, *J. Geophys. Res.*, *111*(D21102), doi:10.1029/2006JD007126, 2006. 104

Wandinger, U., Introduction to lidar, in *Lidar, Range-Resolved Optical Remote Sensing of the Atmosphere*, edited by C. Weitkamp, chap. 1, pp. 1–18, Springer, Singapore, 2005. 18, 19, 20, 24, 25

Wandinger, U., D. Müller, C. Böckmann, D. Althausen, V. Matthias, J. Bösenberg, V. Weiß, M. Fiebig, M. Wendisch, A. Stohl, and A. Ansmann, Optical and microphysical characterization of biomass-burning and industrial-pollution aerosols from multiwavelength lidar and aircraft measurements, *J. Geophys. Res.*, *107*(D21), 8125, doi:10.1029/2000JD000202, 2002. 31

Wang, X., A. Boselli, L. D'Avino, G. Pisani, N. Spinelli, A. Amodeo, A. Chaikovsky, M. Wiegner, S. Nickovic, A. Papayannis, M. R. Perrone, V. Rizi, L. Sauvage, and A. Stohl, Volcanic dust characterization by EARLINET during Etna eruptions in 2001-2002, *J. Atmos. Environ.*, *42*, 893–905, 2008. 4, 104

Warren, R. E., R. G. Vanderbeek, A. Ben-David, and J. L. Ahl, Simultaneous estimation of aerosol cloud concentration and spectral backscatter from multiple-wavelength lidar data, *Applied Optics*, *47*(24), 4309–4320, 2008. 13

Welton, E. J., J. R. Campbell, J. D. Spinhirne, and V. S. Scott III, Global monitoring of clouds and aerosols using a network of micropulse lidar systems, pp. 151–158, doi: 10.1117/12.417040, 2001. 5

Werner, C., Doppler wind lidar, in *Lidar, Range-Resolved Optical Remote Sensing of the Atmosphere*, edited by C. Weitkamp, chap. 12, pp. 325–355, Springer, Singapore, 2005. 5

Whiteman, D. N., Application of Statistical Methods to the Determination of Slope in Lidar Data, *Appl. Opt.*, *38*(15), 3360–3369, doi: 10.1364/AO.38.003360, 1999. 9

Whiteman, D. N., Examination of the traditional Raman lidar technique I. Evaluating the temperature-dependent lidar equations, *Appl. Opt.*, *42*(15), 2571–2592, 2003. 65, 72

Wiart, P., and C. Oppenheimer, Large magnitude silicic volcanism in north Afar: the Nabro Volcanic Range and Ma'alalta volcano, *Bulletin of Volcanology*, *67*, 99–115, 10.1007/s00445-004-0362-x, 2005. 105

Winker, D., J. Pelon, and P. McCormick, Initial Results from CALIPSO, pp. 991–994, *23rd International Laser Radar Conference*, Tokyo Metropolitan Univ., Tokyo, 2006. 5, 18

Winker, D. M., J. R. Pelon, and M. P. McCormick, The CALIPSO mission: spaceborne lidar for observation of aerosols and clouds, pp. 1–11, doi: 10.1117/12.466539, 2003. 105